Universiteit Antwerpen

Faculteit Wetenschappen
Departement Fysica

Charge Transport in Magnetic Topological Insulators

Ladingstransport in Magnetische Topologische Isolatoren

Thesis submitted for the degree of Doctor in Science: Physics at the University of Antwerp

AMIR SABZALIPOUR

Promotor

Prof. Dr. **Bart Partoens**

September 27, 2021

Members of the Jury:

Chair

Prof. dr. **Sara Bals**, Universiteit Antwerpen, Belgium

Promotor

Prof. dr. **Bart Partoens**, Universiteit Antwerpen, Belgium

Members

Prof. dr. **Dirk Lamoen** , Universiteit Antwerpen, Belgium

Prof. dr. **Llorenç Serra**, University of the Balearic Islands, Spain

Prof. dr. **Bart Sorée**, University Antwerp and KULeuven, Belgium

Contact Information

Amir Sabzalipour
Universiteit Antwerpen
Department of Physics
Groenenborgerlaan 171
2020 Antwerpen, België
am.sabzalipour@gmail.com

To Jahan, a friend for all seasons

ACKNOWLEDGEMENTS

The completion of this thesis would not have been possible without the assistance and support of many people. I want to take this chance to express my gratitude to them. First and foremost, I would like to thank my supervisor, Prof. Bart Partoens, for the scientific discussions we had during my Ph.D., for his guidance, constructive criticism, helpful research ideas, patience, and, most importantly, for giving me this opportunity to work on projects that I was very interested in.

I'd like to express my appreciation to our colleagues, Prof. Moslem Mir from Zabol University (Iran) and Dr. Mohammad Zarenia from Medical College of Wisconsin (MCW), for constructive discussions.

Next, I want to acknowledge the members of the condensed matter theory (CMT) group at the University of Antwerp for their friendliness and assistance in any way they could. I appreciate your kindness and for making my time in Antwerp unforgettable. A special thanks go to Hossein, Nikolas, Michael, Slavisa, Zeljko, Misa, Hamideh, Bert, and Ben.

Outside of academics, I am really grateful to my best friends Amir, Mostafa, Esmaeil, Mohammad, Maryam, Zahra, and Nadim for their unconditional support.

Finally, I'd like to thank my family for their unshakeable support over the years, especially my mother for being my biggest fan and my brother (Jahan) for being a friend for all seasons.

ABSTRACT

Novel quantum phases of matter and developing practical control over their characteristics is one of the primary aims of current condensed matter physics. It offers the potential for a new generation of energy, electronic and photonic technologies. Among all the newly found phases of matter, topological insulators are novel phases of quantum matter with fascinating bulk band topology and surface states protected by specific symmetries . For example, at the boundary of a strong topological insulator and a trivial insulator, metallic surface states appear that are protected by time-reversal symmetry. As a result, the bulk continues to be insulating, while the surface can support exotic high-mobility spin-polarized electronic states.

Since there is no such thing as a clean system, impurities and other disorders are always present in materials. Even while impurities appear to be unfavourable to a system at first look, doping the host system with impurities allows us to engineer different electronic properties of systems, such as the Fermi level or electron density. Because of the symmetry protected metallic states in topological insulators, charge transport responds distinctively to magnetic and non-magnetic impurities.

This doctoral dissertation explores how the longitudinal charge transport in magnetic topological thin films and the anomalous Hall effect on the surface of 3D magnetic topological insulators is influenced by point-like and randomly distributed dilute magnetic impurities. We are interested in how charge transport in these systems responds to the orientation of the magnetization orientation and how this response evolves based on the system's main characteristics, such as the magnitude of the Fermi level or gate voltage.

Because topological insulators have a strong spin-orbit coupling, the interaction between conducting electrons and local magnetic impurities is very anisotropic. We will show that this anisotropy even enhances when magnetic topological thin films are exposed to a substrate or gate voltage. Therefor, to properly capture this anisotropy in charge transport calculations, we rely on a generalized Boltzmann formalism together with a modified relaxation time scheme.

We show that magnetic impurities affect the charge transport in topological insulators by inducing a transition selection rule that governs scatterings of electrons between various electronic states. We see that this selection rule is highly sensitive to the spin direction of the magnetic impurities as well as the position of the Fermi level. According to this selection rule and depending on the position of the Fermi level, two different transport regimes are realized in magnetic topological thin films. In one of these regimes, our findings show that a dissipationless charge current can be generated. In other words, even if there are many magnetic impurities in the system, electrons do not notice them and, remarkably, conduct charge without dissipation. Outside this regime, the charge transport is always dissipative and its sensitivity to the spatial orientation of the magnetic impurities can be effectively modulated by a substrate or gate voltage.

In this doctoral thesis, we also explore the anomalous Hall effect (AHE) on the surface of 3D magnetic topological insulators. The AHE is generated by three mechanisms: the intrinsic effect (owing to a nonzero Berry curvature), the side jump effect, and the skew scattering effect. They compete to dominate the AHE in distinct regimes. Analytically, we calculate the contributions of all three mechanisms to the scattering of massive Dirac fermions by magnetic impurities. Our results reveal three transport regimes based on the relative importance of the engaged mechanisms. The identification of these three distinctive transport regimes can assist experimentalists in achieving a regime in which each contribution is dominant over the others, allowing them to measure them separately. Typically, this is not feasible empirically since the total value of the experimentally observed AHE conceals the specific information of each of the three contributions.

Based on our analytical calculations, we prove that the AHE can change sign by varying the orientation of the surface magnetization, the concentration of impurities, and the location of the Fermi level, which is consistent with previous experimental findings. In addition, we show that by suitably adjusting the given parameters, any contribution to the AHE, or even the entire AHE, can be turned off. For example, in a system with in-plane magnetization, one can turn off the AHE by pushing the system into the completely metallic regime.

Furthermore, we demonstrate that any contribution to the AHE, or even the whole AHE, can be turned off by appropriately changing the provided parameters. For example, in a system with in-plane magnetization, the AHE can be turned off by pushing the system into the fully metallic regime.

NEDERLANDSTALIGE ABSTRACT

De zoektocht naar nieuwe kwantumfasen en het realiseren van praktische controle over hun karakteristieken vormt momenteel een van de belangrijkste doelstellingen in de vaste-stoffysica. Het biedt het potentieel voor een nieuwe generatie technologieën. Topologische isolatoren vormen zo'n nieuwe kwantumfase met een fascinerende bulk band topologie en oppervlakte-toestanden beschermd door bepaalde symmetrieën. Zo vormen zich bijvoorbeeld op het grensvlak van een sterke topologische isolator en een triviale isolator metallische oppervlakte-toestanden die beschermd zijn door tijdsomkeersymmetrie. De bulk blijft isolerend, terwijl het oppervlak exotische spin-gepolariseerde elektronische toestanden met een grote mobiliteit ondersteunt.

Een materiaal bevat altijd onzuiverheden en andere vormen van wanorde. Ook al lijkt de aanwezigheid van onzuiverheden op het eerste zicht steeds ongunstig te zijn, laat het doteren van een materiaal met onzuiverheden toe om de elektronische eigenschappen ervan te tunen, zoals het Ferminiveau of de elektronendichtheid. Omwille van de door symmetrie beschermde oppervlakte-toestanden zal de aanwezigheid van magnetische en niet-magnetische onzuiverheden het ladingstransport in topologische isolatoren verschillend beïnvloeden.

In deze thesis wordt bestudeerd hoe het longitudinale ladingstransport in dunne magnetische topologische filmen en het 'anomalous' Hall effect beïnvloed worden door puntachtige en random gedistribueerde magnetische onzuiverheden. We zijn geïnteresseerd in hoe het ladingstransport in deze systemen beïnvloed wordt door de orientatie van de magnetisatie en hoe deze respons afhankelijk is van belangrijke karakteristieken van het systeem, zoals het Fermi-niveau of een aangelegde gate spanning.

Omdat topologische isolatoren een sterke spin-baan koppeling hebben, is de interactie tussen de geleidende elektronen en de lokale magnetische onzuiverheden sterk anisotropisch. We zullen tonen dat deze anisotropie zelfs kan versterkt worden in dunne magnetische topologische filmen die interageren met een substraat of onderhevig zijn aan een gate spanning. Om dit anisotroop ladingstransport volledig te kunnen vatten werd gebruik gemaakt van een veralgemeend Boltzmann formalisme samen met een aangepast

relaxatie-tijd schema.

De magnetische onzuiverheden bepalen het ladingstransport door een selectieregel op te leggen die de verstrooiing van elektronen tussen verschillende elektronische toestanden bepaalt. Deze selectieregel blijkt sterk afhankelijk van de magnetisatierichting van de onzuiverheden en van het Fermi-niveau. Ten gevolge van deze selectieregel en afhankelijk van het Fermi-niveau, kunnen twee verschillende transportregimes gerealizeerd worden in dunne magnetische topologische filmen. Zo kan een weerstandsloze ladingsstroom gegenereerd worden, waarbij de magnetische onzuiverheden de elektronen ongestoord laten passeren. Buiten dit regime is het ladingstransport steeds dissipatief en kan de afhankelijkheid van de oriëntatie van de magnetisatie gemoduleerd worden via een substraat of een gate spanning.

Daarnaast exploreren we in deze thesis ook hoe het 'anomalous' Hall effect (AHE) op het oppervlak van een 3D topologische isolator beïnvloed wordt door de richting van de oppervlakte-magnetisatie en hoe deze respons afhangt van de massa van de Dirac fermionen. Het AHE wordt gegenereerd door drie mechanismen: het intrinsieke effect (t.g.v. een Berry kromming verschillend van nul), het 'side jump' effect, en het 'skew scattering' effect, die elk het AHE kunnen domineren, afhankelijk van het regime. De bijdrage van elk mechanisme tot de verstrooiing van massieve Dirac Fermionen aan magnetische onzuiverheden werd analytisch bepaald. Onze resultaten tonen dat drie verschillende transportregimes kunnen geïdentificeerd worden op basis van het onderlinge relatieve belang van de drie mechanismen. De identificatie van deze drie verschillende trasportregimes kan experimentatoren helpen om een regime te realiseren waarin een mechanisme dominant is, waardoor ze apart kunnen gemeten en bestudeerd worden.

Onze analytische berekeningen tonen ook dat het teken van het AHE kan veranderen door veranderingen in de oriëntatie van de oppervlaktemagnetisatie aan te brengen, de concentratie aan onzuiverheden te wijzigen of het Fermi-niveau aan te passen. Dit is in overeenstemming met experimentele observaties. Daarnaast tonen we dat elk van de drie bijdragen, door het aanpassen van deze parameters, kan uitgezet worden, en dat zelfs het hele AHE kan verdwijnen. Bijvoorbeeld, in een systeem met enkel een magnetisatiecomponent in het vlak kan het AHE uitgezet worden door het systeem volledig in het metallische regime te brengen.

List of abbreviations

TIs	Topological insulators
TR	Time-reversal
3DTI	3D topological insulator
SOC	Spin-orbit coupling
QAH	Quantum anomalous Hall effect
AHE	Anomalous Hall effect
QSH	Quantum spin Hall
TRIMs	TR-invariant momenta points
ARPES	Angle-resolved photoemission spectroscopy
LDOS	Local density of states
TTFs	Topological thin films
MBE	Molecular beam epitaxy
VLS	Vapour–liquid-solid
QLs	Quintuple layers
SIA	Structure inversion asymmetry
RTA	Relaxation time approximation
AMR	Anisotropic Magnetoresistance
MTF	Magnetic topological ultra-thin film
YIG	Yttrium iron garnet
3DMT	Magnetic 3DTI

Table of Contents

CHAPTER 1

INTRODUCTION

Topological insulators (TIs) are of great interest in both fundamental physics and applied technology. Whenever the bulk of a D-dimensional topological insulator, like any other band insulator, is gapped, (D-1)-dimensional gapless states appear on its surfaces or edges [1–3]. These lower-dimensional metallic surface or edge states are protected by particular symmetries, such as time-reversal (TR) or crystalline symmetry [4]. TR invariant three-dimensional insulators are a large family of topological insulators occurring in materials with strong spin-orbit interaction.

Within a certain energy range, surface states of a 3D topological insulator (3DTI) can be described by an effective 2D massless Dirac Hamiltonian [1]. However, terms such as quadratic-in-momentum and anisotropic hexagonal-warping should be considered within the efficient Hamiltonian at higher energies [5–7].

Strong spin-orbit coupling (SOC) in TIs couples the spin of electrons to their momentum, resulting in spin-dependent charge transport [8, 9]. For example, backscattering of electrons from impurities on the surface of a 3DTI is prohibited as long as the impurity potential does not break the TR symmetry [10]. The SOC and the topologically protected edge states give rise to the quantum anomalous Hall effect (QAH) [11, 12], topological magnetoelectric effect [13], and a variety of other novel quantum phenomena [14–18].

All these exotic features of TIs have attracted a lot of interest theoretically and experimentally [1–3]. Revealing these topological transport features on the surface of 3DTIs or in thin topological films is an important direction of research. As there is no such thing as a pure material, impurities will always appear in it, and therefore we must understand how they influence the functioning of the base system. For this purpose, the dependency of charge transport in topological materials on the type of disorder and the range of disorder-electron interaction has been extensively studied [19].

When topological materials are doped with magnetic impurities, the story of charge transport differs significantly from that of non-magnetic topological materials. The collective behaviour of randomly distributed pointlike magnetic impurities in topological insulators will break time-reversal symmetry and forces the system into a gapped system. As a consequence, backscattering is no longer prohibited. This story becomes more interesting, when opposite surfaces in topological materials hybridize, and the substrate (or a gate voltage) breaks inversion symmetry.

1.1 Motivation

Although considerable studies have been devoted to the charge transport in magnetic topological materials in different systems and different regimes, less attention has been paid to the effect of the orientation of the magnetic impurities on the charge transport in 3DTIs.

In this doctoral thesis, we are primarily motivated to investigate how charge transport in magnetic 3DTIs responds to changes in the orientation of magnetization and how this response depends on the system's main characteristics, for example the value of the Fermi level. In addition, we are interested to know how this response can be controlled by external fields. To realize this goal, we investigate theoretically the longitudinal charge conductivity in magnetic topological ultra-thin films in chapters 3 and 4, after describing the applied theoretical methodology in chapter 2.

In chapter 3, we study how changing the spin orientation of point-like, short-range, and randomly distributed dilute magnetic impurities affects the

charge transport in magnetic topological ultra thin films. Magnetic impurities induce a chirality selection rule that governs electron transitions. This selection rule is sensitive to the spin direction of the impurities and the position of the Fermi level. Depending on this transition selection rule induced by the magnetic impurities, two distinct transport regimes are realized.

In chapter 4, we investigate how a substrate (or gate voltage) can affect the response of the charge transport in magnetic topological ultra-thin films to the orientation of the magnetization.

The Boltzmann approach is modified in chapter 5 to explore the anomalous Hall effect (AHE) on the surface of magnetic 3DTIs. In this chapter, we take into account changes in the orientation of the magnetic impurities, in addition to other degrees of freedom, to better understand the physics behind the experimentally observed sign change of the AHE observed in magnetic topological materials [20].

In all three chapters 3, 4 and 5, we rely on low-energy Hamiltonians that capture the fundamental mechanics of these systems. We proceed by giving a brief historical overview of the development of the topological phases and consequently topologically protected transport properties.

1.2 What is topology?

To comprehend the topological aspects of electronic properties of TIs, the concept of topology has first to be clarified. In this section, we make a link between topological properties of shapes in mathematics and topological properties of materials using the *Gauss-Bonnet* theorem. This link highlights the significance of topological quantities in topological materials.

A manifold is a topological space in geometry that, near each point, resembles Euclidean space. If manifold A and B can be adiabatically deformed into each other, they have the same topology. Otherwise, we will call them topologically distinct. Mathematicians develop topological parameters to differentiate various manifolds and objects with the same topology take the same value for a particular topological parameter.

The *Gauss–Bonnet* theorem plays a crucial role in our understanding of

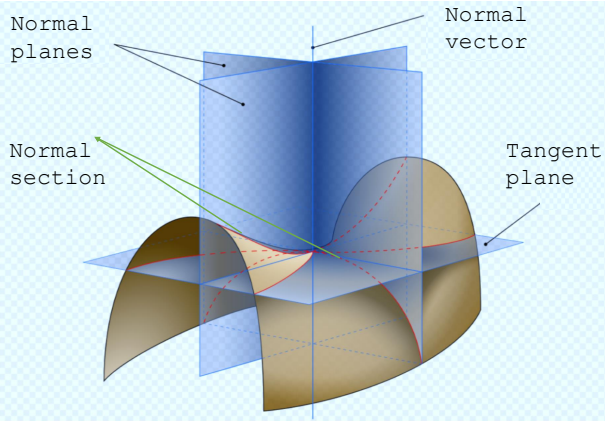

Figure 1.1: Illustration of normal planes, normal vector, normal selection and tangent plane (adopted from Ref. [21]).

topology. This theorem relates the *Gaussian curvature*, as a local property, to the *Euler characteristic*, as a global or topological property for a 2D closed manifold. To define the curvature for a curve at a particular point, we draw a circle to meet the point. The curvature of each drawn circle is defined as $k = \frac{1}{R}$, where R denotes the radius of a particular circle. It is obvious that lots of curves can be drawn at a particular place on a manifold.

As shown in Fig. 1.1, at each point on a 2D manifold, we can find a normal vector that is perpendicular to the surface, and the planes containing the normal vector are referred to as normal planes. The intersection of a normal plane and a 2D manifold yields a curve known as a normal section, and the curvature of this curve is known as the normal curvature. Different normal selections will have different curvatures at most points on a particular 2D manifold. The largest and smallest values of these curvatures are called the principal curvatures, which are denoted by k_1 and k_2. The Gaussian curvature is defined as $\kappa = k_1 k_2$. For example for a sphere $k_1 = k_2 = \frac{1}{R}$ and $\kappa = \frac{1}{R^2}$. The *Euler characteristic* χ was classically defined for the surfaces of polyhedra, and it is $\chi = V - E + F$, where V, E, and F denote the numbers of vertices (corners), edges and faces in the given polyhedron. For example for a octahedron, $V = 6$, $E = 12$, $F = 8$, resulting in $\chi = 2$. For a closed 3D object, $\chi = 2(1 - g)$, where g denotes the genus in the manifold, or in other words, χ measures the number of "handles" on the object. Now, for any compact and two-dimensional manifold, the two introduced concepts, *Euler characteristic* and *Gaussian curvature* can be connected. The integral of the *Gaussian*

curvature over the entire manifold reads

$$\int\int_M \kappa \, dS = 2\pi\chi. \tag{1.1}$$

For every 2D closed manifold, $\int\int_M \kappa \, dS$ over the whole manifold is invariant no matter how the manifold is deformed (adiabatically), and its value only cares about the topology of the manifold M. Eq. 1.1 is somewhat surprising because the *Gaussian curvature* depends on the local geometry of the manifold while the *Euler characteristic* is entirely independent of the geometry. As a result, regardless of how we deform the geometry of the manifold, the same total curvature persists.

The representation of shapes in geometry is essential. A right-angled triangle differs from an equilateral triangle, for example. Topologically, these two triangles, as well as many other forms, are identical. In general, two objects are topologically identical if one of them can be stretched, shrunk, bent, or twisted to look like the other. It is not allowed to tear or attach. A triangle, a square, and a circle are all topologically equivalent, but none are topologically equivalent to a line segment. We would have to tear a triangle to produce a line segment, then stick two line segments together to form a triangle.

After this brief introduction to the concept of topological properties, the question arises: what functions in condensed matter physics as genus and *Gaussian curvature*? The question will be answered in section 1.4.1. We first discuss the function of an energy gap in the topological classification of materials before answering this question.

1.3 The role of the energy gap in the topological classification of materials

To systematically study the electronic properties of crystals and classify them based on their electrical conductivity, we employ band theory which is one of the triumphs of quantum mechanics in the 20th century. Within this theory, Bloch's theorem states that solutions to the Schrödinger equation in a periodic potential take the form of a plane wave modulated by a periodic function.

Bloch's theorem employs the translational symmetry of crystals to distinguish electronic states in terms of their crystal momentum $\boldsymbol{k}$, defined in a periodic Brillouin zone.

The Bloch states $u_{\boldsymbol{k}}$ are eigenstates of the Bloch Hamiltonian $H(\boldsymbol{k})$, defined in a single unit cell of a crystal. The eigenvalues of Bloch Hamiltonian $H(\boldsymbol{k})$, $E(\boldsymbol{k})$ are energy bands that collectively construct the band structure. According to the band structure of an insulator, an energy gap separates the occupied valence band states from the empty conduction band states. The size of the energy gap in good insulators is larger than the size of the energy gap in semiconductors.

In material science, one way to classify materials is based on the size of the gap that appears in their band structure. However, in terms of topology, a particular semiconductor can be adiabatically transformed to a particular perfect insulator. Hence, based on their electronic properties they belong to two distinct classes, while in terms of topology they are in the same class. Generally speaking, quantum phases with an energy gap are topologically equivalent provided that they can be smoothly deformed to each other without closing the gap, as shown in panel a of Fig. 1.2. In other words, insulators are topologically equivalent if there exists an adiabatic path connecting their associated Hamiltonians (in parametric space) provided that the energy gap remains finite. Indeed, such insulators are topologically equivalent to the vacuum which based on Dirac's relativistic quantum theory has an energy gap between conduction and valence bands.

Then, as long as the interior remains insulating, changing the material parameters does not change the topological class which is characterized by the presence (or absence) of robust surface conduction. While the number of holes in closed 2D surfaces can be any positive integer, there are only two topologically distinct types of TR invariant insulators: topological insulators (surface conduction) and trivial insulators (no surface conduction). Just as we can only deform a sphere to a donut if a hole is created, we can only transition between a trivial and a topological insulator if the interior of the materials stops being an insulator. Due to the fact that the surface of a topological insulator has a boundary with air, a trivial insulator, the material must

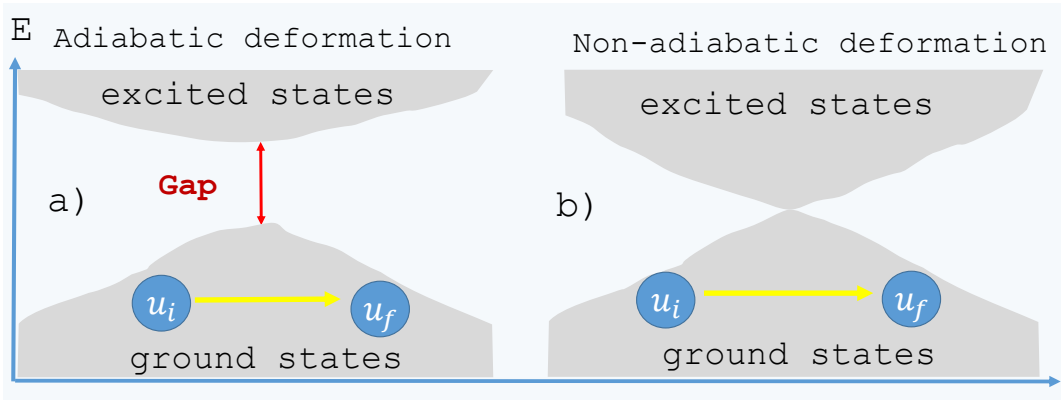

Figure 1.2: (a): Smooth deformation in which there is an adiabatic path connecting a particular state u_i to u_f without closing the gap. (b): Non-smooth deformation. The gap vanishes during the transformation $u_i \rightarrow u_f$.

conduct across the interface to transition between two topologically distinct regions. This is why, regardless of the details, the surface of a topological insulator conducts electricity.

1.4 The quantum Hall effect (QHE)

The electronic states in the QHE are the first discovered topological states. The QHE is a perfect phenomenon in which local non-topological electronic properties are connected to the topological properties, as seen in mathematics. We begin by introducing the classical-quantum Hall effect, which serves as the foundation for the QHE.

The Hall effect was discovered by *Edwin Hall* in 1879. It occurs when a conductor is subjected to a magnetic field and a in-plane electric field. The solution of the motion equation of electrons,

$$m\frac{d^2\mathbf{r}}{dt^2} = -e\boldsymbol{E} - e\mathbf{v}\times\boldsymbol{B}, \tag{1.2}$$

describes the trajectory of an electron in the presence of electric and magnetic fields as follows

$$\mathbf{r}(t) = \mathbf{v}_0 t + \mathbf{r}_0(t), \tag{1.3}$$

where $\mathbf{v}_0 = (\boldsymbol{E}\times\boldsymbol{B})/B^2$, $\mathbf{r}_0(t) = r_0(\cos\omega_c t, \sin\omega_c t, 0)$, $\omega_c = eB/m$. Also, e, m_e and v are the charge, mass and velocity of electrons, respectively. Considering the electric and magnetic fields are perpendicular to each other (i.e. $\mathbf{E}$ =

$E\hat{x}$ and $\mathbf{B} = B\hat{z}$) the solution to Eq. (1.3) is a superposition of a circular motion with frequency $\omega_c = eB/m_e$ (cyclotron frequency), and a linear motion with velocity E/B. Therefore electrons move in a spiral trajectory along the equipotential lines.

However, von Klitzing (1980) discovered the quantized version of the Hall effect [22]. In the QHE, a 2D electron gas, for example in a $GaAs/AlAs$ quantum well is subjected to a strong magnetic field (typically several Tesla) at low Temperatures $T < 4K$. The energy of electrons in the electron gas can be described by the Landau theory, which says that charged particles in a uniform magnetic field have quantised energy, the Landau levels

$$\varepsilon_n = (n + 1/2)\hbar\omega_c, \quad n \in \mathbb{N}. \tag{1.4}$$

Each Landau level is degenerate and can accommodate a large, but finite number of electrons. According to the experimental data observed for the QHE, the Hall resistivity R_H takes the value

$$R_H = \frac{h}{e^2}\frac{1}{\nu}, \tag{1.5}$$

where h is the Planck's constant and ν takes on only integer values in integer QHE. The above transverse resistivity R_H takes on a plateau form, as seen by the green curve in Fig. 1.3. It is constant over a wide range of magnetic fields and moves to the next plateau as the magnetic field vastly varies. When R_H is at a plateau, the longitudinal resistivity ρ_{xx} is zero, and when R_H changes from one plateau to the next, ρ_{xx} spikes. From our classical calculation based on the *Drude* model, the Hall conductivity reads

$$R_H = \frac{B}{n_e e}, \tag{1.6}$$

which depends on the density of electrons n_e. Comparing the Eqs. 1.6 and 1.5, we see that if we choose

$$n_e = \frac{B}{\Phi_0}\nu, \tag{1.7}$$

with $\Phi_0 = \frac{2\pi\hbar}{e}$, we reach the Eq. 1.5. This is indeed the density of electrons required to fill precisely ν landau levels to get Eq. 1.5. Furthermore, when ν Landau levels are filled, there is a gap in the energy spectrum: to occupy the

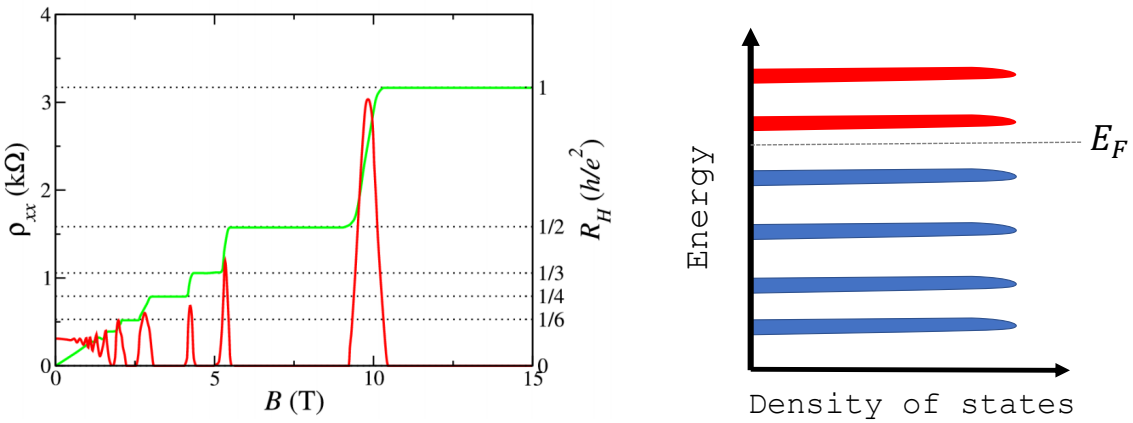

Figure 1.3: (a): Longitudinal (the red line) and transverse resistivities (the green line) observed in the QHE as function of the applied magnetic field. Image adapted from [22]. (b): Density of electronic states in the QHE.

next state costs an energy $\hbar\omega_c$ where ω_c is the cyclotron frequency. As long as we are at a temperature $\kappa_B T \lesssim \hbar\omega_c$, these states will remain empty. When we turn on a small electric field, there is nowhere for the electrons to move: they are stuck in place like in an insulator. This means that the scattering time is infinite and the longitudinal resistivity is zero. In contrary to the bulk, as panel *d* of Fig. 1.4 presents, when an electron orbital center is close to the system's edge, an electric field causes the cyclotron orbits to drift along the edge, resulting in Hall current characterized by quantized Hall conductivity.

1.4.1 The TKNN invariant

What is the distinction between QHE and normal insulators? As explained by *Thouless*, *Kohmoto*, *Nightingale*, and *den Nijs* (TKKN) the answer is a matter of topology [23]. In other words, small changes in the Hamiltonian describing the QHE, such as disorder, have little effect on the amount ν of filled Landau levels. The observed transverse conductance in QHE is a global property that is unaffected by Hamiltonian "deformations". This robustness of the number of edge states seems to be quite close to the robustness of the *Euler characteristic*. This interesting point inspired TKKN to search for a topological invariant characterizing the quantum Hall effect. Their idea relies on the concept of a magnetic unit cell. Suppose the number of flux quanta per

unit cell in a 2D periodic system subjected to a perpendicular magnetic field is rational. In that case, the periodicity is maintained by taking a larger unit cell, demonstrating that the Hall conductance is provided by a topological quantum number, the TKNN integer [24, 25].

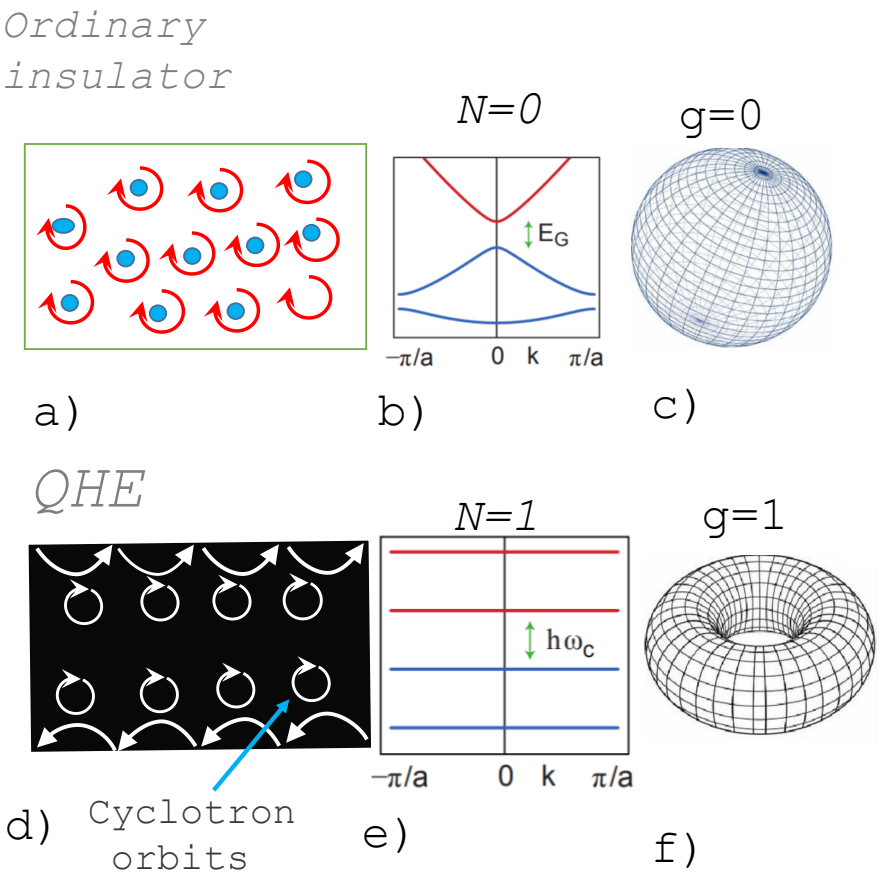

Figure 1.4: (a): The most simple insulator, with electrons bound to atoms in closed shells. (b): A simple model insulating band structure for which the chern number $N = 0$. (c): A sphere with genus $g = 0$. (d): The cyclotron motion of electrons in the QHE. (e): The Landau levels in the QHE for which chern number $N = 1$. (f): A donut with genus $g = 1$.

Topologically, gapped band structures can be identified by looking at the equivalence group of the Hamiltonian $H(\boldsymbol{k})$ that can be smoothly deformed into each other without closing the energy gap. The Chern invariant is a topological tool that can distinguish these groups. The Chern invariant is rooted in fiber bundle theory [26], however it can be physically understood in terms of the Berry phase. When $\boldsymbol{k}$ is transported around a closed-loop, Bloch wave functions $u_{\boldsymbol{k}}$ acquires a well-described Berry phase given by the line integral of $A_m = i\langle u_m(\boldsymbol{k}) \mid \nabla_{\boldsymbol{k}} \mid u_m(\boldsymbol{k})\rangle$. *Thouless* and coworkers showed that

when the Fermi level lies in the gap, the Hall conductance can be written as [23]

$$\sigma_{xy} = N\frac{e^2}{h}, \tag{1.8}$$

where

$$N = \sum n_m = \frac{1}{2\pi}\sum_m \int d^2\mathbf{k}(\nabla \times A_m(\boldsymbol{k})). \tag{1.9}$$

The total Chern number N summed over all occupied bands is invariant even if there are degeneracies between occupied bands, provided the gap separating occupied and empty bands remains finite.

Comparing Eq. (1.8) with the experimentally observed Hall conductance $\sigma_{xy} = \nu\frac{e^2}{h}$ proves that $N = \nu$. The Chern number N is a topological invariant in the sense that it can not change when the Hamiltonian varies smoothly (see panel *a* of Fig. 1.2). The connection between ν and the topological invariant N explains why the experimentally observed Hall conductance is robust against smooth deformations and why the Hall conductance has been measured to one part in 10^9 [27].

We are now prepared to answer the question raised at the end of sections 1.2. We asked what functions as genus and *Gaussian curvature* in condensed matter physics. Now we can say that the Chern number and the Berry curvature play the same role in the band topology of condensed matter systems as genus and *Gaussian curvature* do in the topology of manifolds in mathematics. The Chern number can distinguish the QHE from all gaped system that are topologically equivalent to vacuum, in the same way that genus can distinguish a sphere from a donut, as shown in Fig. 1.4.

In the following sections, we will describe other members of the topological material family that are distinct from ordinary insulators.

1.5 Quantum spin Hall state

The quantum Hall state was the first discovered topological state. As discussed in the last section, the quantum Hall insulator requires a high magnetic field to reveal its topological nature. Then the question arises: Is it essential for a system to be exposed to a magnetic field to acquire topological states?

When time reversal symmetry is preserved in a system, the total Berry curvature

$$\sum \int d^2\mathbf{k} \nabla \times A_m(\boldsymbol{k}), \tag{1.10}$$

is an odd function of momentum and consequently the Hall conductance vanishes [28]. As a result, it was assumed that topological phases required broken TR symmetry. However, *Haldane* made a remarkable discovery in 1988 [29]. He considered an electron model on a honeycomb lattice and demonstrated that the Hall conductance in such a system is quantized to the values $\sigma_{xy} = \frac{e^2}{h}$ in the absence of the magnetic field. Following the discovery of graphene [30–32], whose dispersion is characterized by massless Dirac fermions at two particular places in the Brillouin zone, people became again interested in the *Haldane* model.

Kane and *Mele* found that the addition of spin-orbit coupling can turn graphene into an insulating phase with quantized non-zero spin Hall conductance defined as $\sigma_{xy,s} = \sigma_{xy,\uparrow} - \sigma_{xy,\downarrow}$. They proved that their model gives two QHE states, equivalent to two copies of the *Haldane* model with opposite magnetic fields for the two spin orientations [33]. This phase is known as a quantum spin Hall (QSH) insulator or a 2D time-reversal-invariant topological insulator.

The QSH and the QHE are fundamentally different. Although they both have chiral edge states, as shown in Fig. 1.5, the inclusion of TR symmetry in the QSH significantly changes the system's behaviour. TR symmetry is broken for a single copy of the QHE state by the magnetic field. However, TR is preserved in the combined form because the TR operator reverses both the direction of the magnetic field and the spin.

To preserve TR symmetry, a spin-up electron moving clockwise must match up with a spin-down electron moving counterclockwise. Therefore, the two edge states propagate in opposite directions and with opposite spins in the QSH, as shown in panel *e* of Fig. 1.5. *Kane* and *Mele* demonstrated that spin-orbit coupling can act as a magnetic field with an opposite sign for opposite spins. As panel *e* of Fig. 1.5 demonstrates, TR symmetry is broken for each spin orientation separately in the presence of spin-orbit coupling, but it is preserved for the system as a whole.

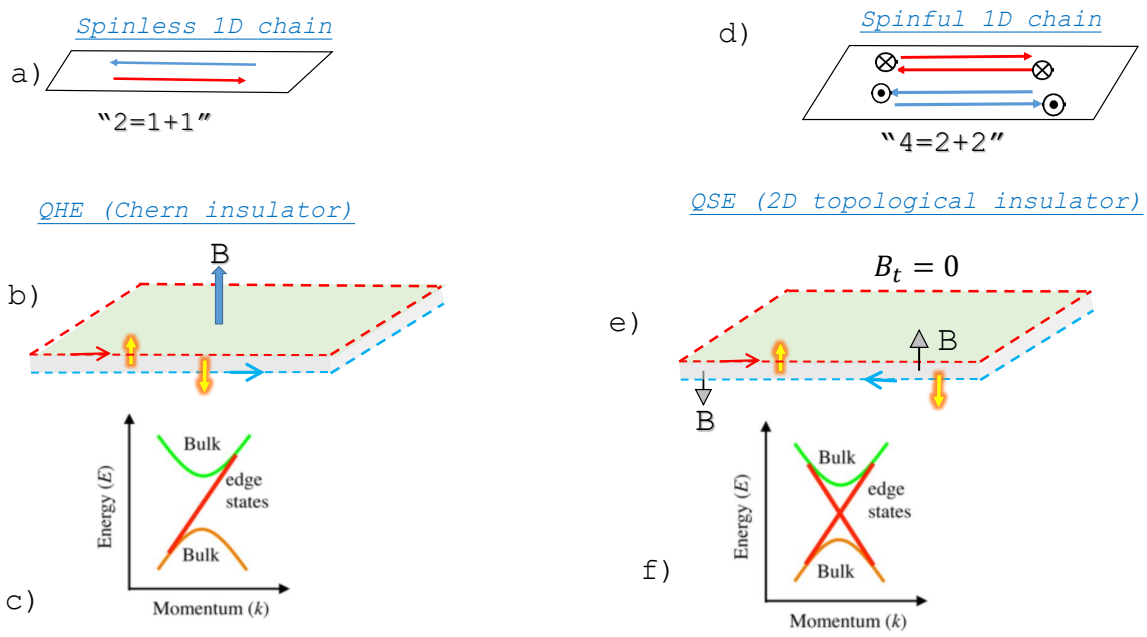

Figure 1.5: (a): An electron has two degrees of freedom, allowing it to travel in both directions. (b): Electrons in the QHE have one degree of freedom and can only move in one direction. (c): Edge states in QHE. (d): Electron degrees of freedom in a one-dimensional spinful chain. (e): The direction of propagation is linked with the spin of the electron, therefore electrons with opposite spins propagate in opposite directions. (f): Edge states in the QSH.

Due to graphene's weak spin-orbit coupling, *Kane* and *Mele's* proposal appeared to be extremely difficult to reach. Soon after, *Bernevig*, *Hughes*, and *Zhang* proposed that QSH states could exist in HgTe and CdTe quantum wells [34]. They expected that the HgTe-based quantum well heterostructure would be capable of hosting a pair of counter-propagating edge states connected by time-reversal symmetry. In 2007, the *Molenkamp* group at the University of Wuerzburg, Germany, confirmed the prediction [35].

1.5.1 Bulk-Edge correspondence

As we explained for the QHE and QSH, a topological state of matter is insulating in the bulk, but it allows gapless edge states that are robust to disorder. As we already discussed, the bulk in the QHE is characterized by the TKNN number (or Chern number).

In the QHE, the Chern number is equal to the number of stable gapless edge states. The bulk topology protects the edge states in this way. But what exactly is behind this "topological protection"? We can say that the bulk

topology is responsible for some fractionalization on the edge states. The typical degrees of freedom for the electron are spatially separated on opposite edges.

As shown by panel *a* of Fig. 1.5, in a one-dimensional spinless channel, an electron has two degrees of freedom: right and left movement. On the other hand, panel *b* of Fig. 1.5 demonstrates that the QHE has only left-moving electrons on the top edge and only right-moving electrons on the bottom edge (or vice versa). As a result of an electron's inability to reverse its direction of travel, backscattering on a particular edge is blocked. The QHE can be compared as a highway, where electrons going in opposite directions must drive in separate lanes. The symbolic equation "2 = 1 + 1" can be used to depict the spatial separation that results in chiral edge channels, where each "1" represents a distinct chirality. This "chiral transport rule" is very effective at suppressing electron scattering because electrons must always move in the same direction to avoid impurities and so cannot backscatter.

The QSH state, on the other hand, can be thought of as two copies of the QHE state, one for each spin, as previously stated. The top edge of a QSH system has just half the degrees of freedom of a one-dimensional spinful system. Because spin is correlated with the propagation direction, the resulting edge states are called helical. As panel *d* and *e* of Fig. 1.5 depict, the symbolic equation "4 = 2 + 2" can be used to depict this new pattern of spatial separation, where each "2" represents a distinct helicity. Although electrons can go now forward and backward on the same edge, there is a new "transport rule" that prevents backscattering: to backscatter, an electron must flip its spin, which is not possible when only non-magnetic impurities are present. The QSH state is a novel topological state of matter because it has a bulk insulating gap and gapless boundary states that are robust to disorder (in the presence of TR symmetry).

When the z-component of the spin of an electron is conserved, each channel in the QSH has a finite opposite Chern number, for instance, $v_{\uparrow} = +1$ and $v_{\downarrow} = -1$. Consequently, the total Chern number would be zero and the Hall conductance in the QSH state disappears. Hence the TKNN or Chern number cannot provide us with a good classification of the QSH states.

The proper topological invariant to characterize this new state is the Z_2 invariant. When the QSH state is trivial, with no robust gapless edge states, this topological invariant is zero, and when the QSH state is nontrivial, it is 1.

In the following sections, we will study the Z_2 invariant in more detail.

1.5.2 The Z_2 invariant

At the interface of two materials with opposite signs of the bulk band gap, the band structure slowly changes as we go across the interface. The energy gap vanishes somewhere along the way, otherwise the two materials would belong to the same topological class. As a consequence, the ordering of bands at the border changes from an inverted to usual material. The band structure of the QSH can be trivial or non-trivial, depending on the details of the edge states and their robustness to disorder. The following section will try to characterize the edge states in trivial and non-trivial QSH states.

1.5.2.1 TR symmetry

Physical laws are considered invariant under TR symmetry if the generated motion obeys the same rules when the movement is reversed. Therefore, according to quantum mechanics,

$$[H,T] = HT - TH = 0, \tag{1.11}$$

where T denote the TR symmetry operator and H is the Hamiltonian of the system. Under the action of the TR symmetry operator, the momentum $\boldsymbol{p} \longmapsto -\boldsymbol{p}$ and the location $\boldsymbol{x}$ preserves. Then to preserve the fundamental commutator $[\boldsymbol{x},\boldsymbol{p}] = i\hbar$, the time reversal operator has to be antiunitary. The antiunitarity property of the time-reversal operation allows to write this operation as a product of a unitary transformation U and the complex conjugation K: $T = UK$. In the case of the spin 1/2 particles we can write $T = i\sigma_y K$ which has the important property $T^2 = -1$ [36].

1.5.2.2 *Kramers* theorem and TR-invariant momenta points (TRIMs)

According to *Kramers* theorem, for a system with a Hamiltonian that obeys Eq. (1.11) all of its eigenstates are at least twofold degenerate. In other words, if we have an eigenstate $|\psi_n\rangle$ with an energy E_n, there is at least one distinct state with the same energy like $T|\psi_n\rangle$. We can prove that $T|\psi_n\rangle$ and $|\psi_n\rangle$ are distinct. If we assume that they are the same, i.e, $T|\psi\rangle = e^{i\phi}|\psi\rangle$ (with $\phi \in \mathbb{R}$), then $T^2|\psi\rangle = Te^{i\phi}|\psi\rangle = e^{-i\phi}T|\psi\rangle = e^{-i\phi}e^{i\phi}|\psi\rangle = |\psi\rangle$, which contradicts $T^2|\psi\rangle = -|\psi\rangle$. Therefore, $T|\psi\rangle$ and $|\psi\rangle$ are distinct sates. These two states are called *Kramers* partners and together make a *Kramers* pair.

In the case of a lattice model, a reduced *Bloch* Hamiltonian on the first Brillouin zone can be introduced as

$$\mathscr{H}(\boldsymbol{k}) = e^{-i\boldsymbol{k}.r} H e^{i\boldsymbol{k}.r} \tag{1.12}$$

with corresponding eigenvalues $E_{\boldsymbol{k}}$ and eigenstates $|u_k\rangle = e^{-ik.r}|\psi_k\rangle$. When the system has TR symmetry, $[H,T] = 0$, the reduced *Bloch* Hamiltonian $\mathscr{H}(\boldsymbol{k})$ satisfies $T\mathscr{H}(\boldsymbol{k})T^{-1} = \mathscr{H}(-\boldsymbol{k})$. Therefore, the *Kramers* partners have opposite momentum and spins, meaning that

$$E(\boldsymbol{k},\uparrow) = E(-\boldsymbol{k},\downarrow). \tag{1.13}$$

Furthermore, if inversion symmetry holds, the following equation holds

$$E(\boldsymbol{k},\uparrow) = E(-\boldsymbol{k},\uparrow). \tag{1.14}$$

If both Eq. 1.13 and 1.14 are simultaneously satisfied, bands are spin degenerate at TR-invariant momenta points ($TRIMs$)

$$E(\boldsymbol{k},\uparrow) = E(\boldsymbol{k},\downarrow). \tag{1.15}$$

In addition bands are spin degenerate at points defined by $-\boldsymbol{k} = \boldsymbol{k} + \boldsymbol{G}$, where $\boldsymbol{G}$ is a reciprocal lattice vector. For a square Brillouin zone, Fig. 1.6 shows four $TRIMs$ $\Gamma_0, \Gamma_1, \Gamma_2, \Gamma_3$. As Fig. 1.7 shows, *Kramers*' theorem requires the electronic states to be at least twofold degenerate at the two $TRIMs$, Γ_0 and Γ_1. Away from these two $TRIMs$, SOC removes this degeneracy. When TR

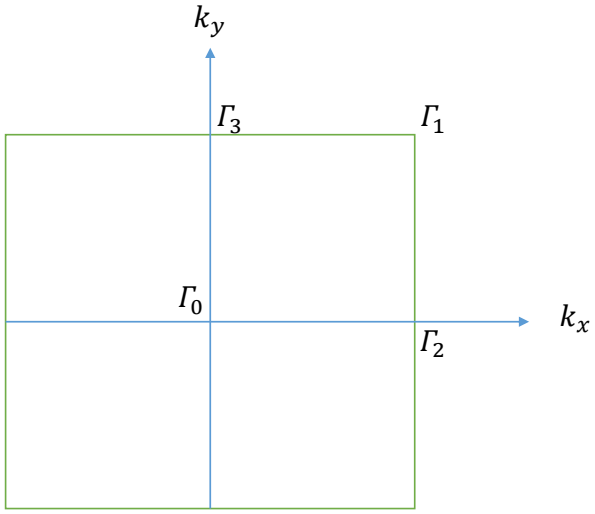

Figure 1.6: Representation of four $TRIMs$ in the Brillouin zone.

symmetry is preserved, the crossing of bands at $TRIMs$ is robust. Compared to zero band gap systems, the introduction of a magnetic field breaks TR symmetry and destroys the $TRIMs$, resulting in a gap in the edge dispersion.

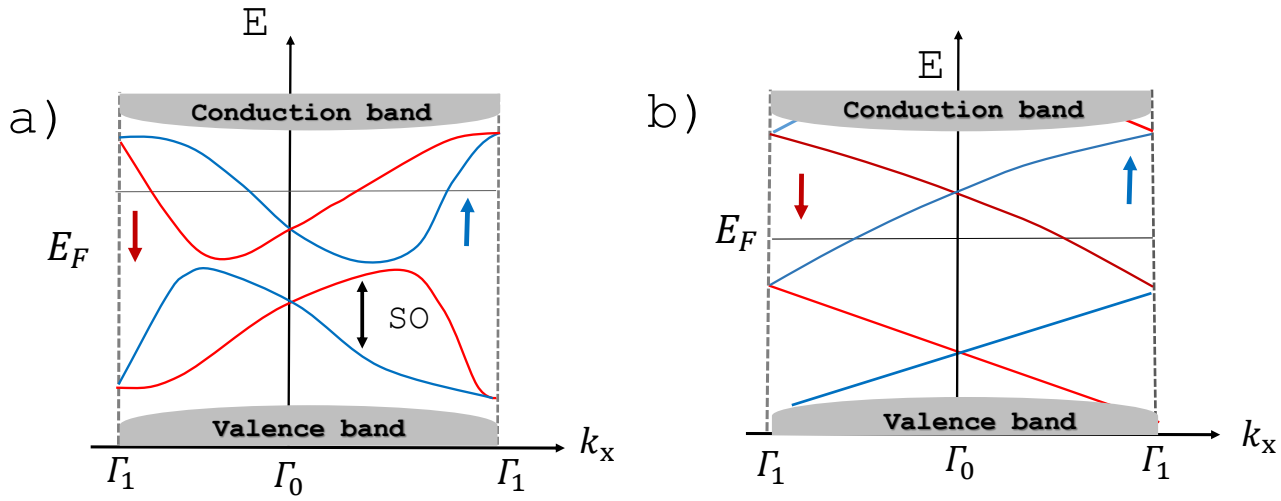

Figure 1.7: Dispersion of edge states with (a) trivial topology and (b) nontrivial topology. The grey bands represent the bulk bands, and E_F denotes the Fermi level. As shown in (a), spin-orbit coupling (SOC) results in band spin splitting, while TR symmetry forms pairs located at $\boldsymbol{k}$ and $-\boldsymbol{k}$.

The band structure corresponding to QSH states is depicted in Fig. 1.7 along $\Gamma_0 - \Gamma_1$. The number of *Kramers* pairs of edge states crossing the Fermi level distinguishes non-trivial topological states from trivial states in the QSH. In panel *a* of Fig. 1.7, there are an even number of *Kramers* pairs of edge states crossing the Fermi level. However, there are always an odd number of

Kramers pair of edge states at the Fermi level in panel *b* of Fig. 1.7. Thus it seems that these two panels describe two topologically distinct phases.

An index can systematically distinguish these two cases as

$$N_k = m + 2p, \tag{1.16}$$

where N_k is the number of *Kramers* pairs of edge states that cross the Fermi energy, and p is an integer number. When N_k is even, $m = 0$ and the system is in its trivial phase, while when N_k is odd $m = 1$ and the systems has a non-trivial topological state. Because m has just two potential values, it is referred to as a Z_2 invariant.

The physical consequence of $m = 1$ is that the corresponding edge states are robust against smooth deformations. Thus, for example, the edge states in panel *a* can be pushed out of the band gap (by tuning the Hamiltonian smoothly) without closing the gap, while this is not possible in panel *b* without closing the gap.

Even though we addressed the Z_2 invariant in terms of the parity of the number of *Kramers* pairs of edge states at the Fermi level in our discussion, the Z_2 invariant is entirely determined by the bulk topology. In the following section, we explain how this topological invariant can be computed in the presence of TR and spatial inversion symmetries.

1.5.2.3 Z_2 invariant in systems with extra symmetry

The vast majority of insulators are conventional insulators. To find topological insulators empirically, we need to define criteria based on their band structure to topologically distinguish them from other conventional systems. The value of the Z_2 invariant is one of these criteria. However, calculating the Z_2 invariants is a difficult task in general.

Kane and *Mele* showed that the Z_2 invariant can be found by using the *Pfaffian* function [37]. Even though this method is tedious, *Murakami* applied it to find the QSH phase in two-dimensional bismuth bilayers [38]. Later *Fu* and *Kane* used Wannier functions instead of Bloch functions to calculate this invariant [39]. Wannier functions are linked to topology through a relation

that connects matrix elements of the position operator in the Wannier basis to the Berry connection.

However, if the crystal has extra symmetry, calculating the Z_2 invariant is much easier. If the z component of the electron's spin S_z is conserved in a 2D system, then up and down spins have independent Chern integers $n_\uparrow$, $n_\downarrow$. However, TR symmetry requires $n_\uparrow + n_\downarrow = 0$, whereas a quantized spin Hall conductivity can be defined by the difference $N_k = n_\uparrow - n_\downarrow$ [40]. For this case, the Z_2 invariant ν can be found by

$$(-1)^\nu = N_k \ \ mod\ 2. \tag{1.17}$$

Comparing the above equation with Eq. 1.16 proves that N_k represents the number of *Kramers* pairs of edge states that cross the Fermi energy.

In addition, when the crystal has inversion symmetry, calculating the Z_2 invariant is much easier. For this case, instead of checking the number of *Kramers* pairs that cross the Fermi energy, the topological invariant ν can be found by determining the parity of the occupied bands at $TRIMs$ [41]. Thus, the existence of inversion symmetry significantly simplifies the evaluation of the Z_2 invariants. In such a system, the bands have a definite parity at the four time-reversal and parity invariant points in the Brillouin zone. Thus, the parity of bands at these points can be used to calculate the Z_2 topological invariants without knowing about the global properties of the energy bands.

At four special points Γ_i the Bloch states are also eigenstates of parity with eigenvalues $\zeta_n(\Gamma_i) = \pm 1$. In this condition, the Z_2 invariant can be represented as the product of the parities of the occupied bands at the $TRIMs$ as

$$(-1)^\nu = \prod_{i=1}^{4} \left(\prod_{n=1}^{N} \zeta_n(\Gamma_i) \right), \tag{1.18}$$

where n runs over the *Kramers* pairs of the $2N$ occupied bands[41]. This method is quite helpful in identifying topological insulators using band structure calculations [42, 43].

1.6 3D Topological insulators

1.6.1 The Z_2 invariant in 3D

For a 2D TI, the Z_2 invariant can be found by taking into account only $TRIMs$ instead of covering the whole Brillouin zone. Unlike the Chern number, which is defined only in even dimensions, the Z_2 index can also be applied to three-dimensional insulators. In 3D, there are eight different $TRIMs$ defined by the reciprocal lattice vectors $\mathbf{b}_1$, $\mathbf{b}_2$, and $\mathbf{b}_3$ as $\mathbf{\Gamma}_{i=n_1n_2n_3} = n_1\mathbf{b}_1 + n_2\mathbf{b}_2 + n_3\mathbf{b}_3$ with $n_i = 0, 1$. For each of these $TRIMs$, we specify a parameter $\delta_{n_1n_2n_3} = \pm 1$, which can be calculated by

$$\delta_i = \frac{\sqrt{\mathrm{Det}[w(\Gamma_i)]}}{\mathrm{Pf}[w(\Gamma_i)]}, \tag{1.19}$$

where the unitary matrix $w_{ij}(\boldsymbol{k}) = \langle u_i(-\boldsymbol{k})|T|u_j(\boldsymbol{k})\rangle$, and Pf denote the *Pfaffian* function and T is the time-reversal operation [41]. It is now possible to construct Z_2 invariants v_0, ν_1, ν_2 and ν_3 as follows

$$(-1)^{\nu_0} = \prod_{n_i=0,1} \delta_{n_1n_2n_3}, \tag{1.20}$$

$$(-1)^{\nu_{i=1,2,3}} = \prod_{n_i=1, n_{j\neq i}=0,1} \delta_{n_1n_2n_3}. \tag{1.21}$$

When $\nu_0 = \nu_1 = \nu_2 = \nu_3 = 0$, the system is a trivial insulator. When $\nu_0 = 0$, and one of the other invariants does not vanish, the system is a weak topological insulator. This weak topological insulator can be constructed by stacking layers of 2D QSH insulator. They are called weak topological insulators, because unlike the 2D helical edge states in the QSH, TR symmetry does not protect them and it is likely that disorder will turn them into trivial insulators.

ν_0 determines whether an even or an odd number of $TRIMs$ (at which band inversion occurs) is enclosed by the surface Fermi circle. When $\nu_0 = 1$, the system is said to be a strong topological insulator. In this case, as panel *b* of Fig. 1.8 shows, there are an odd number of band inversions at the $TRIMs$ in the surface Brillouin zone of a strong topological insulator.

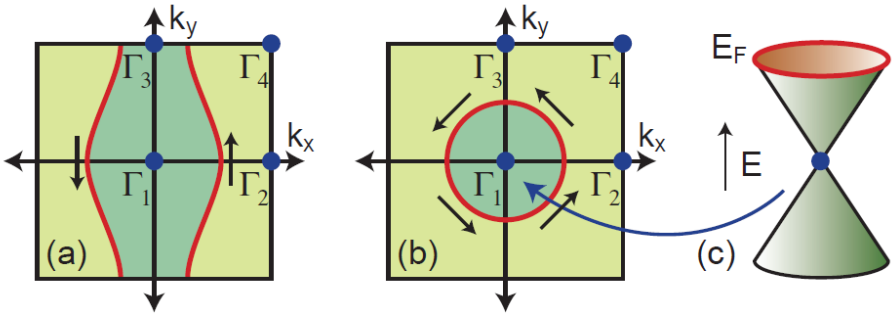

Figure 1.8: (a): Fermi circles for a weak topological insulator. (b): Shows the Fermi circles for a strong topological insulator. (c): The Fermi circle encloses a single Dirac point in the simplest strong topological insulator [44].

1.6.2 Experimental realizations

In 2006, three theoretical groups independently discovered that the topological characterization of the QSH state has a natural generalization in 3D [45–47]. In 2007, Fu, $Kane$, and $Mele$ connected the bulk topological order to the presence of conducting surface states [48]. Later, some other 3D topological insulators (3DTI) were predicted in several real materials, such as $Bi_{1-x}Sb_x$, $HgTe$ [41]. In 2008, the first 3DTI was identified in $Bi_{1-x}Sb_x$ through angle-resolved photoemission spectroscopy (ARPES) [49]. Later soon in 2009, second-generation of 3DTIs, like Bi_2Se_3, were predicted theoretically [50] ans discovered experimentally [51].

The applied transport measurements on 2DTIs are not suitable for transport measurements on 3DTI. However, in 3D, there are other methods for proving the existence of surface states, like $ARPES$. In $ARPES$, a laser beam is shone on the sample's surface, and consequently some electrons are released through the photoelectric effect. The dispersion relation of the surface can be found based on the conservation of energy and measuring the electrons' momentum. Note that surface states are separated from bulk states by the change in the energy of incoming photons: absorption only occurs if there is a component of the electron that travels along the surface.

As predicted [52], the first $ARPES$ experiments on $Bi_{1-x}Sb_x$ revealed an odd number of Dirac cones on the surface states [49], as shown in Fig. 1.9.

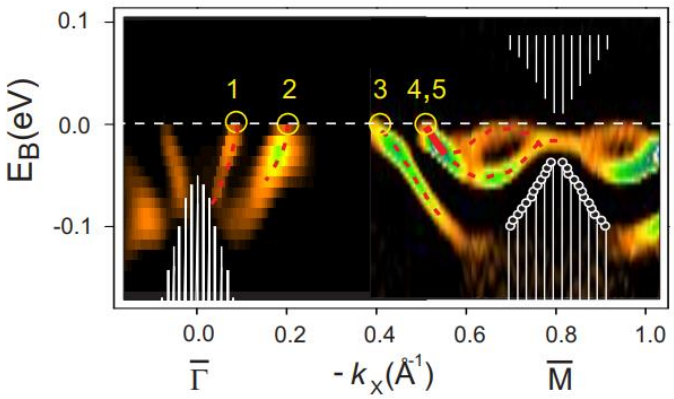

Figure 1.9: The presence of 5 surface states in $Bi_{1-x}Sb_x$ based on $ARPES$ data. The bulk bands are identified by white stripes [49].

As Fig. 1.9 demonstrates, the surface structure of $Bi_{1-x}Sb_x$ was rather complex, and the band gap was very small. As a result, people began looking for materials with a larger band gap and a simpler surface spectrum. They were successful in discovering new materials, which are known as the second generation of 3DTIs.

Second-generation 3DTIs, such as Bi_2Se_3, can provide topologically protected behaviour in ordinary crystals at room temperature and zero magnetic fields. Furthermore, the family of compounds: Bi_2Se_3, Bi_2Te_3, and Sb_2Te_3 are stoichiometric compounds rather than alloys, as in $Bi_{1-x}Sb_x$, and hence can be prepared at higher purity. To highlight the significance of having a pure 3DTI, it is worth mentioning that while 3DTIs are supposed to be resistant to non-magnetic disorder, this can only be shown experimentally in high-purity samples.

As Fig. 1.10 shows, in these new materials a band inversion occurs at $k = 0$, leading to the $(\nu_0 : \nu_1\nu_2\nu_3) = (1;000)$ topological class. The $(\nu_0 : \nu_1\nu_2\nu_3) = (1;000)$ phase observed in the Bi_2Se_3 differs from the $(\nu_0 : \nu_1\nu_2\nu_3) = (1;111)$ phase in $Bi_{1-x}Sb_x$. Even though the phase seen in the Bi_2Se_3 has the same strong topological invariant $\nu_0 = 1$ as $Bi_{1-x}Sb_x$, this series have more potential to be the reference material for future applications. For example, Bi_2Se_3 has a significant band gap of 0.3 eV, indicating that it can exhibit topological insulator behavior at room temperature in its high-purity form.

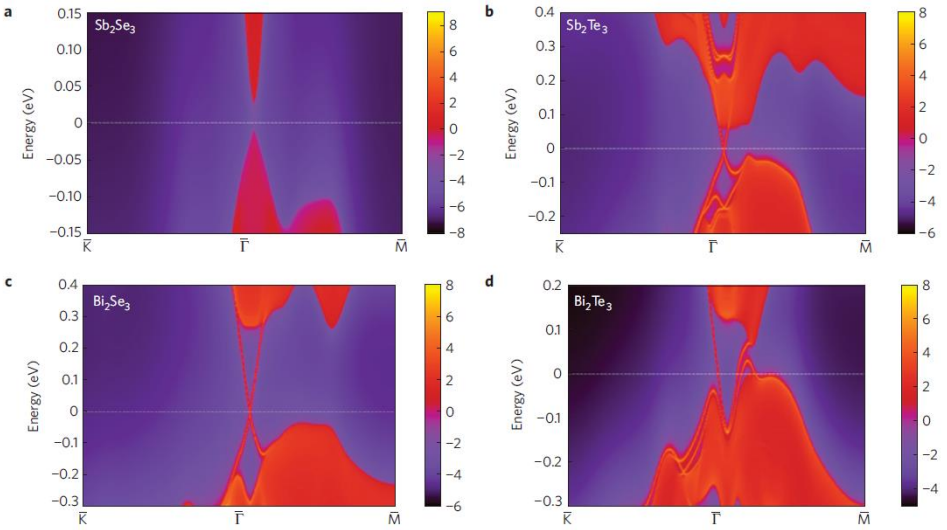

Figure 1.10: Local density of states for Sb_2Se_3 (a), Sb_2Te_3 (b), Bi_2Se_3 (c) and Bi_2Te_3. Except for panel (a), the surface states can be recognized as red lines dispersed in the bulk gap around the Γ point [53].

According to $ARPES$ and theory [51], the Bi_2Se_3 surface state has a nearly idealized single Dirac cone, as shown in Fig. 1.11 [49]. Another remarkable property of a strong 3DTI is that, because the Fermi circle encloses an odd number of Dirac points (single Dirac cone in Bi_2Se_3), the Berry phase gained by an electron traveling around the Fermi circle (see panel b of Fig. 1.11) is π. This fact has important implications for transport in strong topological insulators in the presence of disorder. For example, when there is a weak disorder, the π Berry phase causes antilocalization by changing the sign of the weak localization correction to conductivity [54, 55].

The idea of two channels with opposite spin and propagation direction does not make sense for a 3DTI, contrary to the QSH phase. As panel b of Fig. 1.11 shows, for the surface sates of a 3DTI, the spin lies in-plane but perpendicular to the propagation direction. Panel d of Fig. 1.13 demonstrates that the low energy spectrum around a Dirac point exhibits a cone-like energy spectrum. This cone-like energy spectrum can be written as

$$H_D = \hbar v_F (\boldsymbol{k} \times \sigma)_z \tag{1.22}$$

where the $\hat{z}$-direction is chosen normal to the surface of the 3DTI. Here, v_F, $\boldsymbol{k} = (k_x, k_y)$, are respectively the Fermi velocity, the wave vector, and $\sigma =$

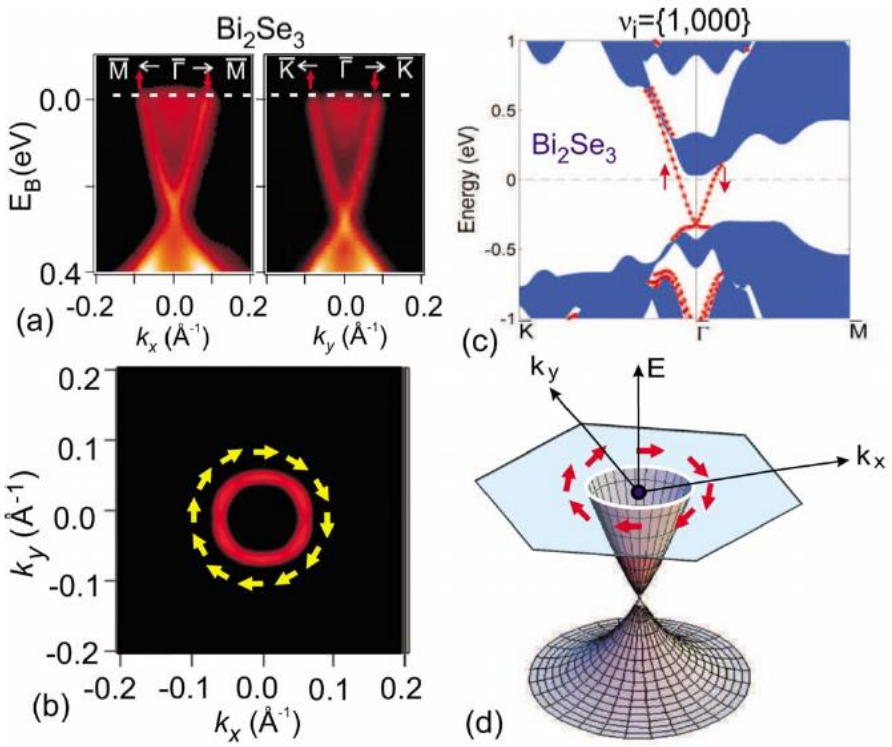

Figure 1.11: (a): Surface electronic states with a single spin-polarized Dirac cone are discovered using ARPES data for Bi_2Se_3. (b): The surface Fermi surface has a left-handed chiral spin texture. (c): Surface electronic structure of Bi_2Se_3. (d): The spin-polarized surface-state dispersion in Bi_2X_3 $(\nu_0 : \nu_1\nu_2\nu_3) = (1;000)$ [44] .

$(\sigma_x, \sigma_y, \sigma_z)$ is the vector of Pauli matrices acting on the spin of the electrons.

1.7 Magnetic 3DTIs

If the surface of a strong 3DTI preserves the protecting symmetries, it hosts a set of two-dimensional surface states and consequently odd numbers of Dirac points. The surface states of a 3DTI provides a unique platform to study the topological characteristics of Dirac points [56, 57].

TR symmetry can be broken by applying an external magnetic field [58–61], doping topological insulators with magnetic atoms [62–65], and by the magnetic proximity effect when a topological insulator is brought in contact with a ferromagnet [66–71]. When the TR symmetry is broken, an energy gap is induced near the Dirac point, which changes the nature of the surface states [72, 73].

The breaking of TR symmetry in a 3DTI can be essential for both funda-

mental and device applications [74–77]. For example, the topological magnetoelectric effect, which allows electric-field driven spin transistors, requires a surface band gap [44, 78]. Another promising example is the quantum anomalous Hall effect, in which gapped surface states are accompanied by back scattering protected dissipationless edge transport channels [79–82].

The breaking of TR symmetry can also allow us to tune the Fermi level in 3DTIs. The Fermi level has to be at or near the surface Dirac point in many interesting theoretical proposals that use topological insulator surfaces. To highlight the importance of the Fermi level, note that it is naturally positioned near the Dirac point in graphene due to carbon atom chemistry. Hence, graphene can be used in basic science and microelectronics since the density of carriers can be adjusted by an applied electrical field. However, the Fermi level in a 3DTI depends on the material electrostatic characteristics and is not always at the Dirac point. Therefore, breaking of TR symmetry, for example by doping the system with magnetic impurities, can vary the Fermi level.

Moreover, 3DTIs have an extremely strong SOC, resulting in band inversion. This large SOC affects the spin of electrons. On the other hand, we know that the spin of electrons can be controlled by magnetic moments, as in magnetic materials. Consequently, when electrons experience both a strong SOC and magnetic interactions there are more degrees of freedom available to control the spin of electrons. When it comes to the charge transport in magnetic 3DTIs, the interplay of the SOC, magnetism and external electric field leads to many exotic features that we discuss in detail in chapters 3, 4 and 5.

1.7.1 Magnetic impurity induced gap

In a strong topological insulator, the surface Fermi circle encloses an odd number of *Kramers* degenerate Dirac points. As we already discussed, the simplest case of a strong 3DTI has a single Dirac point (see panel *a* of Fig. 1.13) which can be described by the Hamiltonian,

$$H_{surface} = \hbar v_F (\boldsymbol{k} \times \sigma)_z, \tag{1.23}$$

where z is perpendicular to the surface and v_F is the Fermi velocity. The above Hamiltonian is similar to the 2D Dirac Hamiltonian for graphene. However, there is one significant distinction between these two cases. In graphene, the Dirac Hamiltonian components indicates the two sublattices or pseudospin degrees of freedom. However, in the case of a strong 3DTI, the two components describe the electron's spin.

When a 3DTI is doped with magnetic impurities and the impurity density is low enough to ignore impurity-impurity interactions, the Hamiltonian given in Eq. 1.23 converts to

$$H_M = H_{surface} + \hat{H}^z_{\text{ex}} + \hat{H}^{\parallel}_{\text{ex}}, \tag{1.24}$$

where

$$\hat{H}^z_{\text{ex}} + \hat{H}^{\parallel}_{\text{ex}} = \sum_r \left(J_z s_z(\mathbf{r})\, S_z(\mathbf{r}) + J_{\parallel} \left(s_x(\mathbf{r})\, S_x + s_y(\mathbf{r})\, S_y \right) \right), \tag{1.25}$$

and J_z and $J_{\parallel}$ are the coupling parameters, $S_i(\boldsymbol{r})$ is the spin of a magnetic impurity at $\boldsymbol{r}$ and $s_i(\boldsymbol{r}) = \psi^{\dagger}(\boldsymbol{r})\sigma_i\psi(\boldsymbol{r})$ is the spin of the surface electrons. For example, when Sb_2Te_3 is doped with vanadium as magnetic impurity, J_z and $J_{\parallel}$ which depend on the overlap between the surface states and the magnetic impurities are found to be in the range of $0.1 - 0.5\ eV$ [83, 84].

In the mean field approximation, the electron-impurity exchange interaction in Eq. (1.25) converts to

$$\hat{H}^z_{\text{ex}} + \hat{H}^{\parallel}_{\text{ex}} \overset{\text{MFA}}{\approx} \mathbf{M} \cdot \vec{\sigma}, \tag{1.26}$$

where $\mathbf{M}$ is the average magnetization. Consequently, in this approximation, the full Hamiltonian in Eq. (1.24) transforms to

$$H_M^{MFA} = \hbar v_F (\boldsymbol{k} \times \sigma)_z + M_x\sigma_x + M_y\sigma_y + M_z\sigma_z, \tag{1.27}$$

with eigenvalues

$$E_{ks} = s\sqrt{\left(\hbar v_F k_x + M_y\right)^2 + \left(\hbar v_F k_y - M_x\right)^2 + (M_z)^2}, \tag{1.28}$$

where $s = \pm$ corresponds to the upper and lower bands. When the average magnetization is in-plane, $M_z = 0$, we can rewrite Eq. (1.27) as $H_M^{MFA} =$

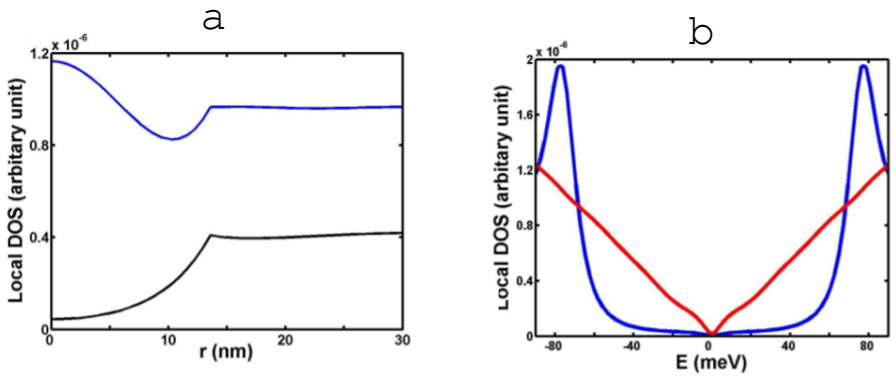

Figure 1.12: (a) Charge local density of states (LDOS) in terms of the distance r from the magnetic impurity for electron energies $E = 30meV$ (black line) and $E = 70meV$ (blue line). (b) Charge LDOS as a function of electron energy E at positions $r = 0$ (blue line) and $r = 20nm$ (red line). In both panels the magnetic impurity strength is $J_z < S_z >= 50meV$ and the coupling range $r_0 = 13\ nm$ [85].

$v_F(\hbar\boldsymbol{k} - e\mathbf{A})\cdot(\hat{\mathbf{z}}\times\hat{\boldsymbol{\sigma}})$. The vector potential $\mathbf{A} = -\dfrac{\mathbf{M}\times\hat{\mathbf{z}}}{ev_F}$ only shifts the position of the Dirac point in the (k_x, k_y) plane. Under the gauge transformation $(k_x, k_y) \rightarrow (q_x + eA_x/\hbar, q_y + eA_y/\hbar)$, this vector potential can be removed, and consequently does not influence the physical observables. Considering this transformation, the energy dispersion in Eq. (1.28) converts to $E_{qs} = s\sqrt{(\hbar v_F)^2\left(q_x^2 + q_y^2\right) + (M_z)^2}$, indicating that only the z-component of the average magnetization can open an energy gap. In what follows, we describe how, in addition to the direction of the magnetic moments, the strength of the exchange interaction, the spatial extension of the impurities, and their density all play essential roles in the gap opening.

The interaction of electrons with a single spatially extended magnetic impurity with a z-direction spin can be defined as follows:

$$\mathscr{H}_{ex} = \sum_{\mathbf{r}} J_z \Theta(\boldsymbol{r} - \boldsymbol{r}_0) S_z s_z(\boldsymbol{r}), \tag{1.29}$$

where $\Theta(\boldsymbol{r} - \boldsymbol{r}_0)$ is the step function and $\boldsymbol{r}_0$ determines the range of the exchange interaction. In panels a and b of Fig. 1.12, the calculated local density of states (LDOS) is shown in terms of the distance r from the magnetic impurity and the energy of electrons, respectively [85]. The black curve in panel a shows that LDOS suppress for $r < r_0 (= 13nm)$ when $E(= 30eV) < J_z < S_z > (= 50meV)$. Panel b of this figure shows LDOS as a function of electron energy E at positions $r = 0nm$ (blue line) and $r = 20nm$ (red line),

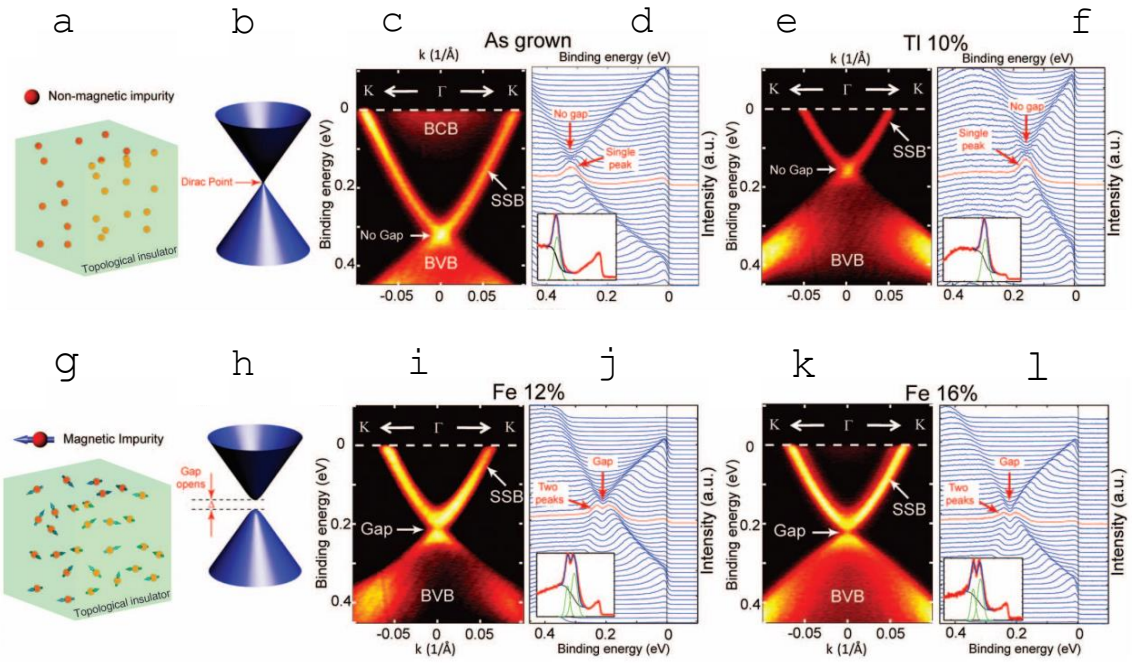

Figure 1.13: $(a-b)$: Gapless dispersion of a non-magnetically doped Bi_2Se_3. $(c-d)$: Absence of a gap in the band structure of a pure Bi_2Se_3. $(e\text{-}f)$: Band structure for a $(Bi_{0.9}TI_{0.1})_2Se_3$. $(g-h)$: Gap creation in magnetically doped Bi_2Se_3. $(i-j)$: Gapped band structure of $(Bi_{0.88}Fe_{0.12})_2Se_{3.7}$. $(k-l)$: Emergence of a gap in the surface band structure of a $(Bi_{0.84}Fe_{0.16})_2Se_{3.7}$ [65].

with $r_0 = 13nm$. Also, this panel indicates that each extended magnetic impurity can generate a gap in its vicinity and the size of the gap depends on the strength of the impurity-electron interaction $J_z < S_z >$. Because each magnetic impurity generates a local gap, we can deduce that when the system is doped with many magnetic impurities, the system is gaped everywhere (at least at the mean-field level). For example, panels i and k of Fig. 1.13 show the opening of a gap in Fe-doped Bi_2Se_3 for two different concentrations of Fe [65]. However, as panels c and e show, doping Bi_2Se_3 with non-magnetic materials can not open an energy gap at the surface band structure.

Panels a and b of Fig. 1.12 illustrate that LDOS converges to the impurity-free value $\frac{|E|}{2\pi\hbar^2 v_f^2}$ when $r > r_0(= 30nm)$ (far from the impurity). As a result of this observation, we can deduce that a weak and point-like magnetic impurity is incapable of opening a significant local gap. Consequently, no significant gap occurs in a system when it is doped with dilute, weak, and point-like magnetic impurities. Also, it is demonstrated that the LDOS around the Dirac point can be disrupted by the formation of low-energy resonance state(s) due

to the presence of a point-like magnetic impurity, but this is insufficient to destroy the Dirac point (locally) [86]. As a result of this findings, as considered in chapters 3, 4, and 5, the dilute and point-like impurities considered in this doctoral dissertation act as local scatterers and do not open a gap.

From a theoretical standpoint, adding the magnetic impurities to the surface of a 3DTI seems promising. However, most of the exciting surface phenomena occur when the surface is insulating, though most ferromagnets in nature are metallic. Then, one needs to place the Fermi level inside the surface energy gap and it is not easy experimentally for all 3DTIs. Furthermore, to open a gap in the surface band structure, the magnetization must be perpendicular to the surface. However, having a magnetization perpendicular to the surface is difficult to achieve experimentally as well.

A topological insulator doped with magnetic impurities can exhibit long-range magnetic ordering in both the metallic and insulating phases in the bulk. Magnetic ordering on the surface can be consequently induced by the bulk magnetization. However, when the Fermi energy is close to the Dirac point the *Ruderman-Kittel-Kasuya-Yosida* (RKKY) interaction, generated by Dirac fermions, is typically ferromagnetic and can form a long-range magnetic ordering on the surface, independent of the bulk magnetic ordering [85]. Therefore, in magnetically doped 3DTIs, a gap can be created in the surface band dispersion, with or without bulk ferromagnetism.

Pushing the Fermi level into the generated surface gap is the next challenging step in observing various fascinating phenomena in topological magnetic insulators. When this challenging step is completed, many striking topological phenomena can now be supported by the generated insulating states, including the image magnetic monopole induced by a point charge[14], the half quantum Hall effect on the surface with a Hall conductance of $\frac{e^2}{2h}$ [87], and a $Kerr-Faraday$ angle quantization in units of the fine structure constant [88].

Furthermore, the gap that appears is tunable, which is a fascinating feature. This exotic characteristic allows one to manipulate surface transport, and also to change the magnetization by an external electric field [89].

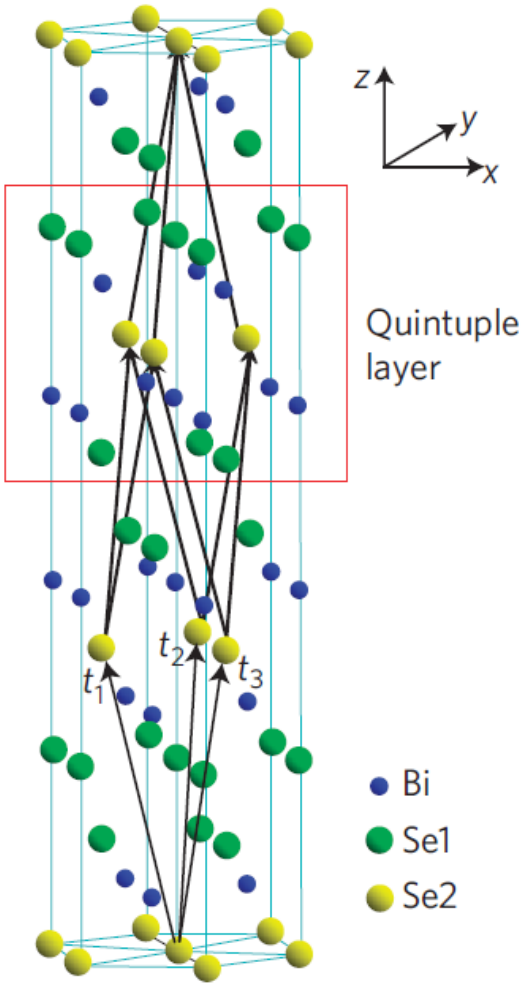

Figure 1.14: Bi_2Se_3 crystal structure with three primitive lattice vectors t_1, t_3, t_3. The red square indicates a quintuple layer [90].

1.8 Thin films of topological insulators

Charge transport in topological thin films (TTFs) is a main topic in this thesis. TTFs are suitable for electrical and spintronic device applications due to their adjustable gap and spin-orbit coupling. Different experimental techniques such as molecular beam epitaxy (MBE) and the vapour–liquid-solid (VLS) method can be used to fabricate TTFs [91, 92]. Quintuple-by-quintuple (see a quintuple layer of Bi_2Se_3 in Fig.1.14) growth of a TTF is possible using modern experimental techniques and precise control of the growth conditions.

A 3DTI is typically made up of two surfaces (top and bottom surfaces, for example). Because the two surfaces of a typical 3DTI are uncorrelated, charge transport on one surface is independent of charge transport on the other one. When the thickness of a thin film is comparable to the decay length of the

surface states into the bulk, the two surface states hybridize. The spatial overlap of the wave functions of the top and bottom surface states open a gap in the energy spectrum of a TTF. For instance, when the thickness of a thin film of Bi_2Se_3 is smaller than six quintuple layers (QLs), the emergence of a gap owing to the finite size effect can be realized [94].

The effective low-energy Hamiltonian for the hybridized Dirac cones on the top and bottom surfaces of a TTF, grown on a substrate, is described by

$$H_{\text{eff}}^{\text{SIA}} = \begin{bmatrix} h_+(k) & V\sigma_0 \\ V\sigma_0 & h_-(k) \end{bmatrix}, \tag{1.30}$$

in which

$$h_{\tau_z}(k) = E_0 - Dk^2 + \hbar v_F(\sigma \times \boldsymbol{k})_z + \tau_z\left(\frac{\Delta}{2} - Bk^2\right)\sigma_z, \tag{1.31}$$

where $\left(\frac{\Delta}{2} - Bk^2\right)$ and V are induced by the finite size effect and substrate, respectively. D and E_0 depend on the characteristics of the TTF and σ_0 is the identity matrix. The basis states of Pauli matrices in the above expression stand for spin-up and spin-down states of real spin. $\tau_z = \pm 1$ corresponds to the upper (lower) 2×2 block in Eq. 1.30.

Each of the two surfaces of a thick topological film has a single gapless Dirac cone, represented in panel *a* of Fig. 1.15 by solid and dashed lines for the top and bottom surfaces, respectively. Due to inter-surface interaction in TTFs, two degenerate Dirac cones in panel *a* are transformed into two degenerate gapped Dirac hyperbolas in panel *b* of Fig. 1.15. The energy spectra of the gapped surface states shown in panel *b* is given by

$$E_\pm = E_0 - Dk^2 \pm \sqrt{\left(\frac{\Delta}{2} - Bk^2\right)^2 + (\hbar v_{\text{F}})^2 k^2}, \tag{1.32}$$

where the +(−) sign stands for the conduction (valence) band. As panel *c* of Fig. 1.15 illustrates, the substrate upon which the film is grown lifts the Dirac cone at the top surface while lowers it at the bottom, removing the Dirac cones' degeneracy. In fact the top surface of the film is exposed to air while the bottom surface is attached to a substrate, then inversion symmetry does not hold in the z-direction, leading to structure inversion asymmetry (SIA). Combination of the inter-surface coupling and SIA generates two non-degenerate gapped Dirac hyperbolas, as shown in panel *d* of Fig. 1.15. The

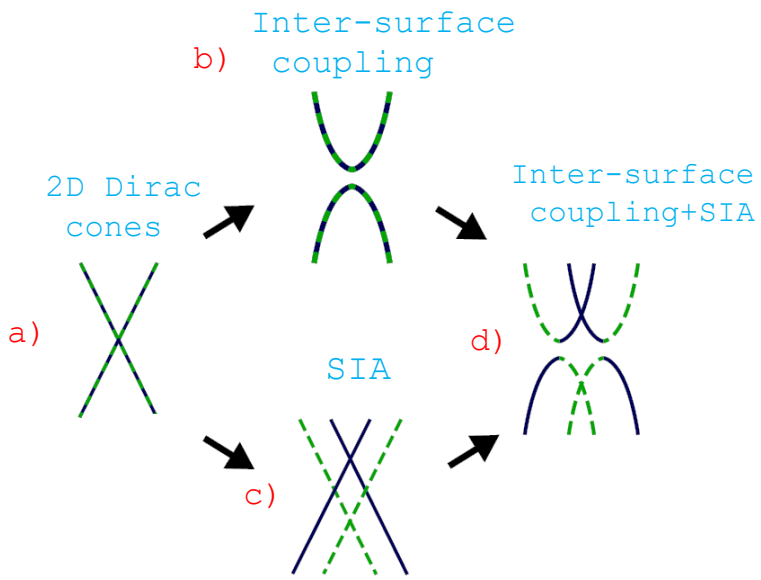

Figure 1.15: The evolution of gapless Dirac cones in the presence of both inter-surface coupling and SIA. The black solid and green dashed lines represent the states located at the top and bottom surfaces. Adapted from [93].

QL	E_0	D (eV Å^2)	Δ (eV)	B (eV Å^2)	V_F ($10^5\ m\ s^{-1}$)	V (eV)
2	-0.470	-14.4	0.252	21.8	4.71	0
3	-0.407	-9.7	0.138	18.0	4.81	0.038
4	-0.363	-8.0	0.070	10.0	4.48	0.053
5	-0.345	-15.3	0.041	5.0	4.53	0.057
6	-0.324	-13.0	0	0	4.52	0.068

Table 1.1: The numerical values used to fit Eq. (1.33) to the experimental data shown in Fig. 1.16. Adapted from [94].

inner (outer) branches of the conduction or valence bands of this system are given by

$$\begin{aligned} E_{1,\pm} &= E_0 - Dk^2 \pm \sqrt{\left(\frac{\Delta}{2} - Bk^2\right)^2 + (V + \hbar v_{\mathrm{F}} k)^2}, \\ E_{2,\pm} &= E_0 - Dk^2 \pm \sqrt{\left(\frac{\Delta}{2} - Bk^2\right)^2 + (V - \hbar v_{\mathrm{F}} k)^2}. \end{aligned} \tag{1.33}$$

Figure 1.16 shows the experimental result acquired by angle-resolved photoemission spectroscopy (ARPES) for 1 to 6 QL of Bi_2Se_3 films [94]. Using values given in table 1.1, Eq. (1.33) can be fitted to these experimental results..

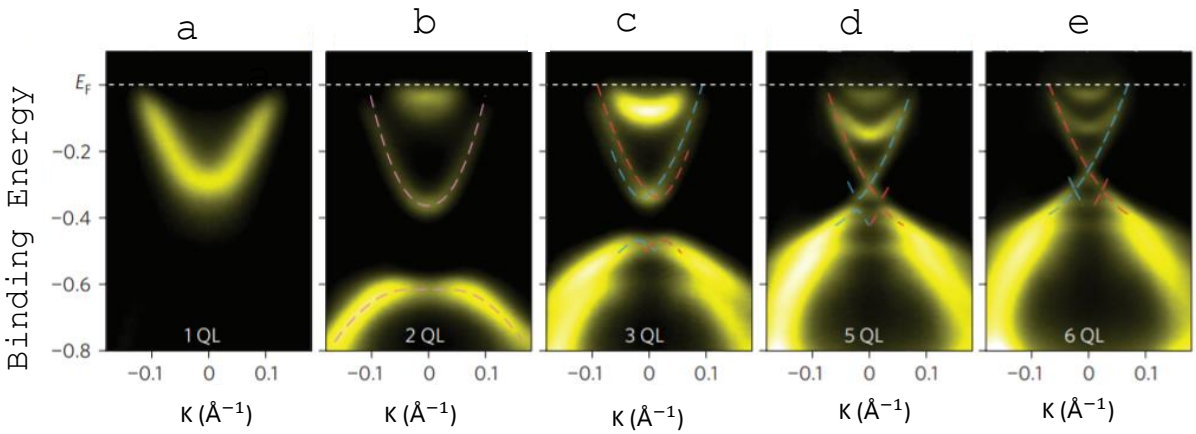

Figure 1.16: a-e: ARPES spectra of 1, 2, 3, 5 and 6 QL of Bi_2Se_3 along the Γ–K direction measured at room temperature. Adapted from [94].

1.9 Structure of the thesis

In this doctoral thesis, we investigate the charge transport in magnetic TIs. There are two major topics in this thesis: (1) the longitudinal charge transport in magnetic topological ultra-thin films (chapter 3 and 4), and (2) the anomalous Hall effect (AHE) on the surface of magnetic 3DTIs (chapter 5).

In chapter 2, we begin by describing the Boltzmann continuum model, which is the method applied in chapters 3, 4 and 5. This chapter describes the electrons' transition rate, relaxation times, and conductivity of the system based on Boltzmann's formalism. The interaction between conducting electrons and the magnetic impurities is anisotropic in magnetic topological ultra-thin films due to the strong intrinsic spin-orbit coupling, as discussed in chapters 3 and 4. Thus, this chapter discusses how to solve the associated Boltzmann equation for these system using a generalized relaxation time approximation. Besides this, because chapter 5 looks at the AHE on the surface of magnetic 3DTIs, the final part of chapter 2 reviews all the related mechanisms, including side jump scattering, skew scattering, and Berry curvature in the presence of magnetic and non-magnetic impurities.

In chapter 3, we study the charge transport in a magnetic topological ultra-thin film in the absence of a substrate. Since the system is very thin, the wave functions of the top and bottom surface states overlap, causing a finite size effect gap to emerge in the band structure. Once this ultra-thin

film comes into contact with a ferromagnet, the gap of the system varies as a result of the induced ferromagnet phase via the proximity effect, resulting in two non-degenerate conduction subbands.

This chapter describes how magnetic impurities affect the charge transport by inducing a chirality selection rule that governs the transitions of electrons. This selection rule is sensitive to the spin direction of the impurities and the position of the Fermi level. Based on these details, two distinct transport regimes are realized. When electrons occupy only the lower conduction subband, a dissipationless charge current is accessible if all magnetic impurities are ordered in-plane. In contrast, when both conduction subbands contribute to the electronic current, the charge transport of a free-standing magnetic topological ultra-thin film is always dissipative, demonstrating how much Fermi level can influence the charge transport in this system.

In chapter 4, we study how charge transport in a magnetic topological ultra-thin film responds to a substrate. We follow the same methodology we used in chapter 3 to calculate the charge transport. Combination of the spin-orbit coupling and structural inversion asymmetry leads to Rashba-like effect in this system, resulting in many exotic transport features.

As it is observed for a free-standing magnetic ultra-thin film, our calculation identifies two distinct regimes for charge transport in a realistic thin film as well. Surprisingly, we will see in this chapter that our results show that a dissipationless charge current can be obtained even in the presence of the substrate (or a gate voltage). Most importantly, we will show that the response of the charge transport in this system to changes in the orientation of the magnetic impurities can be controlled by the substrate potential or a gate voltage.

Finally, in chapter 5, the anomalous Hall conductivity of 3DTIs is studied in terms of the Fermi level, the band gap, the orientation of the surface magnetization, and the concentration of magnetic and non-magnetic impurities using the modified Boltzmann continuum approach along with a generalized relaxation time approximation. The anomalous Hall conductivity is caused by three mechanisms: the intrinsic effect (due to a nonzero Berry curvature), the side jump effect, and the skew scattering effect. They compete to dominate

the anomalous Hall effect in various regimes.

Analytically, we compute the contributions of all three mechanisms to the scattering of massive Dirac fermions by magnetic and nonmagnetic impurities. Our results for the AHE in this system identify three transport regimes depending on the relative relevance of several engaged mechanisms. Understanding the behavior of these three mechanisms, we provide a clear scenario for the recently empirically reported sign change of the AHE.

BIBLIOGRAPHY

[1] S.-Q. Shen, *Topological Insulators: Dirac Equation in Condensed Matters* (Springer-Verlag, Berlin 2012).

[2] M. Hasan et al., Rev. Mod. Phys. **82**, 3045 (2010).

[3] X-L Qi et al., Rev. Mod. Phys. **83** 1057 (2011).

[4] L. Fu, Phys. Rev. Lett. **106** 106802 (2011).

[5] Y. Xia et al., Nat. Phys. **5** 398 (2009).

[6] H. Zhang et al., Nat. Phys. **5** 438 (2009).

[7] Z. Alpichshev et al., Phys. Rev. Lett. **104** 016401 (2010).

[8] D. Culcer et al., Phys. Rev. B **82**, 155457 (2010).

[9] D. Culcer, Physica E **44**, 860 (2012).

[10] P. Roushan *et al.*, Nature **460**, 1106 (2009).

[11] C. X. Liu et al., Phys. Rev. Lett. **101**, 146802 (2008).

[12] R. Yu et al., Science **329**, 61 (2010).

[13] A. M. Essin et al., Phys. Rev. Lett. **102**, 146805 (2009).

[14] X. L. Qi et al., Science **323**, 1184 (2009).

[15] X. L. Qi et al., Rev. Mod. Phys. **83**, 1057 (2011).

[16] L. Fu et al., Phys. Rev. Lett. **102**, 216403 (2009).

[17] X. L. Qi et al., Phys. Rev. B **78**, 195424 (2008).

[18] A. Sabzalipour et al., Phys. Rev. B **100**, 035419 (2019).

[19] D. Culcer et al., Phys. Rev. B **82**, 155457 (2010).

[20] N. Liu et al., Nat. Commun. 9, 1282 (2018).

[21] $https://en.wikipedia.org/wiki/Gaussian_curvature$

[22] K. v. Klitzing et al., Phys. Rev. Lett. **45**, 494 (1980).

[23] D. J. Thouless et al., Phys. Rev. Lett. **49**, 405 (1982).

[24] D. R. Hofstadter, Phys. Rev. B **14**, 2239 (1976).

[25] J. Zak, Phys. Rev. **134**, A1602 (1964).

[26] Nakahara, M., 1990, Geometry, Topology and Physics (Adam Hilger, Bristol).

[27] K. Von Klitzing, Phil. Trans. R. Soc. A **363**, 2203 (2005).

[28] B. A. Bernevig et al., Topological Insulators and Topological Super- conductors, Princeton University Press (2013).

[29] F. D. M. Haldane, Phys. Rev. Lett. **61**, 2015 (1988).

[30] K. Novoselov et al., Nature **438**, 197 (2005).

[31] A. K. Geim et al., Nature materials **6**, 183 (2007).

[32] A. C. Neto et al., Rev. Mod. Phys. **81**, 109 (2009).

[33] C. L. Kane et al., Phys. Rev. Lett. **95**, 146802 (2005).

[34] B. A. Bernevig et al., Phys. Rev. Lett. **96**, 106802 (2006).

[35] M. Konig et al., Science **318**, 770 (2007).

[36] J. J. Sakurai, Modern Quantum Mechanics, Addison-Wesley (1994).

[37] C. L. Kane et al., Phys. Rev. Lett. **95**, 146802 (2005).

[38] S. Murakami, Phys. Rev. Lett. **97**, 236805 (2006).

[39] L. Fu et al., Phys. Rev.B **74**, 195312 (2006).

[40] D. N. Sheng et al., Phys. Rev. Lett. **97**, 036808 (2006).

[41] L. Fu et al., Phys. Rev. B **76**, 045302 (2007).

[42] H. Zhang et al., Nat. Phys., **5**, 438 (2009).

[43] H. M. Guo et al., Phys. Rev. Lett. **103**, 206805 (2009).

[44] M. Z. Hasan et al., Rev. Mod. Phys., **82**, 3045 (2010).

[45] L. Fu et al., Phys. Rev. Lett. **98**, 106803 (2007).

[46] J. E. Moore et al., Phys. Rev. B **75**, 121306(R) (2007).

[47] R. Roy, Phys. Rev. B **79**, 195321 (2009).

[48] L. Fu et al., Phys. Rev. Lett. **98**, 106803 (2007).

[49] D. Hsieh et al., Nature(London) **452**, 970 (2008).

[50] H. Zhang et al., Nat. Phys. **5**, 438 (2009).

[51] Y. Xia et al., Nat. Phys. **5**, 398 (2009).

[52] O. V. Yazyev et al., Phys. Rev. Lett., **105**, 266806 (2010).

[53] H. Zhang et al., Nat. Phys., **5**, 438 (2009).

[54] H. Suzuura et al., Phys. Rev. Lett. **89**, 266603 (2002).

[55] S. Hikami et al., Prog. Theor. Phys. **63**, 707 (1980).
[56] X.-L. Qi et al., Phys. Rev. B **78**, 195424 (2008).
[57] X.-L. Qi et al., Nat. Phys. **4**, 273 (2008).
[58] A. B. Sushkov et al., Phys. Rev. B **82**, 125110 (2010).
[59] G. S. Jenkins et al., Phys. Rev. B **82**, 125120 (2010).
[60] G. M. Gusev et al., Phys. Rev. B **84**, 121302(R) (2011).
[61] A. A. Zyuzin et al., Phys. Rev. B **83**, 245428 (2011).
[62] I. Lee et al., Proc. Natl. Acad. Sci. **112**, 1316 (2015).
[63] S. Y. Xu et al., Nature Phys. **8**, 616 (2012).
[64] L. A. Wray et al., Nature Phys. **7**, 32 (2011).
[65] Y. L. Chen et al., Science **329**, 659 (2010).
[66] I. Vobornik et al., Nano Lett. **11**, 4079 (2011).
[67] M. Li et al., Phys. Rev. Lett. **115**, 087201 (2015).
[68] F. Yang et al., Phys. Rev. B **94**, 075304 (2016).
[69] Peng Wei et al., Phys. Rev. Lett. **110**, 186807 (2013).
[70] T. Hesjedal and Y. Chen, Nature Materials **16**, 3 (2017).
[71] F. Katmis et al., Nature **533**, 513 (2016).
[72] Q. Liu et al., Phys. Rev. Lett. **102**, 156603 (2009).
[73] D. A. Abanin et al., Phys. Rev. Lett. **106**, 136802 (2011).
[74] W. Luo et al., Phys. Rev. B, **87(8)** (2013).
[75] R. D. Li et al., Nat. Phys. **6(4)**, 284 (2010).
[76] X. L. Qi et al., Science **323(5918)**, 1184 (2009).
[77] Q. Liu et al., Phys. Rev. Lett. **102(15)**, 156603 (2009).
[78] L. A. Wray, Nat. Phys. **8**, 705 (2012).
[79] C. Z. Chang et al., Science **340**, 167 (2013).
[80] Q. K. Xue. Natl. Sci. Rev. **1**, 31 (2014).
[81] J. Wang et al., Phys. Rev. Lett., **111**, 136801 (2013).
[82] R. Yu et al., Science **329**, 61 (2010).
[83] J. S. Dyck et al., Phys. Rev. B **6**5, 115212 (2002).
[84] Z. Zhou et al., Appl. Phys. Lett. **87**, 112503 (2005).
[85] Q. Liu et al., Phys. Rev. Lett. **102**, 156603 (2009).
[86] R. R. Biswas et al., Phys. Rev. B **81**, 233405 (2010).

[87] A. M. Essin et al., Phys. Rev. Lett. **102**, 146805 (2009).

[88] J. Maciejko et al., Phys. Rev. Lett. **105**, 166803 (2010).

[89] T. Yokoyama et al., Phys. Rev. B **81**, 121401(R) (2010).

[90] H. Zhang et al., Nat. Phys. **5**, 438 (2009).

[91] G. Zhang et al., Appl. Phys. Lett. **95**, 053114 (2009).

[92] H. Peng et al., Nature Mater **9**, 225 (2010).

[93] W.- Y. Shan et al., New J. Phys. **12**, 43048 (2010).

[94] Y. Zhang et al., Nat. Phys. **6**, 584 (2010).

CHAPTER 2

CHARGE TRANSPORT IN THE SEMICLASSICAL FORMALISM

Since in chapters 3, 4, 5 of this thesis, the Boltzmann semiclassical approach is employed to investigate the longitudinal and transverse conductivity of a topological insulator, this chapter is devoted to the description of this methodology. The disordered topological insulators studied in this thesis host magnetic and non-magnetic impurities. Depending on the type of these impurities, electrons' scattering off the impurities can be isotropic or anisotropic. Hence, in the following sections, we thoroughly describe the Boltzmann transport formalism and the correct relaxation time scheme for the charge transport calculation in isotropic and anisotropic systems.

2.1 Transport of electrons in a perfect crystal

Electrons undergo no scattering in a perfect crystal, resulting in an infinite relaxation time and charge conductivity. This dissipationless charge current in a perfect crystal is inconsistent with our classical picture for the motion of electrons. According to our classical point of view, electrons collide with ions when they move inside a crystal, reducing their energy and velocity. In contrast, according to electrons' wave nature, a wave can propagate through a periodic array of ions without energy loss due to coherent constructive inter-

ference [1]. Note that even in a perfect crystal, phonon-related fluctuations can reduce the conductivity, though for short times or at very low temperatures, phonon-related fluctuations have a negligible effect on the electron transport, so it is possible to consider a material without scattering.

Unlike perfect crystals, electrons always scatter off impurities, vacancies, or other imperfections and lose their energy in realistic materials. At very low temperature, in contrary to many conduction-limiting mechanisms which depend on the temperature, scattering from impurities plays the dominant role in the charge transport. In what follows, we discuss step by step the effect of ions, external fields, and impurities on the charge transport of electrons within the semiclassical framework.

2.2 The free-electron model versus the semiclassical model

In solid-state physics, the free-electron model was the first and the simplest model employed to investigate dynamics of electrons in an electron gas. It was developed in 1927, mainly by Arnold Sommerfeld, who combined the classical Drude model with quantum mechanical Fermi–Dirac statistics.

The free-electron theory considers metals as composed of a quantum electron gas in which ions play almost no role, and electrons are free particles. This model can resolve many of the inconsistencies arising from the Drude model and gives insight into several other properties of metal. In the free-electron theory, electrons move between different scattering events according to the classical equations of motion. According to the quantum mechanical point of view, these classical equations can be interpreted as the evolution of wave packets constructed from free electron states.

The De Broglie wavelength of electrons is given by

$$\lambda = \frac{h}{p}, \tag{2.1}$$

which, $h = 4.13566 \times 10^{-15}\ eV.s^{-1}$, and is about 1 Angstrom. This value is comparable to the inter-atomic spacing in common crystals. Therefore, when

electrons interact with the ions, the electrons reveal their wave nature. However, the free-electron theory disrespects this fact and hence presents several inadequacies that contradict experimental results. For example, this model gives several physical quantities with the wrong temperature dependence or with no dependence like the electrical conductivity. It also cannot explain the existence of long mean free paths of electrons at low temperatures. In addition, it fails to predict the behavior that originates from the motion of ions and phonon scattering at very low temperature.

Contrary to the free-electron theory, the semiclassical model takes into account the effect of ions on the transport of electrons. This model respects the wave nature of electrons when they interact with ions. The known effective Hamiltonian of the electrons in the system provides us with the energy of electrons (as a function of the electron's momentum) and consequently the velocity of Bloch's electrons. Therefore, the crystal periodic potential plays a crucial role in the system's transport calculation in this model. In other words, instead of using the plane waves (free particles in the free-electron model), we use Bloch waves (electrons+ions) in the semiclassical model. In this sense the semiclassical framework represents a generalization of the free electron model.

2.3 The effect of external fields in semi-classical model

In the previous section, we discussed that we are not allowed to treat electrons as particles when it comes to the interaction between electrons and ions. However, in this section, we explain that we can treat the electrons as particles when we investigate their response to slowly varying potentials.

According to the *Heisenberg uncertainty principle*,

$$\Delta x \Delta p \sim \hbar \tag{2.2}$$

where, Δx and Δp are uncertainties in the position and momentum of the electrons, respectively. If we want to consider the electrons as particles, they

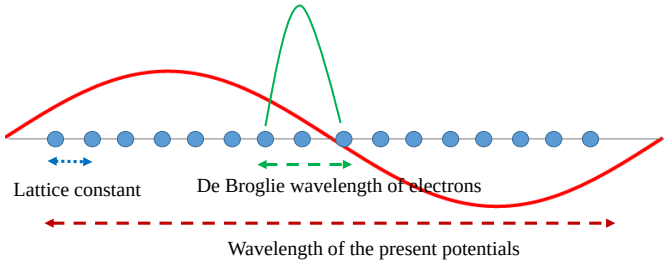

Figure 2.1: Compares the *de Broglie* wavelength of an electron with the wavelength of an external field and the lattice constant of a crystal.

must have well defined positions,

$$\frac{\Delta x}{x} << 1. \tag{2.3}$$

For conducting electrons, the above equation gives

$$\frac{1}{k_F} << x, \tag{2.4}$$

where $\frac{1}{k_F} \sim a$, a is the lattice constant of a crystal and k_F is the Fermi momentum. Therefore, if the region in which the electrons move is much larger than the lattice constant, electrons can be described by states that are well-defined in position space and momentum space. In most materials, the mean free path of electrons is on the order of hundreds of angstroms and decreases with temperature. For these materials, the semiclassical description can be satisfactorily employed .

As the transport of electrons through a system is induced by an electric field, the electron response to this external field needs to be taken into account in the transport calculation. External fields usually slightly change over the atomic spacing dimensions, see Fig. 2.1. For example, visible light changes over a thousand angstroms. Then, the semiclassical model can be applied for describing the response of electrons to these external fields. However, contrary to this case, by reducing the external field's wavelength to, for example, X-rays, the semiclassical approach is not applicable.

In the semiclassical regime, the time evolution of the position $\mathbf{r}$ and momentum $\hbar\mathbf{k}$ of the electrons exposed to the external electric field $\mathbf{E}$ and magnetic field $\mathbf{B}$ are given by

$$\dot{\mathbf{r}} = \mathbf{v}_k = \frac{\hbar\mathbf{k}}{m} = \frac{1}{\hbar}\nabla_k \varepsilon_k, \tag{2.5}$$

$$\dot{\mathbf{k}} = -\frac{e}{\hbar}(\mathbf{E} + \dot{\mathbf{r}} \times \mathbf{B}), \tag{2.6}$$

where ε_k is the energy of the electrons in the state k.

Let us understand the above equations using the free-electron theory and the semiclassical theory. The free-electrons theory indicates that the above equations describe the behavior of a wave packet constructed from plane waves (free particles)

$$\psi(\mathbf{r},t) = \sum_{\boldsymbol{k}'} g(\boldsymbol{k}') \exp[i\left(\boldsymbol{k}' \cdot \mathbf{r} - \frac{\hbar k'^2 t}{2m}\right)] \ , \ \ g(\boldsymbol{k}') \approx 0, |\boldsymbol{k} - \boldsymbol{k}'| > \Delta k, \tag{2.7}$$

where $\mathbf{r}$ and $\mathbf{k}$ are the mean position and momentum about which the above wave packet is localized. However, the same equations have a different meaning within the semiclassical theory. In semiclassical theory, they describe the behavior of a wave packet constructed from Bloch levels in a given band,

$$\psi_n(\mathbf{r},t) = \sum_{\boldsymbol{k}'} g(\boldsymbol{k}') \psi_{n\boldsymbol{k}'} \exp[\frac{i}{\hbar}\varepsilon_n(k')t] \ , \ \ g(\boldsymbol{k}') \approx 0, |\boldsymbol{k} - \boldsymbol{k}'| > \Delta k. \tag{2.8}$$

Since Δk is small compared with the Brillouin zone's size, ε_k varies little over the present levels in the wave packet. Therefore, Eq. 2.5 can be interpreted as the group velocity of the wave packet. In short, the classical equations of motion describe the dynamical behavior of free particles in the free-electron theory, and Bloch electrons in the semiclassical theory.

2.4 The evolution of the electron distribution function

In the semiclassical point of view electrons are characterized by their coordinates $\mathbf{r}$ and momentum $\mathbf{p}$, in six-dimensional phase space. The distribution function in a six-dimensional space specifies how many particles are in an element of $\Delta\mathbf{r}\ \Delta\mathbf{p}$. In contrast, particles in quantum mechanics cannot be described by a well-defined coordinate and momentum simultaneously. However, a statistical ensemble of quantum particles can be described by a function of $\mathbf{p}$ and $\mathbf{r}$ that is similar to the distribution function in the classical picture. If this function in quantum mechanics only slowly depends on the coordinates, it can be identified with the classical particles' distribution function.

Calculating the transport properties of a system by the semiclassical method requires a nonequilibrium distribution function of electrons $f(\mathbf{k},\mathbf{r},t)$ so that $f(\mathbf{k},\mathbf{r},t)\frac{\Delta\mathbf{k}\Delta\mathbf{r}}{4\pi^3}$ is the number of electrons at time t in the semiclassical phase space volume $\Delta\mathbf{k}\ \Delta\mathbf{r}$ about point $\mathbf{r}$ and $\mathbf{k}$. In this section, we systematically take into account the effect of external fields and impurities on the transport of the conducting electrons and finally extract the Boltzmann transport equation which yields the nonequilibrium distribution function of Bloch electrons.

In equilibrium, the quantum distribution function f_0 is the Fermi-Dirac distribution function,

$$f_0 = \frac{1}{1+\exp[\frac{\varepsilon_k-\mu}{\kappa_B T}]}, \tag{2.9}$$

where $\kappa_B = 8.61733\times10^{-5} eVK^{-1}$ is the Boltzmann constant and T is the temperature of the system. Note that the Fermi-Dirac distribution function is independent of the scattering of electrons from the present impurities. When the system is driven out of equilibrium, the distribution function of electrons evolves due to: 1) external fields or a temperature gradient, 2) scatterings from the impurities, 3) diffusion. In what follows, we discuss the role of each of them in the evolution of the electron distribution function.

2.4.1 The effect of external fields on the electron distribution function

According to the classical equation of motion, the momentum of electrons evolves under the action of the external fields $\mathbf{E}$ and $\mathbf{B}$ as

$$\dot{\mathbf{k}} = -\frac{e}{\hbar}(\mathbf{E}+\dot{\mathbf{r}}\times\mathbf{B}). \tag{2.10}$$

Electrons with momentum $\mathbf{k}-\dot{\mathbf{k}}\delta t$ at time $t=0$ will have momentum $\mathbf{k}$ at time δt. Thus,

$$f_{\mathbf{k}}(\mathbf{r},\delta t) = f_{\mathbf{k}-\dot{\mathbf{k}}\delta t}(\mathbf{r},0), \tag{2.11}$$

which leads to

$$\frac{\partial f_{\mathbf{k}}(\mathbf{r},\delta t)}{\partial t}\Big)_{fields} = -\frac{e}{\hbar}(\mathbf{E}+\mathbf{v}_k\times\mathbf{B})\frac{\partial f_{\mathbf{k}}(\mathbf{r},\delta t)}{\partial\mathbf{k}}. \tag{2.12}$$

2.4.2 The effect of diffusion on the electron distribution function

Let's assume that there is an electron in location $\mathbf{r}-\mathbf{v}_k\delta t$ at time $t=0$ that moves a distance $\mathbf{v}_k\delta t$ with velocity $\mathbf{v}_k$, and reaches the point $\mathbf{r}$ at time δt. Therefore, the number of electrons around $\mathbf{r}$ at time δt is equal to the number of electrons around $\mathbf{r}-\mathbf{v}_k\delta t$ at time $t=0$,

$$f_{\mathbf{k}}(\mathbf{r},\delta t)=f_{\mathbf{k}}(\mathbf{r}-\mathbf{v}_k\delta t,0). \tag{2.13}$$

Therefore,

$$f_{\mathbf{k}}(\mathbf{r},0)+\frac{\partial f_{\mathbf{k}}(\mathbf{r},0)}{\partial t}\cdot\delta t=f_{\mathbf{k}}(\mathbf{r},0)-\frac{\partial f_{\mathbf{k}}(\mathbf{r},0)}{\partial \mathbf{r}}\cdot\mathbf{v}_k\delta t \tag{2.14}$$

which for a general time result in

$$\frac{\partial f_{\mathbf{k}}(\mathbf{r},t)}{\partial t}\Big)_{diffusion}=-\frac{\partial f_{\mathbf{k}}(\mathbf{r},t)}{\partial \mathbf{r}}\cdot\mathbf{v}_k. \tag{2.15}$$

2.4.3 The effect of scatterings on the electron distribution function

Let $W(\mathbf{k},\mathbf{k}')$ define the rate of a scattering from the occupied state $\mathbf{k}$ to the empty state $\mathbf{k}'$. To study electron transport in a quantum regime, we need to find the scattering matrix (or T-matrix) of the electrons. Within the semiclassical framework, the scattering rate, as a classical object, can be obtained by its connection to the scattering matrix through Fermi's golden rule. However, only the absolute value of the T-matrix elements are present in the scattering rate. Consequently, all the phase information of the T-matrix elements is lost. In this section, we forget about the golden rule's insufficiency, but later we will discuss how we can restore all the missing phase information.

The transition rate $W_{\mathbf{kk}'}$ for the scattering of itinerant electrons from state $\boldsymbol{k}$ to state $\boldsymbol{k}'$ within the first Born approximation is given by [2, 3]

$$W_{\mathbf{kk}'}=\frac{2\pi n_{im}}{\hbar}|T_{\mathbf{kk}'}|^2\delta(\varepsilon_{k'}-\varepsilon_k), \tag{2.16}$$

with n_{im} the impurity concentration and the scattering T-matrix defined as

$$T_{\mathbf{k}\mathbf{k}'} = \langle \psi_{\mathbf{k}} | V_{sc} | \psi_{\mathbf{k}'} \rangle, \tag{2.17}$$

where $|\psi_{\mathbf{k}}\rangle$ and $|\psi_{\mathbf{k}'}\rangle$ are the initial and final states of the electrons, and V_{sc} is the scattering potential operator. The rate of change of the distribution function $f_{\mathbf{k}}$ due to scatterings is related to the scattering rate as

$$\frac{\partial f_{\mathbf{k}}}{\partial t}\Big)_{scattering} = \sum_{\mathbf{k}'} f_{\mathbf{k}'}[1 - f_{\mathbf{k}}]W_{\mathbf{k}'\mathbf{k}} - f_{\mathbf{k}}[1 - f_{\mathbf{k}'}]W_{\mathbf{k}\mathbf{k}'}. \tag{2.18}$$

The first term in the right-hand side of the above integral denotes the rate at which an electron from an occupied state $\mathbf{k}'$ (with the occupation number $f_{\mathbf{k}'}$) scatters into an empty state $\mathbf{k}$ (with the occupation number $f_{\mathbf{k}}$), and the second term is the loss term. The scattering rate $W_{\mathbf{k}'\mathbf{k}}$ may depend on the filling factor $f_{\mathbf{k}}$. When scatterings are particle–particle collisions, generally speaking, the energy of the involved particles is not conserved during the scattering time. However, at low energies electrons scatter off impurities without energy loss. For this type of scatterings, the scattering rate is independent of the filling factors. In addition for elastic scattering , the scattering rate is symmetric under the exchange of indexes $\mathbf{k}$ and $\mathbf{k}'$, so $W_{\mathbf{k}\mathbf{k}'} = W_{\mathbf{k}'\mathbf{k}}$. Consequently,

$$\frac{\partial f_{\mathbf{k}}}{\partial t}\Big)_{scattering} = \sum_{\mathbf{k}'} [f_{\mathbf{k}'} - f_{\mathbf{k}}]W_{\mathbf{k}'\mathbf{k}}. \tag{2.19}$$

2.5 The Boltzmann equation

There will be no net change in the distribution function under steady-state conditions, and hence the total sum of the partial derivative terms obtained above will be zero,

$$\frac{\partial f_{\mathbf{k}}}{\partial t}\Big)_{diffusion} + \frac{\partial f_{\mathbf{k}}}{\partial t}\Big)_{fields} + \frac{\partial f_{\mathbf{k}}}{\partial t}\Big)_{scattering} = 0. \tag{2.20}$$

We rewrite the nonequilibrium distribution function of electrons as

$$f_{\mathbf{k}} = f_0 + g_{\mathbf{k}}, \tag{2.21}$$

where $g_{\mathbf{k}}$ is the deviation of the electron distribution function from the equilibrium case. Simplifying Eqs. (2.12), (2.15), (2.19) and using (2.21) results

in

$$\begin{aligned} &-\mathbf{v}_{\mathbf{k}} \cdot \nabla_r f_0 - \tfrac{e}{\hbar}(\mathbf{E} + \mathbf{v}_{\mathbf{k}} \times \mathbf{B}) \nabla_k f_0 \\ &= -\frac{\partial f_{\mathbf{k}}}{\partial t}\Big)_{scattering} + \mathbf{v}_{\mathbf{k}} \cdot \nabla_r g_{\mathbf{k}} + \tfrac{e}{\hbar}(\mathbf{E} + \mathbf{v}_{\mathbf{k}} \times \mathbf{B}) \cdot \nabla_{\boldsymbol{k}} g_{\mathbf{k}}. \end{aligned} \tag{2.22}$$

Keeping terms only to first order in the electric field gives

$$\begin{aligned} &-\frac{\partial f_0}{\partial \varepsilon_{\mathbf{k}}} \cdot \mathbf{v}_{\mathbf{k}} \cdot \left[-\frac{(\varepsilon_{\mathbf{k}} - \mu)}{T} \nabla T + e\mathbf{E} - \nabla \mu \right] \\ &= -\frac{\partial f_{\mathbf{k}}}{\partial t}\Big)_{\text{scattering}} + \mathbf{v}_{\mathbf{k}} \cdot \nabla_r g_{\mathbf{k}} + \tfrac{e}{\hbar}(\mathbf{v}_{\mathbf{k}} \times \mathbf{B}) \cdot \nabla_{\boldsymbol{k}} g_{\mathbf{k}}. \end{aligned} \tag{2.23}$$

For steady states of non-interacting electrons in a spatially homogeneous system (on scales much larger than the distance between scatterers) in which the external applied electric field is uniform in space, and also the temperature of the system is constant over the whole system, the above equation simplifies to

$$(-e)(-\frac{\partial f_0}{\partial \varepsilon_k})\, \mathbf{v}_{\mathbf{k}} \cdot \mathbf{E} = -\frac{\partial f_{\mathbf{k}}}{\partial t}\Big)_{\text{scattering}}. \tag{2.24}$$

The above equation for a system with multiple conduction subbands is given by

$$(-e)(-\frac{\partial f_0^{\mu}}{\partial \varepsilon_k})\, \mathbf{v}_{\mathbf{k}}^{\mu} \cdot \mathbf{E} = \sum_{\mathbf{k}',\mu'} [f_{\mathbf{k}'}^{\mu'} - f_{\mathbf{k}}^{\mu}]\, W_{\mathbf{k}'\mathbf{k}}^{\mu\mu'}, \tag{2.25}$$

where μ is the band index. The above equation is known as Boltzmann equation. This equation is very powerful because it takes care of the summation of various unlimited series of Feynman diagrams in the quantum linear response theory and keeps the physical meaning of all expressions transparent.

2.5.1 The standard relaxation time scheme

The Boltzmann equation is a very complex equation that can be analytically solved only under simplifying assumptions. Within the relaxation time approximation (RTA), we assume that the perturbation $g_{\mathbf{k}}^{\mu}$ decays in time as

$$g_{\mathbf{k}}^{\mu}(t) = g_{\mathbf{k}}^{\mu}(0) \exp[-t/\tau_{\mathbf{k}}^{\mu}], \tag{2.26}$$

where $\tau_{\mathbf{k}}^{\mu}$ represents the time constant for relaxation of the perturbation. This effective relaxation time $\tau_{\mathbf{k}}^{\mu}$ has, in general, no well-defined meaning and does

not adequately describe the experimentally observed transport properties. Following the RTA,

$$-\frac{\partial f_{\mathbf{k}}^{\mu}}{\partial t}\Big)_{\text{scattering}} = -\frac{\partial g_{\mathbf{k}}^{\mu}}{\delta t} = \frac{g_{\mathbf{k}}^{\mu}}{\tau_{\mathbf{k}}^{\mu}}. \tag{2.27}$$

By using the above equation along with Eq. (2.24) we arrive at

$$g_{\mathbf{k}}^{\mu} = -\frac{\partial f_{\mathbf{k}}^{\mu}}{\partial t}\Big)_{\text{scattering}} \cdot \tau_{\mathbf{k}}^{\mu} = e\left(-\frac{\partial f_0^{\mu}}{\partial \varepsilon_k^{\mu}}\right)\left(\mathbf{v}_{\mathbf{k}}^{\mu}\cdot\mathbf{E}\right)\tau_{\mathbf{k}}^{\mu}. \tag{2.28}$$

When all the scattering events are isotropic, the transition rate depends only on the angle between $\mathbf{k}$ and $\mathbf{k}'$, $\phi_{-} = \phi_{\mathbf{k}} - \phi_{\mathbf{k}'}$. Now, combining Eq. (2.25) with the above equation gives

$$-e\left(-\frac{\partial f_0^{\mu}}{\partial \varepsilon_k^{\mu}}\right)(\mathbf{v}_{\mathbf{k}}^{\mu}\cdot\mathbf{E}) = e\left(-\frac{\partial f_0^{\mu}}{\partial \varepsilon_k^{\mu}}\right)\sum_{\mathbf{k}'} W_{\mathbf{k}\mathbf{k}'}^{\mu\mu'}(\tau_{\mathbf{k}'}^{\mu'}\mathbf{v}_{\mathbf{k}'}^{\mu}\cdot\mathbf{E} - \tau_{\mathbf{k}}^{\mu}\mathbf{v}_{\mathbf{k}}^{\mu}\cdot\mathbf{E}). \tag{2.29}$$

For isotropic scatterings, the relaxation time of electrons only depends on the energy of the electrons (and not on their momentum), then for the elastic scatterings $\tau_{\mathbf{k}}^{\mu} = \tau_{\mathbf{k}'}^{\mu} = \tau_k^{\mu}$. Accordingly, we finally end up with the frequently used standard relaxation time τ_k^{μ}, as follows

$$\frac{1}{\tau_k^{\mu}} = \sum_{\mathbf{k},\mu'} W_{\mathbf{k}\mathbf{k}'}^{\mu\mu'}\left(1 - \frac{\mathbf{v}_{\mathbf{k}'}^{\mu'}\cdot\mathbf{E}}{\mathbf{v}_{\mathbf{k}}^{\mu}\cdot\mathbf{E}}\right). \tag{2.30}$$

τ_k^{μ} is constant on the whole Fermi surface when the Fermi energy is fixed. After finding the relaxation time τ_k^{μ}, the electron distribution function is given by

$$g_{\mathbf{k}}^{\mu} = e\left(-\frac{\partial f_0^{\mu}}{\partial \varepsilon_k}\right)\left(\mathbf{v}_{\mathbf{k}}^{\mu}\cdot\mathbf{E}\right)\Big[\sum_{\mathbf{k},\mu'} W_{\mathbf{k}\mathbf{k}'}^{\mu\mu'}(1 - \frac{\mathbf{v}_{\mathbf{k}'}^{\mu}\cdot\mathbf{E}}{\mathbf{v}_{\mathbf{k}}^{\mu}\cdot\mathbf{E}})\Big]^{-1}. \tag{2.31}$$

With this nonequilibrium electron distribution function, the isotropic response of the system to the externally applied electric field can be calculated by

$$\sigma_{\alpha\beta} = -\frac{e}{AE_{\beta}}\sum_{\mathbf{k},\mu} v_{\alpha}^{\mu}(\mathbf{k})[f_0^{\mu} + g_{\mathbf{k}}^{\mu}], \tag{2.32}$$

where α and $\beta = x, y$ and A is the system's surface area.

2.5.2 The modified relaxation time scheme

In anisotropic systems, the conducting electrons' dynamics is highly sensitive to the direction of external electric field. Therefore, depending on the direction of the external electric field, electrons have different relaxation times. To capture this anisotropy in the transport of electrons, Schliemann and Loss proposed [4] the following expression for g_k,

$$g^{\mu}_{\mathbf{k}} = -e(-\frac{\partial f^{\mu}_0}{\partial \varepsilon^{\mu}_k}) v^{\mu}_{\mathbf{k}} E \Big[\frac{\tau^{\mu}_{\parallel}(k)}{1+\left(\frac{\tau^{\mu}_{\parallel}(k)}{\tau^{\mu}_{\perp}(k)}\right)^2} + \frac{\tau^{\mu}_{\perp}(k)}{1+\left(\frac{\tau^{\mu}_{\perp}(k)}{\tau^{\mu}_{\parallel}(k)}\right)^2} \Big], \tag{2.33}$$

where

$$\frac{1}{\tau^{\mu}_{\parallel}(k)} = \sum_{\mathbf{k}',\mu'} W^{\mu\mu'}_{\mathbf{k}\mathbf{k}'} [1 - \frac{v^{\mu}_{\mathbf{k}'}}{v^{\mu}_{\mathbf{k}}} \cos\phi_-], \tag{2.34}$$

$$\frac{1}{\tau^{\mu}_{\perp}(k)} = \sum_{\mathbf{k}',\mu'} W^{\mu\mu'}_{\mathbf{k}\mathbf{k}'} \frac{v^{\mu'}_{\mathbf{k}'}}{v^{\mu}_{\mathbf{k}}} \sin\phi_-. \tag{2.35}$$

Based on this method, after evaluating the above integrals for each k-point of the Fermi surface separately, the nonequilibrium distribution function that solves the Boltzmann equation can be obtained. Contrary to the author's claim, the given expressions in Eqs. (2.34) and (2.35) do not correctly capture the present anisotropy in the electron dynamics, because the $\tau^{\mu}_{\perp}(k)$ and $\tau^{\mu}_{\parallel}(k)$ only partially capture the anisotropy. The expressions Eqs. (2.34) and (2.35) for $\tau^{\mu}_{\perp}(k)$ and $\tau^{\mu}_{\parallel}(k)$ are found assuming that they depend only on the energy of the electrons. However, in anisotropic systems, they depend also on the momentum of electrons. Therefore, the result contradicts the underlying assumptions.

However, later in 2009 a substantial improvement in solving the Boltzmann equation for anisotropic systems was made by Výborný and *et al.* [5]. According to this new method (the modified relaxation time scheme), the nonequilibrium distribution function of electrons moving with velocity $\mathbf{v}^{\mu}_{\mathbf{k}} = v^{\mu}_k(\cos\phi_k, \sin\phi_k, 0)$ in the presence of a external electric field $\mathbf{E} = E(\cos\chi, \sin\chi, 0)$ is given by

$$f_{\mathbf{k}} = f^{\mu}_0 + g^{\mu}_{\mathbf{k}} = f^{\mu}_0 + e\frac{\partial f^{\mu}_0}{\partial \varepsilon_k} v_{\mathbf{k}} E \left(\tau^{\mu}_1(\boldsymbol{k})\cos\chi + \tau^{\mu}_2(\boldsymbol{k})\sin\chi\right), \tag{2.36}$$

in which two proposed relaxation times $\tau_1^\mu(\mathbf{k})$ and $\tau_2^\mu(\mathbf{k})$ can have positive as well as negative values, in contrast to the standard relaxation time that is always positive. In addition, unlike the standard relaxation time, the two introduced relaxation times in Eq. (2.36) are sensitive to the direction of the driving electric field. For a system with isotropic dispersion, $\varepsilon_{\mathbf{k}} = \varepsilon_k$, substituting Eq. (2.36) in the Boltzmann equation gives,

$$v_{\mathbf{k}}^\mu \cos(\phi_{\mathbf{k}} - \chi) = \sum_{\mathbf{k}'} \Big(\Big[v_{\mathbf{k}}^\mu \tau_1^\mu(\boldsymbol{k}) - v_{\mathbf{k}'}^{\mu'} \tau_1^{\mu'}(\boldsymbol{k}') \Big] \cos\chi + \Big[v_{\mathbf{k}}^\mu \tau_2^\mu(\boldsymbol{k}) - v_{\mathbf{k}'}^{\mu'} \tau_2^{\mu'}(\boldsymbol{k}') \Big] \sin\chi \Big) W_{\mathbf{k}\mathbf{k}'}^{\mu\mu'}. \tag{2.37}$$

When $\mathbf{E} = E\hat{x}$, $\chi = 0$, the above equation results in

$$\tau_1^\mu(\boldsymbol{k}) = \frac{\cos\phi_{\mathbf{k}} + \sum\limits_{\mathbf{k}',\mu'} \tau_1^{\mu'}(\boldsymbol{k}')\, W_{\mathbf{k}\mathbf{k}'}^{\mu\mu'}\, \dfrac{v_{\mathbf{k}'}^{\mu'}}{v_{\mathbf{k}}^{\mu}}}{\sum\limits_{\mathbf{k}',\mu'} W_{\mathbf{k}\mathbf{k}'}^{\mu\mu'}}, \tag{2.38}$$

and if $\mathbf{E} = E\hat{y}$, $\chi = \frac{\pi}{2}$, we arrive at

$$\tau_2^\mu(\boldsymbol{k}) = \frac{\sin\phi_{\mathbf{k}} + \sum\limits_{\mathbf{k}',\mu'} \tau_2^{\mu'}(\boldsymbol{k}')\, W_{\mathbf{k}\mathbf{k}'}^{\mu\mu'}\, \dfrac{v_{\mathbf{k}'}^{\mu'}}{v_{\mathbf{k}}^{\mu}}}{\sum\limits_{\mathbf{k}',\mu'} W_{\mathbf{k}\mathbf{k}'}^{\mu\mu'}}. \tag{2.39}$$

The above two integral equations are two decoupled inhomogeneous *Fredholm equations* of the second kind expressed in the form of

$$F(x) = q(x) + \lambda \int_a^b S(x,y) F(y) dy. \tag{2.40}$$

Given the function $S(x,y)$, and $q(x)$, the problem is to find the unknown function $F(x)$. One practical way to solve these *Fredholm equations* of the second kind is to expand the unknown function $F(y)$ in Fourier series. Therefore, we also replace the two unknown functions $\tau_i^\mu(\boldsymbol{k})$ in Eqs. (2.38) and (2.39) with their Fourier expansions $\tau_i^\mu(\boldsymbol{k}) = \sum_n (\tau_{in}^{\mu c}(k)\cos n\phi_{\boldsymbol{k}} + \tau_{in}^{\mu s}(k)\sin n\phi_{\boldsymbol{k}})$. Next, solving the following system of equations yields the Fourier coefficients $\tau_{in}^{\mu c}(k)$ and $\tau_{in}^{\mu s}(k)$ for $i = 1,2$,

$$\begin{cases} \pi\ \tau_{1n}^{\mu c}(k) - \int \left[\dfrac{\cos\phi_{\boldsymbol{k}} + \sum\limits_{\mathbf{k}',\mu',n} \left[\left(\tau_{1n}^{\mu c}(k')\cos n\phi_{\boldsymbol{k}'} + \tau_{1n}^{\mu s}(k')\sin n\phi_{\boldsymbol{k}'} \right) W_{\mathbf{k}\mathbf{k}'}^{\mu\mu'} \dfrac{v_{\mathbf{k}'}^{\mu'}}{v_{\mathbf{k}'}^{\mu'}} \right]}{\sum\limits_{\mathbf{k}',\mu'} W_{\mathbf{k},\mathbf{k}'}^{\mu\mu'}} \right] \cos n\phi_{\mathbf{k}'} d\phi_{\mathbf{k}'} = 0 \\ \pi\ \tau_{1n}^{\mu s}(k) - \int \left[\dfrac{\cos\phi_{\boldsymbol{k}} + \sum\limits_{\mathbf{k}',\mu',n} \left[\left(\tau_{1n}^{\mu' c}(k')\cos n\phi_{\boldsymbol{k}'} + \tau_{1n}^{\mu' s}(k')\sin n\phi_{\boldsymbol{k}'} \right) W_{\mathbf{k}\mathbf{k}'}^{\mu\mu'} \dfrac{v_{\mathbf{k}'}^{\mu'}}{v_{\mathbf{k}'}^{\mu'}} \right]}{\sum\limits_{\mathbf{k}',\mu'} W_{\mathbf{k},\mathbf{k}'}^{\mu\mu'}} \right] \sin n\phi_{\mathbf{k}'} d\phi_{\mathbf{k}'} = 0 \end{cases}, \tag{2.41}$$

$$\begin{cases} \pi\ \tau_{2n}^{\mu c}(k) - \int \left[\dfrac{\sin\phi_{\boldsymbol{k}} + \sum\limits_{\mathbf{k}',\mu',n} \left[\left(\tau_{2n}^{\mu c}(k')\cos n\phi_{\boldsymbol{k}'} + \tau_{2n}^{\mu s}(k')\sin n\phi_{\boldsymbol{k}'} \right) W_{\mathbf{k}\mathbf{k}'}^{\mu\mu'} \dfrac{v_{\mathbf{k}'}^{\mu'}}{v_{\mathbf{k}}^{\mu}} \right]}{\sum\limits_{\mathbf{k}',\mu'} W_{\mathbf{k}\mathbf{k}'}^{\mu\mu'}} \right] \cos n\phi_{\mathbf{k}'} d\phi_{\mathbf{k}'} = 0 \\ \pi\ \tau_{2n}^{\mu s}(k) - \int \left[\dfrac{\sin\phi_{\boldsymbol{k}} + \sum\limits_{\mathbf{k}',\mu',n} \left[\left(\tau_{2n}^{\mu c}(k')\cos n\phi_{\boldsymbol{k}'} + \tau_{2n}^{\mu s}(k')\sin n\phi_{\boldsymbol{k}'} \right) W_{\mathbf{k}\mathbf{k}'}^{\mu\mu'} \dfrac{v_{\mathbf{k}'}^{\mu'}}{v_{\mathbf{k}'}^{\mu'}} \right]}{\sum\limits_{\mathbf{k}',\mu'} W_{\mathbf{k}\mathbf{k}'}^{\mu\mu'}} \right] \sin n\phi_{\mathbf{k}'} d\phi_{\mathbf{k}'} = 0 \end{cases}. \tag{2.42}$$

Note that conservation of the number of particles imposes

$$N = \sum_{\boldsymbol{k},\mu} f_0^{\mu} = \sum_{\boldsymbol{k},\mu} (f_0^{\mu} + g_{\boldsymbol{k}}^{\mu}), \tag{2.43}$$

so that, $\sum\limits_{\mathbf{k},\mu} g_{\mathbf{k}}^{\mu} = 0$, and hence all the constant terms in the Fourier expansions are zero. Depending on the system under study the above two systems of equations Eq. (2.41) and (2.42) can be solved analytically or numerically. Next, the contribution of each band to the conductivity of a system can be obtained by

$$\begin{aligned} \sigma_{\alpha\beta}^{\mu} = & \frac{e^2}{AE_{\beta}} \sum_{\boldsymbol{k}} \mathbf{v}_{\alpha}^{\mu}(k) \mathrm{v}_k^{\mu}\ E\ \tau_1^{\mu}(\boldsymbol{k}) \delta(\varepsilon_k^{\mu} - \varepsilon_F) \cos\chi + \\ & \frac{e^2}{AE_{\beta}} \sum_{\boldsymbol{k}} \mathbf{v}_{\alpha}^{\mu}(k) \mathrm{v}_k^{\mu}\ E\ \tau_2^{\mu}(\boldsymbol{k}) \delta(\varepsilon_k^{\mu} - \varepsilon_F) \sin\chi. \end{aligned} \tag{2.44}$$

Finally, finding the contribution of electrons from all conduction subbands yields the total conductivity $\sigma_{\alpha\beta} = \sum\limits_{\mu} \sigma_{\alpha\beta}^{\mu}$.

By defining the *Anisotropic Magnetoresistance*(AMR) as

$$AMR = \frac{\sum\limits_{\mu} (\sigma_{xx}^{\mu} - \sigma_{yy}^{\mu})}{\sum\limits_{\mu} (\sigma_{xx}^{\mu} + \sigma_{yy}^{\mu})}, \tag{2.45}$$

we can systematically measure the degree of sensitivity of the charge current to the direction of applied electric field. It is evident that the *AMR* is zero isotropic systems for which $\sigma^{\mu}_{xx} = \sigma^{\mu}_{yy}$.

2.6 The semiclassical framework for the anomalous Hall effect (AHE)

This semiclassical Eq. (2.25) deals only with gauge-invariant quantities, such as the scattering rate, band velocity, and the distribution function. Nevertheless, since in this equation, the only role of the electric field is to accelerate wave packets, and the only role of impurities is to produce incoherent instantaneous events, it is clear that this approach must often be insufficient. In studying the AHE, more than ever, we need to modify the semiclassical framework to incorporate all the relevant phenomena correctly. In the following section, we first introduce the AHE and all the extrinsic mechanisms (side jump and skew scattering) and intrinsic mechanism (anomalous velocity) that play a role in the AHE. Next, we discuss how the Boltzmann equation can be modified to correctly capture these effects in the AHE. As we will discuss, we will add some corrections to the band velocity of the electrons, transition rate, and also the electron distribution function to prepare the Boltzmann equation for studying the AHE.

2.6.1 The anomalous Hall effect

When a non-ferromagnetic metallic sample is exposed to an external perpendicular magnetic field, a voltage difference is generated across the plane of the sample due to the *Lorentz* force. This observed voltage generates a transverse current. This well-known phenomenon was first discovered by *Edwin Hall* in 1879 [6]. The Hall resistivity is given by

$$\rho_{xy} = R_0\, B, \tag{2.46}$$

where $R_0 = \dfrac{1}{n\, e}$ is the Hall coefficient. The Hall effect provides us such an accurate tool to measure the concentration and type of charge carriers (electrons or

holes). Due to the significant influence of the Hall effect on condensed matter physics, it is frequently called the queen of solid-state transport experiments.

One year later in 1880 [7], Hall discovered that the transverse charge current was ten times larger in ferromagnetic iron than in non-magnetic conductors. For such a ferromagnetic system it is empirically shown that

$$\rho_{xy} = R_0\, B + R_s M, \tag{2.47}$$

where R_s is the anomalous Hall coefficient. The second term caused by magnetization M is independent of the external magnetic field and then persists even in the absence of the external magnetic field. Surprisingly, in some materials, the magnetization contribution to the generated Hall current is significantly dominant. For example, in nickel, the anomalous Hall coefficient is about 100 times larger than the ordinary Hall coefficient near the Curie temperature [8].

Even though the AHE is a well-recognized phenomenon, it has been an enigmatic problem for almost a century, and there is still debate about its origin in various materials. The main reason is that understanding the AHE requires knowledge about some topological concepts that have been formulated only recently. However, now it is clear that the AHE originates from three effects: skew scattering, side jump, and non-zero Berry curvature. The side jump and skew scattering rely on the disorder, while the non-zero Berry-phase curvature is an intrinsic effect. In what follows, we will explain these three effects separately.

2.6.2 The intrinsic contribution to the AHE

In 1954, Karplus and Luttinger (KL) [8] proposed that the AHE is a consequence of the spin-orbit interaction that is present in ferromagnetic materials. Owing to the spin-orbit interaction, the electrons acquire an anomalous velocity when an external electric field is applied, which depends on their spins, as shown in Fig. 2.2(a) and is perpendicular to both the electric field and the magnetization's mean direction. Surprisingly, in ferromagnetic materials, the average of the anomalous velocity over all occupied electronic states can be

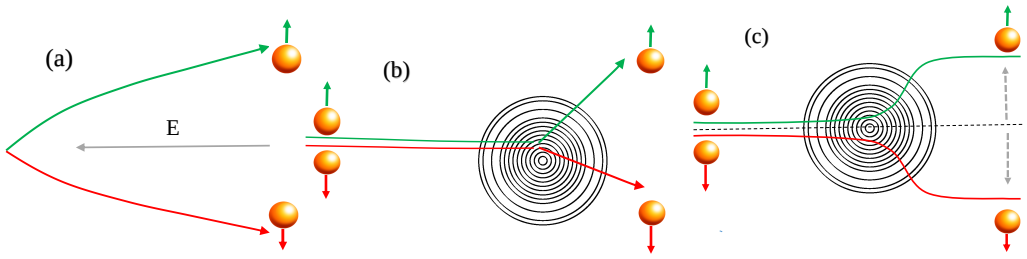

Figure 2.2: (a): Intrinsic effect due to the Berry curvature, (b): skew scattering, (c): and coordinate shift .

non-zero. Since this non-zero anomalous velocity does not rely on disorder, it has been referred to as the intrinsic mechanism of the AHE.

When Karplus and Luttinger proposed the intrinsic mechanism for the AHE, the concept of Berry phase was not recognized. Berry in 1984 [9] showed that the phase of a quantum system is a non-arbitrary quantity that can be measured in some cases. After the proposal of the Berry phase, Chang et al. [10] and Sundaram et al. [11] connected the already observed anomalous velocity in the AHE and the Berry phase. They demonstrated that the Berry phase can be used to explain the anomalous velocity of Bloch electrons and that the integral of the Berry curvature over all occupied Bloch states can be used to determine the anomalous Hall conductivity. The anomalous velocity is given by

$$\boldsymbol{v}_{\boldsymbol{k}}^{an} = -\dot{\boldsymbol{k}} \times (\nabla_{\boldsymbol{k}} \times \boldsymbol{A}_{\boldsymbol{k}}), \tag{2.48}$$

where $\boldsymbol{A}_{\boldsymbol{k}} = i\langle u_{\boldsymbol{k}} | \nabla_{\boldsymbol{k}} | u_{\boldsymbol{k}} \rangle$ is the Berry connection, and $u_{\boldsymbol{k}}(\mathbf{r}) = e^{-i\boldsymbol{k}\cdot\boldsymbol{r}}\psi_{\boldsymbol{k}}(\boldsymbol{r})$. As will be shown later, the semiclassical framework takes into account this anomalous velocity to properly study the AHE.

2.6.3 The skew scattering contribution to the AHE

KL model only studied the AHE in a perfect crystal without any scatterings from disorder or impurities and therefore is known as the intrinsics contribution to the AHE. Soon after the KL model, Smit [12, 13] argued that the AHE vanishes in a perfect crystal and proposed the skew-scattering as the primary mechanism behind the AHE. Skew scattering is an extrinsic mechanism due to the presence of impurities in a material.

When an electron approaches a charged impurity, it experiences an electric field. In the presence of spin-orbit interaction, this electric field generates a magnetic field that is perpendicular to both the electric field and the velocity of electrons. The generated magnetic field is inhomogeneous in space because it depends on the electron's velocity and scattering potential, and both of them vary in space. This inhomogeneous magnetic field gives rise to a different Zeeman energy for electrons with opposite spins. Therefore, as shown in Fig. 2.2(b), electrons with opposite spins scatter with different angles, which is called skew scattering. In what follows, we will discuss how this asymmetric scattering can be captured in the semiclassical framework.

Within the semiclassical framework, the scattering rate, as a classical object, can be obtained by its connection to the scattering matrix through Fermi's golden rule. However, it should be noted that only the absolute value of the T-matrix elements are present in the scattering rate. Consequently, all the phase information of the T-matrix elements is lost. In this section we will discuss how we can restore this missing phase information.

The electron state after scattering $\psi_{\mathbf{k}'}$ in Eq. (2.51) satisfies the Lippmann-Schwinger equation

$$|\psi_{\mathbf{k}'}\rangle = |\psi_{\mathbf{k}}\rangle + \frac{V_{sc}}{\varepsilon_{k'} - H_0 + i\eta}|\psi_{\mathbf{k}'}\rangle. \tag{2.49}$$

For weak disorder, $|\psi_{\mathbf{k}'}\rangle$ can be approximated by a truncated series in powers of $V_{\mathbf{k}\mathbf{k}'} = \langle\psi_{\mathbf{k}}|V_{sc}|\psi_{\mathbf{k}'}\rangle$. By applying Eq. (2.49) and Eq. (2.17), $T_{\mathbf{k}\mathbf{k}'}$ up to third order in V_{sc} is given by

$$T_{\mathbf{k}\boldsymbol{k}'} = V_{\boldsymbol{k}\boldsymbol{k}'} + \sum_{\boldsymbol{k}''} \frac{V_{\boldsymbol{k}\boldsymbol{k}''}V_{\mathbf{k}''\boldsymbol{k}'}}{\varepsilon_k - \varepsilon_{k''} + i\eta} + \sum_{\boldsymbol{k}'''}\sum_{\boldsymbol{k}''} \frac{V_{\boldsymbol{k}\boldsymbol{k}''}V_{\mathbf{k}''\boldsymbol{k}'''}V_{\boldsymbol{k}'''\boldsymbol{k}'}}{(\varepsilon_k - \varepsilon_{k''} + i\eta)(\varepsilon_k - \varepsilon_{k'''} + i\eta)}. \tag{2.50}$$

Substituting this expansion for $T_{kk'}$ into

$$W_{\mathbf{k}\mathbf{k}'} = \frac{2\pi}{\hbar}|T_{\mathbf{k}\mathbf{k}'}|^2\delta(\varepsilon_{k'} - \varepsilon_k), \tag{2.51}$$

leads to the following scattering rate up to fourth order in the scattering potential

$$W_{\mathbf{k}\mathbf{k}'} = W^{(2)}_{\mathbf{k}\mathbf{k}'} + W^{(3)}_{\mathbf{k}\mathbf{k}'} + W^{(4)}_{\mathbf{k}\mathbf{k}'}\ , \tag{2.52}$$

where $W^{(2)}_{\mathbf{k}\mathbf{k}'}$ is symmetric under changing $\mathbf{k} \longleftrightarrow \mathbf{k}'$, and is given by

$$W^{(2)}_{\mathbf{k}\mathbf{k}'} = \frac{2\pi}{\hbar}\langle|V_{\mathbf{k}\mathbf{k}'}|^2\rangle_{dis}\,\delta(\varepsilon_k - \varepsilon_{k'})\ , \tag{2.53}$$

where dis denotes averaging over all possible distributions of impurities in our system. For dilute and randomly placed impurities, it has been shown that $\langle|V_{\mathbf{kk'}}|^2\rangle_{dis} \sim n_{im}$ [2], with n_{im} the concentration of impurities. As a result, electron transport is influenced by the strength of the electron-impurity interaction as well as the density of impurities. One of the main contributions to the AHE originates from skew scattering. In order to investigate this contribution, we need to calculate the asymmetric part of the transition rate, $W^{(a)}_{\mathbf{kk'}} = \dfrac{W_{\mathbf{kk'}} - W_{\mathbf{k'k}}}{2}$. The first asymmetric term is given by

$$W^{(3)}_{\boldsymbol{kk'}} = \frac{2\pi}{\hbar}\left(\sum_{\boldsymbol{k''}} \frac{\langle V_{\boldsymbol{kk'}} V_{\boldsymbol{k'k''}} V_{\boldsymbol{k''k}}\rangle_{dis}}{\varepsilon_k - \varepsilon_{k''} - i\eta} + c.c.\right)\delta(\varepsilon_k - \varepsilon_{k'}) \,. \tag{2.54}$$

$W^{(3)}_{\boldsymbol{kk'}}$ itself can be written as a sum of a symmetric term $W^{(3s)}$ and an asymmetric term $W^{(3a)}$. Then, $W^{(3)}_{\boldsymbol{kk'}} = W^{(3a)}_{\boldsymbol{kk'}} + W^{(3s)}_{\boldsymbol{kk'}}$, where $W^{(3s/a)}_{\boldsymbol{kk'}} = \dfrac{W^{(3)}_{\boldsymbol{kk'}} \pm W^{(3)}_{\boldsymbol{k'k}}}{2}$. Since the symmetric part of $W^{(3)}_{\boldsymbol{kk'}}$

$$W^{(3s)}_{\boldsymbol{kk'}} = \frac{4\pi}{\hbar} P\left(\sum_{\boldsymbol{k''}} \frac{Re[\langle V_{\boldsymbol{kk'}} V_{\boldsymbol{k'k''}} V_{\boldsymbol{k''k}}\rangle_{dis}]}{\varepsilon_k - \varepsilon_{k''}}\right), \tag{2.55}$$

just renormalizes $W^{(2)}_{\boldsymbol{kk'}}$, it does not introduce a new physical contribution to the scattering and is further not considered. Note, P in the above equation refers to the *principal value*. The remaining asymmetric term $W^{(3a)}_{\boldsymbol{kk'}}$ can be expressed as

$$W^{(3a)}_{\boldsymbol{kk'}} = \frac{-(2\pi)^2}{\hbar}\delta(\varepsilon_k - \varepsilon'_k) \times \sum_{\boldsymbol{k''}} Im\langle(V_{\boldsymbol{kk'}} V_{\boldsymbol{k'k''}} V_{\boldsymbol{k''k}})\rangle_{dis}\delta(\varepsilon_k - \varepsilon_{k''}) \,. \tag{2.56}$$

This contribution scales with the impurity concentration (for a so-called non-Gaussian disorder model [18]) as $(V_{\boldsymbol{kk'}} V_{\boldsymbol{k'k''}} V_{\boldsymbol{k''k}})_{dis} \sim n_{im}$. Consequently we can expect that the transverse conductivity associated to this term will be inversely proportional to n_{im} [2]. Therefore, this contribution to the conductivity of the system dominates in very dilute systems.

Two different scattering processes contribute to the fourth order expression for the scattering rate. A fourth order scattering process can occur at a single defect, but also two second order scattering processes can occur at two different defects. As the sequence of scatterings that lead to these two

second order pair scattering events is arbitrary, this process leads to three contributions in the expression for $W^{(4)}_{\boldsymbol{k}\boldsymbol{k}'}$ [14]

$$\begin{aligned} W^{(4)}_{kk'} = &\sum_{\boldsymbol{k}''}\sum_{\boldsymbol{k}'''}\left[\frac{\langle V_{\boldsymbol{k}'''\boldsymbol{k}}V_{\boldsymbol{k}\boldsymbol{k}''}\rangle_{dis}}{\varepsilon_k-\varepsilon_{k''}+i\eta}\frac{\langle V_{\boldsymbol{k}''\boldsymbol{k}'}V_{\boldsymbol{k}'\boldsymbol{k}'''}\rangle_{dis}}{\varepsilon_k-\varepsilon_{k'''}-i\eta}\right]\times\ \delta(\varepsilon_k-\varepsilon_{k'}) \\ &+\sum_{\boldsymbol{k}''}\sum_{\boldsymbol{k}'''}\left[\frac{\langle V_{\boldsymbol{k}''\boldsymbol{k}}V_{\boldsymbol{k}\boldsymbol{k}'}\rangle_{dis}}{\varepsilon_k-\varepsilon_{k'''}-i\eta}\frac{\langle V_{\boldsymbol{k}'\boldsymbol{k}'''}V_{\boldsymbol{k}'''\boldsymbol{k}''}\rangle_{dis}}{\varepsilon_k-\varepsilon_{k''}-i\eta}+c.c\right]\times\ \delta(\varepsilon_k-\varepsilon_{k'}) \\ &+\sum_{\boldsymbol{k}''}\sum_{\boldsymbol{k}'''}\left[\frac{\langle V_{\boldsymbol{k}\boldsymbol{k}'}V_{\boldsymbol{k}'\boldsymbol{k}'''}\rangle_{dis}}{\varepsilon_k-\varepsilon_{k'''}-i\eta}\frac{\langle V_{\boldsymbol{k}'''\boldsymbol{k}''}V_{\boldsymbol{k}''\boldsymbol{k}}\rangle_{dis}}{\varepsilon_k-\varepsilon_{k''}-i\eta}+c.c\right]\times\ \delta(\varepsilon_k-\varepsilon_{k'}). \end{aligned} \tag{2.57}$$

The factors like $\langle V_{\boldsymbol{k}'''_l}V_{\boldsymbol{k}\boldsymbol{k}''}\rangle_{dis}$ are all proportional to n_{im}, and therefore these contributions to $W^{(4)}_{\boldsymbol{k}\boldsymbol{k}'}$ are proportional to n^2_{im}. The fourth order contribution due to a scattering event at a single impurity contains factors like $\langle V_{\boldsymbol{k}\boldsymbol{k}''}V_{\boldsymbol{k}''\boldsymbol{k}'''}V_{\boldsymbol{k}''\boldsymbol{k}'}V_{\boldsymbol{k}'\boldsymbol{k}}\rangle_{dis}$ which are proportional to n_{im}. This non-Gaussian correlation yields a term in the transition rate which is physically similar to $W^{(3a)}_{\boldsymbol{k}\boldsymbol{k}'}$ (with respect to the concentration of impurities) but much smaller. Therefore we only consider the contribution of the two second order pair scattering events in $W^{(4)}_{\boldsymbol{k}\boldsymbol{k}'}$. The term $W^{(4)}_{\boldsymbol{k}\boldsymbol{k}'}$ expressed above is responsible for producing the second contribution of the skew scattering in the anomalous Hall conductivity, in the non-crossing approximation, similar to the results presented in the appendix of Ref. [14]. This second contribution of the skew scattering is disorder-independent. In the weak disorder limit that we consider, the energy width of the Bloch state spectral peaks is smaller than the gap, allowing us to ignore direct interband scattering. Therefore we will only consider intraband transitions in calculating $W^{(2)}_{\boldsymbol{k}\boldsymbol{k}'}$ and $W^{(3)}_{\boldsymbol{k}\boldsymbol{k}'}$. We consider electron transport in electron doped systems, thus the Fermi level ε_F lies inside the conduction band. However, for $W^{(4)}_{\boldsymbol{k}\boldsymbol{k}'}$ we also incorporate the off-diagonal scattering matrix elements as they produce virtual transitions that mix states in the two bands in a way which is ultimately crucial [15].

2.6.4 The side jump contribution to the AHE

During a scattering event, not only the momentum of engaged particles but also the coordinate of particles vary. This effect was first realized by Berger [16]. When a wave packet scatters from an impurity with spin-orbit interaction, the scattered wave packet will experience a deflection in the

transverse direction, as shown in Fig. 2.2(c). This occurred deflection depends on the spin of the electrons. After averaging over many scatterings, such random deflections cancel each other, and only changes of the momentum is considered. Hence, usually, such a displacement during the scattering time is ignored in the transport calculation. However, when the Berry curvature is non-zero, this anomalous coordinate shift does not disappear. Note, the side jump and intrinsic contributions are distinguishable in systems with complex band structures [17], because they have different dependence on the system parameters. The anomalous deflection which electrons experience during scattering time $\delta \boldsymbol{r}_{\boldsymbol{k}\boldsymbol{k}'}$ is given by the following gauge invariant expression [18, 19]

$$\delta \mathbf{r}_{\mathbf{k}',\mathbf{k}} = \left\langle u_{\mathbf{k}'} \mid i\frac{\partial}{\partial \mathbf{k}'} u_{\mathbf{k}'} \right\rangle - \left\langle u_{\mathbf{k}} \mid i\frac{\partial}{\partial \mathbf{k}} u_{\mathbf{k}} \right\rangle - \hat{\mathbf{D}}_{\mathbf{k}',\mathbf{k}} Arg\left(V_{\mathbf{k}',\mathbf{k}}\right), \tag{2.58}$$

where $Arg(V_{\boldsymbol{k}\boldsymbol{k}'})$ is the argument of $V_{\boldsymbol{k}\boldsymbol{k}'}$ and

$$\hat{\mathbf{D}}_{\mathbf{k}',\mathbf{k}} = \frac{\partial}{\partial \mathbf{k}'} + \frac{\partial}{\partial \mathbf{k}}. \tag{2.59}$$

While the phase information of the scattering amplitude is absent in the first-order Born approximation, the third term on the right hand side of Eq. (2.58) is responsible for restoring this information to the dynamics of the charge carriers.

There are two distinct effects due to the anomalous coordinate shift. First one is an additional correction to the velocity of electrons, $\mathbf{v}_{\mathbf{k}}^{sj} = \sum_{\mathbf{k}'} W_{\mathbf{k}\mathbf{k}'} \delta \mathbf{r}_{\mathbf{k}\mathbf{k}'}$, and the second one is a change in the potential energy of the electrons if an external electric field exists,

$$\Delta U_{\mathbf{k}',\mathbf{k}} = e\mathbf{E} \cdot \delta \mathbf{r}_{\mathbf{k}',\mathbf{k}}. \tag{2.60}$$

2.7 The Boltzmann formalism for the AHE

This section will explain how the Boltzmann transport formalism can correctly incorporate the intrinsic and extrinsic effects in the AHE for a system with a single conduction band.

2.7.1 The velocity of electrons

To obtain the current density of the system $\mathbf{J} = \sum_k \mathbf{v}_k f_k$, we need to calculate the velocity $\mathbf{v}_k$ of the itinerant electrons and also their distribution function $f_{\mathbf{k}}$ in the presence of an external electric field and randomly placed dilute magnetic and non-magnetic impurities. The conventional semi-classical approach just studies electrons at scattering events and ignores the evolution of the wave packets during the scattering time interval where a side jump can occur. Furthermore, in a system with broken either time reversal or inversion symmetries, an additional term should be added to the velocity expression of electrons to incorporate properly the effect of the non-zero Berry-phase curvature in the electron dynamics. If we incorporate both extra effects, which are missing in the conventional semiclassical approach, the velocity can be written as

$$\mathbf{v}_{\mathbf{k}} = \frac{1}{\hbar}\nabla_{\mathbf{k}}\varepsilon_k - \dot{\mathbf{k}} \times (\nabla_k \times \mathbf{A}_{\mathbf{k}}) + \sum_{\mathbf{k}'} W_{\mathbf{k}\mathbf{k}'}\delta\mathbf{r}_{\mathbf{k}\mathbf{k}'}. \tag{2.61}$$

2.7.2 Distribution function

After obtaining all terms for the velocity expression of the electrons, the next step is to calculate the distribution function of the electrons. Therefore we write the electron distribution function as follows

$$f_k = f^0 + g_k^s + g_k^{a1} + g_k^{a2} + g_k^{ad} \ . \tag{2.62}$$

The largest deviation from the Fermi-Dirac distribution is given by g_k^s. It arises from the symmetric part of the scattering rate $W_{kk'}^{(2)}$ and also describes the longitudinal conductivity. g_k^{a1} is defined as the deviation due to the asymmetric part of the scattering rate $W_{kk'}^{(3a)}$, and g_k^{a2} due to $W_{kk'}^{(4)}$. Finally, g_k^{ad} is responsible for capturing the effect of the side jump. Substituting the transition rate $W_{kk'}$ expressed in Eq. (2.52) along with the above non-equilibrium distribution function into Eq. (2.29), we obtain the following self consistent

time-independent integral equations

$$-e\mathbf{E}\cdot\mathbf{v}_{\mathbf{k}}\left(-\frac{\partial f^0}{\partial\varepsilon_k}\right)=\sum_{k'}W^{(2)}_{kk'}\left(g^s_k-g^s_{k'}\right)\,, \tag{2.63}$$

$$\sum_{k'}W^{(3a)}_{kk'}\left(g^s_k-g^s_{k'}\right)+\sum_{k'}W_{kk'}\left(g^{a1}_k-g^{a1}_{k'}\right)=0\,, \tag{2.64}$$

$$-e\mathbf{E}\cdot\mathbf{v}^{sj}_{\mathbf{k}}\left(-\frac{\partial f^0}{\partial\varepsilon_k}\right)=\sum_{\mathbf{k}'}W_{\mathbf{k}\mathbf{k}'}\left(g^{ad}_{\mathbf{k}}-g^{ad}_{\mathbf{k}'}\right)\,, \tag{2.65}$$

$$\sum_{k'}W^{(4)}_{\mathbf{k}\mathbf{k}'}(g^s_{\mathbf{k}}-g^s_{\mathbf{k}'})+\sum_{\mathbf{k}'}W_{\mathbf{k}\mathbf{k}'}(g^{a2}_{\mathbf{k}}-g^{a2}_{\mathbf{k}'})=0. \tag{2.66}$$

In the presence of an external electric field $\mathbf{E}$, electrons acquire an extra potential energy $\Delta U_{\mathbf{k}\mathbf{k}'}=-e\mathbf{E}\cdot\delta\mathbf{r}_{kk'}$ during the side jump $\delta\mathbf{r}_{\mathbf{k}\mathbf{k}'}$. Since the energy of the electrons is conserved during elastic scattering, this change in potential energy during a side jump event should be compensated by a change in the kinetic energy of the electrons given by $\Delta\varepsilon_{kk'}=\varepsilon_{k'}-\varepsilon_k=e\mathbf{E}\cdot\delta\mathbf{r}_{\mathbf{k}\mathbf{k}'}$. Therefore, based on conservation of energy, one obtains $\sum_{\mathbf{k}'}W_{kk'}[(f^0(\varepsilon_k)-f^0(\varepsilon_{k'})]=-e\mathbf{E}\cdot\mathbf{v}^{sj}_{\mathbf{k}}\left(-\frac{\partial f^0}{\partial\varepsilon_k}\right)$, which reduces to Eq. (2.65) based on $\sum_{\mathbf{k}'}W_{\mathbf{k}\mathbf{k}'}[(f^0(\varepsilon_k)+g^{ad}_{\mathbf{k}})-(f^0(\varepsilon_{k'})+g^{ad}_{k'})]=0$. As $g^{a1}_{\mathbf{k}},g^{a2}_{\mathbf{k}}$ and $g^{ad}_{\mathbf{k}}$ are small compared to g^s_k, we approximate $W_{\mathbf{k}\mathbf{k}'}$ in Eqs. (2.64), (2.65) and (2.66) by $W^{(2)}_{\mathbf{k}\mathbf{k}'}$.

It is now interesting to deduce how each contribution to the distribution function scales with the impurity concentration. Since $w^{(2)}_{\mathbf{k}\mathbf{k}'}\sim n_{im}$, we find, based on equation Eq. (2.63), that $g^s_{\mathbf{k}}\sim n^{-1}_{im}$. Like $W^{(2)}_{\mathbf{k}\mathbf{k}'}$, $W^{(3a)}_{\mathbf{k}\mathbf{k}'}\sim n_{im}$, therefore referring to Eq. (2.64) shows that $g^{a1}_{\mathbf{k}}\sim n^{-1}_{im}$. As it is clear that $\mathbf{v}^{sj}_{\mathbf{k}}\sim W^{(2)}_{\mathbf{k}\mathbf{k}'}\sim n_{im}$, then based on Eq. (2.65) one can conclude that $g^{ad}_{\mathbf{k}}\sim n^0_{im}$. Finally, let us consider g^{a2}_k. Since $w^{(4)}_{ll'}\sim n^2_{im}$ and $g^s_l\sim n^{-1}_{im}$ we come to the conclusion that $g^{a2}_l\sim n^0_{im}$.

2.7.3 Current density

The next step is to calculate the relevant terms in the current density. Using Eqs. (2.61) and (2.62), the charge current density is given by

$$\begin{aligned}\boldsymbol{J}&=-e\sum_l f_l v_l\\&\simeq\boldsymbol{J}^{an}+\boldsymbol{J}^{s}+\boldsymbol{J}^{ad}+\boldsymbol{J}^{sj}+\boldsymbol{J}^{sk1}+\boldsymbol{J}^{sk2}\,,\end{aligned} \tag{2.67}$$

where $\boldsymbol{J}^{an} = -e\sum_l f^0(\varepsilon_l)v_l^{an}$ is the anomalous current density, $\boldsymbol{J}^s = -e\sum_l g_l^s v_{0l}$ is the regular contribution to the charge current, arising from impurity scattering events within the first-order Born approximation, $\boldsymbol{J}^{ad} = -e\sum_l g_l^{ad} v_{0l}$ and $\boldsymbol{J}^{sj} = -e\sum_l g_l^s v_l^{sj}$ are consequences of the side jump effect on the distribution function and the electron velocity, respectively. $\boldsymbol{J}^{sk1} = -e\sum_l g_l^{a1} v_{0l}$ and $\boldsymbol{J}^{sk2} = -e\sum_l g_l^{a2} v_{0l}$ result from skew scattering. In the second line of Eq. (2.67), among the 15 terms we just consider 6 terms non-negligible. It is obvious that $\sum_l f_l^0(v_{0l} + v_l^{sj}) = 0$ for the equilibrium distribution function. In addition, we have ignored the small contributions $\sum_l(g_l^{a1} + g_2^{a2} + g_l^{ad})v_l^{sj}$. Moreover, as v_{an} is already linear in the electric field, the non-linear contributions to the current $\sum_l(g_l^s + g_l^{a1} + g_l^{a2} + g_l^{ad})v_l^{an}$ are also omitted.

In order to solve the integral equations (2.63), (2.64), (2.65) and (2.66), we rely on the generalized relaxation-time approach. In this approach, the different contributions to the non-equilibrium distribution function are written as

$$g_{\mathbf{k}}^p = eE\left[\lambda_{1\mathbf{k}}^p \cos\chi + \lambda_{2\mathbf{k}}^p \sin\chi\right]\frac{\partial f_0}{\partial \varepsilon_k}\,. \tag{2.68}$$

Here, p stands for s, $a1$, $a2$ and ad. χ is the angle of $\mathbf{E}$ with the $\hat{x}$-direction, $\lambda_{i\mathbf{k}}^p$ $(i = 1,2)$ are the generalized mean free paths of the charge carriers. In anisotropic systems, the size of the mean free paths of electrons depends on the relative direction of the drift velocity of the electrons respect to the external electric field. Hence, in order to capture this anisotropy, two different mean free paths are introduced in the proposal for the electron distribution function, namely $\lambda_{1\mathbf{k}}^p$ and $\lambda_{2\mathbf{k}}^p$. $\lambda_{1\mathbf{k}}^p$ corresponds to those electrons that move parallel to the external electric field and $\lambda_{2\mathbf{k}}^p$ for those electrons that move perpendicular to the external electric field. Then, since in isotropic systems, electrons feel the same scattering potential in every direction, the form of this proposal for the distribution function of the electrons reduces to the well-known relaxation time formalism in isotropic systems.

Considering now an electric field in the $\hat{x}$ or $\hat{y}$ direction $E = E\hat{x}_i$ $(\hat{x}_1 = \hat{x}, \hat{x}_2 = \hat{y})$ and substituting g_l^p from Eq. (2.68) into Eqs. (2.63), (2.64), (2.65) and (2.66), we arrive at

$$\mathbf{v}_{\mathbf{k}} \cdot \hat{x}_i = \sum_{\mathbf{k}'} W_{\mathbf{k}\mathbf{k}'}^{(2)}\left[\lambda_{i\mathbf{k}}^s - \lambda_{i\mathbf{k}'}^s\right], \tag{2.69}$$

$$\mathbf{v}_{\mathbf{k}}^{sj} \cdot \hat{x}_i = \sum_{\mathbf{k}'} W_{\mathbf{k}\mathbf{k}'}^{(2)} \left[\lambda_{i\mathbf{k}}^{ad} - \lambda_{i\mathbf{k}'}^{ad} \right] , \tag{2.70}$$

$$\sum_{\mathbf{k}'} W_{\mathbf{k}\mathbf{k}'}^{(2)} \left[\lambda_{i\mathbf{k}}^{a1} - \lambda_{i\mathbf{k}'}^{a} \right] + \sum_{\mathbf{k}'} W_{\mathbf{k}\mathbf{k}'}^{(3a)} \left[\lambda_{i\mathbf{k}}^{s} - \lambda_{i\mathbf{k}'}^{s} \right] = 0, \tag{2.71}$$

$$\sum_{\mathbf{k}'} W_{\mathbf{k}\mathbf{k}'}^{(4)} \left[\lambda_{i\mathbf{l}}^{s} - \lambda_{i\mathbf{k}'}^{s} \right] + \sum_{\mathbf{k}'} W_{\mathbf{k}\mathbf{k}'}^{(2)} \left[\lambda_{i\mathbf{k}}^{a2} - \lambda_{i\mathbf{k}'}^{a2} \right] = 0. \tag{2.72}$$

To solve the above equations, all mean free paths λ_{ik}^{p} are expanded in Fourier series. Finally we obtain the Fourier coefficients and consequently the corrections to the distribution function of electrons caused by each of the involved mechanism in the AHE.

BIBLIOGRAPHY

[1] G. D. Mahan, Condensed Matter in a Nutshell, Princeton University Press 2011.

[2] W. Kohn and J. M. Luttinger, Phys. Rev. **108**, 590 (1957).

[3] R. Karplus and J. M. Luttinger, Phys. Rev. **95**, 1154 (1954).

[4] J. Schliemann, D. Loss, Phys. Rev. B **68**, 165311 (2003).

[5] K. Výborný et al., Phys. Rev. B **79**, 045427 (2009).

[6] E. H. Hall, Am. J. Math. **2**, 287 (1879).

[7] E. H. Hall, Philos. Mag. **12**, 157 (1881).

[8] R. Karplus and J. M. Luttinger, Phys. Rev. **95**, 1154 (1954).

[9] M. V. Berry, Proc. R. Soc. 392, 45 (1984).

[10] M. C. Chang and Q. Niu, Phys. Rev. B **53**, 7010 (1996).

[11] G. Sundaram and Q. Niu, Phys. Rev. B **59**, 14915 (1999).

[12] J. Smit, Physica **21**, 877 (1955).

[13] J. Smit, Physica **24**, 39 (1958).

[14] C. Xiao et al., Phys. Rev. B **95**, 035426 (2017).

[15] N. A. Sinitsyn et al., Phys. Rev. B **75**, 045315 (2007).

[16] L. Berger, Phys. Rev. B **2**, 4559 (1970).

[17] N. A. Sinitsyn, J. Phys.: Condens. Matter **20**, 023201 (2008).

[18] N. A. Sinitsyn *et al.*, Phys. Rev. B **73**, 075318 (2006).

[19] N. A. Sinitsyn et al., Phys. Rev. B **72**, 045346 (2005).

CHAPTER 3

CHARGE TRANSPORT IN A FREE STANDING MAGNETIC TOPOLOGICAL ULTRA THIN FILM

In a 3D topological insulator (3DTI), the conducting electrons on the surface interact with the impurities present in the surface and bulk. A possible way to decrease the bulk's effect on the surface transport is increasing the surface-to-volume ratio, making the 3DTI thinner. Interestingly, when the thickness of a topological ultra-thin film (TTF) is comparable with the decay length of the surface states into the bulk, the wave functions of the top and bottom surface states overlap, which leads to opening a gap in the surface band structure [1–4]. For example, this regime is realized in a thin film of Bi_2Se_3 when its thickness is less than six quintuple layers (QLs) [6].

In this chapter, we investigate the charge transport of massive Dirac fermions in a magnetic topological ultra-thin film (MTF) in the presence of short-range and randomly placed dilute magnetic impurities. The magnetic impurities are localized scattering centres that force massive Dirac fermions to change their host state. When the magnetic impurities are not aligned fully perpendicular to the MTF, the short-range interaction between them and the conducting electrons is anisotropic due to the spin-momentum locking of electrons. By applying the semi-classical Boltzmann formalism, [24–26], and using a modified relaxation time scheme [27], to truly capture the effect of the present anisotropic interactions, the charge transport of a MTF is

investigated.

Note, even though the emergence of the finite size effect gap in a MTF reduces the system's conductivity, we show that a MTF can provide us with a system in which the massive Dirac fermions generate a dissipation-less charge current in the presence of magnetic impurities.

Interestingly, we found that the charge current of a MTF is always dissipative when both non-degenerate massive Dirac cones in a MTF are filled with electrons. Nevertheless, all the possible electronic transitions are forbidden by the chirality selection rule when only a single band is filled, and the magnetic impurities are aligned in-plane. Remarkably, in consequence, the charge transport along a MTF will be dissipation-less. Finally, let us emphasize that the observed fully suppression of the resistivity is a consequence of the hybridization induced gap and hence is not achievable in a 3DTI.

To explain our findings, we address a chirality selection rule induced by magnetic impurities. This chirality selection rule governs electrons' inter-subband and intra-subband transitions. The chirality selection rule is strongly dependent on the spatial orientation of the magnetic impurities. Then, by changing the magnetic impurities' tilt angle, the chirality selection rule changes, and consequently, the intra-subband and inter-subband transitions of conducting electrons will be influenced.

In this chapter, Sec. 3.1, presents the effective Hamiltonian for a MTF and the applied formalism. In Sec. 3.2.1, we investigate the charge transport of a MTF in the two-band regime. The charge transport and the resistivity of a MTF in the single-band regime is studied in Sec. 3.2.2. In Sec. 3.3, we summarize our findings and conclude with our main results.

3.1 Hamiltonian and formalism

A thick topological film has two surfaces, in which each surface hosts helical gapless states with a specific spin texture (see panel *a* in Fig. 3.1). As the thick film becomes thinner, the gapless helical states on the opposite surfaces start to hybridize. As panel *b* of Fig. 3.1 shows, this hybridization opens a gap of 2Δ in the energy spectrum of the thin film. The size of the hybridization induced

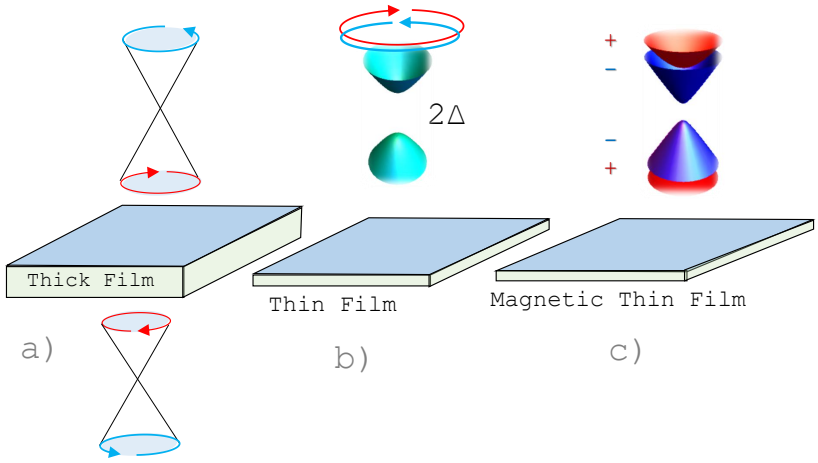

Figure 3.1: (Color online) (a) Schematic view of a topological thick film with different spin texture for electrons in the upper and lower surface. (b) A topological thin film with an energy gap of 2Δ opened by hybridization between two opposite surfaces. (c) Illustration of how magnetization M further changes the electronic spectrum of a thin film.

gap decays exponentially with the thickness of the system[5]. For example, it has been experimentally demonstrated that increasing the thickness of a Bi_2Se_3 thin film reduces the energy gap and when the thickness reaches $6nm$ the gap disappears [6, 7]. However, in this chapter, the size of the hybridization induced gap is fixed, and the thickness dependency of this gap is not considered in our calculations.

A gap in the surface states of a 3DTI opens if time-reversal symmetry (TRS) is broken [8, 9]. The TRS can be broken in a 3DTI by exerting an external magnetic field on the system [10–13], by doping the system with magnetic impurities[14–17], and by the magnetic proximity effect when a topological insulator is brought in contact with a ferromagnet [18–23]. Breaking the TRS in a 3DTI destroys the chiral surface states, though it cannot remove the surface states' degeneracy. In contrast to this system, in a MTF, TRS breaking converts two degenerate massive Dirac cones to two non-degenerate massive Dirac cones, as shown in panel c of Fig. 3.1.

The Hamiltonian describing low energy electrons in a MTF is given by [4, 28]

$$\mathscr{H}_0 = \hbar v_F(k_y\sigma_1 - k_x\sigma_2)\otimes\tau_3 + \Delta_m\sigma_3\otimes 1 + \Delta\otimes\tau_2, \tag{3.1}$$

on the bases of $|t\uparrow\rangle$, $|t\downarrow\rangle$, $|b\uparrow\rangle$, and $|b\downarrow\rangle$, where t and b denote the top and bottom surface states and $\uparrow$, $\downarrow$ represent the spin-up and spin-down states,

respectively. σ_i and τ_i (i = 1, 2, 3) are Pauli matrices in the spin and surface space, respectively.

Δ_m can originate from the magnetic proximity effect. For example, it has been shown that this magnetic proximity effect occurs when EuS, a ferromagnetic insulator with a band gap of 1.6 eV, and a T_C (Curie temperature) of 16 K is grown on a 20 quintuple-layer (QL) thick Bi_2Se_3 [29]. Also, this effect is observed when a 15-nm-thick $Bi_{0.5}Sb_{1.5}Te_3$ thin film is in contact with a 15- or 40-nm-thick $SrRuO_3$ [30]. In another experimental work, a $(Bi_xSb_{1-x})_2Te$ thin film becomes ferromagnetic by proximity coupling in a heterostructure with yttrium iron garnet (YIG), a magnetic insulator, as evidenced by the measured anomalous Hall effect (AHE) [31].

In this work, we restrict ourselves to the low energy regime and keep terms up to linear order in momentum k. In the presence of the inversion symmetry, we assume that v_F is the same for both surface states. Switching to new bases $|\pm\uparrow\rangle$, $|\pm\downarrow\rangle$, with $|\pm\uparrow\rangle = (|t\uparrow\rangle \pm |b\uparrow\rangle)/\sqrt{2}$ and $|\pm\downarrow\rangle = (|t\downarrow\rangle \pm |b\downarrow\rangle)/\sqrt{2}$, H_0 reduces to the two decoupled block-diagonal matrix

$$H_0 = \begin{pmatrix} h_+ & 0 \\ 0 & h_- \end{pmatrix}, \tag{3.2}$$

where $h_\nu = \hbar v_F(k_y\sigma_x - \nu k_x\sigma_y) + (\Delta + \nu\Delta_m)\sigma_z$. The energy dispersion of this Hamiltonian is given by

$$\varepsilon_\nu^s = s\sqrt{(\hbar v_f k)^2 + (\Delta + \nu\Delta_m)^2}, \tag{3.3}$$

where $s = +/-1$ denotes the conduction/valence band. The chiral index ν distinguishes the outer subbands ($\nu = +$) from the inner subbands ($\nu = -$). The chiral index of the inner subbands is of the opposite sign to the sign of $\Delta \cdot \Delta_m$, while the chiral index of the outer subbands is the sign of $\Delta \cdot \Delta_m$. The last term in H_ν, $(\Delta + \nu\Delta_m)$, is the mass term. The value of the energy gap for the outer subbands is $2|\Delta + \Delta_m|$ and $2|\Delta - \Delta_m|$ for the inner subbands, (see Fig. 3.2).

The chiral basis states that diagonalize the Hamiltonian H_0 in Eq. (3.2), are $\psi_\nu^s = u_\nu^s e^{i\boldsymbol{k}\cdot\boldsymbol{r}}$, where

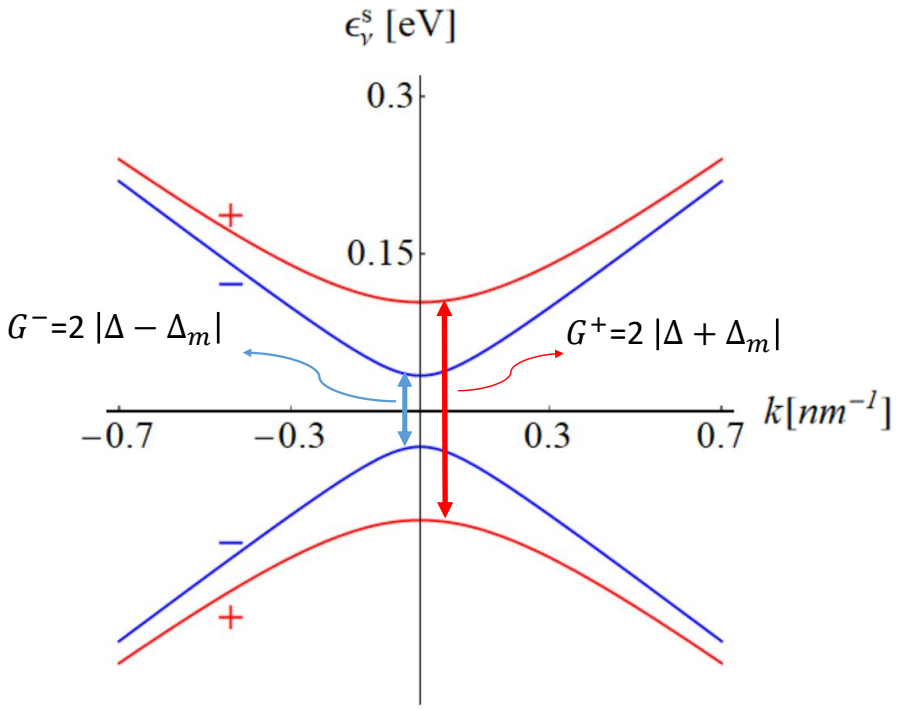

Figure 3.2: Band structure of a Bi_2Se_3 MTF, for v_F=4.8 (10^5 m s^{-1}), Δ=69 meV, and Δ_m=35 meV [6].

$$|u_\nu^s\rangle = \frac{1}{\sqrt{2}} \begin{pmatrix} \frac{1+\gamma_+^s}{\sqrt{1+\gamma_+^s}} i e^{-i\phi_{\boldsymbol{k}}}\ \delta_{\nu,+1} \\ \frac{1-\gamma_+^s}{\sqrt{1-\gamma_+^s}}\ \delta_{\nu,+1} \\ -i\frac{1+\gamma_-^s}{\sqrt{1+\gamma_-^s}} e^{i\phi_{\boldsymbol{k}}}\ \delta_{\nu,-1} \\ -\frac{1-\gamma_-^s}{\sqrt{1-\gamma_-^s}}\ \delta_{\nu,-1} \end{pmatrix}, \tag{3.4}$$

$\gamma_\nu^s(k) = \dfrac{\Delta + \nu\Delta_m}{\varepsilon_\nu^s}$, $\langle u_\nu^s | | u_{\nu'}^{s'} \rangle = \delta_{s,s'}\delta_{\nu,\nu'}$ and the $\delta_{\nu,\nu'}$ is the Kronecker delta. For a MTF, these so-called *surface states* emerge in the entire film. Nevertheless, they always lie in the bulk energy gap and therefore can be distinguished from the bulk states.

In order to find the charge current of massive Dirac fermions in a MTF, the non-equilibrium distribution function of the massive Dirac fermions $f_{\boldsymbol{k}}$ should be obtained. We assume that the electric field is weak, hence we consider $f_{\boldsymbol{k}}^\nu = f_k^0 + \delta f_{\boldsymbol{k}}^\nu$, where $f_{\boldsymbol{k}}^\nu$ denotes the non-equilibrium distribution function of electrons residing in band ν and state $\boldsymbol{k}$ and f_k^0 is the equilibrium Fermi-Dirac

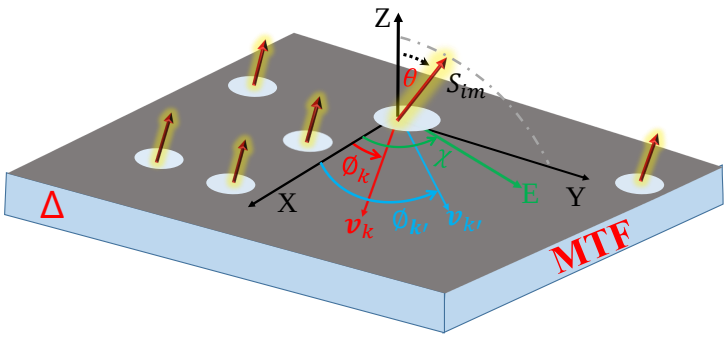

Figure 3.3: An electron under the presence of an electric field $\boldsymbol{E} = E(\cos\chi, \sin\chi, 0)$ scatters off a particular point like magnetic impurity $\boldsymbol{S}_{im} = S_{im}(0, \sin\theta, \cos\theta)$, with initial velocity $\mathbf{v}_k = \mathrm{v}_k(\cos\phi_{\boldsymbol{k}}, \sin\phi_{\boldsymbol{k}}, 0)$ and final velocity $\mathbf{v}_{k'} = \mathrm{v}_{k'}(\cos\phi_{\boldsymbol{k}'}, \sin\phi_{\boldsymbol{k}'}, 0)$.

distribution function. Note, f^0_k does not contribute to the current and $\delta f^\nu_{\boldsymbol{k}}$ is linear in the applied electric field $\boldsymbol{E}$. Since only the Fermi electrons contribute to the charge transport, $s = +1$, we drop the index s in what follows. We apply the semi-classical Boltzmann equation (BE)

$$\frac{\partial f^\nu_{\boldsymbol{k}}}{\partial t} - e(-\frac{\partial f^0}{\partial \varepsilon^\nu_{\boldsymbol{k}}})\boldsymbol{E}.\mathbf{v}^\nu_{\boldsymbol{k}} = \sum_{\nu',\boldsymbol{k}'} W^{\nu\nu'}(\boldsymbol{k},\boldsymbol{k}')\left(f^{\nu'}_{\boldsymbol{k}} - f^\nu_{\boldsymbol{k}'}\right), \tag{3.5}$$

to find the distribution function of charge carriers in the presence of the external electric field $\boldsymbol{E} = E(\cos\chi, \sin\chi, 0)$ (see Fig. 3.3) and the dilute and randomly placed magnetic impurities. During the scattering time, the itinerant electrons with velocity $\mathbf{v}^\nu_{\boldsymbol{k}} = \nabla_{\boldsymbol{k}}\varepsilon^\nu_{\boldsymbol{k}} = \mathrm{v}^\nu_k(\cos\phi_{\boldsymbol{k}}, \sin\phi_{\boldsymbol{k}}, 0)$, scatter from band ν and state $\boldsymbol{k}$ to band ν' and state $\boldsymbol{k}'$, with transition rate $W^{\nu\nu'}(\boldsymbol{k},\boldsymbol{k}')$.

We model the interaction between an arbitrary electron located at $\boldsymbol{r}$ and a single magnetic impurity at $\boldsymbol{R}_{im}$ as $V_{sc}(\boldsymbol{r} - \boldsymbol{R}_{im}) = J\delta(\boldsymbol{r} - \boldsymbol{R}_{im})\boldsymbol{S}_{im} \cdot \boldsymbol{S}_e$, where $\boldsymbol{S}_e = h\sigma/2$ stands for the spin of the electron, J is the exchange coupling, and $\boldsymbol{S}_{im} = S_{im}(0, \sin\theta, \cos\theta)$ is the spin of the magnetic impurity, (see Fig. 3.3). The delta function refers to the short-range nature of the electron-impurity interaction. We can treat the spin of magnetic impurities classically in the regime of large magnetic spin $|S_{im}|$, weak interaction J, and $J|S|$=constant. Without loss of generality, we assume that the mean magnetic moment of the impurities is in the yz plane, as shown in Fig. 3.3. Because the direction of the electric field can be adjusted, this assumption has no physical consequence. We suppose that the fluctuations around the average magnetic moment are negligible, thus all magnetic impurities are parallel. This alignment can be validated experimentally by applying an external magnetic field for a short

period and then switching it off [65]. Depending on how electrons interact with random and point-like impurities, the BE is solved differently. If the scattering potential V_{sc} scatters electrons isotropically, the relaxation time scheme suggests the following form for the non-equilibrium distribution function at zero temperature [33],

$$\delta f^{\nu}_{is}(\boldsymbol{k}) = e\frac{\partial f^0}{\partial \varepsilon^{\nu}_k}\mathrm{v}^{\nu}_k \, E \, \tau^{\nu}_{is}(\cos\phi_{\boldsymbol{k}}\cos\chi + \sin\phi_{\boldsymbol{k}}\sin\chi), \tag{3.6}$$

where

$$\frac{1}{\tau^{\nu}_{is}(\boldsymbol{k})} = \sum_{\boldsymbol{k}',\nu'} W^{\nu\nu'}(1 - \frac{\mathrm{v}^{\nu'}_{k'}}{\mathrm{v}^{\nu}_k}\cos[\phi_{\boldsymbol{k}'} - \phi_{\boldsymbol{k}}]). \tag{3.7}$$

and $\tau^{\nu}_{is,1} = \tau^{\nu}_{is}\cos\phi_{\boldsymbol{k}}$ and $\tau^{\nu}_{is,2} = \tau^{\nu}_{is}\sin\phi_{\boldsymbol{k}}$.

However, this method does not apply to our work because, even though the low energy dispersion of a MTF is isotropic, due to the in-plane component of the magnetic impurities, the scattering potential is not isotropic. To capture this anisotropy, Eq. (3.6) should be modified as follows [27]

$$\delta f^{\nu}_{\boldsymbol{k}} = e\frac{\partial f^0}{\partial \varepsilon^{\nu}_k}\mathrm{v}^{\nu}_k \, E \, (\tau^{\nu}_1(\boldsymbol{k})\cos\chi + \tau^{\nu}_2(\boldsymbol{k})\sin\chi), \tag{3.8}$$

where $\tau^{\nu}_i(\boldsymbol{k})$ are the modified relaxation time.

By applying Eq. (3.5) for both bands simultaneously, and substituting Eq. (3.8) for $f^{\nu}_{\boldsymbol{k}}$, one arrives at the following set of equations,

$$\begin{aligned}
&\cos(\phi_{\boldsymbol{k}} - \chi) - \sum_{\boldsymbol{k}',\nu'} W^{+\nu'}\big[\tau^{+}_1(\boldsymbol{k}) - \tau^{\nu'}_1(\boldsymbol{k}')\frac{\mathrm{v}^{\nu'}_{k'}}{\mathrm{v}^{+}_k}\big]\cos\chi - \sum_{\boldsymbol{k}',\nu'} W^{+\nu'}\big[\tau^{+}_2(\boldsymbol{k}) - \tau^{\nu'}_2(\boldsymbol{k}')\frac{\mathrm{v}^{\nu'}_{k'}}{\mathrm{v}^{+}_k}\big]\sin\chi = 0 \\
&\cos(\phi_{\boldsymbol{k}} - \chi) - \sum_{\boldsymbol{k}',\nu'} W^{-\nu'}\big[\tau^{-}_1(\boldsymbol{k}) - \tau^{\nu'}_1(\boldsymbol{k}')\frac{\mathrm{v}^{\nu'}_{k'}}{\mathrm{v}^{-}_k}\big]\cos\chi - \sum_{\boldsymbol{k}',\nu'} W^{-\nu'}\big[\tau^{-}_2(\boldsymbol{k}) - \tau^{\nu'}_2(\boldsymbol{k}')\frac{\mathrm{v}^{\nu'}_{k'}}{\mathrm{v}^{-}_k}\big]\sin\chi = 0.
\end{aligned} \tag{3.9}$$

By following the method described in Sec. 2.5.2, the Eqs. (3.9) can be solved. The result gives us the Fourier coefficients $\tau^{\nu c}_{1n}$, $\tau^{\nu s}_{1n}$, $\tau^{\nu c}_{2n}$, $\tau^{\nu s}_{2n}$. Accordingly, by obtaining these coefficients, one can straightforwardly find the corresponding relaxation times $\tau^{\nu}_i(\boldsymbol{k}) = \sum_n(\tau^{\nu c}_{in}\cos n\phi_{\boldsymbol{k}} + \tau^{\nu s}_{in}\sin n\phi_{\boldsymbol{k}})$. Finally, replacing functions $\tau^{\nu}_1(\boldsymbol{k})$ and $\tau^{\nu}_2(\boldsymbol{k})$ in Eq. (3.8) with the found relaxation times yields the distribution function of the electrons with a particular chirality.

Next, the contribution of each band to the conductivity of the MTF can be obtained by

$$\begin{aligned}\sigma^{\nu}_{\alpha\beta} =& \frac{e^2}{AE_\beta}\sum_{\boldsymbol{k}} \mathbf{v}^{\nu}_{\alpha}(k)\mathrm{v}^{\nu}_{k}\, E\, \tau^{\nu}_{1}(\boldsymbol{k})\delta(\varepsilon^{\nu}_{k}-\varepsilon_F)\cos\chi \\ &+ \frac{e^2}{AE_\beta}\sum_{\boldsymbol{k}} \mathbf{v}^{\nu}_{\alpha}(k)\mathrm{v}^{\nu}_{k}\, E\, \tau^{\nu}_{2}(\boldsymbol{k})\delta(\varepsilon^{\nu}_{k}-\varepsilon_F)\sin\chi,\end{aligned} \tag{3.10}$$

where α and β denote x and y directions. Finally, finding the contribution of all electrons from these two bands yields the total conductivity $\sigma_{\alpha\beta} = \sum_{\nu}\sigma^{\nu}_{\alpha\beta}$.

3.2 Results

We divide our discussion into two parts. In the first part, Sec. 3.2.1, we assume that both bands are filled with electrons, and both are involved in the charge transport. In this regime the Fermi energy is thus arranged to be above the bottom of the subband with plus chirality. In the second part, Sec. 3.2.2, only the subband with minus chirality is filled and contributes to the conductivity. Since our results show completely distinctive features in these two regimes, we present them separately.

3.2.1 Two-band regime

Being in the two-band regime requires $\Delta + \Delta_m \leqslant \varepsilon_F$, where $\Delta + \Delta_m$ is the energy of electrons with plus chirality at the Γ point ($\boldsymbol{k} = 0$). Defining $\tilde{\varepsilon}_F = \frac{\varepsilon_F}{\Delta}$ and $\tilde{\Delta}_m = \frac{\Delta_m}{\Delta}$, the condition $1+\tilde{\Delta}_m \leqslant \tilde{\varepsilon}_F$ guarantees that the system is properly driven in the two-band regime.

3.2.1.1 Transition rate and lifetime of electrons

The transition rate $W^{\nu\nu'}(\boldsymbol{k},\boldsymbol{k}')$ for electrons determines how likely a scattering event is in which an electron from band ν and state $\boldsymbol{k}$ scatters off a magnetic impurity and ends up being in band ν' and state $\boldsymbol{k}'$, by respecting the conservation of energy. By using the Eq. (3.4), the scattering T-matrix

$$T^{\nu\nu'}(\boldsymbol{k},\boldsymbol{k}') = \begin{pmatrix} T^{++} & T^{+-} \\ T^{-+} & T^{--} \end{pmatrix}, \tag{3.11}$$

within the first Born approximation is given by

$$T = JS_{im}\begin{pmatrix} -\cos\theta\ (\mathscr{T}_1^{++} - \mathscr{T}_2^{++}\ e^{i(\phi_{\boldsymbol{k}'}-\phi_{\boldsymbol{k}})}) & -i\sin\theta\ (\mathscr{T}_1^{+-} - \mathscr{T}_2^{+-}\ e^{i(\phi_{\boldsymbol{k}'}+\phi_{\boldsymbol{k}})}) \\ i\sin\theta\ (\mathscr{T}_1^{-+} - \mathscr{T}_2^{-+}\ e^{-i(\phi_{\boldsymbol{k}'}+\phi_{\boldsymbol{k}})}) & \cos\theta\ (\mathscr{T}_1^{--} - \mathscr{T}_2^{--}\ e^{-i(\phi_{\boldsymbol{k}'}+\phi_{\boldsymbol{k}})}) \end{pmatrix}, \tag{3.12}$$

where $\mathscr{T}_1^{\nu\nu'} = \sqrt{(1-\gamma_\nu^+(k))(1-\gamma_{\nu'}^+(k'))}$, $\mathscr{T}_2^{\nu\nu'} = \sqrt{(1+\gamma_\nu^+(k))(1+\gamma_{\nu'}^+(k'))}$. According to the Eq. (2.16) transition rate $W^{\nu\nu'}(\boldsymbol{k},\boldsymbol{k}')$ of the electrons becomes

$$\begin{aligned}\bar{W}^{\nu\nu'}(\boldsymbol{k},\boldsymbol{k}') = \cos^2\theta[(1/2)[(\mathscr{T}_1^{\nu\nu'})^2 + (\mathscr{T}_2^{\nu\nu'})^2] - \mathscr{T}_1^{\nu\nu'}\mathscr{T}_2^{\nu\nu'}\cos(\phi_{\boldsymbol{k}'} - \phi_{\boldsymbol{k}})]\delta_{\nu\nu'}\delta(\varepsilon_k^\nu - \varepsilon_{k'}^{\nu'}) + \\ \sin^2\theta[(1/2)[(\mathscr{T}_1^{\nu\nu'})^2 + (\mathscr{T}_2^{\nu\nu'})^2] + \mathscr{T}_1^{\nu\nu'}\mathscr{T}_2^{\nu\nu'}\cos(\phi_{\boldsymbol{k}'} + \phi_{\boldsymbol{k}})](1-\delta_{\nu\nu'})\delta(\varepsilon_k^\nu - \varepsilon_{k'}^{\nu'}),\end{aligned} \tag{3.13}$$

where $\bar{W}^{\nu\nu'}(\boldsymbol{k},\boldsymbol{k}') = \frac{\hbar W^{\nu\nu'}(\boldsymbol{k},\boldsymbol{k}')}{\pi J^2 S_{im}^2 n_{im}}$. In Eq. (3.13), the first and second terms correspond to the intra-subband and inter-subband scatterings, respectively. Note that while intra-subband scatterings are isotropic, inter-subband scatterings are anisotropic. Therefore, depending on whether the chirality of electrons is preserved during the scatterings or not, the scattering event is isotropic or anisotropic.

As Fig. 3.4 shows the most and least probable intra-subband scatterings of Fermi electrons $\bar{W}_F^{++}(\phi_{\boldsymbol{k}},\phi_{\boldsymbol{k}'})$ are respectively backward, $\phi_{\boldsymbol{k}'} - \phi_{\boldsymbol{k}} = \pm\pi$, and forward scatterings, $\phi_{\boldsymbol{k}'} - \phi_{\boldsymbol{k}} = 2n\pi$, with $n = 0$, 1 or -1. However, the most and the least probable inter-subband scatterings occur when $\phi_{\boldsymbol{k}'} + \phi_{\boldsymbol{k}} = \pi$ or 3π, and $\phi_{\boldsymbol{k}'} + \phi_{\boldsymbol{k}} = 2n\pi$, respectively. Therefore, these two possible scatterings are very distinct. For example, there is always a huge chance for all electrons to be backscattered during an intra-subband transition, while a few electrons have this chance in an inter-subband scattering.

Apart from that, intra-subband and inter-subband scatterings can be clearly distinguished by their responses to the variation in the surface magnetisation direction. According to Fig. 3.4, changing the direction of the magnetic impurities, from zero to $\frac{\pi}{2}$, decreases the transition rate for all intra-subband scatterings by three orders of magnitude, while it enhances the transition rate for all inter-subband scatterings by two orders of magnitude. Besides, note that changing the orientation of the magnetic impurities weakens or strengthens different scattering events without changing the profile of the transition rate against $\phi_{\boldsymbol{k}}$ and $\phi_{\boldsymbol{k}'}$.

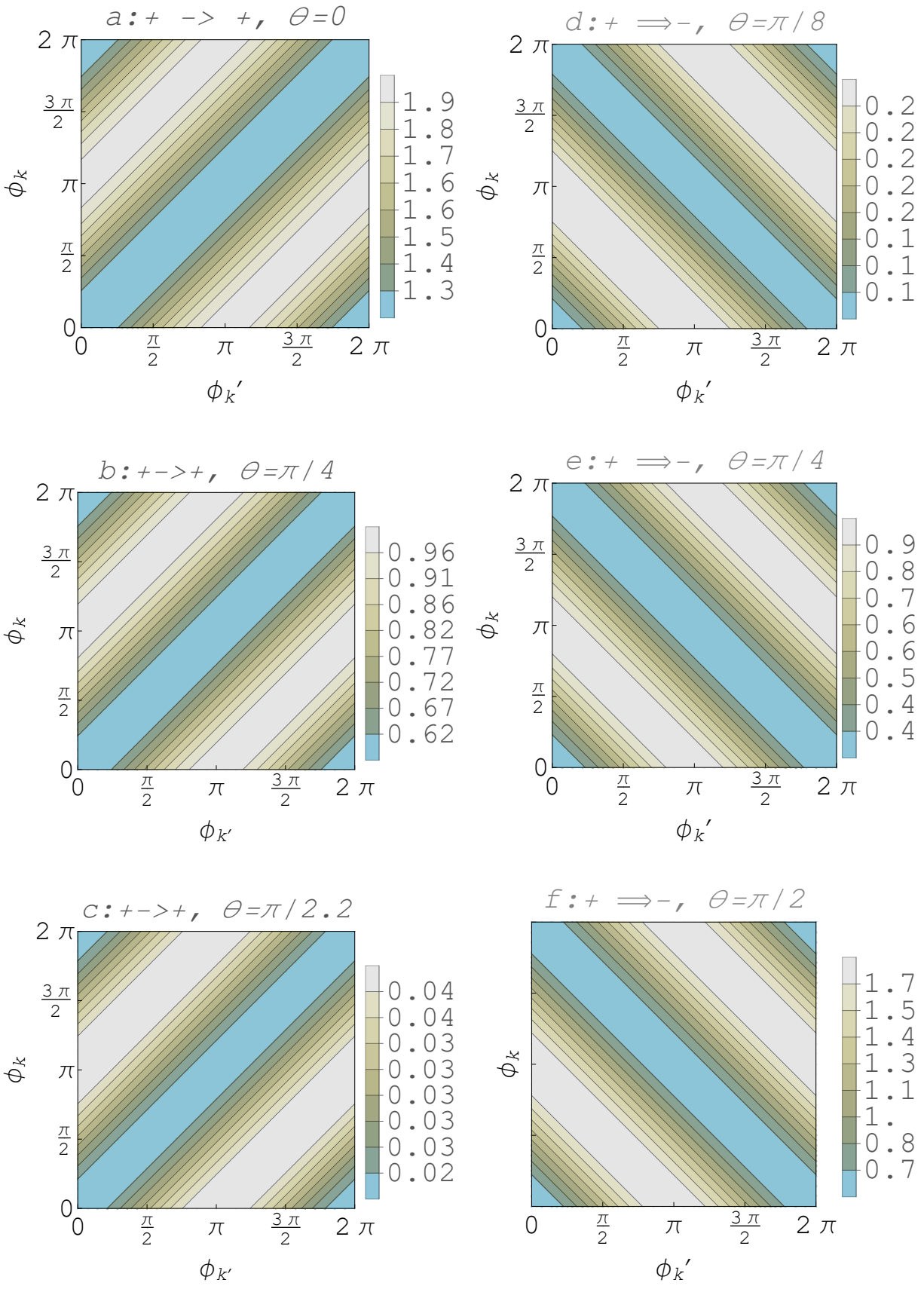

Figure 3.4: $\bar{W}^{\nu\nu'}(\boldsymbol{k},\boldsymbol{k}')$ for Fermi electrons in an intra-subband scattering $(+ \longmapsto +)$ and an inter-subband scattering $(+ \longmapsto -)$ versus direction of $\boldsymbol{k}$ and $\boldsymbol{k}'$, for different orientations of the magnetic impurities θ, and for $\tilde{\Delta}_m = 0.5$, $\tilde{\varepsilon}_F = 2$.

Even though there is no net charge current along the system in the absence of the external electric field, still the electrons travel between the allowed states. Having the transition rate of different scattering events let us calculate how long an electron remains in its host state that helps us to have a broader view of the dynamics of conducting electrons.

Using Eq. (3.13) the lifetime of an electron with chirality ν is given by

$$\tau_q^{\nu} = (\sum_{\boldsymbol{k}',\nu'} W^{\nu\nu}(\boldsymbol{k},\boldsymbol{k}'))^{-1} = \frac{t_0/2}{1+\gamma_{\nu}^2\cos^2\theta+\gamma_{\nu}\gamma_{\nu'}\sin^2\theta}, \tag{3.14}$$

where $t_0 = \frac{4\hbar^3 v_F^2}{\varepsilon_k^{\nu} J^2 S_{im}^2 n_{im}}$. Note that in the above expression if $\nu = +$ then $\nu' = -$, and vice versa. According to the above equation, while τ_q^- decreases by increasing θ, τ_q^+ increases. Therefore, in the absence of an electric field, by increasing θ from 0 to $\frac{\pi}{2}$, electrons travel from the subband with minus chirality to the other subband with plus chirality. Finally, all electrons end up having the same lifetime for $\theta = \frac{\pi}{2}$. We can conclude that by changing the orientation of the magnetic impurities, one can change the occupation number of electrons in each subband.

Considering that in the absence of an external electric field, there is no preferred scattering event, all transition rates can be weighted equally, as is done in the calculation of the lifetime. But, with the external electric field, the distribution of electrons in different states changes to make some of the possible scatterings more favorable for the charge transport, and suppresses other unfavorable transitions.

3.2.1.2 Conductivity

The BE takes into account both the effect of the electric field and the impurities in the system's charge transport. As Eq. (3.13) implies, charge conduction in a MTF consists of both isotropic and anisotropic transitions. Since these two types of events are correlated, their contributions to the total charge current cannot be separated. Hence, we employ the modified relaxation time scheme for all the possible scattering events in the MTF to obtain the conducting electrons' relaxation times. In what follows, we first compare the found modified relaxation times with the calculated standard relaxation times, to

prove the requirement of the modified relaxation time. By applying the Eqs. (3.13) and (3.7) the standard relaxation time of an electron in band ν and state $\mathbf{k}$ will be

$$\tau_{is}^{\nu}(\boldsymbol{k}) = \frac{t_0}{4 + (\gamma_{\nu}^2 - 1)(1 + 2\sin^2\theta\cos^2\phi_{\boldsymbol{k}})}. \tag{3.15}$$

The standard relaxation time scheme is applicable only when all the scattering events are isotropic, in which the transition rate depends only on the angle between $\boldsymbol{k}$ and $\boldsymbol{k}'$, $\Delta\phi = \phi_{\boldsymbol{k}} - \phi_{\boldsymbol{k}'}$. Consequently, the corresponding relaxation time depends only on the magnitude of $\boldsymbol{k}$, not on its direction. Nevertheless, the expression in Eq. (3.15) contradicts this point. The apparent contradiction implies that the system is not isotropic. However, we can ignore this contradiction and still follow this approach in order to just make an estimation for the relaxation time, without going through a lengthy calculation that solving Eq. (3.9) requires. We will demonstrate that the value of the standard relaxation times $\tau_{is,i}^{\nu}$ deviate too much from the modified relaxation times τ_i^{ν} in a system with in-plane magnetization.

Fig. 3.5 quantitatively compares $\tilde{\tau}_i^{\nu} = \frac{\tau_i^{\nu}}{t_0}$, with $\tilde{\tau}_{is,i}^{\nu} = \frac{\tau_{is,i}^{\nu}}{t_0}$. In all panels dashed and solid curves correspond to the electrons with minus and plus chirality, respectively.

As Eq. (3.13) indicates, when the MTF has a perpendicular magnetization, all electrons keep their chirality unchanged during a scattering event and encounter an isotropic transition. Therefore, it is obvious why these two methods produce the same relaxation times. However, when one increases the in-plane component of the magnetization, the standard relaxation time starts to deviate from the other accurate ones. At $\theta = \frac{\pi}{2}$, the value of the standard relaxation time differs too much from the accurate value, especially for electrons with minus chirality. In addition, changing the orientation of the magnetic impurities from $\theta = 0$ to $\frac{\pi}{2}$ makes electrons with minus chirality distinguishable from those with plus chirality by referring to their relaxation times.

Eq. (3.9) correctly captures the anisotropy of scattering events by including the two different modified relaxation times τ_1^{ν} and τ_2^{ν} for each subband and

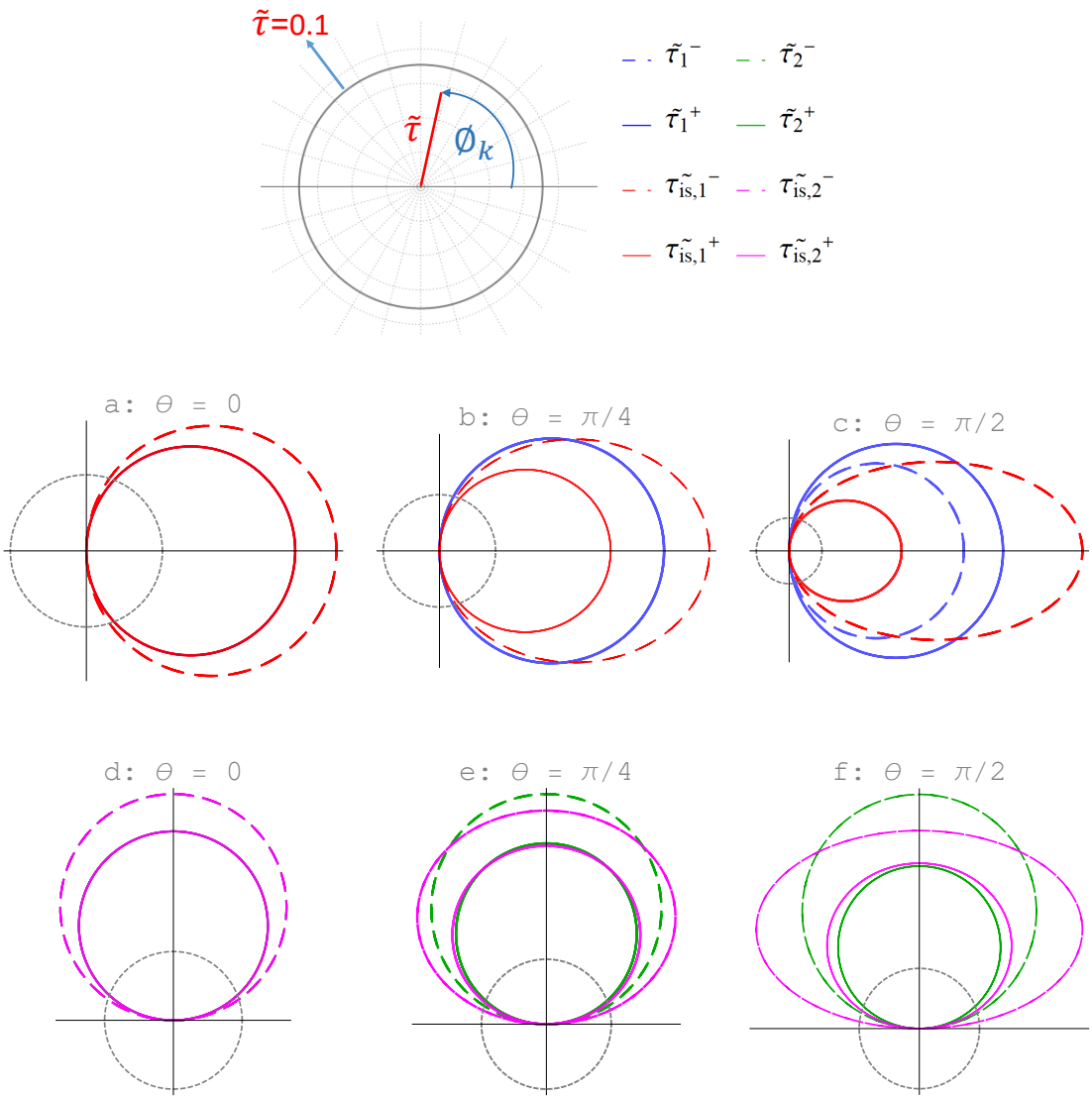

Figure 3.5: Modified relaxation times $\tilde{\tau}_i^\nu$ and standard relaxation times $\tilde{\tau}_{is,i}^\nu$ are shown versus $\phi_{\boldsymbol{k}}$ for three different orientations of the magnetic impurities, $\theta = 0, \frac{\pi}{4}, \frac{\pi}{2}$. In all panels dashed and solid curves correspond to the electrons with minus and plus chirality, respectively.

provide us with,

$$\tau_i^\nu(\boldsymbol{k}) = \frac{\tau_q^\nu}{t_0}\Big(\big[t_0 - \lambda_\nu\ \tau_{i1}^{\nu c} + \lambda_{\nu'}\tan^2\theta\tau_{i1}^{\nu' c}\big]\delta_{i1}\cos\phi_{\boldsymbol{k}} + \big[t_0 - \lambda_\nu\tau_{i1}^{\nu s} - \lambda_{\nu'}\tan^2\theta\tau_{i1}^{\nu' s}\big]\delta_{i,2}\sin\phi_{\boldsymbol{k}}\Big), \tag{3.16}$$

where

$$\tau_{11}^{\nu c} = \frac{\Lambda_{\nu'}(1+\tan^2\theta) + t_0}{\Lambda_\nu\Lambda_{\nu'}(1-\tan^4\theta) + t_0[t_0 + \Lambda_\nu + \Lambda_{\nu'}]}\bar{\tau}_q^\nu, \tag{3.17}$$

$$\tau_{21}^{\nu s} = \frac{\Lambda_{\nu'}(1-\tan^2\theta) + t_0}{\Lambda_\nu\Lambda_{\nu'}(1-\tan^4\theta) + t_0[t_0 + \Lambda_\nu + \Lambda_{\nu'}]}\bar{\tau}_q^\nu, \tag{3.18}$$

and $\lambda_\nu(k) = [1-\gamma_\nu^2(k)]\cos^2\theta$, $\Lambda_\nu = \lambda_\nu\tau_q^\nu$ and $\bar{\tau}_q^\nu = t_0\tau_q^\nu$.

By using Eq. (3.10) along with the given relaxation times by Eq. (3.16), we arrive at the following expressions for the two components of the contribution of each subband in the total conductivity,

$$\sigma_{xx}^{\nu}[\frac{e^2}{h}] = \frac{2\Gamma^{\nu}(\Gamma^{\nu'}+1)\sigma_0}{1+[\Gamma^{\nu}+\Gamma^{\nu'}]\cos^2\theta+\Gamma^{\nu}\Gamma^{\nu'}\cos 2\theta},$$
$$\sigma_{yy}^{\nu}[\frac{e^2}{h}] = \frac{2\Gamma^{\nu}(\Gamma^{\nu'}\cos 2\theta+1)\sigma_0}{1+[\Gamma^{\nu}+\Gamma^{\nu'}]\cos^2\theta+\Gamma^{\nu}\Gamma^{\nu'}\cos 2\theta}, \tag{3.19}$$

where

$$\Gamma^{\nu} = \frac{\tilde{\varepsilon}_F^2-(1+\nu\tilde{\Delta}_m)^2}{2(\tilde{\varepsilon}_F^2+[1+\nu\tilde{\Delta}_m][1+\nu\tilde{\Delta}_m\cos 2\theta])}, \tag{3.20}$$

and $\sigma_0 = \dfrac{\hbar^2 v_F^2}{n_{im}S_{im}^2 J^2}$. Also we found that $\sigma_{xy}^{\nu} = \sigma_{yx}^{\nu} = 0$. The total conductivities of the system in the x and the y directions can be obtained by $\sigma_{xx} = \sum_{\nu=\pm}\sigma_{xx}^{\nu}$, and $\sigma_{yy} = \sum_{\nu=\pm}\sigma_{yy}^{\nu}$.

3.2.1.3 The effect of magnetic impurities

The contribution of each subband to the total conductivity along with the total conductivity versus θ are shown in Fig. 3.6. In panel a the Fermi energy lies close to the bottom of the subband with plus chirality, and in panel b the Fermi energy lies far from the bottom of the subband with plus chirality.

As Fig. 3.6(a) demonstrates, electrons in the subband with minus chirality contribute significantly more to the total conductivity of a MTF, regardless of the direction of the external electric field. As Fig. 3.7 shows, when the electric field is applied along the y direction, the value of the relaxation time of electrons with minus chirality, τ_2^- is always greater than the value of the relaxation time of electrons with opposite chirality, τ_2^+ for any given value of θ. In addition, electrons with minus chirality drift faster than others, see Fig. 3.8. Since the charge conductivity is only controlled by these two parameters, it can be understood why the contribution of electrons with minus chirality is significantly higher for this case.

When the electric field is applied in the x direction, the same discussion for the dominance of electrons with minus chirality in controlling the total

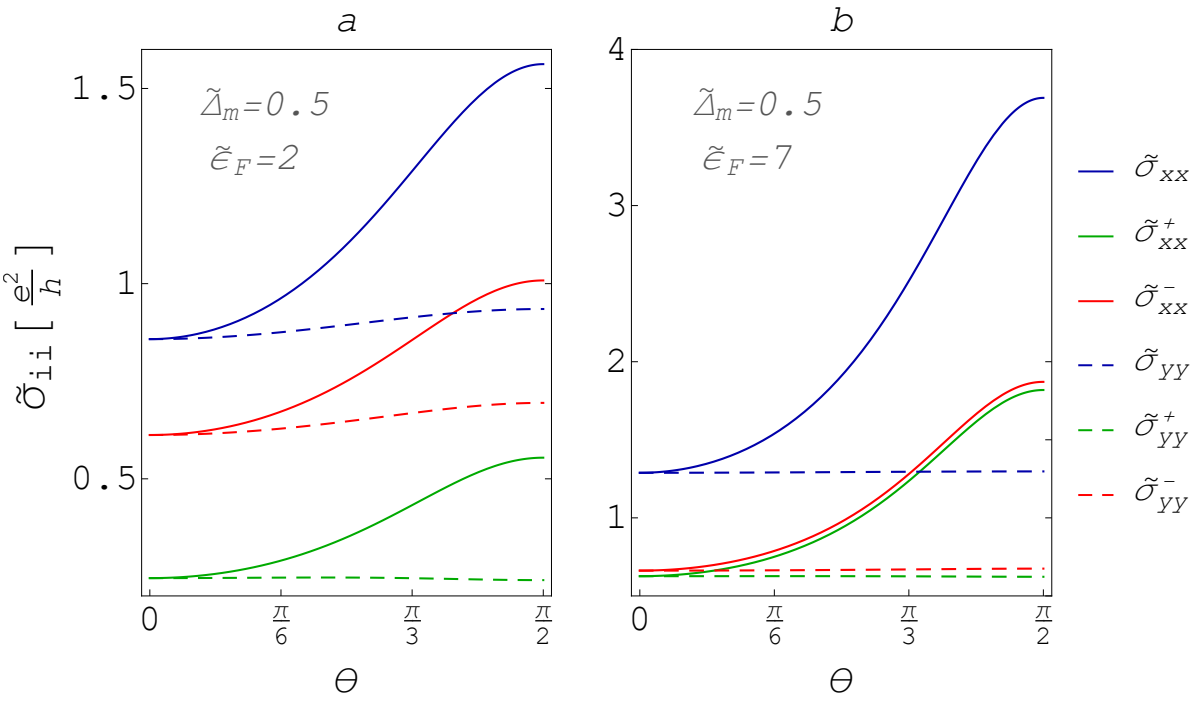

Figure 3.6: The scaled contribution of each subband, $\tilde{\sigma}^{\nu}_{ii} = \frac{\sigma^{\nu}_{ii}}{\sigma_0}$ to the total conductivity and the scaled total conductivity $\tilde{\sigma}_{ii} = \frac{\sigma_{ii}}{\sigma_0}$ with respect to θ when $\tilde{\Delta}_m = 0.5$ and $\tilde{\varepsilon}_F = 2$ in panel a, and for $\tilde{\varepsilon}_F = 7$ in panel b.

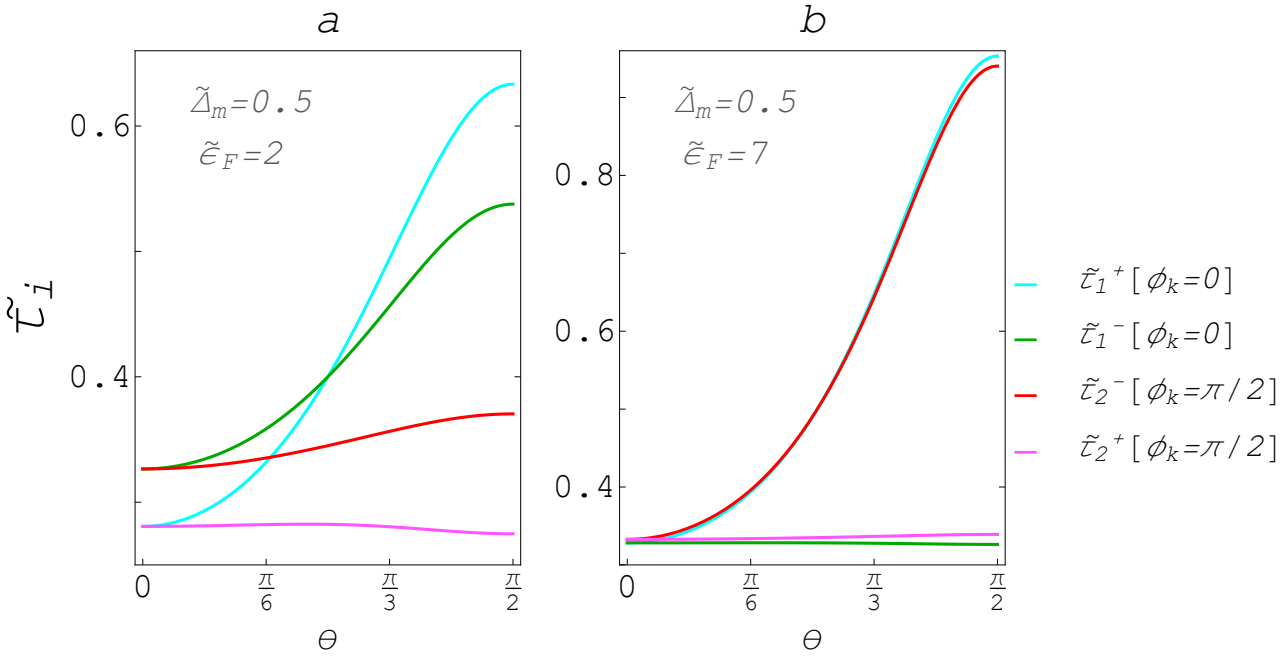

Figure 3.7: Panels a and b are the scaled relaxation times $\tilde{\tau}^{\nu}_i = \frac{\tau^{\nu}_i}{\tau_0}$ associated to the given conductivities in Fig. 3.6.

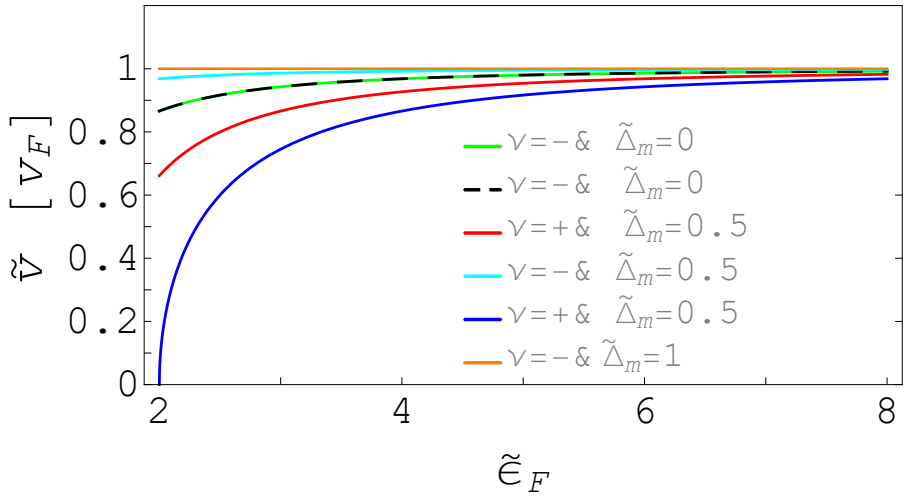

Figure 3.8: The velocity of the Fermi electrons versus $\tilde{\varepsilon}_F$ for different values of $\tilde{\Delta}_m$.

conductivity is valid only when the magnetization orientation is between $0 < \theta < \frac{\pi}{4}$. Beyond this regime, $\frac{\pi}{4} < \theta < \frac{\pi}{2}$, the relaxation time of electrons with minus chirality, τ_1^- (green curve panel *a* in Fig. 3.7), is shorter than the relaxation time of electrons with plus chirality, τ_1^+(cyan curve in the same panel Fig. 3.7). However, even though electrons with minus chirality experience more scattering events than others, in this case, their larger velocity compensates for this. Hence, they again dominate the total conductivity, even in the regime of $\frac{\pi}{4} < \theta < \frac{\pi}{2}$.

Moreover, if one fills conduction subbands with more electrons, Fermi electrons in subbands with opposite chirality end up having very similar relaxation times (see panel *b* of Fig. 3.7), regardless of the direction of the external electric field. In addition, as Fig. 3.8 shows, all electrons conduct charge with the same velocity when $\tilde{\varepsilon}_F$ is large. Therefore, as all curves in Fig. 3.6 demonstrate, all high energy electrons, regardless of their chirality contribute equally to the charge current.

Notice that all the conductivities shown in Fig. 3.6 strongly depend on the orientation of the magnetic impurities only when the electric field is applied in the x direction. Surprisingly, the total conductivity and the contribution of each subband almost do not vary with θ when the electric field is applied along the y direction.

The weak dependence of σ_{yy}^{ν} and σ_{yy} on θ can be understood by looking at the spin torque of electrons induced by the magnetic impurities during

the scattering time. With an electric field in the y direction, the average momentum of the electrons is also in the y direction. In a 3D TI, the spin of the electrons would be oriented along the x direction due to the spin-momentum locking. In the case of a MTF, the spin can also have a small z component: $\langle S_z^e \rangle = \frac{\Delta + \nu\Delta_m}{\varepsilon_k}$ (the smallest value is reached for electrons with minus chirality $\nu = -$ and for high energy electrons). Nevertheless, the spin of the electrons is in this case always approximately perpendicular to the spin of the magnetic impurities (which lies in the yz plane), especially for high-energy electrons and for electrons with negative chirality. Consequently, the torque will be large, and independent of θ, resulting in a small conductivity, almost independent of θ. In case the electric field is along the x direction, the angle between the spin of the electron and the magnetic impurities depends strongly on θ, and thus also the torque, resulting in a strong θ dependence for σ_{xx}.

3.2.1.4 Anisotropic magneto-resistance

In this section we systematically measure the degree of sensitivity of the charge current to the direction of the electric field by calculating the anisotropic magneto-resistance (AMR) for each subband AMR^ν and the total AMR

$$\begin{aligned} AMR &= \frac{\sum_\nu (\sigma_{xx}^\nu - \sigma_{yy}^\nu)}{\sum_\nu (\sigma_{xx}^\nu + \sigma_{yy}^\nu)}, \\ AMR^\nu &= \frac{\sigma_{xx}^\nu - \sigma_{yy}^\nu}{\sigma_{xx}^\nu + \sigma_{yy}^\nu}. \end{aligned} \tag{3.21}$$

The external electric field affects the momentum of electrons, and due to the large spin-momentum locking, it consequently affects the spins of electrons. On the other hand, since the spin of electrons interacts with the spin of magnetic impurities, the external electric field subsequently influences the strength of scatterings and, consequently, the system's conductivity. Then, it is obvious why changing the direction of the external electric field can strongly affect the conductivity of a MTF.

By using Eqs. (3.19) and (3.21), we find

$$AMR^\nu = \frac{\sigma_{xx}^\nu - \sigma_{yy}^\nu}{\sigma_{xx}^\nu + \sigma_{yy}^\nu} = \frac{\Gamma^{\nu'} \sin^2\theta}{1 + \Gamma^{\nu'} \cos^2\theta}. \tag{3.22}$$

According to Eq. (3.22), for a MTF with a fully out of plane magnetization, $\theta = 0$, the value of AMR^{ν} is zero for both bands and as we already knew, the system is isotropic. On the other hand, for a MTF with a completely in-plane magnetization, $AMR^{\nu}[\theta = \frac{\pi}{2}] = \Gamma^{\nu'}$. Accordingly, the value of the AMR^{ν} for each band ranges from 0 to $\Gamma^{\nu'}$.

According to Eq. (3.22), AMR^{ν} depends on $\Gamma^{\nu'}$, which implies that the anisotropy in the conductivity of a particular band originates from the inter-subband scatterings, in agreement with Eq. (3.13).

Figs. 3.9(a) and 3.9(b) compare the AMR with AMR^{+} and AMR^{-}, in terms of θ, with $\tilde{\varepsilon}_F$=2, 7, and $\tilde{\Delta}_m$=0.5. All curves increase by increasing θ, regardless of the value of $\tilde{\varepsilon}_F$ and the chirality of the electrons. This is due to the fact that the strength of inter-subband scattering, which is responsible for the anisotropy, increases by increasing θ, see Eq. (3.13).

As Fig. 3.6(a) demonstrates, when the Fermi energy lies on the bottom of the band with plus chirality, $\tilde{\varepsilon}_F = 2$, $(\sigma^{+}_{xx} - \sigma^{+}_{yy}) \simeq (\sigma^{-}_{xx} - \sigma^{-}_{yy})$, though $(\sigma^{-}_{xx} + \sigma^{-}_{yy}) \gtrsim (\sigma^{+}_{xx} + \sigma^{+}_{yy})$, which eventually leads to $AMR^{+} \gtrsim AMR^{-}$, (see Fig. 3.9(a)). Hence, for this case, electrons with plus chirality play the important role in the anisotropy of the derived conductivity of the MTF.

For the case of $\tilde{\varepsilon}_F = 7$, (Fig. 3.9(b)), $\sigma^{+}_{xx} \simeq \sigma^{-}_{xx}$ and $\sigma^{+}_{yy} \simeq \sigma^{-}_{yy}$, which results in $AMR^{+} \simeq AMR^{-}$. Therefore, electrons that reside in the top of their host bands have the same share in generating the anisotropy in the conductivity.

The red curves in Figs. 3.9(a) and 3.9(b) demonstrate that the anisotropy in the total conductivity increases by increasing θ. This is due to the fact that σ_{xx} diverges greatly from σ_{yy} by increasing θ (see Figs. 3.6).

Now, we assume that all the magnetic impurities are aligned in a fixed particular direction and consider that the Fermi energy position is also fixed. Note that the value of the hybridization induced gap Δ is fixed in this work. However, the size of the energy gap $2|\Delta + \nu\Delta_m|$ can be altered by changing the value of Δ_m. In what follows, we investigate how the degree of the anisotropy in each band's conductivity and the total conductivity can be controlled by tuning the size of the energy gap.

Fig. 3.9(c) shows AMR^{-}, AMR^{+} and AMR versus $\tilde{\Delta}_m$, for two values of θ and with $\tilde{\varepsilon}_F = 2$. As expected, the contribution of each band and also the total

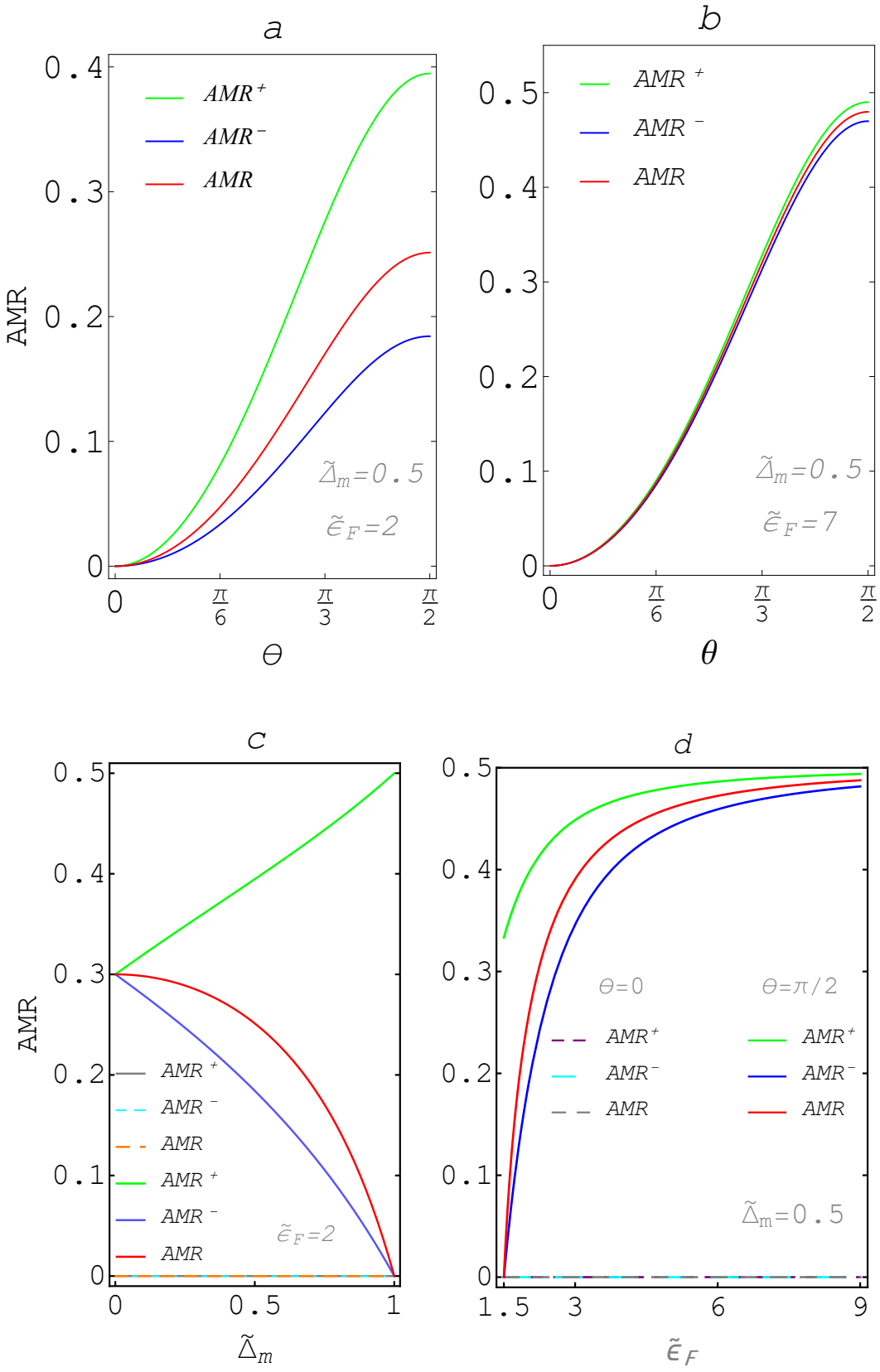

Figure 3.9: The AMR, AMR^{-}, AMR^{+} with respect to θ, $\tilde{\varepsilon}_F$, $\tilde{\Delta}_m$.

conductivity is isotropic when all magnetic impurities are aligned perpendicular to the surface of a MTF. In case of having all the magnetic impurities aligned in-plane, AMR^{-} and AMR have a decreasing trend versus $\tilde{\Delta}_m$, while AMR^{+} has an increasing trend against $\tilde{\Delta}_m$.

When $\theta = \frac{\pi}{2}$, based on Eq. (3.13), just inter-subband scatterings are possible for electrons, regardless of their chirality. In addition, as Eq. (3.13) indicates, the transition rate $W^{vv'}(\boldsymbol{k},\boldsymbol{k}')$ for an inter-subband scattering is symmetric with respect to the chirality index. Accordingly, the probability of an inter-subband scattering is independent of the chirality of electrons. However, during an inter-subband transition, the band with minus chirality can host much more electrons. Therefore, the produced conductivity by electrons with plus chirality is much more anisotropic compared to the generated current by electrons with minus chirality, see Fig. 3.9(c). Regarding the anisotropy in the total charge current, because the transition rate of all inter-subband scatterings decreases with increasing $\tilde{\Delta}_m$, the amount of produced anisotropy decreases (the red curve in Fig. 3.9(c)).

Now, we assume that the size of the energy gap is kept fixed, and we discuss how changing the value of the Fermi energy can change the amount of anisotropy in the conductivity of each band and the total conductivity. We have so far considered that the anisotropy in the conductivity of a particular band and the total charge current vanishes if the magnetic impurities are aligned perpendicular to the surface. In the case of $\theta = \frac{\pi}{2}$, by increasing $\tilde{\varepsilon}_F$, not only the transition rate for all possible inter-subband scatterings increases but also the number of occupied states by electrons after an inter-subband scattering increases, regardless of their chirality. Therefore AMR^{-}, AMR^{+} and AMR enhance by increasing $\tilde{\varepsilon}_F$ (see Fig. 3.9(d))

3.2.1.5 Comparison between the charge conductivities of a MTF and a magnetic 3DTI (3DMT)

By comparing the conductivity of a MTF with the conductivity of a 3DMT we can understand how the hybridization between the top and bottom surfaces of a MTF affects the system's charge conductivity.

In a 3DTI the thickness of the system is much larger than the decay

length of the surface states into the bulk and the wave functions of the top and bottom surfaces do not overlap. As a result, the 3DTI is a gapless system. In fact, the value of the hybridization induced gap Δ decays exponentially as a function of the thickness of the system [6]. In the absence of Δ and Δ_m, the dispersion of a 3DTI consists of two degenerate massless Dirac cones.

For what follows, we split our discussion into two parts. In the first part, we assume that both the MTF and the 3DMT lack the magnetic dopants that induce the gap Δ_m. In the second part, we investigate the effect of including Δ_m. In a TTF, two Dirac cones are degenerate, but unlike the dispersion of a 3DTI, these two Dirac cones are always massive due to the permanent presence of the hybridization induced gap Δ.

In Figs. 3.10(a) and 3.10(b) we compare the charge conductivity of a TTF and a 3DTI [34] versus $\tilde{\varepsilon}_F$, and for two distinct orientations of the magnetic impurities $\theta = 0, \frac{\pi}{2}$. Here, we assume that the Fermi energy is fixed, and the size of $\tilde{\varepsilon}_F$ can be altered by tunning the Δ. These two panels show that the conductivity of a 3DTI is larger than the conductivity of a TTF, regardless of the direction of the external electric field and the orientation of the magnetic impurities. Decreasing the value of Δ, by increasing the thickness of the system, increases $\tilde{\varepsilon}_F$ and consequently enhances the charge conductivity of the TTF. For large values of $\tilde{\varepsilon}_F$, which correspond to a significantly thick TTF, the charge conductivity of a TTF is the same as of a 3DTI.

According to Fig. 3.10(a), when the external electric field is applied in the x direction, the charge conductivity of a TTF differs significantly from the charge conductivity of a 3DTI if $\theta = \frac{\pi}{2}$. However, this is not true when the spins of the magnetic impurities are perpendicular to the surface of the TTF, i.e $\theta = 0$. In contrast to the case of $\boldsymbol{E} = E\hat{x}$, Fig. 3.10(b) shows that when $\boldsymbol{E} = E\hat{y}$, the difference between the charge conductivity of a TTF and a 3DTI is insensitive to the variations in the orientation of the magnetic impurities. The zero conductivity of the TTF corresponds to the situation in which the Fermi energy lies at the bottom of both subbands. It should be noticed that since the Fermi energy is fixed in the conduction subband of the 3DTI, its conductivity is always nonzero and constant.

Now, we compare the conductivity of a 3DMT with the conductivity of a

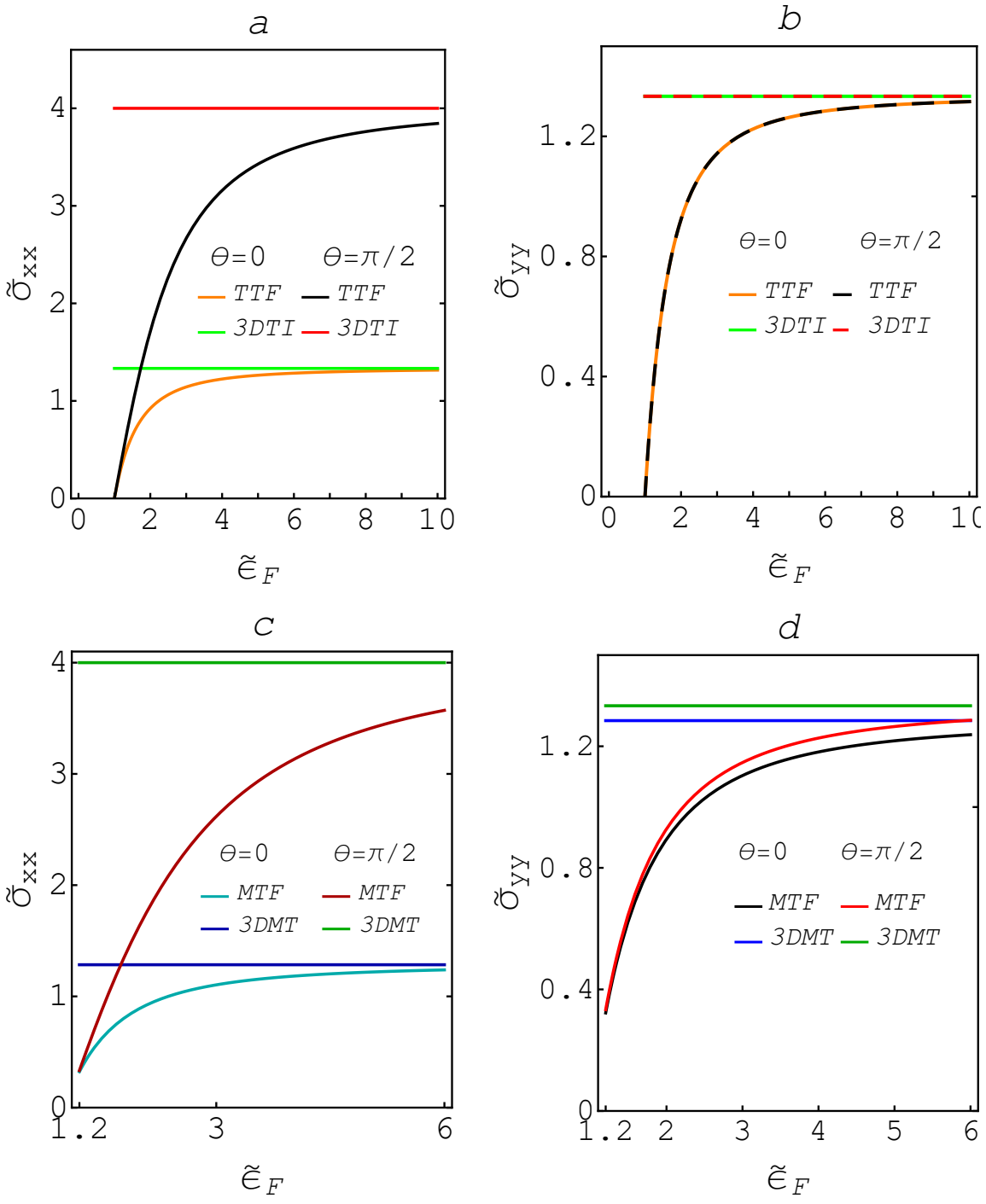

Figure 3.10: The two scaled components of the conductivity $\tilde{\sigma}_{xx} = \frac{\sigma_{xx}}{\sigma_0}$ and $\tilde{\sigma}_{yy} = \frac{\sigma_{yy}}{\sigma_0}$ of a 3DTI and a TTF are shown in panels a and b. Panels c and d show the two component of the conductivity of a 3DMT and a MTF.

MTF. By dopping a 3DTI with strong magnetic dopants, the time-reversal symmetry is broken, which leads to the removal of the surface chiral states and the conversion of the degenerate massless Dirac cones to degenerate massive Dirac cones. However, in contrast to the 3DMT, the breaking of the time-reversal symmetry in a TTF removes also this degeneracy and consequently results in dispersion with two non-degenerate massive Dirac cones, each with distinct chirality, see Fig. 3.2.

Figs. 3.10(c) and 3.10(d) show that the conductivity of a 3DMT is larger than the conductivity of a MTF. By decreasing the size of the hybridization induced gap, increasing $\tilde{\varepsilon}_F$, the difference between the conductivity of these two systems decreases.

When all the magnetic impurities lie in-plane, it is shown that the conductivity of a 3DMT is insensitive to a change in the size of Δ_m [34]. In the same condition, due to the hybridization between two opposite surfaces in a MTF, the charge conductivity is highly sensitive to any change in Δ_m and consequently in the size of the gap $2|\Delta \pm \Delta_m|$. Then, the insensitivity of the charge conductivity of such a system to the gap implies that the system is thick enough, and the finite size effect gap is absent. By comparing the sensitivity of the charge conductivity to the gap for different samples with different thicknesses, the critical thickness for a certain system at which a crossover from a 3DMT to an MTF occurs can be determined.

Breaking the time-reversal symmetry decreases the conductivity of the 3DMT, and accordingly increases its resistivity. When the Fermi energy lies in the conduction band, there is always a non-zero resistivity against the charge transport since the degenerate bands both are simultaneously involved in the charge transport. However, in the absence of time-reversal symmetry in a MTF, we can reach a regime in which the resistivity is zero. This will be clarified in detail in Sec. 3.2.2.

3.2.1.6 Effect of the gap

In this section, we investigate how changing the size of the gap, $2(\Delta + \nu\Delta_m)$, influences the charge transport in a MTF. Here, we keep the value of Δ constant and just change the size of Δ_m.

Fig. 3.11 presents the conductivity of each band and the total conductivity of the MTF versus $\tilde{\Delta}_m = \frac{\Delta_m}{\Delta}$, for two critical values of θ, 0 and $\frac{\pi}{2}$, in a system with constant Fermi energy and Δ, i.e constant $\tilde{\varepsilon}_F$. According to Fig. 3.11(a), increasing Δ_m raises the contribution of electrons with plus chirality and decreases the conductivity of electrons with minus chirality, whatever is θ or the direction of the electric field. The shown behavior of the total conductivity in Fig. 3.11(b) can be generally explained by checking the response of velocity and occupation number of electrons to $\tilde{\Delta}_m$. For this purpose, in what follows, we will check the response of the occupation number of electrons to $\tilde{\Delta}_m$, and the velocity of electrons.

When $\theta = \pi/2$, the electron occupation number in both bands is the same at $\tilde{\Delta}_m = 0$ according to Figs. 3.12(a) and 3.12(b). When the size of Δ_m increases, although the occupation number of electrons with minus chirality increases, the yellow curve in Figs. 3.12(a) and 3.12(b), the occupation number of conducting electrons with plus chirality decreases and finally reaches zero value at $\tilde{\Delta}_m = 1$, see the blue curves in Figs. 3.12(a) and 3.12(b). The velocity of electrons in both bands interestingly shows a similar trend (see Fig. 3.12(c)). Therefore, when the external electric field is applied in the x direction and $\theta = \pi/2$, since the total occupation number of electrons, the red curve in Fig. 3.12(a), and the average velocity of electrons, the red curve in Fig. 3.12(c), both decrease by increasing the value of $\tilde{\Delta}_m$, the total corresponding conductivity decreases for $\theta = \pi/2$, the green curve in Fig. 3.11(b).

When the external electric field is applied in the y direction the corresponding conductivity changes too slowly (almost constant) for $\theta = \frac{\pi}{2}$, as the total occupation number of electrons (green curve in Fig. 3.12(b)) changes too slowly for this case and dominates the behavior of the conductivity. For other orientation of the magnetic impurities the calculated conductivity can also be understood in this way.

3.2.2 The single-band regime

Here, we investigate the charge transport of a MTF when only the band with minus chirality is filled. To keep the MTF in this regime the Fermi energy can range within $\Delta - \Delta_m \leqslant \varepsilon_F \leqslant \Delta + \Delta_m$.

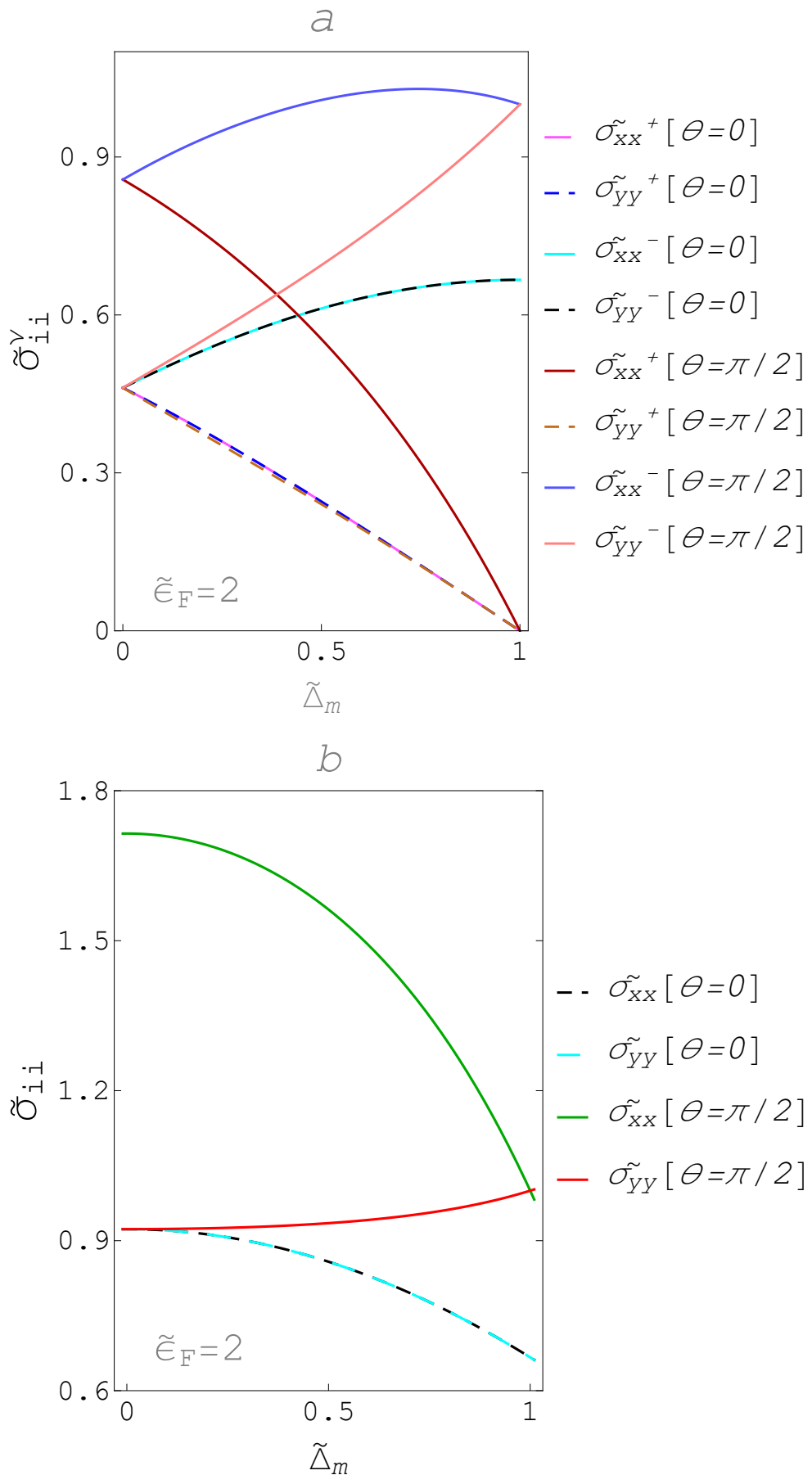

Figure 3.11: The contribution of each band to the total conductivity (a), and the total conductivity (b) versus $\tilde{\Delta}_m$ for two critical values of θ and when $\tilde{\varepsilon}_F = 2$.

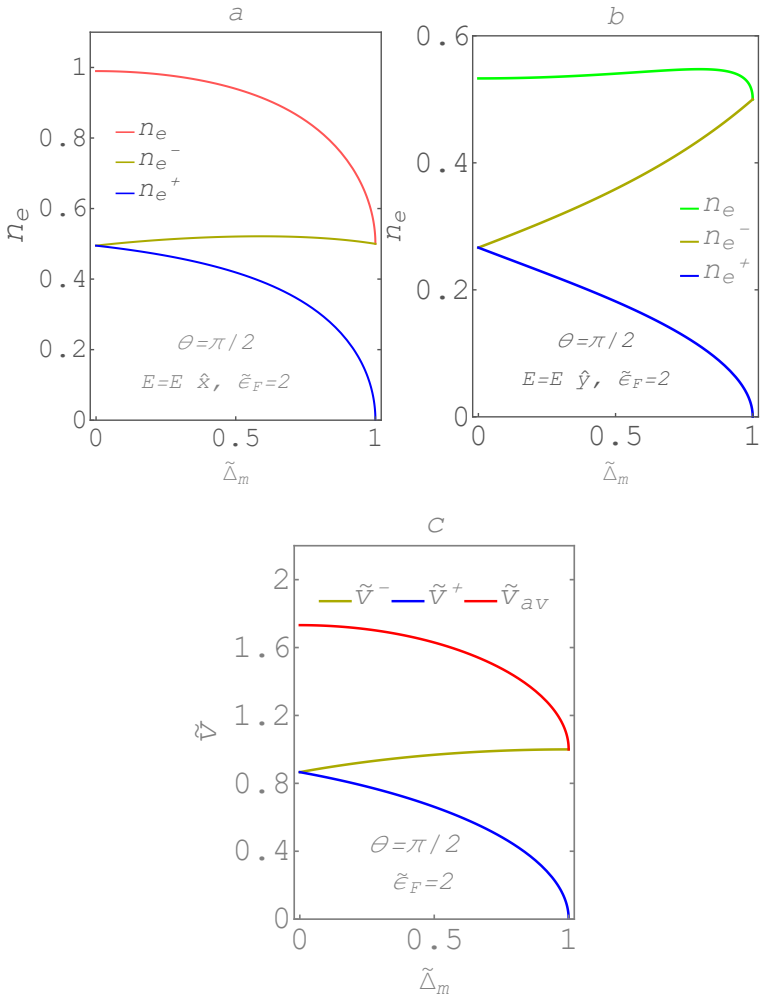

Figure 3.12: Panels a and b show the occupation number of electrons in each band with respect to $\tilde{\Delta}_m$ for constant values of θ and $\tilde{\varepsilon}_F$. Panel c shows the velocity of electrons with distinctive chirality against $\tilde{\Delta}_m$.

If only electrons with minus chirality participate in transport, it is expected that the generated charge current shows some exotic features, which are absent in the two-band regime. To explain why we have such an expectation, let us check the chiral selection rule, which governs electrons' transition between different states in a MTF. The interaction between an electron and a local magnetic impurity is given by

$$H_m = H_m^{(1)} + H_m^{(2)}, \tag{3.23}$$

where

$$H_m^{(1)} = JS_{im}\cos\theta \begin{pmatrix} \sigma_z & 0 \\ 0 & -\sigma_z \end{pmatrix}, \qquad H_m^{(2)} = JS_{im}\sin\theta \begin{pmatrix} 0 & -i\,\sigma_z \\ i\,\sigma_z & 0 \end{pmatrix}, \tag{3.24}$$

in the spin-chirality Hilbert space. The full Hamiltonian of electrons is $H = H_0 + H_m$. To check how the chirality of electrons varies through different transitions, one can define the chirality operator in the spin-chirality basis set as

$$C = \sigma_0 \otimes \tau_z = \begin{pmatrix} 1 & 0 & 0 & 0 \\ 0 & 1 & 0 & 0 \\ 0 & 0 & -1 & 0 \\ 0 & 0 & 0 & -1 \end{pmatrix}, \tag{3.25}$$

where $C^*C = CC^* = \mathbb{1}$, $C^2 = 1$ and $C\,|u_\nu^s\rangle = \nu\,|u_\nu^s\rangle$. We can check the possible conservation of chirality by calculating the commutator $[H,C]$. Using Eq. (3.2), Eq. (3.24) and Eq. (3.25) we arrive at

$$[H,C] = [H_0,C] + [H_m^{(1)},C] + [H_m^{(2)},C]. \tag{3.26}$$

Since $[H_0,C] = 0$, and $[H_m^{(1)},C] = 0$, one finds $[H,C] = [H_m^{(2)},C]$. We can conclude that scatterings caused by $H_m^{(1)}$ has to conserve chirality (corresponding to the intra-subband transitions), while scatterings caused by $H_m^{(2)}$ change the chirality (corresponding to the inter-subband transitions). When all the magnetic impurities are perpendicular to the surface, $\theta = 0$, one finds $H_m^{(2)} = 0$, and consequently only intra-subband transitions are allowed. For an in-plane orientation of the magnetic impurities, $\theta = \pi/2$, one finds $H_m^{(1)} = 0$, and only inter-subband transitions can occur. In the single-band regime inter-subband transitions are forbidden because of the conservation of energy. A dissipationless charge current can therefore be expected in the single-band regime for a MTF if $\theta = \pi/2$.

Now, we calculate the resistivity of a MTF in this regime to prove this exciting finding. Since in what follows, we discuss the charge transport of just electrons with minus chirality, we drop the chirality index for the sake of

convenience. The found transition rate for the electrons with minus chirality is

$$\bar{W}(\boldsymbol{k},\boldsymbol{k}') = \cos^2\theta[1+\gamma^2+\cos\phi_-(\gamma^2-1)]\delta(\varepsilon_k-\varepsilon_{k'}), \tag{3.27}$$

where $\phi_- = \phi_{\boldsymbol{k}'} - \phi_{\boldsymbol{k}}$, $\bar{W} = \frac{\hbar w}{\pi J^2 S_{im}^2 n_{im}}$, $\gamma = \frac{\Delta - \Delta_m}{\varepsilon_k}$. As Eq. (3.27) shows, the out of plane component of the magnetic impurities controls the transition of electrons. By weakening this component of the magnetic impurities, the scattering probability decreases for all possible scattering events, and eventually vanishes at $\theta = \frac{\pi}{2}$. In other words, if all the magnetic impurities lie in-plane, electrons stay forever in their host state and never scatter into the other states.

Substituting Eq. (3.27) in Eq. (3.9) yields the following relaxation time for electrons in this regime

$$\tau_{\boldsymbol{k}} = \frac{t_0}{\cos^2\theta}\frac{1}{3+\gamma^2}\cos\phi_{\boldsymbol{k}}. \tag{3.28}$$

This indicates that the relaxation time of electrons increases by increasing θ and diverges at $\theta = \frac{\pi}{2}$, which once again confirms that electrons with minus chirality do not encounter any scattering events in this situation.

Replacing the relaxation time in Eq. (3.10) with Eq. (3.28) yields the following charge conductivity of electrons in this regime

$$\begin{aligned} &\sigma_{xx}[\frac{e^2}{h}] = \sigma_{yy}[\frac{e^2}{h}] = \frac{\sigma_0}{\cos^2\theta}\frac{\tilde{\varepsilon}_F^2 - (\tilde{\Delta}_m - 1)^2}{3\tilde{\varepsilon}_F^2 + (\tilde{\Delta}_m - 1)^2}, \\ &\sigma_{xy} = \sigma_{yx} = 0. \end{aligned} \tag{3.29}$$

Accordingly, the resistivity matrix will be

$$\rho = \sigma^{-1} = \begin{pmatrix} \rho_{xx} & \rho_{xy} \\ \rho_{yx} & \rho_{yy} \end{pmatrix} = \rho_{xx}\begin{pmatrix} 1 & 0 \\ 0 & 1 \end{pmatrix}, \tag{3.30}$$

where $\rho_{xx}[\frac{h}{e^2}] = \rho_{yy}[\frac{h}{e^2}] = \rho_0\cos^2\theta\ \frac{3\tilde{\varepsilon}_F^2 + (\tilde{\Delta}_m - 1)^2}{\tilde{\varepsilon}_F^2 - (\tilde{\Delta}_m - 1)^2}$, and $\rho_0 = \frac{n_{im}S_{im}^2 J^2}{\hbar^2 v_F^2}$.

This result also shows another remarkable finding: the conductivity of a MTF in the single-band regime is always isotropic, $\sigma_{xx} = \sigma_{yy}$, in contrary to the extracted conductivity for this system in the two-band regime, Eq.

(3.19). The anisotropy in the conductivity for a MTF in the two-band regime originates from the magnetic impurities' in-plane component. However, in the single-band regime, the in-plane component of the magnetic impurities is not able to scatter electrons, see Eq. (3.27), and consequently, the calculated conductivity for this regime is isotropic.

Fig. 3.13(a) shows this resistivity as a function of θ. It decreases by increasing θ, and indeed eventually vanishes at $\theta = \frac{\pi}{2}$, regardless of the value of $\tilde{\varepsilon}_F$, and $\tilde{\Delta}_m$. This provides us with another criterion to distinguish the single-band regime from the two-band regime in the charge transport of a MTF. Since Δ is constant, the value of the energy gap $2|\Delta - \Delta_m|$ decreases by increasing the value of Δ_m. Therefore, by increasing the value of Δ_m, or $\tilde{\Delta}_m$, the conductivity increases, and consequently, the corresponding resistivity decreases (Fig. 3.13(b)).

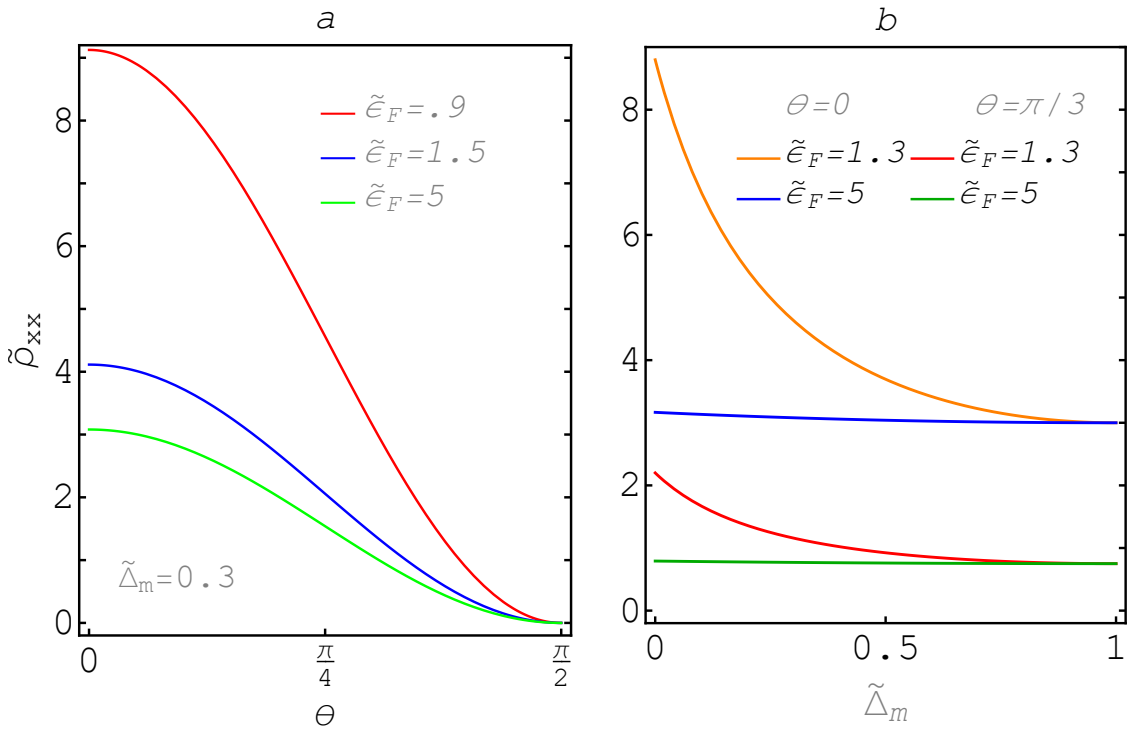

Figure 3.13: The scaled resistivity $\tilde{\rho}_{xx} = \frac{\rho_{xx}}{\rho_0}$ of a MTF in the single-band regime versus θ (a), and $\tilde{\Delta}_m$ (b).

Finally, we want to stress that the charge current in this regime stays dissipationless as long as the chirality selection rule remains unchanged. The presence of extra effects can modify the band dispersion and may break the chirality selection rule, making the charge current dissipative. For example,

an in-plane magnetic field causes the band dispersion to be an asymmetric, tilted Dirac cone [35, 36]. Hence, it can generate a finite resistivity in this regime. A perpendicular electric field can also modify the transition selection rule by breaking the inversion symmetry [37], even though the dispersion relation remains symmetric.

3.3 Conclusion

The charge transport of a magnetic topological ultra-thin film (MTF) is investigated by applying the Boltzmann semi-classical formalism along with a modified relaxation time scheme. Two distinct regimes are identified depending on whether both conduction bands are engaged in the charge transport or not. For each regime, the relaxation times of electrons and the system's charge conductivity are found analytically. When both conduction bands are filled with electrons, the generated charge current is anisotropic. In contrast to this regime, we found that the conductivity of a MTF is isotropic when only a single conduction band is involved in the transport. The extracted conductivity in both of these regimes is highly sensitive to the orientation of the magnetic impurities, the size of the energy gap, and the Fermi level's value.

Interestingly, the magnetic impurities induce a chirality selection rule that governs electrons' transitions during different scattering events. When both of the conduction bands are filled, the charge current is always dissipative. Nevertheless, when only a single band is occupied, the chiral selection rule forbids all the transport channels for electrons if the magnetic impurities lie in plane. In consequence, the charge transport in a MTF will be surprisingly dissipation-less.

This study provides a criterion to specify a crossover from a 3DTI to a MTF. When all the magnetic impurities are in-plane in a 3DMT, the measured charge conductivity is insensitive to the gap. In contrast, in a MTF with in-plane magnetic impurities, the charge conductivity is highly sensitive to the gap. This criterion can be used to determine the critical thickness for a certain system at which a crossover from a 3DMT to a MTF occurs.

BIBLIOGRAPHY

[1] J. Linder et al., Phys. Rev. B **80**, 205401 (2009).

[2] C. X. Liu et al., Phys. Rev. B **81**, 041307(R) (2010).

[3] H. Z. Lu et al., Phys. Rev. B **81**, 115407 (2010).

[4] W. Y. Shan et al., New J. Phys. **12**, 043048 (2010).

[5] B. Zhou et al., Phys. Rev. Lett. **101**, 246807 (2008).

[6] Y. Zhang et al., Nat. Phys. **6**, 584(2010).

[7] H. Liang et al., Nano Lett. **12**, 1486(2012).

[8] Q. Liu et al., Phys. Rev. Lett. **102**, 156603 (2009).

[9] D. A. Abanin et al., Phys. Rev. Lett. **106**, 136802 (2011).

[10] A. B. Sushkov et al., Phys. Rev. B **82**, 125110 (2010).

[11] G. S. Jenkins et al., Phys. Rev. B **82**, 125120 (2010).

[12] G. M. Gusev et al., Phys. Rev. B **84**, 121302(R) (2011).

[13] A. A. Zyuzin et al., Phys. Rev. B **83**, 245428 (2011).

[14] I. Lee et al., Proc. Natl. Acad. Sci. **112**, 1316 (2015).

[15] S. Y. Xu et al., Nature Phys. **8**, 616 (2012).

[16] L. A. Wray et al., Nature Phys. **7**, 32 (2011).

[17] Y. L. Chen et al., Science **329**, 659 (2010).

[18] I. Vobornik et al., Nano Lett. **11**, 4079 (2011).

[19] M. Li et al., Phys. Rev. Lett. **115**, 087201 (2015).

[20] Fan Yang et al., Phys. Rev. B **94**, 075304 (2016).

[21] Peng Wei et al., Phys. Rev. Lett. **110**, 186807 (2013).

[22] T. Hesjedal et al., Nature Materials **16**, 3 (2017).

[23] F. Katmis et al., Nature **533**, 513 (2016).

[24] N. A. Sinitsyn, J. Phys.: Condens. Matter **20**, 023201 (2008).

[25] N. A. Sinitsyn et al., Phys. Rev. B **73**, 075318 (2006).

[26] N. A. Sinitsyn et al., Phys. Rev. B **72**, 045346 (2005).

[27] K. Vyborný et al., Phys. Rev. B **79**, 045427 (2009).

[28] J. Wang et al., Phys. Rev. B **89**, 085106 (2014).

[29] P. Wei et., Phys. Rev. Lett. **110**, 186807 (2013).

[30] G. Koren, Phys. Rev. B. **97**, 054405 (2018).

[31] G. Koren et al., Nano Lett. **15**, 5835 (2015).

[32] Y. Taguchi et al., Science **291**, 2573 (2001).

[33] G. D. Mahan 2011 Condensed Matter in a Nutshell (Princeton, NJ: Princeton University Press)

[34] A. Sabzalipour et al., J. Phys.: Condens. Matter **27** 115301(2015).

[35] S. H. Zheng et al., Phys. Rev. **101**, 041408(R) (2020).

[36] A. A. Taskin et al., Nat. Commun. **8**, 1340 (2017).

[37] H. Z. Lu et al., Phys. Rev. Lett. **111**, 146802 (2013).

CHAPTER 4

THE EFFECT OF STRUCTURAL INVERSION ASYMMETRY ON THE CHARGE TRANSPORT IN MAGNETIC TOPOLOGICAL ULTRA-THIN FILMS

In a TTF grown on a substrate the inversion symmetry is not preserved along the z direction (normal to the thin film) since the top surface is exposed to the air while the bottom surface is attached to the substrate. This is also the case when an external perpendicular electric field is exerted on a TTF. This structural inversion asymmetry (SIA) splits each spin-degenerate band into two subbands separated in momentum space [39]. This Rashba-like effect (the combination of SOC and SIA) can be controlled by a gate voltage. The tunability of the band structure in a TTF is important for spintronic devices like Datta-Das spin field-effect transistors [40], in which the spin structure is electrically tuned.

In this chapter, we combine the breaking of time-reversal symmetry (TRS) and SIA: we explore the role of a substrate or a perpendicular electric field on the charge transport of a magnetic topological ultra-thin film grown on a substrate (MTF), in the presence of short-range and randomly placed dilute magnetic impurities. In a previous chapter, we investigated the transport properties of a free-standing MTF. Here we demonstrate that SIA enhances the anisotropy induced by the magnetic impurities. We combine the Boltzmann formalism [41–43] with a modified relaxation time scheme [44] to

appropriately describe this strong anisotropy in the charge transport.

As we will describe later, our analytical and numerical results reveal two different transport regimes. When only a single conduction subband contributes to the charge transport, a dissipationless charge current can exist. This effect occurs when the current generating external electric field is parallel to fully in-plane oriented magnetic impurities. Interestingly, this dissipationless current does not happen if both conduction subbands are involved in the transport. We further show that the effect that the magnetic impurities have on the charge transport in a MTF can be tuned by a gate voltage (or the substrate). We comprehensively study different scattering events and discuss the underlying physics behind our numerical and analytical results.

We have organized the rest of this chapter as follows. In Sec. 4.1, we introduce the effective Hamiltonian for a MTF, and briefly discuss the applied methodology. Sec. 4.3 presents our result and discussion. Secs. 4.3.1 and 4.3.2 present our discussion on the charge transport of a MTF in the single-subband and two-subband regimes, respectively. Sec. 4.4 sums up our findings and discussion with the principal results.

4.1 Hamiltonian and basic notations

The setup of the system under study is shown in Fig. 4.1. We base our study on the effective Hamiltonian which describes the surface states of a MTF as

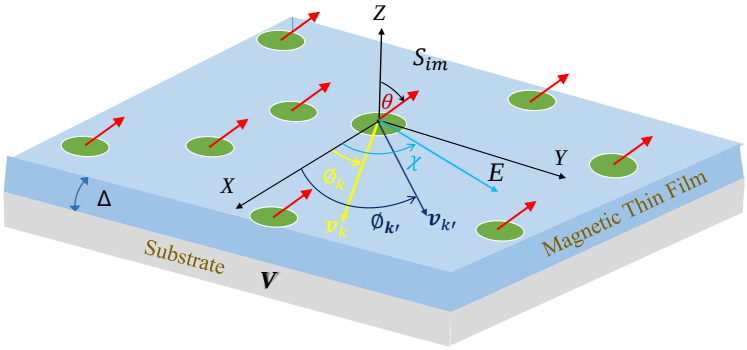

Figure 4.1: An electron under the presence of an electric field $\boldsymbol{E} = E(\cos\chi, \sin\chi, 0)$ scatters off a particular point like magnetic impurity $\boldsymbol{S}_{im} = S_{im}(0, \sin\theta, \cos\theta)$, with initial velocity $\mathbf{v}_k = \mathrm{v}_k(\cos\phi_{\boldsymbol{k}}, \sin\phi_{\boldsymbol{k}}, 0)$ and final velocity $\mathbf{v}_{k'} = \mathrm{v}_{k'}(\cos\phi_{\boldsymbol{k}'}, \sin\phi_{\boldsymbol{k}'}, 0)$.

derived in Refs. [46–48]. The Hamiltonian is given by

$$\mathscr{H}_0 = \begin{pmatrix} \Delta + \Delta_m & i\alpha e^{-i\phi_{\boldsymbol{k}}} & V & 0 \\ -i\alpha e^{i\phi_{\boldsymbol{k}}} & -\Delta - \Delta_m & 0 & V \\ V & 0 & -\Delta + \Delta_m & i\alpha e^{-i\phi_{\boldsymbol{k}}} \\ 0 & V & -i\alpha e^{i\phi_{\boldsymbol{k}}} & \Delta - \Delta_m \end{pmatrix}, \tag{4.1}$$

where $\alpha = \hbar v_F k$ with v_F being the Fermi velocity of electrons, and $\phi_{\boldsymbol{k}} = \arctan(k_y/k_x)$, see Fig. 4.1. Δ describes the hybridization gap, Δ_m is the gap that originates from the magnetic exchange field, and V represents the SIA. The effect of different contributions Δ, Δ_m and V on the electronic band structure are now introduced successively.

A thick topological film has two surfaces, and each surface hosts helical gapless states. The corresponding band structure for these surface states is shown in Fig. 4.2(a) for $\Delta = \Delta_m = V = 0$. When the thickness of a topological thin film is small, the spin-polarized states in opposite surfaces hybridize, leading to a hybridization gap of 2Δ at the Dirac point, as shown in Fig. 4.2(b). The size of this gap depends on the thickness of the sample [34].

Experimentally, TTFs have been doped with magnetic atoms in order to create MTFs in which time-reversal symmetry is broken. For example, $(Bi,Sb)_2Te_3$ and Bi_2Se_3, have been doped with Cr [49–54], V [55, 56] or Fe [57]. A ferromagnetic phase can now be formed through different mechanisms [16–26], and consequently this induces the gap Δ_m in the surface band structure.

The SIA between the top and bottom surfaces is represented by the SIA potential V in the Hamiltonian (4.1). Even though a TTF is gapped due to the hybridization between the top and bottom surfaces ($\Delta \neq 0$), the massive Dirac fermions are still degenerate. A substrate or a perpendicular electric field removes this degeneracy. While Δ is a characteristic of the system, the energy gap of a MTF can be engineered by Δ_m and V, giving rise to new transport features which will be discussed in this work.

Under a unitary transformation [48], the Hamiltonian (4.1) transforms

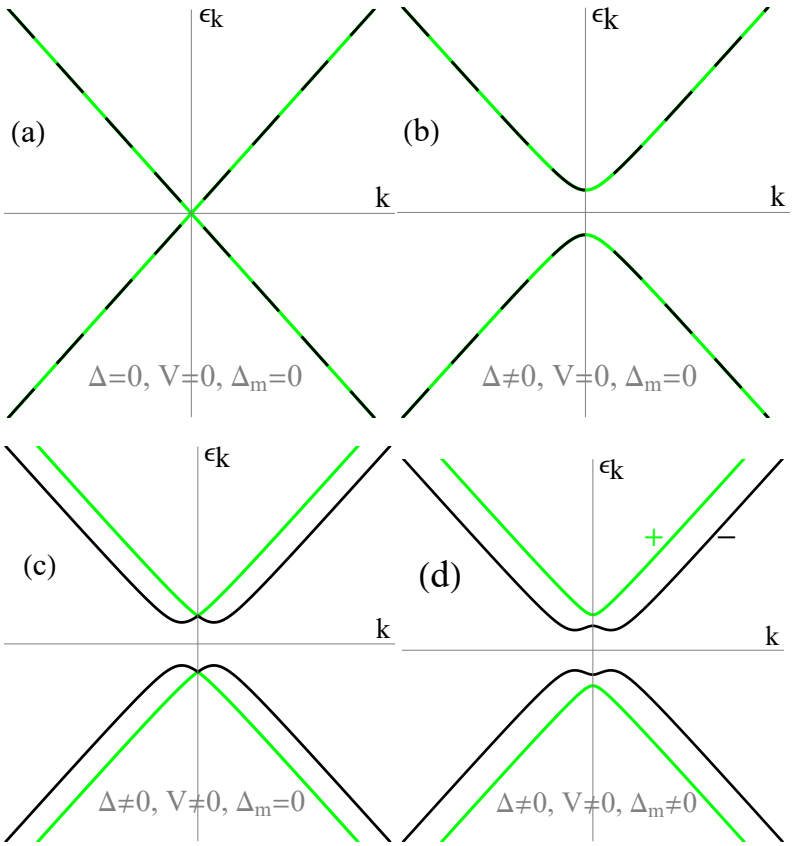

Figure 4.2: Band Structure of a 3DTI (a), TTF (b), TTF with SIA (c), and a MTF including SIA (d).

into two 2×2 blocks

$$H_0 = \begin{pmatrix} \Gamma + \Lambda & 0 & 0 & -i\eta e^{-i\phi_k} \\ 0 & -(\Gamma - \Lambda) & -i\eta e^{i\phi_k} & 0 \\ 0 & i\eta e^{-i\phi_k} & \Gamma - \Lambda & 0 \\ i\eta e^{i\phi_k} & 0 & 0 & -(\Gamma + \Lambda) \end{pmatrix}, \tag{4.2}$$

where $\eta = \alpha \cos\Theta$, $\Gamma = \sqrt{(\alpha \sin\Theta)^2 + \Delta_m^2}$, $\cos\Theta = \frac{\Delta}{\Lambda}$, and $\Lambda = \sqrt{\Delta^2 + V^2}$. The eigenstates of the Hamiltonian H_0 are

$$\psi_\mu^s = \frac{1}{\sqrt{1 + (\beta_\mu^s)^2}} \begin{pmatrix} i\ \delta_{\mu,+1}\ \beta_\mu^s \\ i\ \delta_{\mu,-1}\ \beta_\mu^s \\ \delta_{\mu,-1}\ e^{i\phi_{\boldsymbol{k}}} \\ \delta_{\mu,+1}\ e^{-i\phi_{\boldsymbol{k}}} \end{pmatrix} e^{i\boldsymbol{k}\cdot r}, \tag{4.3}$$

with corresponding eigenenergies $\varepsilon_\mu^s = s\sqrt{(\Gamma+\mu\Lambda)^2+\eta^2}$, with $\beta_\mu^s = \sqrt{\dfrac{1+\mu\gamma_\mu^s}{1-\mu\gamma_\mu^s}}$, and $\gamma_\mu^s = \dfrac{\Gamma+\mu\Lambda}{\varepsilon_\mu^s}$. The dispersion of this system consists of two bands, the outer bands labeled by $\mu = 1$ and the inner bands by $\mu = -1$, see Fig. 4.2(d). The energy gaps between the bands are $G_\pm = \Delta_m \pm \sqrt{\Delta^2+V^2}$.

4.2 Boltzmann formalism for the charge current

In the presence of a weak charge transport generating electric field, linear response theory gives

$$\boldsymbol{J} = -e\sum_{\boldsymbol{k},\mu}(f_{\boldsymbol{k}}^0 + \delta f_{\boldsymbol{k}}^\mu)\mathbf{v}_{\boldsymbol{k}}^\mu = \sigma\boldsymbol{E}, \tag{4.4}$$

where $\boldsymbol{J}$, σ and $\boldsymbol{E}$ are the current density, charge conductivity and in-plane applied electric field, respectively. The summation runs over the allowed states for electrons within all bands. $f_{\boldsymbol{k}}^0 + \delta f_{\boldsymbol{k}}^\mu$ denotes the non-equilibrium distribution function for the electrons and $f_{\boldsymbol{k}}^0$ is the Fermi-Dirac distribution function. We apply the Boltzmann equation to find $\delta f_{\boldsymbol{k}}^\mu$ for massive Dirac Fermions in a MTF in the presence of an electric field $\boldsymbol{E} = E\,(\cos\chi, \sin\chi, 0)$, see Fig. 4.1, and of dilute, point-like and randomly located magnetic impurities.

For steady states of non-interacting electrons in a spatially homogeneous system (on scales much larger than the distance between the scatterers), the Boltzmann equation reads

$$-e(-\frac{\partial f^0}{\partial\varepsilon_{\boldsymbol{k}}^\mu})\boldsymbol{E}.\mathbf{v}_{\boldsymbol{k}}^\mu = \sum_{\mu',\boldsymbol{k}'} w^{\mu\mu'}(\boldsymbol{k},\boldsymbol{k}')\left(f_{\boldsymbol{k}}^\mu - f_{\boldsymbol{k}'}^{\mu'}\right), \tag{4.5}$$

where $\mathbf{v}_{\boldsymbol{k}}^\mu = \nabla_{\boldsymbol{k}}\varepsilon_{\boldsymbol{k}}^\mu = \mathrm{v}_k^\mu(\cos\phi_{\boldsymbol{k}}, \sin\phi_{\boldsymbol{k}}, 0)$ is the band velocity of the electrons. Note that we have dropped the index s in the above expression as only the Fermi electrons contribute to the charge transport. The transition rate $w^{\mu\mu'}(\boldsymbol{k},\boldsymbol{k}')$ for the scattering of itinerant electrons from band μ and state $\boldsymbol{k}$ to band μ' and state $\boldsymbol{k}'$ within the first Born approximation is given by [58]

$$w^{\mu\mu'}(\boldsymbol{k},\boldsymbol{k}') = \frac{2\pi n_{im}}{\hbar}|\langle\boldsymbol{k},\mu|V_{sc}|\boldsymbol{k}',\mu'\rangle|^2\delta(\varepsilon_{\boldsymbol{k}}^\mu - \varepsilon_{\boldsymbol{k}'}^{\mu'}), \tag{4.6}$$

where n_{im} denotes the density of the magnetic impurities. The density of the magnetic impurities is proportional to $n_{im} \sim \frac{N_a\, x}{a^3}$, where N_a is the number of atoms per unit cell of the host material, a is the lattice constant, and x is the concentration of magnetic impurities. Taking typical values $x \sim 0.01$, $a^3 \sim 150\text{Å}^3$, and $N_a \sim 5$, we get $n_{im} \sim 10^{20}\ cm^{-3}$.

We model the interaction between an arbitrary electron located at $\boldsymbol{r}$ and a single magnetic impurity at $\boldsymbol{R}_{im}$ as $V_{sc}(\boldsymbol{r}) = J(\boldsymbol{r}-\boldsymbol{R}_{im})\boldsymbol{S}_{im}\cdot\boldsymbol{S}_e$, where $\boldsymbol{S}_e = h\sigma/2$ denotes the spin of the electron, and $\boldsymbol{S}_{im}$ is the spin of the magnetic impurities. In dilute magnetic systems, the exchange coupling takes the form $J(\boldsymbol{r}-\boldsymbol{R}_{im}) = J_0\delta(\boldsymbol{r}-\boldsymbol{R}_{im})$. Based on first-principles calculations, it has been shown that for Bi_2Te_3 lightly doped with Mn, J_0 ranges from $0.125\ meV$ to $8\ meV$ [59]. We assume that the magnetic impurities are all ordered in the same direction and each of them lies in the yz plane, $\boldsymbol{S}_{im} = S_{im}(0, \sin\theta, \cos\theta)$, as shown in Fig. 4.1.

By considering $\mathscr{H}_0$ as the base Hamiltonian, the interaction between the weak localized magnetic impurities, which act as local scatterers, and the electrons is taken into account perturbatively. Thus, we write the full Hamiltonian as

$$\mathscr{H} = \mathscr{H}_0 + \mathscr{V}_{sc}, \tag{4.7}$$

where $\mathscr{V}_{sc} = J_0\delta(\boldsymbol{r}-\boldsymbol{R}_{im})\tau_0 \otimes \boldsymbol{S}_{im}\cdot\boldsymbol{S}_e$ and τ_0 is a 2×2 unit matrix.

Under the same unitary transformation that converts $\mathscr{H}_0$ into H_0, the perturbation term $\mathscr{V}_{sc}$ converts into the following block diagonal form

$$V_{sc} = \begin{pmatrix} h_+ & 0 \\ 0 & h_- \end{pmatrix}, \tag{4.8}$$

with

$$\begin{aligned} h_\pm = {} & \pm\sin\phi_{\boldsymbol{k}}\sin\theta\Big(\cos\phi_{\boldsymbol{k}}[1-\cos\Phi] \mp \sin\Phi\cot\theta\Big)\tau_x \\ & \pm\sin\theta\Big(\cos\Phi\cos^2\phi_{\boldsymbol{k}} + \sin^2\phi_{\boldsymbol{k}} \pm \cot\theta\sin\Phi\cos\phi_{\boldsymbol{k}}\Big)\tau_y \\ & +\sin\theta\Big(\cot\theta\cos\Phi \mp \sin\Phi\cos\phi_{\boldsymbol{k}}\Big)\tau_z, \end{aligned} \tag{4.9}$$

where $\cos\Phi = \frac{\Delta_m}{\Gamma}$ and τ_i $(i = x, y, z)$ are the Pauli matrices. The full Hamiltonian in the new basis is $H = H_0 + V_{sc}$.

The scattering of massive Dirac fermions from local magnetic scatterers is highly anisotropic due to the in-plane component of the magnetic impurities. Furthermore, the SIA enhances this strong anisotropy. As a result, in order to accurately capture the anisotropic nature of electron transport, the following expression for $\delta f^{\mu}_{\boldsymbol{k}}$ is proposed [44]

$$\delta f^{\mu}_{\boldsymbol{k}} = e\frac{\partial f^0}{\partial \varepsilon^{\mu}_{k}}\, \boldsymbol{E}\, (\lambda^{\mu}_1(\boldsymbol{k})\cos\chi + \lambda^{\mu}_2(\boldsymbol{k})\sin\chi), \tag{4.10}$$

where $\lambda^{\mu}_i(\boldsymbol{k})$ are the mean free paths of electrons. Using Eq. (4.5) for both conduction subbands $\mu = \pm$, and substituting Eq. (4.10) for $\delta f^{\mu}_{\boldsymbol{k}}$, one arrives at the following set of equations

$$\begin{aligned}
&\mathrm{v}^{+}_{k}\cos(\phi_{\boldsymbol{k}}-\chi) - \sum_{\boldsymbol{k}',\mu'} w^{+\mu'}\left[\lambda^{+}_1(\boldsymbol{k}) - \lambda^{\mu'}_1(\boldsymbol{k}')\right]\cos\chi \\
&\qquad - \sum_{\boldsymbol{k}',\mu'} w^{+\mu'}\left[\lambda^{+}_2(\boldsymbol{k}) - \lambda^{\mu'}_2(\boldsymbol{k}')\right]\sin\chi = 0, \\
&\mathrm{v}^{-}_{k}\cos(\phi_{\boldsymbol{k}}-\chi) - \sum_{\boldsymbol{k}',\mu'} w^{-\mu'}\left[\lambda^{-}_1(\boldsymbol{k}) - \lambda^{\mu'}_1(\boldsymbol{k}')\right]\cos\chi \\
&\qquad - \sum_{\boldsymbol{k}',\mu'} w^{-\mu'}\left[\lambda^{-}_2(\boldsymbol{k}) - \lambda^{\mu'}_2(\boldsymbol{k}')\right]\sin\chi = 0.
\end{aligned} \tag{4.11}$$

One practical way to solve this set of equations is replacing the two unknown functions $\lambda^{\mu}_i(\boldsymbol{k})$ with their Fourier expansion $\lambda^{\mu}_i(\boldsymbol{k}) = \sum_n(\lambda^{\mu c}_{in}\cos n\phi_{\boldsymbol{k}} + \lambda^{\mu s}_{in}\sin n\phi_{\boldsymbol{k}})$, which leads to

$$\begin{aligned}
&\mathrm{v}^{+}_{k}\delta_{i,1}\cos\phi_{\boldsymbol{k}} + \mathrm{v}^{+}_{k}\delta_{i,2}\sin\phi_{\boldsymbol{k}} \\
&- \sum_{\boldsymbol{k}',\mu',n} w^{+\mu'}\left[\lambda^{+c}_{in}(\boldsymbol{k})\cos n\phi_{\boldsymbol{k}} - \lambda^{\mu' c}_{in}(\boldsymbol{k}')\cos n\phi_{\boldsymbol{k}'}\right] \\
&- \sum_{\boldsymbol{k}',\mu',n} w^{+\mu'}\left[\lambda^{+s}_{in}(\boldsymbol{k})\sin n\phi_{\boldsymbol{k}} - \lambda^{\mu' s}_{in}(\boldsymbol{k}')\sin n\phi_{\boldsymbol{k}'}\right] \\
&= 0, \\
&\mathrm{v}^{-}_{k}\delta_{i,1}\cos\phi_{\boldsymbol{k}} + \mathrm{v}^{-}_{k}\delta_{i,2}\sin\phi_{\boldsymbol{k}} \\
&- \sum_{\boldsymbol{k}',\mu',n} w^{-\mu'}\left[\lambda^{-c}_{in}(\boldsymbol{k})\cos n\phi_{\boldsymbol{k}} - \lambda^{\mu' c}_{in}(\boldsymbol{k}')\cos n\phi_{\boldsymbol{k}'}\right] \\
&- \sum_{\boldsymbol{k}',\mu',n} w^{-\mu'}\left[\lambda^{-s}_{in}(\boldsymbol{k})\sin n\phi_{\boldsymbol{k}} - \lambda^{\mu' s}_{in}(\boldsymbol{k}')\sin n\phi_{\boldsymbol{k}'}\right] \\
&= 0.
\end{aligned} \tag{4.12}$$

Solving Eqs. (4.12) gives us $\lambda_{1n}^{\mu c}$, $\lambda_{1n}^{\mu s}$, $\lambda_{2n}^{\mu c}$, $\lambda_{2n}^{\mu s}$, from which $\lambda_1^\mu(\boldsymbol{k})$ and $\lambda_2^\mu(\boldsymbol{k})$ can be obtained. Accordingly, replacing functions $\lambda_1^\mu(\boldsymbol{k})$ and $\lambda_2^\mu(\boldsymbol{k})$ in Eq. (4.10) with the obtained mean free paths yields the distribution function of the electrons $f_{\boldsymbol{k}}^\mu$. Now that we have found the distribution function of electrons residing in a particular band, the contribution of each band to the longitudinal conductivity is given by

$$\begin{aligned}\sigma_{ii}^\mu = &\frac{e^2}{AE_i}\sum_{\boldsymbol{k}} \mathbf{v}_i^\mu(k) E\ \lambda_1^\mu(\boldsymbol{k})\delta(\varepsilon_k^\mu - \varepsilon_F)\cos\chi + \\ &\frac{e^2}{AE_i}\sum_{\boldsymbol{k}} \mathbf{v}_i^\mu(k)\ E\ \lambda_2^\mu(\boldsymbol{k})\delta(\varepsilon_k^\mu - \varepsilon_F)\sin\chi,\end{aligned} \tag{4.13}$$

where $i = x, y$. Adding the contributions of both bands yields the total longitudinal conductivity, $\sigma_{ii} = \sum_\mu \sigma_{ii}^\mu$.

Note that the non-equilibrium distribution function of electrons $f_{\boldsymbol{k}}^\mu$ depends on temperature through $\frac{\partial f^0}{\partial \varepsilon_k^\mu}$. The critical temperature T_c beyond which the magnetization vanishes on the surface of a TI can be estimated using [60–62]

$$k_B T_c = \frac{S(S+1)\, a^2\, x}{6\pi\hbar^2 v_F^2} J_0^2(\varepsilon_c - \varepsilon_F), \tag{4.14}$$

where ε_c and ε_F are the cut-off energy and the Fermi energy, respectively. With the typical values $x = 0.01$, $a = 10$ Å, $\varepsilon_c = 100\ meV$, $\varepsilon_F = 80\ meV$, $S = 1$, $J_0 = 10\ meV$, and $v_F = 4 \times 10^5 ms^{-1}$, the critical temperature T_c is about $3K$. Scanning tunneling microscopy measurements in $Bi_{1.91}Mn_{0.09}Te_3$ report on magnetic ordering up to $T_c = 12$K [63]. In Ref. [63] it was also demonstrated that for temperatures below 12K, magnetic exchange interactions are very weak and Mn clusters are absent. In a different experiment on a Sb_2Te_3 tetradymite structure doped with low concentrations of vanadium, $T_c \sim 10$K was measured [64]. The critical temperature of the systems to which our present formalism applies is thus of the order of $10K$. To obtain analytical relations, we perform our calculations at zero temperature and approximate $\frac{\partial f^0}{\partial \varepsilon_k^\mu}$ with the Dirac delta function $\delta(\varepsilon_k^\mu - \varepsilon_F)$, as done in Eq. (4.13).

We emphasize that the terms beyond the first Born approximation are not taken into account, as well as the effect of non-zero Berry curvature, because it is only responsible for the anomalous Hall effect.

4.3 Results

We present our results in two subsections. In Sec. 4.3.1, we assume that only the band $\mu = -1$ is filled and contributes to the conductivity. In Sec. 4.3.2, both bands $\mu = \pm$ are filled with electrons and both are involved in the charge transport. Since a MTF possesses completely distinctive features in these two regimes, we present them separately.

4.3.1 Single-subband regime

In this section we assume that the Fermi level is such that only the conduction subband labeled with $\mu = -1$, shown in Fig. 4.2d, is filled with electrons and contributes to the charge transport. First, we find the T-matrix associated with the intra-subband scatterings, $T^{--}(\boldsymbol{k},\boldsymbol{k}') = \langle\, \boldsymbol{k},\mu=-1|\mathcal{V}_{sc}|\boldsymbol{k}',\mu'=-1\rangle$, which determines the scattering amplitude between two eigenstates of the Hamiltonian H_0, $|\boldsymbol{k},\mu=-1\rangle$ and $|\boldsymbol{k}',\mu'=-1\rangle$. Using Eqs. (4.3), (4.6), and (4.9), we obtain

$$\begin{aligned}|\bar{T}^{--}|^2 =& \frac{\sin^2\theta}{(1+\beta_-^2)^2}\Big(\xi_-^2\cot^2\theta(1+\beta_-^4-2\,\beta_-^2\cos\delta\phi)\\ &-(\xi_-^2-1)(1+\beta_-^4+2\,\beta_-^2\cos\delta\phi)\cos^2\phi_{\boldsymbol{k}}\\ &-2\xi_-\sqrt{1-\xi_-^2}\,(\beta_-^4-1)\cot\theta\cos\phi_{\boldsymbol{k}}\Big),\end{aligned} \tag{4.15}$$

where $\delta\phi = \phi_{\boldsymbol{k}} - \phi_{\boldsymbol{k}'}$, $\xi_- = \dfrac{\Delta_m\Lambda}{\sqrt{\Delta^2\Delta_m^2 + V^2\left((\varepsilon_{\boldsymbol{k}}^-)^2-\Delta^2\right)}+V^2}$, and $|\bar{T}^{--}(\boldsymbol{k},\boldsymbol{k}')|^2 = \frac{|T^{--}(\boldsymbol{k},\boldsymbol{k}')|^2}{J_0^2 S_{im}^2 n_{im}}$. Then, Eq. (4.6), yields the transition rate for intra-subband scatterings $w^{--}(\boldsymbol{k},\boldsymbol{k}') = \frac{2\pi}{\hbar}|T^{--}(\boldsymbol{k},\boldsymbol{k}')|^2\delta(\varepsilon_{\boldsymbol{k}}^- - \varepsilon_{\boldsymbol{k}'}^-)$. With this transition rate for the Fermi electrons in the single-subband regime, we use the numerical results obtained from Eqs. (4.12) in Eq. (4.13) to compute the charge conductivity. Fig. 4.3 presents the two dimensionless longitudinal components of the resistivity, ρ_{xx}/ρ_0 and ρ_{yy}/ρ_0, with $\rho_0 = \dfrac{1}{\sigma_0} = \dfrac{n_{im}S_{im}^2J_0^2}{\hbar^2 v_F^2}\dfrac{h}{e^2}$. Note that ρ_{xx}/ρ_0 and ρ_{yy}/ρ_0, both are independent of J_0, n_{im} and v_F.

First we consider a free-standing MTF, i.e. without SIA ($V = 0$). As the red curves in Figs. 4.3(a) and 4.3(c) show, both components of the longitudinal

resistivity vanish in such a free-standing MTF, when all the magnetic impurities are in-plane, i.e. $\theta = \pi/2$, and regardless of the direction of the in-plane external electric field. For a free-standing MTF, Eq. (4.15) becomes

$$|\bar{T}^{--}|^2(V=0) = \frac{\cos^2\theta}{(1+\beta_-^2)^2}(1+\beta_-^4 - 2\,\beta_-^2\cos\delta\phi), \tag{4.16}$$

and consequently, Fermi electrons do not undergo any scattering when $\theta = \pi/2$, and remain forever in their host subband. As a result, the charge current is dissipationless, $\rho_{xx}(V=0) = \rho_{yy}(V=0) = 0$.

By breaking the inversion symmetry with the emergence of V, ρ_{xx}/ρ_0 becomes non-zero for $\theta = \pi/2$, while ρ_{yy}/ρ_0 remains zero, as shown by the red curves in Figs. 4.3(b) and 4.3(d). To find the underlying fact behind this exotic feature of a MTF with SIA, we check the transition selection rule induced by the in-plane magnetic impurities. For this purpose, we first explain why the charge current in the single-subband regime of a free standing MTF is dissipationless when the magnetic impurities are in-plane. Following that, we investigate how the inversion symmetry breaking affects the current transition selection rule.

Since the transition selection rule in a free-standing MTF can be well explained in the spin-chirality space, we map the Hamiltonian $\mathscr{H}_0$, given by Eq. (4.1), into this space. Under the unitary transformation $U\mathscr{H}_0U^\dagger$, $\mathscr{H}_0$ transforms into

$$\mathscr{H}'_0 = U\mathscr{H}_0U^\dagger = \begin{pmatrix} h'_+ & V\sigma_x \\ V\sigma_x & h'_- \end{pmatrix}, \tag{4.17}$$

with

$$U = \begin{pmatrix} 1 & 0 & 0 & 0 \\ 0 & 1 & 0 & 0 \\ 0 & 0 & 0 & 1 \\ 0 & 0 & 1 & 0 \end{pmatrix}, \tag{4.18}$$

and $h'_\nu = \hbar v_F(k_y\sigma_x - \nu k_x\sigma_y) + (\Delta + \nu\Delta_m)\sigma_z$. $\nu = \pm 1$ are the eigenvalues of the chirality operator defined as

$$C = \sigma_0 \otimes \tau_z = \begin{pmatrix} 1 & 0 & 0 & 0 \\ 0 & 1 & 0 & 0 \\ 0 & 0 & -1 & 0 \\ 0 & 0 & 0 & -1 \end{pmatrix}. \tag{4.19}$$

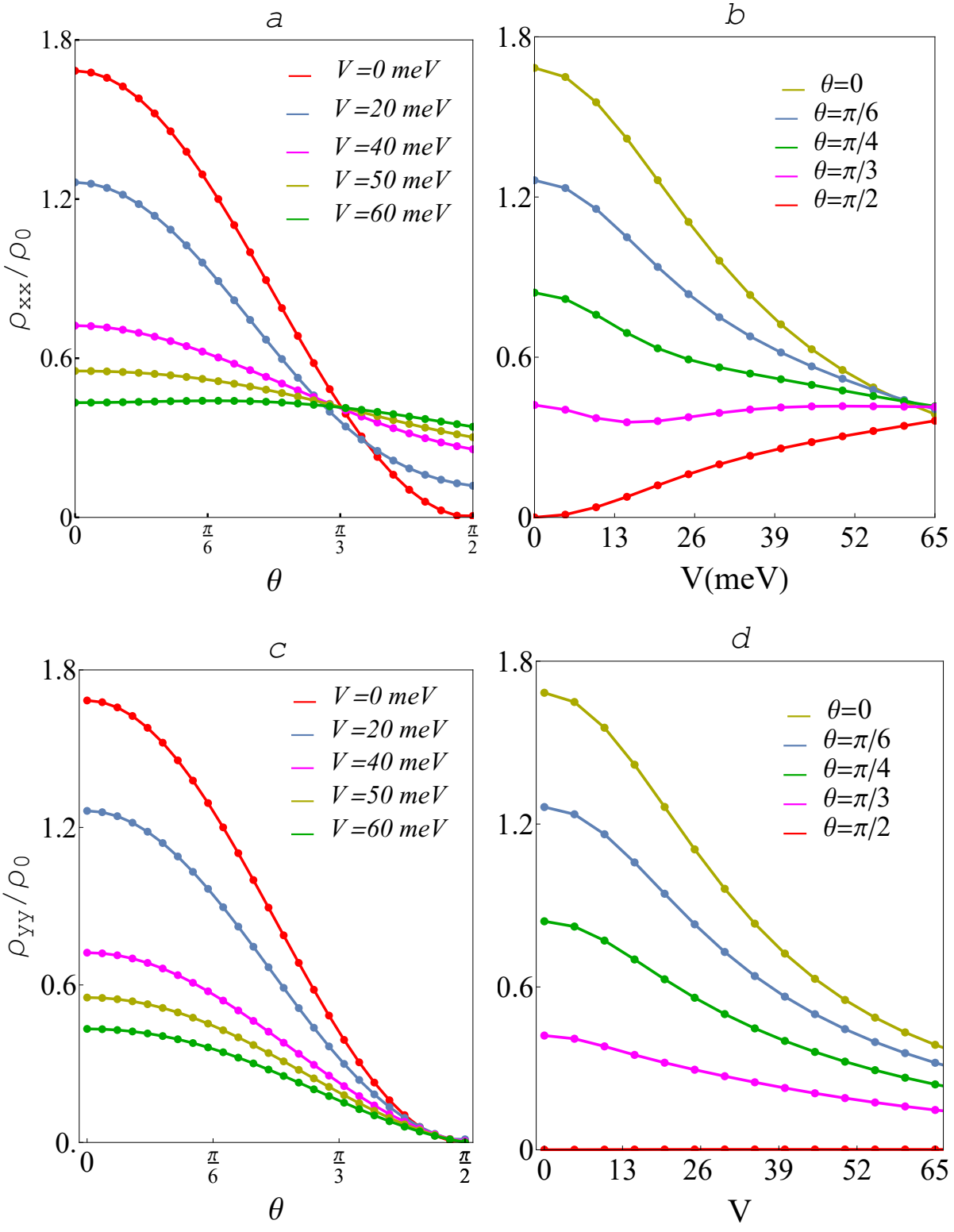

Figure 4.3: The resistivity of a MTF with SIA in the single-subband regime, for $\Delta = 69\ meV$, $\Delta_m = 40\ meV$, and $\varepsilon_F = 100\ meV$, against θ and V. Panels (a) and (b) correspond to the resistivity of the system when the in-plane external electric field is perpendicular to the plane of the magnetic impurities, and panels (c) and (d) show the resistivity when the in-plane external electric field is parallel to the plane of the magnetic impurities.

For a free-standing MTF (i.e. without SIA), $[\mathscr{H}'_0, C] = 0$. Therefore, the two subbands of the system have distinctive chirality values, for the lower energy conduction subband $\nu = -1$, and for the higher energy conduction subband $\nu = +1$. In the same way, for the case of $\theta = \pi/2$, $\mathscr{V}_{sc}$ transforms into

$$\mathscr{V}'_{sc} = U\mathscr{V}_{sc}U^{\dagger} = J_0 S_{im}\delta(\boldsymbol{r} - \boldsymbol{R}_{im})\begin{pmatrix} 0 & -i\,\sigma_z \\ i\,\sigma_z & 0 \end{pmatrix}. \tag{4.20}$$

Considering Eqs. (4.19) and (4.20), $[C, \mathscr{V}'_{sc}] \neq 0$. Consequently, when all the magnetic impurities lie in-plane, $\theta = \frac{\pi}{2}$, the only allowed scatterings are those in which the chirality of electrons is not preserved. However, in the single-subband regime, such inter-subband scatterings would not respect the conservation of energy and therefore are forbidden. This finding corresponds with Eq. (4.16), in which $|\bar{T}^{--}|^2(\theta = \pi/2) = 0$. As a consequence, $\rho_{xx}[V = 0, \theta = \pi/2] = \rho_{yy}[V = 0, \theta = \pi/2] = 0$.

For a MTF with SIA, $V \neq 0$ and following Eqs. (4.17) and (4.19) yields $[C, \mathscr{H}'_0] \neq 0$, indicating a subband with a mixture of different chiralities. Consequently, the in-plane magnetic impurities can not block all the scattering channels within the $\mu = -1$ band anymore. However, by checking the transition rate of the electrons, Eq. (4.15), we realize that $|\bar{T}^{--}|^2[\theta = \pi/2] \sim \cos\phi_{\boldsymbol{k}}$, implying that this transition rate stays zero for all the charge carriers with $\phi_{\boldsymbol{k}} = 3\pi/2$ and these electrons still do no undergo any scattering. $\phi_{\boldsymbol{k}} = 3\pi/2$ corresponds to the direction of the charge current when the in-plane external electric field is along the y direction, which explains the dissipationless current $(\rho_{yy}/\rho_0)[\theta = \pi/2] = 0$ for all values of V, as shown in Figs. 4.3(c) and 4.3(d).

It is also insightful to study the role of the mean free path of the electrons in these results. Hence, we calculate the dimensionless effective mean free path of electrons defined as $\lambda_1/\lambda_0 = \lambda^{-c}_{1,1}/\lambda_0$, and $\lambda_2/\lambda_0 = \frac{\lambda^{-s}_{2,1}}{\lambda_0}$, with $\lambda_0 = \frac{\hbar^3 v_F^3}{n_{\rm im} J_0^2 S_{im}^2}$ using the numerical results obtained from Eqs. (4.12).

As expected from the transition selection rule, the numerical result for the effective mean free paths of the electrons diverges at $\theta = \pi/2$ in Fig. 4.4, when the inversion symmetry is conserved. When the external electric field is applied along the x direction, the mean free paths of the electrons become finite by breaking the inversion symmetry, $V \neq 0$, whatever the value of θ, as

shown in Fig. 4.4(a). However, when $V \neq 0$ and the electric field is along the y direction, Fig. 4.4(c) shows still infinite values for the mean free paths of the electrons at $\theta = \pi/2$.

Figs. 4.4(a) and 4.4(c) show that the mean free paths of the electrons increase with increasing θ, for any given value of V and regardless of the direction of the electric field. Combining this with the fact that the velocity of electrons is independent of θ, it explains why the resistivity in Figs. 4.3(a) and 4.3(c) decreases with increasing θ.

When the external electric field is exerted along the y direction, the mean free paths of the electrons, as shown in Fig. 4.4(d), increases against V. On the contrary, as V increases, the velocity of the electrons decreases, see Fig. 4.5. In other words, even though the SIA (causing V to differ from zero) makes electrons travel longer before being scattered off the magnetic impurities, it slows them down in this single-subband regime. Eventually the effect of the substrate on the mean free path of the electrons dominates, and the resistivity of the system decreases with increasing V, as shown in Fig. 4.3(d). The situation is different when the electric field is perpendicular to the plane of the magnetic impurities, thus in the x direction. In this case, the mean free paths of the electrons can show an increasing as well as a decreasing trend with respect to V, depending on the spatial orientation of the magnetic impurities. Consequently, the resistivity of a MTF with SIA can decrease or increase due to the substrate, as shown in Fig. 4.3(b).

4.3.2 Two-subband regime

In this regime, the Fermi level is positioned such that both bands $\mu = \pm$ contribute to the charge transport in the MTF. Contrary to the single-subband regime, charge carriers undergo not only intra-subband but also inter-subband scatterings in the two-subband regime. Hence, in what follows, we investigate the probability of both scattering types. Based upon Eqs. (4.3), (4.6), and (4.9), the probabilities for intra-subband and inter-subband scattering are respectively given by

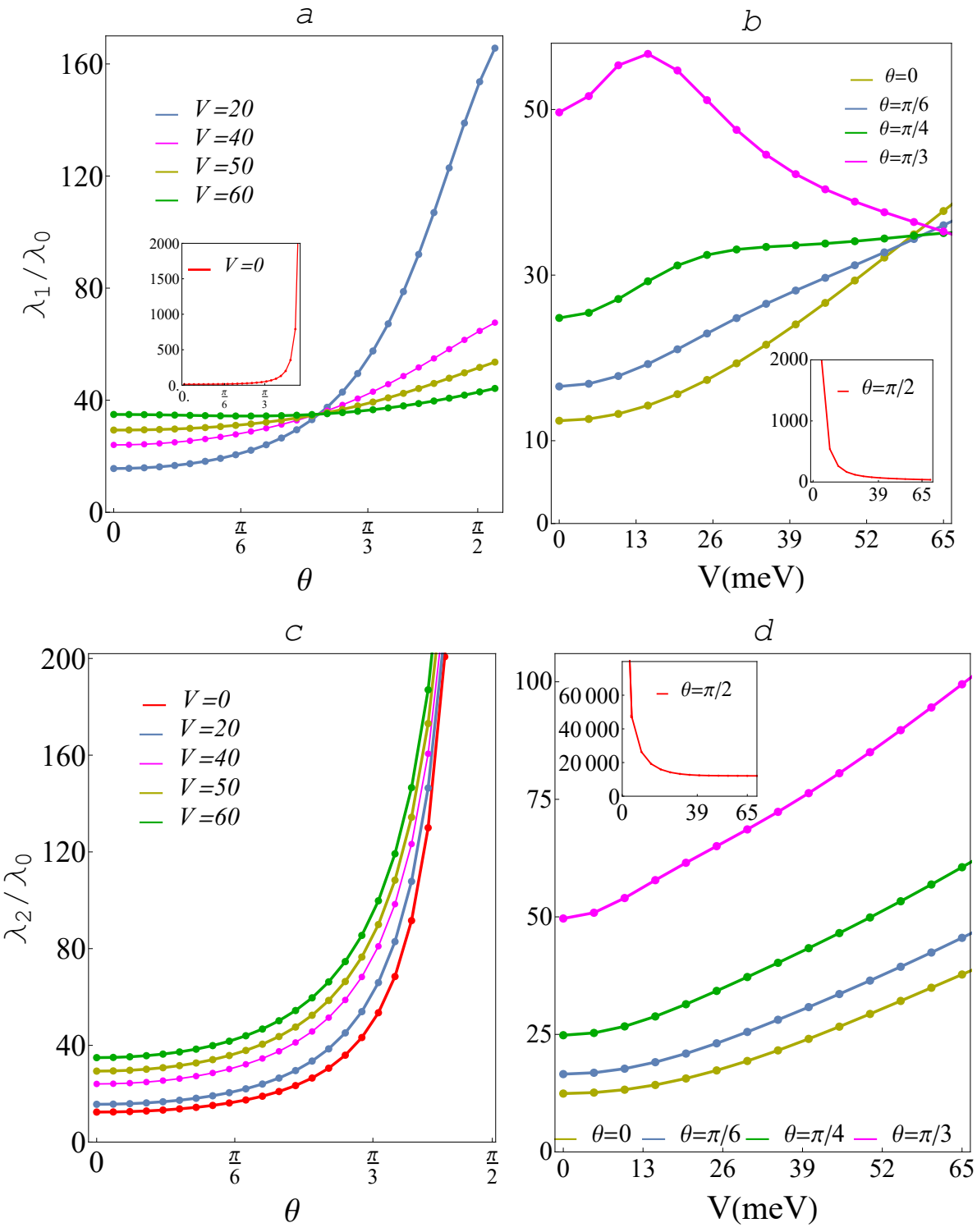

Figure 4.4: The mean free paths of the electrons in the single-subband regime, in terms of θ and V when $\Delta = 69\ meV$, $\Delta_m = 40\ meV$, and $\varepsilon_F = 100\ meV$. Panels (a) and (b) correspond to the system in which the external electric field is perpendicular to the plane of the magnetic impurities (the x direction), and panels (c) and (d) show the mean free paths of the electrons when the electric filed is parallel to the plane of the magnetic impurities (the y direction).

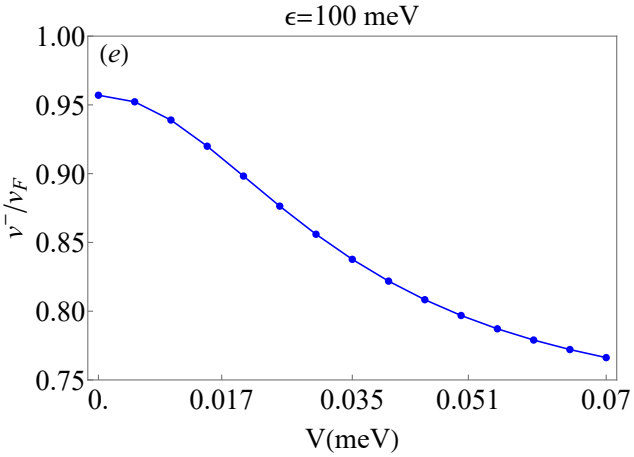

Figure 4.5: The velocity of the electrons against V.

$$
\begin{aligned}
|\bar{T}^{\mu\mu}|^2 = \frac{\sin^2\theta}{(1+\beta_\mu^2)^2} \times \Bigg(& \left[\xi_\mu^2 \cot^2\theta (1+\beta_\mu^4 - 2\,\beta_\mu^2 \cos\delta\phi)\right] \\
& - \left[(\xi_\mu^2 - 1)(1+\beta_\mu^4 + 2\,\beta_\mu^2 \cos\delta\phi)\cos^2\phi_{\boldsymbol{k}}\right] \\
& - \left[2\xi_\mu \sqrt{1-\xi_\mu^2}\,(\beta_\mu^4 - 1)\cot\theta\cos\phi_{\boldsymbol{k}}\right]\Bigg),
\end{aligned}
\tag{4.21}
$$

$$
\begin{aligned}
|\bar{T}^{\mu\mu'}|^2 = & \frac{\sin^2\theta}{2(\beta_\mu^2+1)(\beta_{\mu'}^2+1)} \times \\
& \Bigg(\beta_\mu\beta_{\mu'}\Big[[\xi_\mu+1]^2\cos(\phi_{\boldsymbol{k}'}+\phi_{\boldsymbol{k}}) - (\xi_\mu^2-1)\cos(\phi_{\boldsymbol{k}'}+3\phi_{\boldsymbol{k}}) + [\xi_\mu-1]^2\cos(\phi_{\boldsymbol{k}'}+5\phi_{\boldsymbol{k}})\Big] \\
& - \Big[4(1-\beta_\mu^2\beta_{\mu'}^2)\xi_\mu\sqrt{1-\xi_\mu^2}\cos\phi_{\boldsymbol{k}}\cot\theta + 2(1+\beta_\mu^2\beta_{\mu'}^2)[1-\xi_\mu^2]\cot^2\theta\Big] \\
& + \Big[(1+\beta_\mu^2\beta_{\mu'}^2)\Big(1+\xi_\mu^2+[\xi_\mu^2-1]\cos 2\phi_{\boldsymbol{k}}\Big)\Big]\Bigg),
\end{aligned}
\tag{4.22}
$$

where $|\bar{T}^{\mu\mu'}(\boldsymbol{k},\boldsymbol{k}')|^2 = \frac{|T^{\mu\mu'}(\boldsymbol{k},\boldsymbol{k}')|^2}{J_0^2 S_{im}^2 n_{im}}$, and $\xi_\mu = \frac{\Delta_m \Lambda}{\sqrt{\Delta^2\Delta_m^2 + V^2\left((\varepsilon_{\boldsymbol{k}}^\mu)^2 - \Delta^2\right)} + \mu V^2}$. For a free standing MTF, Eq. (4.21) that deals with intra-subband scattering in the two-subband regime, becomes

$$
|\bar{T}^{\mu\mu}|^2(V=0) = \frac{\cos^2\theta}{(1+\beta_\mu^2)^2}(1+\beta_\mu^4 - 2\,\beta_\mu^2\cos\delta\phi),
\tag{4.23}
$$

which indicates that this type of scattering is isotropic. We can conclude that the SIA makes the probability of the intra-subband scatterings strongly

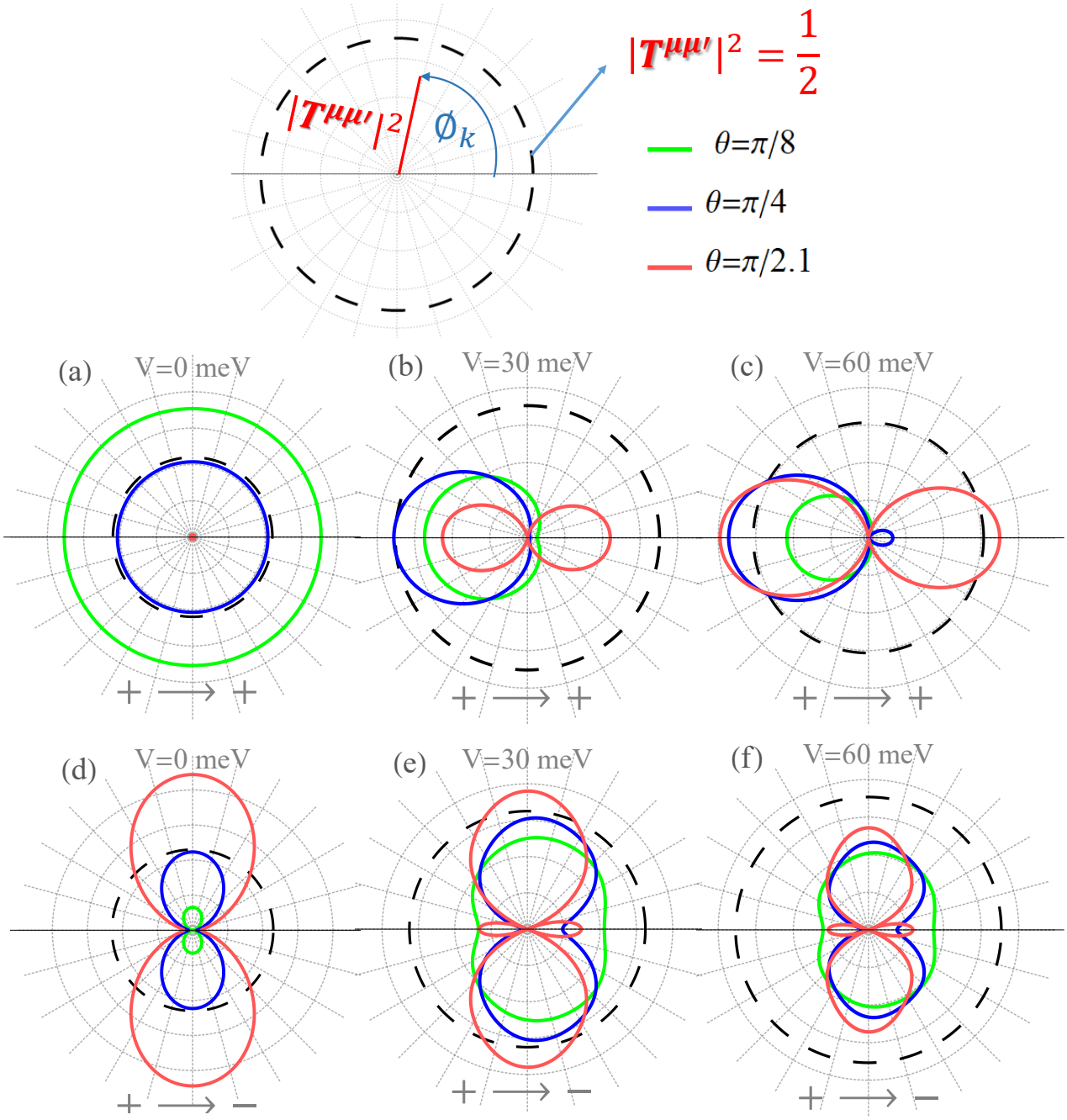

Figure 4.6: The probability of intra-subband back-scattering (a-c), and inter-subband back-scatterings (d-f), when $\varepsilon_F = 300\ meV$, $\Delta = 69\ meV$, $\Delta_m = 40\ meV$.

dependent on the direction of an electron, $\phi_{\boldsymbol{k}}$. As an example, for the case of intra-subband back-scatterings, $|\bar{T}^{++}|^2$ is shown in panels $a-c$ of Fig. 4.6, with respect to $\phi_{\boldsymbol{k}}$ for some values of θ. As panel a demonstrates, the probability of a certain intra-subband back-scattering is constant with respect to $\phi_{\boldsymbol{k}}$, and decreases by increasing θ, regardless of the value of $\phi_{\boldsymbol{k}}$. However, the

substrate changes this specific behavior of the probability of back-scatterings against θ. In other words, depending on the direction of the electrons and the value of V, increasing the value of θ can increase or decrease the value of the back-scattering probability in the intra-subband transitions.

For a free-standing MTF, the probability for the inter-subband transitions given by Eq. (4.22), converts to

$$|\bar{T}^{\mu\mu'}|^2(V=0) = \frac{\sin^2\theta}{(\beta_\mu^2+1)(\beta_{\mu'}^2+1)}\Big(1+\beta_\mu^2\beta_{\mu'}^2+2\beta_\mu\beta_{\mu'}\cos(\phi_{\boldsymbol{k}'}+\phi_{\boldsymbol{k}})\Big). \tag{4.24}$$

The above equation specifies that the inter-subband scatterings are anisotropic even in the absence of SIA. Following Eq. (4.22), SIA further enhances the degree of anisotropy for this type of scatterings. As an example, $|\bar{T}^{+-}|^2$ is depicted in panels $d-f$ of Fig. 4.6 for inter-subband backscatterings. These panels demonstrate that the probability of the inter-subband back-scatterings does not have a constant trend against θ. Depending on the value of V, altering the spatial orientation of the magnetic impurities can enhance or reduce the probability for a specific inter-subband back-scattering. This finding can also be proven for all other possible inter-subband transitions.

We can conclude that the probability of all possible transitions in a MTF with SIA is highly sensitive to the initial direction of the electrons, $\phi_{\boldsymbol{k}}$. Since the direction of charge carriers is coupled to the direction of the in-plane external electric field, the charge transport will be strongly dependent on this direction of the applied electric field. Moreover, the impact of a particular spatial ordering of the magnetic impurities on the scattering rate of electrons can be controlled by the substrate (or a gate voltage). Therefore we can anticipate that this exciting feature will manifest itself in the macroscopic transport properties like the mean free path of the charge carriers and charge conductivity of the system.

Based on the numerical results obtained form Eqs. (4.12), we compute the dimensionless effective mean free paths of the electrons defined as $\lambda_1^\mu/\lambda_0 = \lambda_{1,1}^{\mu c}/\lambda_0$, and $\lambda_2^\mu/\lambda_0 = \lambda_{2,1}^{\mu s}/\lambda_0$, with $\lambda_0 = \frac{\hbar^3 v_F^3}{n_{\rm im} J_0^2 S_{im}^2}$. When the external electric field is applied along the x direction, the obtained numerical mean free paths for both bands are shown against θ in Figs. 4.7(a) and 4.7(c), and in terms of V in Figs. 4.7(b) and 4.7(d). As Figs. 4.7(b) and 4.7(d) show, depending on

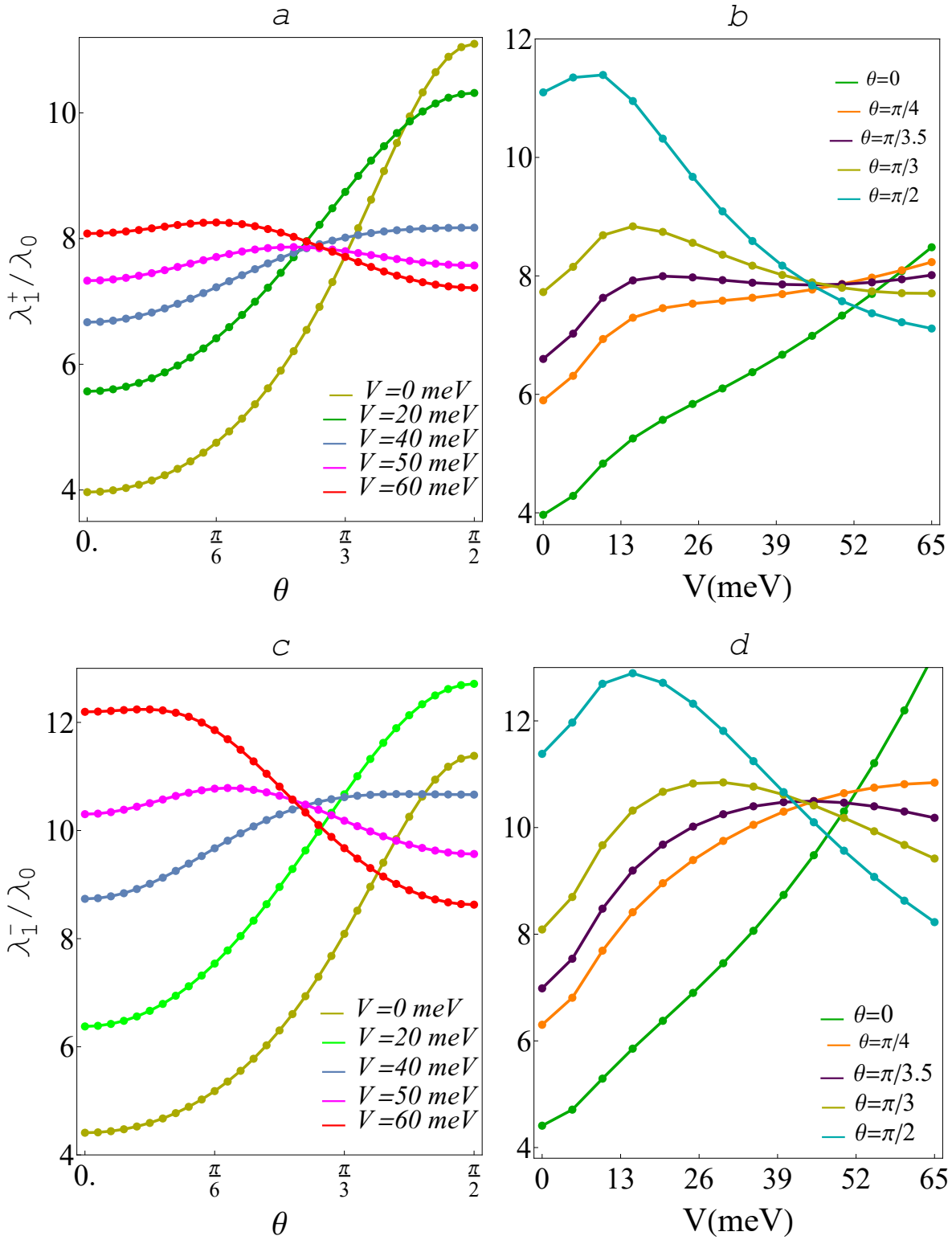

Figure 4.7: Mean free paths of the Fermi electrons residing in bands $\mu = \pm$ moving along the x direction versus θ (a, c), and V (b, d), when $\Delta = 69\ meV$, $\Delta_m = 40\ meV$, and $\varepsilon_F = 300\ meV$.

the spatial ordering of the magnetic impurities, increasing V can increase or decrease the average distance which electrons travel before being scattered by the magnetic impurities. For example, when the magnetic impurities all are aligned perpendicular to the surface of the MTF, $\theta = 0$, if V increases the mean free path of electrons will always increase, see the green curves in Figs. 4.7(b) and 4.7(d). In contrary, when all the magnetic impurities are in-plane, $\theta = \pi/2$, the average travel distance of electrons during different scattering events will decrease as V increases (see the cyan curves in Figs. 4.7(b) and 4.7(d)).

Figs. 4.7(a) and 4.7(c) also show that, in a free-standing MTF ($V = 0$), varying the spatial orientation of the magnetic impurities from $\theta = 0$ to $\theta = \pi/2$ causes the electrons to travel further before being scattered. However, the emergence of the SIA drastically changes this trend. For example, as the red curves in Fig. 4.7(a) and 4.7(c) show, for some particular value of V, increasing θ from 0 to $\pi/2$, causes electrons in both bands to travel shorter distances during their relaxation time. Therefore, the value of V can be adjusted to keep the mean free paths of the electron nearly independent of the spatial ordering of the magnetic impurities.

Moreover, Fig. 4.8 shows that for small values of V, the SIA slightly increases the velocity of electrons in subband +, though slows down a bit the flow of electrons arising from subband −. For larger values of V, the velocity of electrons in both subbands cannot be altered by changing V. In general, the substrate has a negligible effect on the velocity of electrons.

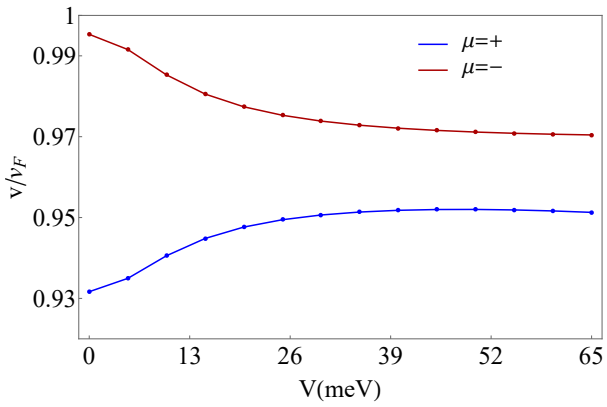

Figure 4.8: Velocity of electrons in a MTF versus the SIA potential V.

Following Eq. (4.13), the substrate can control the contribution of each

band in the total conductivity by the velocity of the electrons and their mean free path. As we already discussed, the SIA potential V has a negligible effect on the velocity of electrons in each band. Therefore, it is expected that the conductivity of the system is only determined by the mean free path of the electrons with respect to θ and V. In what follows, we will verify this expectation first for the conductivity in the x direction.

By using Eq. (4.13), we add up the contribution of each subband to obtain the total conductivity of the system. For the case where the external electric field is perpendicular to the plane of the magnetic impurities (x direction), the dimensionless quantity σ_{xx}/σ_0 is shown in Figs. 4.9(a) and 4.9(b), in terms of V and θ, respectively. As shown in Fig. 4.9(a), the trend of σ_{xx}/σ_0 against V, can be strictly upward, almost independent of V, or downward, depending on the spatial ordering of the magnetic impurities. The yellow and green curves in Fig. 4.9(a) show that when the in-plane component of the magnetic impurities is small, σ_{xx}/σ_0 has a strictly upward trend against V. On the contrary, when the in-plane component of the magnetic impurities is significant, the charge conductivity has a decreasing trend against the substrate potential. Furthermore, if the magnetic impurities are properly aligned, the σ_{xx}/σ_0 is almost insensitive to the substrate potential, particularly for large values of the SIA potential.

As in a free-standing MTF θ rises from 0 to $\pi/2$, σ_{xx}/σ_0 rises steeply, as shown by the yellow curve in Fig. 4.9(b). In an MTF with SIA, the substrate, on the other hand, has the ability to significantly moderate this trend toward θ. As shown by the red curve in Fig. 4.9(b), for large values of V, conductivity decreases by rising θ, which is in total contrast to the behavior of charge conductivity in a free-standing MTF (the yellow curve).

When the external electric field is applied in the y direction, the mean free path of electrons for both subbands is given in terms of θ in Figs. 4.10(a) and 4.10(c), and in terms of V in Figs. 4.10(b) and 4.10(d). In contrast to the mean free path of the electrons shown in Figs. 4.7(b) and 4.7(d), Figs. 4.10(b), 4.10(d) demonstrate that the mean free paths of electrons in all subbands always increase due to the SIA, regardless of the spatial ordering of the magnetic impurities. In addition, the yellow curves in Figs. 4.10(a), 4.10(c)

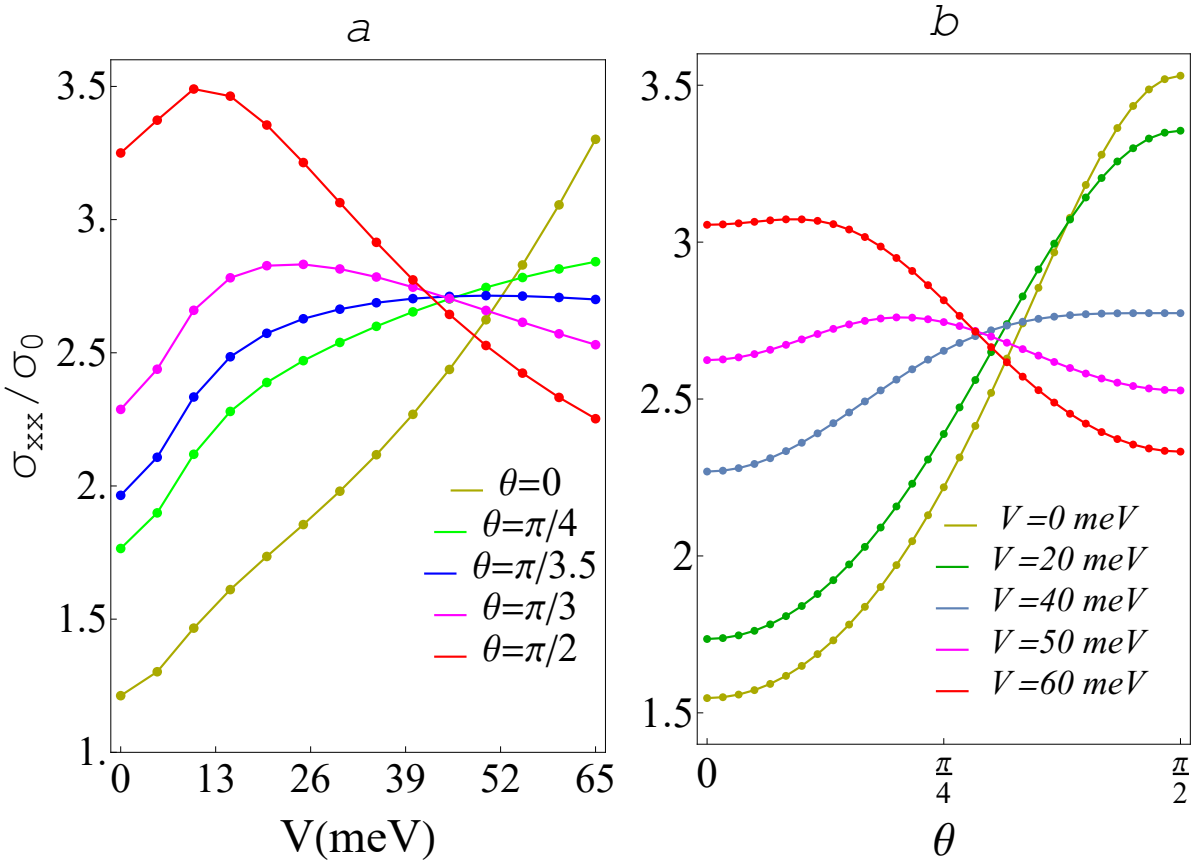

Figure 4.9: Longitudinal conductivity of a MTF in the two-subband regime along the x direction in terms of V (a) and θ (b), for $\Delta = 69\ meV$, $\Delta_m = 40\ meV$, and $\varepsilon_F = 300\ meV$.

demonstrate that the mean free path of electrons in a free-standing MTF ($V = 0$), is constant for all of θ. This is also valid for the electrons in the "–" band of a MTF with SIA, as shown by the blue and green curves in Fig 4.10(c). However, when the SIA potential is significant, by increasing θ, electrons travel shorter distances during their relaxation time in both subbands, as demonstrated by the red curves in Figs. 4.10(a) and 4.10(c).

Considering that the SIA has a negligible effect on the velocity of electrons, we can again anticipate that the longitudinal conductivity along the y direction will follow the same trend as observed for the mean free path of electrons in Fig. 4.10. We take into account the contribution of both bands in the total charge conductivity of a MTF with SIA by using Eq. (4.13). Fig. 4.11 shows the final result of dimensionless conductivity σ_{yy}/σ_0. The observed conductivity has the same trend as found for the mean free path of electrons, as predicted.

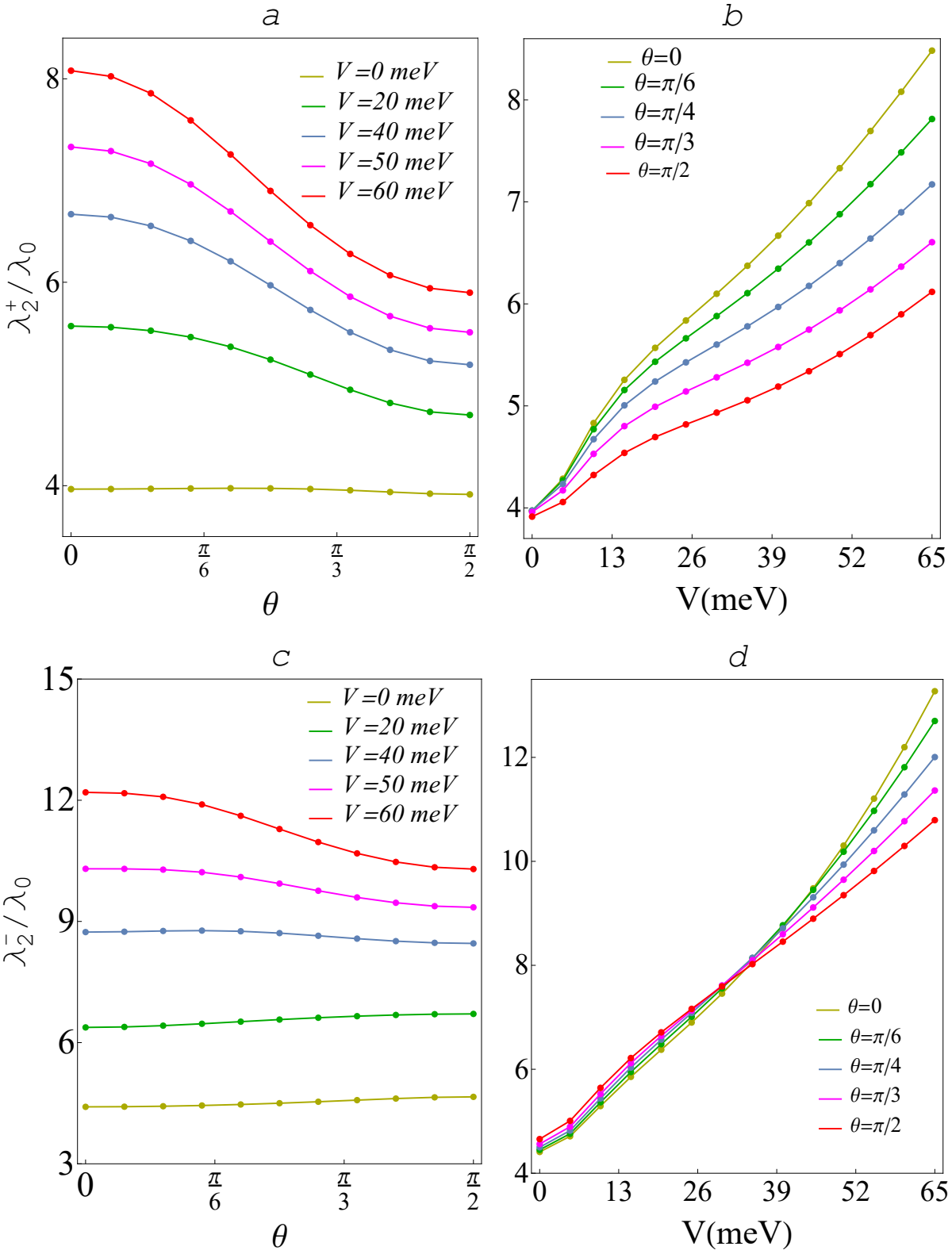

Figure 4.10: Mean free paths of the electrons residing in bands $\mu = \pm$ moving along y direction versus θ (a, c), and V (b, d), if $\Delta = 69\ meV$, $\Delta_m = 40\ meV$, and $\varepsilon_F = 300\ meV$.

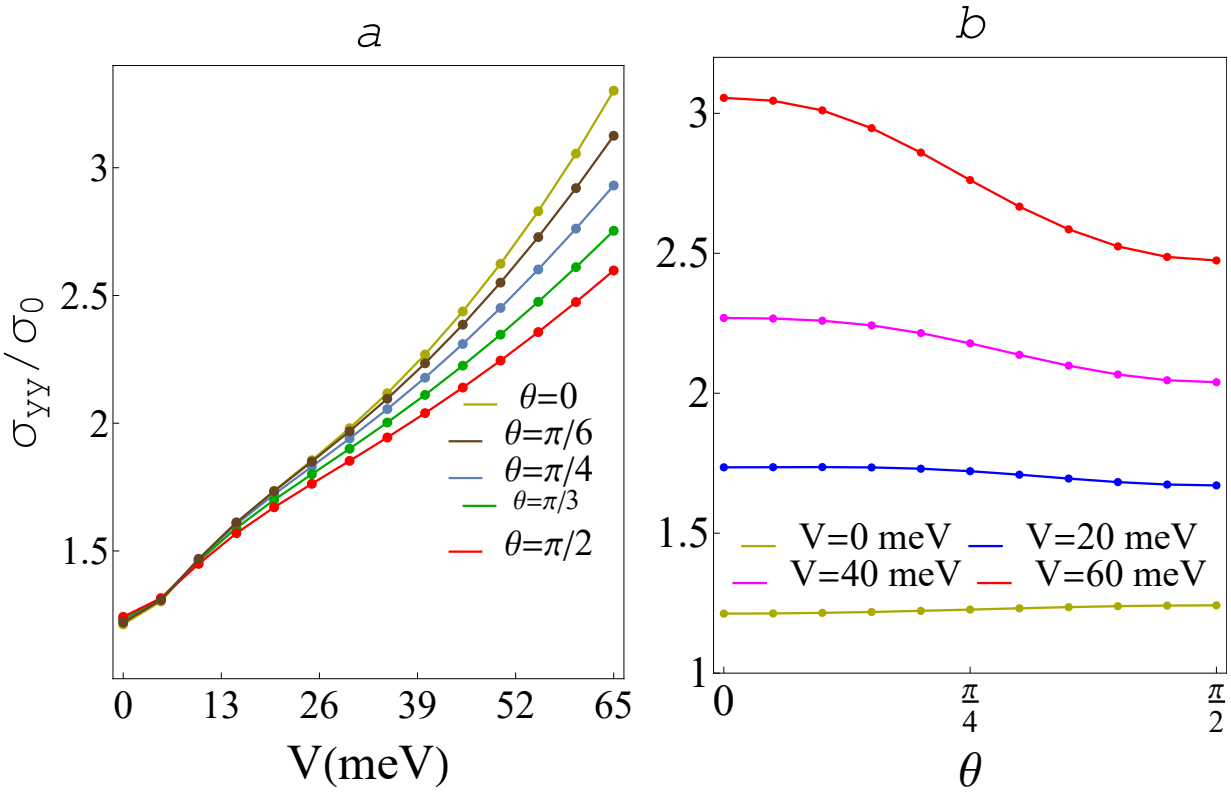

Figure 4.11: Longitudinal conductivity of a MTF with SIA in the two-subband regime along the y direction in terms of V (a) and θ (b), for $\Delta = 69\ meV$, $\Delta_m = 40\ meV$, and $\varepsilon_F = 300\ meV$.

In other words, as shown in Fig. 4.11(a), SIA always enhances σ_{yy}/σ_0 in a MTF, regardless of the spatial orientation of the magnetic impurities. Also, when the SIA potential is insignificant, the longitudinal conductivity along the y direction is almost independent of the spatial ordering of the magnetic impurities, as shown by the yellow and blue curves in Fig. 4.11(b). When the values of the SIA potential is significant, increasing the in-plane component of the magnetic impurities reduces the charge conductivity along the y direction.

As a result, we can conclude that the substrate or gate voltage can only affect the effect of magnetic impurities on charge transport when the applied electric field is directed in the x direction.

To explain why the substrate (or gate voltage) can not control the magnetic impurities' effect on the charge current when the electric field is along the y direction, the spin expectation values of the electrons are considered. The spin expectation values of the effective components of electron's spin S_y and

S_z are given by

$$\langle S_z^\mu \rangle = \mu \frac{\Delta_m(\Delta^2+\zeta)}{\varepsilon_{\boldsymbol{k}}^\mu \zeta}, \tag{4.25}$$

$$\langle S_y^\mu \rangle = -\mu \sqrt{1-\frac{\Delta_m^2(\Delta^2+V^2)}{\zeta}}\cos\phi_{\boldsymbol{k}}, \tag{4.26}$$

where $\zeta = -\mu V^2 + \sqrt{\Delta^2(\Delta_m^2 - V^2) + (V\varepsilon_{\boldsymbol{k}}^\mu)^2}$. According to Eq. 4.26, $\langle S_y^\mu \rangle$ is clearly sensitive to the direction of the in-plane external electric field. When the external electric field is applied in the y direction, the main contribution to the charge current comes from the electrons with $\phi_{\boldsymbol{k}} = \frac{3\pi}{2}$. Then, based on Eq. (4.26), $\langle S_y^\mu \rangle = 0$. Therefore, the SIA potential can only alter the strength of the interaction between magnetic impurities and electrons through S_z^μ. However, this is not the case when the external electric field is applied in the x direction. For this case, both effective components of the electron's spin are non-zero, and so the SIA potential has more degrees of freedom to influence the interaction between the electrons and magnetic impurities. As a result, the SIA can strongly influence the response of the charge conductivity to the spatial orientation of the magnetic impurities, as shown in Figs. 4.9(b) and 4.9(b). A large value of the SIA potential can even reverse the trend of $\sigma_{xx}[\theta]$ from strictly increasing to decreasing.

4.4 Conclusions

In summary, using the Boltzmann semiclassical formalism and a modified relaxation time scheme we investigated the charge transport in magnetic topological ultra-thin films subjected to structural inversion asymmetry and for general orientations of the magnetic impurities. We analytically derived the scattering rates for all possible intra- and inter-subband transitions and discussed the calculated conductivities in terms of the mean free path of electrons and their velocity.

Depending on the number of conduction subbands involved in the charge transport, two different transport regimes are realized. When the electrons occupy only the lower conduction subband, a dissipationless charge current is found if all the magnetic impurities lie in-plane, and the in-plane external

electric field is applied parallel to them. In contrast, we found that the charge current is always dissipative when both conduction subbands contribute to the electronic current.

We further demonstrated that the conductivity is always highly sensitive to the direction of the in-plane external electric field, implying extensive anisotropic charge transport. The magnetic impurities' effect on the charge transport can be controlled by the strength of the structure inversion asymmetry (for example by the strength of a gate voltage). Therefore, by tuning the gate voltage one can make the charge current nearly independent of the spatial orientation of the present impurities.

Although a direct comparison with experiments is not yet possible, however, our theoretical results may explain previous experimental observations. The strong effect of the magnetization direction on the charge transport of MTFs was shown in $(Bi_{0.5}Sb_{0.5})_2Te_3/(Cr_{0.08}Bi_{0.54}Sb_{0.38})_2Te_3$ bilayer heterostructures grown on a $GaAs$ substrate, in which the magnetization direction could be switched by a giant spin–orbit torque. The resulting charge transport was shown to be highly sensitive to the magnetization direction [65]. The strong influence of structural inversion asymmetry was also observed in Cr-doped $(Bi_{1-y}Sb_y)_2Te_3$, $Cr_{0.15}(Bi_{0.1}Sb_{0.9})_{1.85}Te_3$ samples grown on dielectric $SrTiO_3$ substrates, showing a non-monotonic trend of the longitudinal conductivity against gate voltage [66].

BIBLIOGRAPHY

[1] J. E. et al., Phys. Rev. B **75**, 121306(R) (2007).

[2] X. L. Qi et al., Phys. Rev. B **78**, 195424 (2008).

[3] D. Hsieh et al., Phys. Rev. Lett. **103**, 146401 (2009).

[4] L. Fu et al., Phys. Rev. Lett. **76**, 045302 (2007).

[5] X.-L. Qi et al., Rev. Mod. Phys. **83**, 1057 (2011).

[6] L. Fu et al., Phys. Rev. Lett. **98**, 106803 (2007).

[7] B. A. Bernevig et al., Science **314**, 1757 (2006).

[8] M. Z. Hasan et al., Rev. Mod. Phys. **82**, 3045 (2010).

[9] L. Fu, Phys. Rev. Lett. **106**, 106802 (2011).

[10] C. X. Liu et al., Phys. Rev. Lett. **101**, 146802 (2008).

[11] R. Yu et al., Science **329**, 61 (2010).

[12] A. M. Essin et al., Phys. Rev. Lett. **102**, 146805 (2009).

[13] X. L Qi et al., Science **323**, 1184 (2009).

[14] Q. Liu et al., Phys. Rev. Lett. **102**, 156603 (2009).

[15] D. A. Abanin et al., Phys. Rev. Lett. **106**, 136802 (2011).

[16] A. B. Sushkov et al., Phys. Rev. B **82**, 125110 (2010).

[17] G. S. Jenkins et al., Phys. Rev. B **82**, 125120 (2010).

[18] G. M. Gusev et al., Phys. Rev. B **84**, 121302(R) (2011).

[19] A. A. Zyuzin et al., Phys. Rev. B **83**, 245428 (2011).

[20] I. Lee et al., Proc. Natl. Acad. Sci. **112**, 1316 (2015).

[21] S. Y. Xu et al., Nature Phys. **8**, 616 (2012).

[22] L. A. Wray et al., Nature Phys. **7**, 32 (2011).

[23] Y. L. Chen et al., Science **329**, 659 (2010).

[24] I. Vobornik et al., Nano Lett. **11**, 4079 (2011).

[25] M. Li et al., Phys. Rev. Lett. **115**, 087201 (2015).

[26] Fan Yang et al., Phys. Rev. B **94**, 075304 (2016).
[27] R. Yu et al., Science **329**, 61 (2010).
[28] C. Z. Chang et al., Science **340** 167, (2013).
[29] X. Kou et al., Phys. Rev. Lett. **113**, 137201 (2014).
[30] Y. Xing et al., New J. Phys. **20**, 043011 (2018).
[31] N. Nagaosa et al., Rev. Mod. Phys. **82**, 1539 (2010).
[32] Y. Ni et al., IEEE Transactions on Magnetics **52**, 4002304 (2016).
[33] Y. Zhang et al., Nat. Phys. **6**, 584 (2010).
[34] Y. Sakamoto et al., Phys. Rev. B **81**, 165432 (2010).
[35] J. Linder et al., Phys. Rev. B **80**, 205401 (2009).
[36] C. X. Liu et al., Phys. Rev. B **81**, 041307(R) (2010).
[37] H. Z. Lu et al., Phys. Rev. B **81**, 115407 (2010).
[38] W. Y. Shan et al., New J. Phys. **12**, 043048 (2010).
[39] Y. Zhang et al., Nat. Phys. **6**, 584 (2010).
[40] S. Datta et al., Appl. Phys. Lett. **56**, 665 (1990).
[41] N. A. Sinitsyn, J. Phys.: Condens. Matter **20**, 023201 (2008).
[42] N. A. Sinitsyn et al., Phys. Rev. B **73**, 075318 (2006).
[43] N. A. Sinitsyn et al., Phys. Rev. B **72**, 045346 (2005).
[44] K. Vyborný et al., Phys. Rev. B **79**, 045427 (2009) .
[45] A. Sabzalipour et al., New J. Phys. **22**, 123004 (2020).
[46] W. Y. Shan et al., New J. Phys. **12**, 043048 (2010).
[47] H. Z. Lu et al., Phys. Rev. B **81**, 115407 (2010).
[48] H. Z. Lu et al., Phys. Rev. Lett. **111** 146802 (2013) .
[49] C. Z. Chang et al., Science **340**, 167 (2013).
[50] A. Kandala et al., Nat. Commun. **6**, 7434 (2015).
[51] J. G. Checkelsky et al., Nat. Phys. **10**, 731 (2014) .
[52] X. Kou et al., Nat. Commun. **6**, 8474 (2015).
[53] Y. Feng et al., Phys. Rev. Lett. **115**, 126801 (2015).
[54] X. Kou et al., Phys. Rev. Lett. **113**, 137201 (2014).
[55] C. Z. Chang et al., Nat. Mater. **14**, 473 (2015) .
[56] S. Grauer et al., Phys. Rev. B **92**, 201304(R) (2015).
[57] R. Yu et al., Science **329**, 61 (2010).

[58] W. Kohn et al., Phys. Rev. **108**, 590 (1957).

[59] J. Henk et al., Phys. Rev. Lett. **109**, 07680 (2012).

[60] T. Jungwirth et al., Rev. Mod. Phys. **78**, 809 (2006).

[61] Q. Liu et al., Phys. Rev. Lett. **102** 156603 (2009).

[62] G. Rosenberg et al., Phys. Rev. B **85**, 195119 (2012).

[63] Y. S. Hor et al., Phys. Rev. B **81**, 195203 (2010).

[64] J. S. Dyck et al., Phys. Rev. B **65**, 115212 (2002).

[65] Y. Fan et al., Nature Mater **13**, 699 (2014).

[66] C. Z. Chang et al., Science **340**, 167 (2013).

CHAPTER 5

THE ANOMALOUS HALL EFFECT IN MAGNETIC TOPOLOGICAL INSULATORS

This chapter presents the study of the anomalous Hall effect (AHE) on the surface of a 3D magnetic topological insulator. As we discussed in section 2.6, the anomalous Hall effect is one of the most fundamental transport properties of magnetic materials. This phenomenon is the manifestation of the Hall effect in systems without time-reversal symmetry. This effect has been an enigmatic problem for almost a century and still remains a poorly understood phenomenon. Understanding the rich physics behind this effect in different systems presents a deep insight into magnetic materials. It also enables us to introduce novel properties which can be used in new devices for prospective technological advances in spintronics, random access memory, etc. [1, 2].

A magnetic topological insulator with strong spin-orbit coupling is a valuable host medium for realizing both the quantized version of the AHE [3–5], and the unquantized version of the AHE [6, 7].

The dependency of surface charge transport on the type of disorder and the range of disorder-electron interaction has been extensively studied theoretically [8, 9]. The collective behavior of randomly distributed point-like magnetic impurities on the surface and in the bulk of a topological insulator can break time-reversal symmetry and drive the system into a gapped system. This introduced gap in spin space influences, via the spin-orbit coupling, the

charge dependent properties of the massive Dirac fermions.

Although considerable studies have been devoted to the AHE in different systems and different regimes[10–14], less attention has been paid to this phenomenon in magnetic topological insulators. In the literature, the AHE that arises from scattering of massive Dirac fermions off non-magnetic impurities has been studied using the Boltzmann kinetic equation and the microscopic Kubo-Streda formalism [15, 16], and off magnetic impurities, with an out-of-plane magnetization based on the kinetic equation for the density matrix, [17].

In this chapter, we investigate the importance of the magnetization direction in the AHE. We thoroughly study the three distinct contributions to the AHE, the contribution arising from the intrinsic Berry-phase curvature [18–20], the extrinsic side-jump effect [21, 22], and the skew scattering effect [23]. Fully analytical expressions for these contributions to the anomalous Hall conductivity arising from magnetic impurities with arbitrary magnetization direction are derived. Our method was chosen to incorporate this anisotropy of the scattering potential properly. However, we also apply our method to derive the contributions of non-magnetic isotropic scatterers. In this way, we complete our discussion and it allows us to compare our results for non-magnetic impurities with those that already have been reported in literature [24].

We found that the calculated AHE can also change sign if one changes the magnetic easy axis from fully out-of-plane to in-plane. Interestingly, such sign change of the AHE with respect to the spatial orientation of the magnetization has already been experimentally observed in ultra-thin $Co^{0.3nm}/Pd^{0.5nm}$ multilayers [25]. Besides, it has recently been shown experimentally that the AHE can undergo a sign change by altering the spatial orientation of an applied magnetic field in non-magnetic $ZrTe_5$, which is a candidate for a Dirac or Weyl semmimetal [26]. To the best of our knowledge, a sign change of the AHE with respect to the spatial orientation of the surface magnetization has not been reported experimentally for the surface of a topological insulator, and therefore further experiments on this material can test our model.

Many AHE related experiments have been conducted, and in some of them, a sign change has been reported against temperature, gate voltage,

thickness, etc. Different studies have been performed to understand these observed sign changes [27–30].

Moreover, this work presents a clear and different scenario behind the sign change of the AHE on the surface of a magnetic TI. Two terms with opposite signs compete simultaneously to take control of this conductivity. These terms consist of contributions from the three different effects: the Fermi level, the spatial orientation of the surface magnetization and/or the concentration of impurities. Exerting an external electric field determines the charge carriers' momentum direction, which is locked to their spin. Also, by altering the orientation of the TI's surface magnetization by an applied field, the scattering potential's strength can be changed, and by changing the Fermi level, the spin orientation can be altered. Accordingly, the size and sign of each contribution can vary. Then, since the relative importance of the total positive and negative terms changes, the AHE can undergo a sign and size change against Fermi level, concentration of impurities, and spatial orientation of the surface magnetization.

Further, the detailed information of each of the three contributions (intrinsic Berry-phase curvature, side jump effect and skew scattering effect) to the AHE is hidden in the total value of the experimentally measured AHE. Investigating each of these contributions to the AHE experimentally separately is therefore not possible. Here, we discuss how one can overcome this problem by determining the regimes in which each contribution is dominant over the others.

We have organized the rest of this chapter as follows. In Sec. 5.1, we introduce the effective model of massive Dirac Fermions on the surface of a magnetically doped three-dimensional topological insulator. The obtained results are shown in Sec. 5.2. In Sec. 5.3 we summarize our findings and conclude with our main results. Finally, some more detailed results are collected in the appendices and the derivation of essential expressions to ease tracing some previous sections' results.

5.1 Model Hamiltonian

The *minimal* effective Hamiltonian describing massive Dirac Fermions on the surface of a 3D TI is given by

$$H_D = \hbar v_F (\boldsymbol{k} \times \sigma)_z + M\sigma_z, \tag{5.1}$$

where the $\hat{z}$-direction is chosen normal to the surface of the TI. Here, v_F, $\boldsymbol{k} = (k_x, k_y)$, and M are respectively the Fermi velocity, the wave vector, and the mass of the surface Dirac electrons, and $\sigma = (\sigma_x, \sigma_y, \sigma_z)$ is the vector of Pauli matrices acting on the spin of the electrons. v_F and M are material dependent parameters. For example, in Bi_2Se_3, $v_F \simeq 5 \times 10^5\ ms^{-1}$ [31], and Dirac massless Fermions have a linear dispersion in the energy range $0 \lesssim E - E_D \lesssim 0.3\ eV$, with E_D the energy at the Dirac point. In Ref. [32], it was shown that a gap of 50 meV can be introduced in the surface band structure in Fe doped Bi_2Se_3, $(Bi_{0.88}Fe_{0.12})_2Se_3$, leading to $M \simeq 25$ meV.

The eigenvalues and eigenvectors of H_D are

$$\psi_{\boldsymbol{k},\alpha}(r) = \frac{e^{i\boldsymbol{k}\cdot\mathbf{r}}}{\sqrt{A(1+\xi_k^{2\alpha})}} \begin{pmatrix} e^{-i\phi_{\boldsymbol{k}}/2} \\ i\alpha\xi_k^{\alpha}\, e^{i\phi_{\boldsymbol{k}}/2} \end{pmatrix} \tag{5.2}$$

$$\varepsilon_{k,\alpha} = \alpha\ \varepsilon_k = \alpha\sqrt{(\hbar v_F k)^2 + M^2}\ , \tag{5.3}$$

where α labels the conduction ($\alpha = +1$) and valence ($\alpha = -1$) bands, $k = |\boldsymbol{k}|$, $\xi_k = \sqrt{(1-\gamma_k)/(1+\gamma_k)}$, with $\gamma_k = M/\varepsilon_k$, and $\phi_{\boldsymbol{k}} = \arctan(\frac{k_y}{k_x})$ refers to the direction of the wave vector of the surface electrons (see also Fig. 5.1). In the following we will also label the eigenstates and energies with the index $l \equiv (\boldsymbol{k}, \alpha)$ as the combined (momentum, band) index.

The presence of dilute and randomly placed magnetic impurities on the surface of a 3D TI scatter electrons and influence the system's transport properties. We model the interaction between an electron located at r and a single magnetic impurity at R_m (m stands for magnetic impurities) as

$$V^m(\mathbf{r} - \mathbf{R}_m) = J\delta(r - \mathbf{R}_m)\ \mathbf{S}_m \cdot s, \tag{5.4}$$

where S_m and $s = \hbar\sigma/2$ are the impurity spins and the electron, respectively. J is the exchange coupling, and the Dirac delta function refers to the short-range

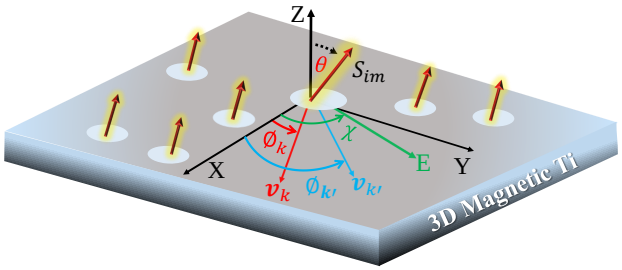

Figure 5.1: Schematical overview of the system under study: a magnetic impurity on the surface of a TI, with its magnetization in the yz-plane, tilted over an angle θ. An electron with initial wave vector k approaches the impurity and elastically scatters off the impurity with $\phi_{k'}$ as the polar angle for k'.

nature of the electron-impurity interaction we have considered in this study. In the regime of large magnetic spin $|S| \to \infty$, weak interaction $J \to 0$ and $J|S|$=constant, we can treat the spin of the magnetic impurities classically. We assume that the magnetic impurities align in the same direction and lie in the yz-plane. Since the system is not usually pure and often contains non-magnetic impurities, we also consider the effect of non-magnetic impurities on the charge transport. Accordingly, we model the interactions between an electron positioned at r and a single non-magnetic impurity at R_{nm} (nm stands for the non-magnetic impurities) as

$$V^{nm}(\mathbf{r}-\mathbf{R}_{nm}) = V_0^{nm}\delta(\mathbf{r}-\mathbf{R}_{nm}), \tag{5.5}$$

where V_0^{nm} denotes the strength of this interaction. The massive Dirac Hamiltonian H_D is a consequence of very strong spin-orbit coupling in the TI's crystal lattice with many heavy atoms. Therefore, in the presence of such a strong spin-orbit potential, we disregard the correction to Eq. (5.5) due to the spin-orbit effect of a single impurity atom [23]. We relied on the modified Boltzmann formalism [37] separately for these two kinds of impurities to obtain analytical results for the different contributions to the AHE in a magnetic TI.

An overview of the system with some important definitions is shown in Fig. 5.1.

5.2 Results and Discussions

In this section, we present our results for the anomalous Hall response on a 3D topological insulator's surface. Different regimes can be identified. As we discussed in section 2.6, some contributions to the anomalous Hall conductivity are independent of the impurity concentration, and others are inversely proportional. Therefore we can express the anomalous Hall conductivity of the system as

$$\sigma_{ij}^{AHE} = \sigma_{ij}^{int.AHE} + \sigma_{ij}^{ext.AHE}, \tag{5.6}$$

where we label the term $\sigma_{ij}^{ext.AHE}$ as extrinsic because it depends on impurities' concentration, while we label the term $\sigma_{ij}^{int.AHE}$ as intrinsic because it is independent of the concentration of impurities. If only the first term is significant and the second term is negligible, we call this regime the intrinsic regime, and when the first term is minimal and negligible, the system is in the extrinsic regime. If both contributions are comparable, the system is in the intermediate regime. Since the system's anomalous Hall response behaves differently in these distinctive regimes, they are discussed separately in the following sections.

5.2.1 The intrinsic regime

$\sigma_{ij}^{int.AHE}$ originates from three effects simultaneously, namely the Berry-phase curvature, the side jump effect and the skew scattering. Except the contribution arising from the Berry-phase curvature, the other contributions in this regime originate from the impurities, even though the expressions of their corresponding conductivities do not depend on the concentration of impurities. In this section, we first investigate each contribution to the $\sigma_{ij}^{int.AHE}$, and then the anomalous Hall conductivity in the intrinsic regime will be studied.

5.2.1.1 Berry curvature contribution

Unlike side jump and skew scattering, this contribution does not rely on the presence of impurities and interestingly produces a non-zero conductivity

even in a pure system. As we already mentioned, the non-zero Berry-phase curvature causes an anomalous velocity v_l^{an} and consequently contributes to the AHE by $\boldsymbol{J}^{an} = -e\sum_l f^0(\varepsilon_l)v_l^{an}$. In order to calculate this term, one has to consider the contributions of all electrons residing in the whole Fermi sea, instead of just considering those electrons in the conduction band. Using the eigenstates in Eq. (5.2), one arrives at the following expression for the anomalous velocity

$$\mathbf{v}^{an}_{\boldsymbol{k},\alpha} = -\dot{\boldsymbol{k}} \times \Omega_{k,\alpha} = \frac{e\mathbf{E}}{\hbar} \times \frac{-\alpha M v_F^2 \hbar^2}{2\left(k^2 v_F^2 \hbar^2 + M^2\right)^{3/2}} \hat{z} = \frac{e\mathbf{E}}{\hbar} \times \frac{-\alpha M v_F^2 \hbar^2}{2\varepsilon^3_{k,\alpha}} \hat{z}. \tag{5.7}$$

This correction to the velocity of electrons produces following contribution to the conductivity of the system:

$$\sigma^{an}_{xy} = \frac{-e^2}{\hbar}\left[\int_0^{k_F} \Omega_{k,+} \frac{d^2\boldsymbol{k}}{(2\pi)^2} + \int_0^{\infty} \Omega_{k,-} \frac{d^2\boldsymbol{k}}{(2\pi)^2}\right] = -\frac{1}{2m}\frac{e^2}{h}, \tag{5.8}$$

and consequently $\sigma^{an}_{xy}[\frac{e^2}{h}] = -\frac{1}{2m}$, with $m = \frac{\varepsilon_F}{M}$ and $\sigma^{an}_{yx} = -\sigma^{an}_{xy}$. Like this expression, all contributions to the AHE are given in units of $\frac{e^2}{h}$. This contribution can be regarded as an "unquantized" version of the quantum Hall effect which is given by $\sigma^{QHE}_{xy} = -\frac{1}{2}$. This term changes within $0 \leq |\sigma^{an}_{ij}[m]| \leq 0.5$, if $1 \leq m \leq \infty$ and since is inversely proportional to $m = \frac{\varepsilon_F}{M}$, it obviously turns off in the gaples regime ($M = 0$). We will show that of the three involved contributions to the AHE, this contribution dominates the AHE when $m = 1$, not only in the intrinsic regime but also in the intermediate regime. Additionally, note that this contribution to the AHE is an intrinsic contribution originating from the entire band, whereas other extrinsic contributions arising from impurities can be regarded as corrections to this term.

5.2.1.2 Side Jump related contributions

As we indicated before, there are two distinct effects due to the anomalous coordinate shift: the side jump $\delta r_{\boldsymbol{k}\boldsymbol{k}'}$ and a change in the energy of the electron. After averaging over many scattering events, side jumps do not cancel out and give rise to a non-zero contribution $\boldsymbol{v}^{sj}_{\boldsymbol{k}}$ to the velocity of the electrons given in Eq. (2.61). This correction to the velocity of the electrons itself changes the conductivity of the electrons and we call this contribution σ^{sj}_{ij}. The second

effect is the energy change of an electron when it makes a deflection $\delta r_{\boldsymbol{k}\boldsymbol{k}'}$ in the presence of an external electric field E. This change in its potential energy is given by $e\ \delta r_{\boldsymbol{k}\boldsymbol{k}'} \cdot \mathbf{E}$, which eventually leads to the deviation of the distribution function of the electrons that we indicate as g_l^{ad} in Eq. (2.62). We now separately discuss the resultant conductivities σ_{ij}^{sj} and σ_{ij}^{ad}.

Using the eigenvectors of the conductive massive Dirac Fermions given in Eq. (5.2) and applying Eq. (2.58), we obtain the deflections $\delta r^m_{\boldsymbol{k}\boldsymbol{k}'}$ and $\delta r^{nm}_{\boldsymbol{k}\boldsymbol{k}'}$ due to the magnetic and non-magnetic scatterings, and they are given by

$$\begin{aligned}\delta r^m_{\boldsymbol{k}\boldsymbol{k}'}[\frac{\hbar v_F}{\varepsilon_k}] = &\frac{\gamma(1/2-c)}{\sqrt{(1-\gamma^2)}}[\hat{\phi}_{\boldsymbol{k}'} - \hat{\phi}_{\boldsymbol{k}}] + c\tan\theta[\cos\phi_{\boldsymbol{k}'}\ \hat{\phi}_{\boldsymbol{k}} - \cos\phi_{\boldsymbol{k}}\ \hat{\phi}_{\boldsymbol{k}'}] + \\ &(2c\gamma^2\tan\theta\sin\phi_-\cos\phi_+ - c\sqrt{\gamma^2-\gamma^4}\sin 2\phi_-)[\hat{\boldsymbol{k}} + \hat{\boldsymbol{k}}'],\end{aligned} \tag{5.9}$$

$$\delta r^{nm}_{\boldsymbol{k}\boldsymbol{k}'}[\frac{\hbar v_F}{\varepsilon_k}] = \frac{\gamma(1-\gamma^2)^{1/2}}{4(\cos^2\phi_- + \gamma^2\sin^2\phi_-)}(\sin 2\phi_-[\hat{\boldsymbol{k}}+\hat{\boldsymbol{k}}'] - 2\sin^2\phi_-[\hat{\phi}_{\boldsymbol{k}'} - \hat{\phi}_{\boldsymbol{k}}]), \tag{5.10}$$

where the two vectors $\hat{\boldsymbol{k}}$ and $\hat{\phi}_{\boldsymbol{k}}$ are unit vectors in spherical coordinates, respectively in the radial and polar direction, θ is the tilting angle of the randomly placed point-like magnetic impurities on the surface of the magnetic TI, $c = \left(2\sin^2\phi_- + 2[\gamma_k\cos\phi_- + \sqrt{1-\gamma_k^2}\tan\theta\cos\phi_+]^2\right)^{-1}$, $\gamma = \gamma_k = \dfrac{M}{\varepsilon_k}$, and $\phi_\pm = \dfrac{\phi_{\boldsymbol{k}} \pm \phi_{\boldsymbol{k}'}}{2}$. Since electrons undergo two distinctive and independent scattering events, magnetic and non-magnetic, we treat them separately. As Eq. (5.9) shows, the side jump of an electron during a magnetic scattering strongly depends on its incident angle $\phi_{\boldsymbol{k}}$, scattering angle $\phi_{\boldsymbol{k}'}$ and also θ, the tilting angle with respect to the $\hat{z}$-direction of the magnetic orientation of the surface impurities.

Fig. 5.2 illustrates the direction of occurred coordinate shift during the scattering of electrons from magnetic impurities (illustrated by blue vectors) and non-magnetic impurities (illustrated by red vectors) in terms of ϕ_k and $\phi_{k'}$, for different values of $m = \frac{1}{\gamma_k} = \frac{\varepsilon_k}{M}$ (with ε_{k_F} the Fermi level) and θ. The background color in all panels of Fig. 5.2 shows the scattering probability $|T^m_{kk'}|^2$ (with $J^2S_m^2 = 1$), given by

$$\left|T^m_{kk'}\right|^2 = \left|\frac{2\gamma_k}{1+\gamma_k^2}\sin\theta\cos\phi_+ + \frac{1-\gamma_k^2}{1+\gamma_k^2}\cos\theta\cos\phi_- + i\cos\theta\sin\phi_-\right|^2. \tag{5.11}$$

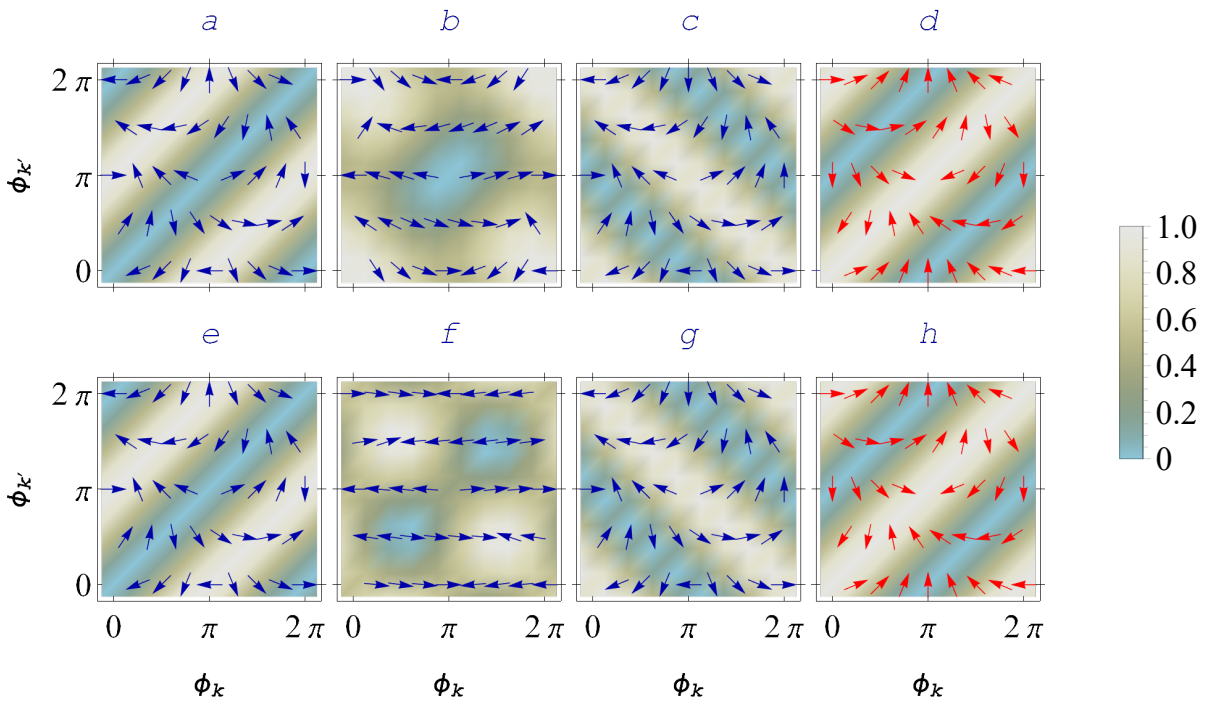

Figure 5.2: (Color online) Side jump vectors of electrons during scattering off magnetic impurities $\delta r^{m}_{kk'}$ are shown in panels $a-c$, $e-g$ and for scattering off non-magnetic impurities $\delta r^{nm}_{kk'}$ in panels d and h, in terms of ϕ_k, $\phi_{\boldsymbol{k}'}$, for different values of θ and $m = \frac{\varepsilon_F}{M}$. In panel a, $(\theta, m) = (0, 1.1)$, in b $(\theta, m) = (\frac{\pi}{4}, 1.1)$ and in c, $(\theta, m) = (\frac{\pi}{2}, 1.1)$. In the second row, $(\theta, m) = (0, 8)$, $(\frac{\pi}{4}, 8)$ and $(\frac{\pi}{2}, 8)$ in panels e, f and g, respectively. In addition, $\delta r^{nm}_{kk'}$ is shown in terms of ϕ_k and $\phi_{k'}$ for $m = 1.1$ and 8, in panel o and p, respectively.

Blue corresponds to zero probability, beige with the highest probability. Moreover, the size of the shown side jump vectors in Fig. 5.2 is given by Fig. 5.3.

In the first row in Fig. 5.2, m is taken equal to 1.1, the Fermi energy is thus just above the lowest surface conduction band state. In panel a the magnetization is chosen to be perpendicular to the surface of the TI ($\theta = 0$). Panel a of Fig. 5.3 shows that the side jump for this case is maximal when $\phi_{k'} \approx \phi_k \pm \frac{n\pi}{2}$, with n an odd number, and is minimal when $\phi_{k'} \approx \phi_k \pm n\pi$, with n an integer.

In panel b of this figure the side jump and the corresponding probabilities for a magnetic scattering event are shown for a magnetization direction rotated in the yz-plane with $\theta = \frac{\pi}{4}$. Note that the probability for many scattering events increases, however as panel b of Fig. 5.3 demonstrates, just in a small region of the $(\phi_k, \phi_{k'})$ space the electrons feel a considerable side jump

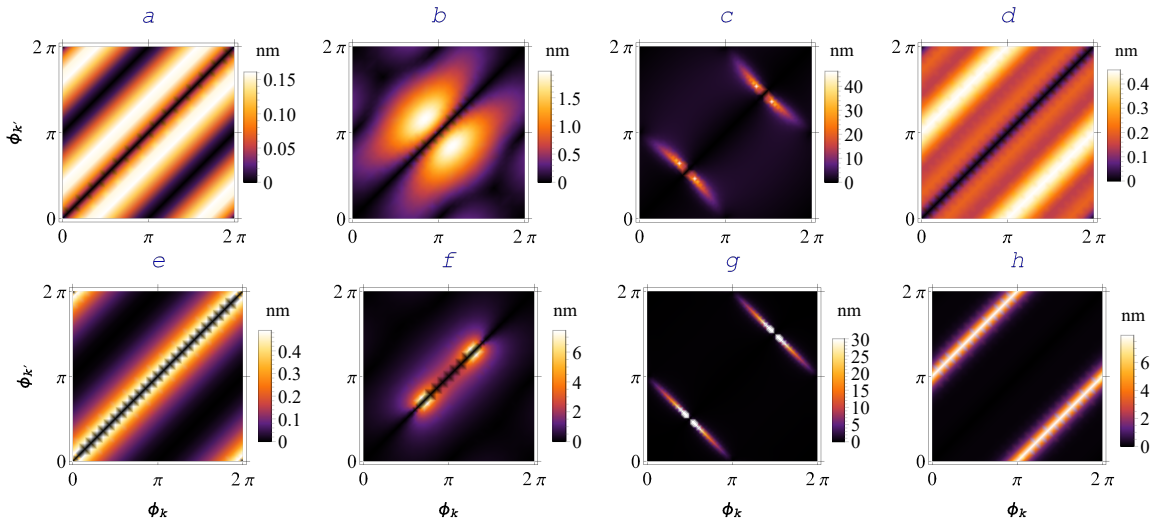

Figure 5.3: Numerical value of $\delta r^m_{kk'}$ for an Fe-doped topological insulator Bi_2Se_3 with $v_F \simeq 5\times10^5 ms^{-1}$ and $M = 25$ meV against ϕ_k and $\phi_{k'}$, for different values of θ and $m = \frac{\varepsilon_{k_F}}{M}$. In panel a, $(\theta, m) = (0, 1.1)$, in b $(\theta, m) = (\frac{\pi}{4}, 1.1)$ and in c, $(\theta, m) = (\frac{\pi}{2}, 1.1)$. In the second row, $(\theta, m) = (0, 8)$, $(\frac{\pi}{4}, 8)$ and $(\frac{\pi}{2}, 8)$ in panels e, f and g, respectively. In addition, $\delta r^{nm}_{kk'}$ is shown in terms of ϕ_k and $\phi_{k'}$ for $m = 1.1$ and 8, in panel o and p, respectively.

coordinate shift. Increasing θ further to $\frac{\pi}{2}$ (thus ending up in a magnetization in the $\hat{y}$-direction) decreases the size of coordinate shift for many scattering events, demonstrated by panel c of Fig. 5.3. The second row of Figs. 5.2, 5.3 show what happens with the side jump if the Fermi level is increased up to $m = \frac{\varepsilon_k}{M} = 8$, again for the same θ values. Note that for a large number of scattering events with different incident and scattering angle $(\phi_k, \phi_{k'})$, the size of the anomalous coordinate shift decreases (in comparison to the upper row), though based on Eq. (5.11) its scattering probability in general increases. Thus, the side jump effect will be maximal for low Fermi level values.

In panels d and h of Figs. 5.2 and 5.3 the coordinate shifts vector, $\delta r_{kk'}$ are shown for Fermi electrons in a non-magnetic scattering event. The background profiles shown in panels d and h of Fig. 5.2 represent the scattering probability (with V_0^2=1), now given by

$$\left|T^{nm}_{kk'}\right|^2 = (1 + [\gamma_k^2 - 1]\sin^2\phi_-), \tag{5.12}$$

with $V_0 = V_0^{nm}$. It is clear from panels d and h of these two figures that the general trend for $\delta r^{nm}_{kk'}$ is that the size of the side jump and the corresponding scattering event probability are π out of phase.

In addition, Fig. 5.3 shows that magnetic side jump events can undergo a one order of magnitude change in their numerical values, by changing the spatial orientation of the surface magnetization from $\theta = 0$ to $\frac{\pi}{4}$, and also from $\frac{\pi}{4}$ to $\frac{\pi}{2}$.

Combining the found $\delta r_{kk'}$ with the Eqs. 2.16, 5.11, and 5.12 yields

$$\begin{aligned} \mathbf{v}_k^{m.sj} &= \sum_{\mathbf{k}'} W_{\mathbf{k}\mathbf{k}'}^m \delta \mathbf{r}_{\mathbf{k}\mathbf{k}'}^m = \vartheta_k^m \left[(1 + 2\sin^2\theta) \sin\phi_k \, \hat{x} - \cos\phi_k \, \hat{y} \right], \\ \mathbf{v}_k^{nm.sj} &= \sum_{\mathbf{k}'} W_{\mathbf{k}\mathbf{k}'} \delta \mathbf{r}_{\mathbf{k}\mathbf{k}'}^{nm} = \vartheta_k^{nm} \hat{\phi}_k, \end{aligned} \tag{5.13}$$

where $\vartheta_k^m = \dfrac{S_m^2 J^2 n_{im}}{8\hbar^2 v_F} \Lambda_k$ and $\vartheta_k^{nm} = \dfrac{V_0^2 n_{inm}}{2\hbar^2 v_F} \Lambda_k$ with $\Lambda_k = \gamma_k \sqrt{1 - \gamma_k^2}$ and n_{inm} the concentration of the non-magnetic impurities. Both of these velocity expressions are only non-zero for gapped systems (i.e. $\gamma_k \neq 0$) and therefore this effect is a consequence of the gap opening. Also note that Eq. (5.13) show that $\mathbf{v}_k{}^{nm.sj}$ is always perpendicular to the band velocity $\mathbf{v}_k$ (directed in the $\hat{k}$ direction), in contrary to $\mathbf{v}_k{}^{m.sj}$. Only when all magnetic impurities are aligned perpendicular to the surface of the TI (i.e. $\theta = 0$) or when the electrons move on the surface of the TI in the direction perpendicular to the in-plane component of the magnetization (i.e. $\phi_k = 0$) we find $\mathbf{v}_k^{m.sj} \parallel \mathbf{v}_k^{nm.sj}$.

To better trace the behavior of the side jump velocity of the electrons during a magnetic scattering event, Fig. 5.4 is provided to show $\mathbf{v}_k^{m.sj}$ as function of θ and ϕ_k. Here ϑ_k^m was set to 1 and background color representing $\cos\varphi$, with φ the angle between $\mathbf{v}_k^{m.sj}$ and $\mathbf{v}_k$. This figure now reveals when the side jump contribution to the transverse conductivity is largest.

This figure demonstrates that by increasing θ the side jump velocity $\mathbf{v}_k^{m.sj}$ increases (indicated by the increase in length of the black arrows in Fig. 5.4) and consequently a larger transverse conductivity can be expected. The average band velocity of itinerant electrons in the presence of an external electric field along the $\hat{x}/\hat{y}$ direction would be along the $-\hat{x}$ /$-\hat{y}$ direction, corresponding to $\phi_k = \pi$ and $\phi_k = \frac{3\pi}{2}$, respectively. Fig. 5.4 shows that the side jump velocity $\mathbf{v}_k^{m.sj}$ of electrons for $\phi_k = \pi$ is along the $\hat{y}$ direction and for $\phi_k = \frac{3\pi}{2}$ is along the $-\hat{x}$ direction. Therefore, for the corresponding transverse

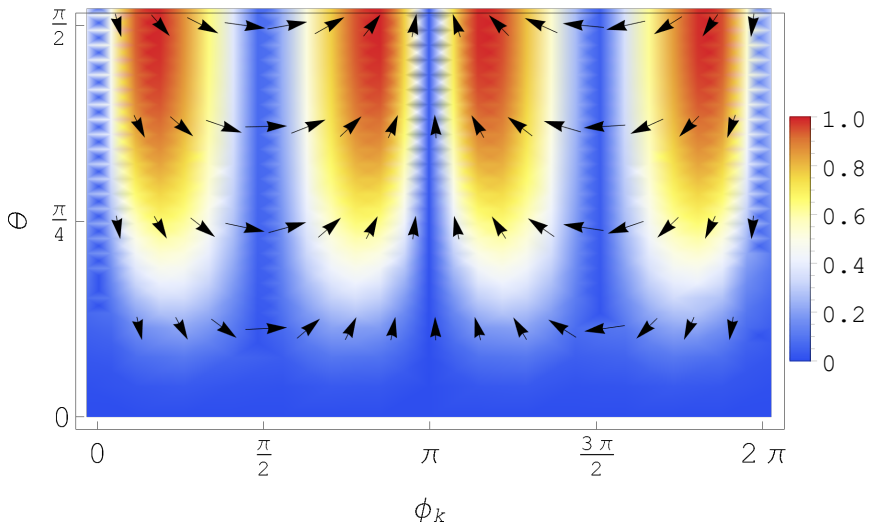

Figure 5.4: $\mathbf{v}_k^{m.sj}$ is shown as a function of ϕ_k and θ, with ϑ_k^m=1 . The background color shows $\cos\varphi$, with φ the angle between $\mathbf{v}_k^{m.sj}$ and $\mathbf{v}_k$.

conductivities (see section 2.7.3),

$$\sigma_{ij}^{m.sj} = \frac{e^2}{AE_j}\sum_{\boldsymbol{k}} \mathbf{v}_i^{m.sj} g_k^{m.sj}, \tag{5.14}$$

we can expect that $\sigma_{yx}^{m.sj} < 0$ and $\sigma_{xy}^{m.sj} > 0$. Furthermore, from the background color of Fig. 5.4 which shows $\cos\varphi$ with φ the angle between $\mathbf{v}_k^{m.sj}$ and $\mathbf{v}_k$, we can deduce that the area for which $\mathbf{v}_k^{m.sj} \cdot \mathbf{v}_k \sim 0$ is larger around $\phi_k = \frac{3\pi}{2}$ than for $\phi_k = \pi$, resulting in $|\sigma_{xy}^{m.sj}| > |\sigma_{yx}^{m.sj}|$.

Now we are ready to derive all side jump contributions in the charge conductivity of the massive Dirac fermions due to the magnetic impurities $\boldsymbol{J}^{tot.m.sj} = \boldsymbol{J}^{m.sj} + \boldsymbol{J}^{m.ad}$ and the non-magnetic impurities $\boldsymbol{J}^{tot.nm.sj} = \boldsymbol{J}^{nm.sj} + \boldsymbol{J}^{nm.ad}$. In order to find $\boldsymbol{J}^{m.ad}$ and $\boldsymbol{J}^{nm.ad}$, we need to solve the corresponding Eq. (2.70). We obtain all the mean free paths $\lambda_i^{m.ad}$ and $\lambda_i^{nm.ad}$ by relying on their Fourier expansions (see Appendix 5.B) and obtain the following corresponding charge conductivities

$$\sigma_{xy}^{m.ad} = \frac{2(1-m^2)}{4m(4m^2\cos^2\theta + g(m^2+\cos 2\theta))}, \tag{5.15}$$

$$\sigma_{yx}^{m.ad} = \frac{(2-\cos 2\theta)(m^2+\cos 2\theta)(g-2)}{4m(\cos 4\theta - 1 + (m^2+\cos 2\theta)(g-2))}, \tag{5.16}$$

$$\sigma_{xy}^{nm.ad} = -\sigma_{yx}^{nm.sj} = \frac{1-m^2}{m(m^2+3)}, \tag{5.17}$$

with $g = \dfrac{\left(4[m^4+1]+2m^2[4\cos 2\theta+\cos 4\theta-1]\right)^{1/2}}{\left|m^2+\cos 2\theta\right|}$. Because $\mathbf{J}^{sj} = -e\sum_k g_k^s \mathbf{v}^{sj}$ and using the already reported distribution function g_k^s in Ref. [33], we come to the conclusion that $\sigma_{ij}^{m.sj} = \sigma_{ji}^{m.ad}$ and $\sigma_{ij}^{nm.sj} = \sigma_{ij}^{nm.ad}$, for $i \neq j$.

How a contribution to the correction of the transverse charge conductivity of a system is linked to the longitudinal conductivity has always been a vital question in this context. The following connections are found

$$\sigma_{xy}^{m.sj} = \sigma_{yx}^{m.ad} = \frac{2-\cos 2\theta}{4m}\,\tilde{\sigma}_{yy}^{m.s}, \tag{5.18}$$

$$\sigma_{yx}^{m.sj} = \sigma_{xy}^{m.ad} = -\frac{1}{4m}\,\tilde{\sigma}_{xx}^{m.s}, \tag{5.19}$$

$$\sigma_{ij}^{nm.ad} = \sigma_{ij}^{nm.sj} = -\frac{1}{m}\tilde{\sigma}_{ii}^{nm.s}, \tag{5.20}$$

with $\tilde{\sigma}_{ii}^{m.s} = \sigma_{ii}^{m.s}/\sigma_0^m$, $\tilde{\sigma}_{ii}^{nm.s} = \sigma_{ii}^{nm.s}/\sigma_0^{nm}$, $\sigma_0^m = 2\hbar^2 v_F^2/(n_{im}J^2S_m^2)$ and $\sigma_0^{nm} = 2\hbar^2 v_F^2/(n_{inm}V_0^2)$.

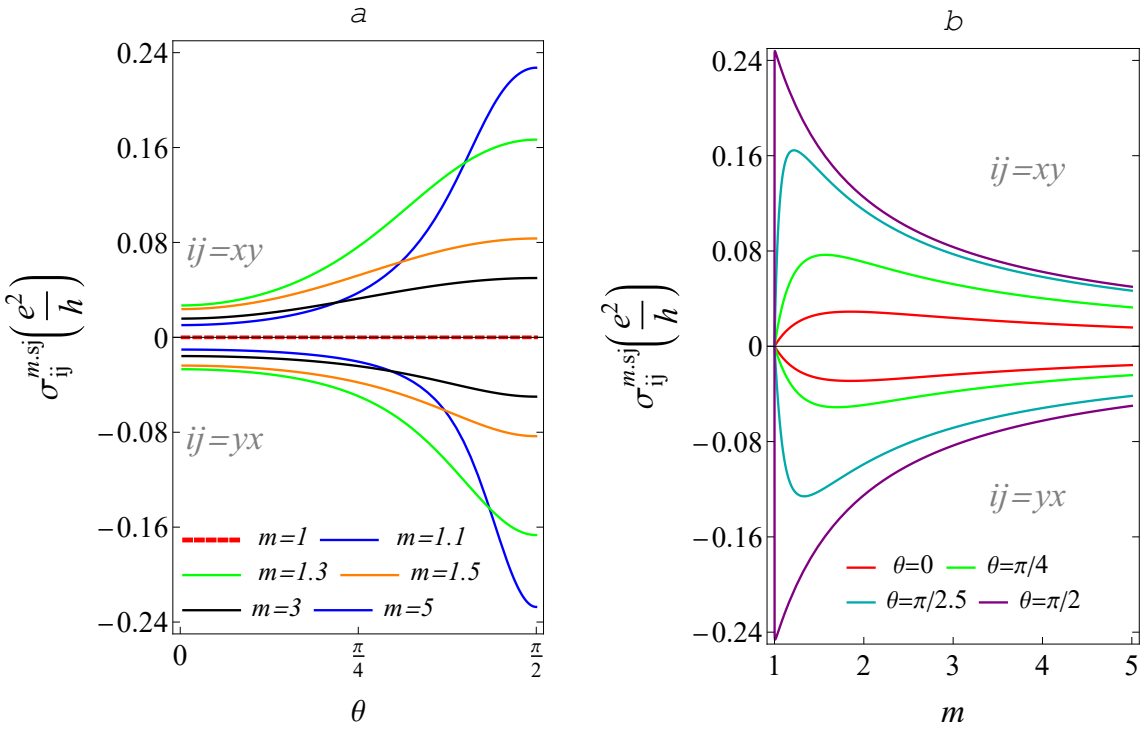

Figure 5.5: $\sigma_{xy}^{m.sj}$ and $\sigma_{yx}^{m.sj}$ are plotted in terms of θ for some different values of m in panel a, and in terms of m for some different values of θ in panel b, respectively.

$\sigma^{m.sj}$ is plotted against θ for some different values of m in panel a of Fig. 5.5 and also in terms of m for some different values of θ in panel b

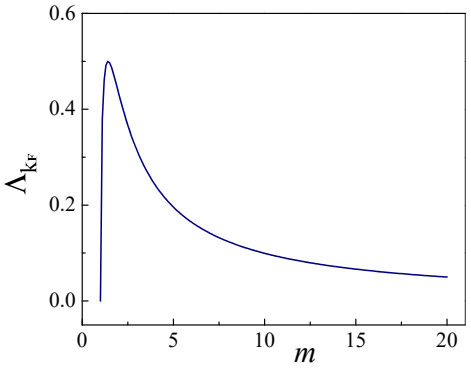

Figure 5.6: Λ_{k_F} function of m.

of this figure. In case of $\theta = 0$, $|\sigma_{xy}^{m.sj}| = |\sigma_{yx}^{m.sj}|$ and putting aside the sign of these conductivities, the system behaves isotropically relative to the external electric field direction. Increasing θ increases the magnitude of the transverse conductivities, and this is caused by the interplay between two factors. Firstly, the backscattering probability is the main mechanism which suppresses both longitudinal and transverse conductivity. By increasing θ, the backscattering probability $w^{(2.m)}(k,-k) \sim [(1-\gamma_k^2)\sin^2\theta\sin^2\phi_k + \cos^2\theta]$ decreases, so the transverse conductivity will increase. Secondly, angular part of the magnetic side jump velocity $[\ 1+4\sin^2\phi_k(\sin^2\theta+\sin^4\theta)\ ]^{1/2}$ increases with increasing θ and subsequently the conductivity increases. As it is clear from panel b of the figure, $\sigma^{m.sj}$ is zero if we put the chemical potential exactly on the lowest state of the surface band structure ($m = 1$ or $\mu = M$). Beyond $m = 1$, $\sigma^{m.sj}$ experiences a peak close to $m = 1$, and thereafter decreases by increasing m for all values of θ. This non-monotonic feature of the conductivity arises from the non-angular part of the side jump velocity (Λ_k) which has the same trend against m (as shown in Fig. 5.6). Therefore, deviating the system a bit from the insulating state and being far enough away from the perfect metallic state $m \gg 1$ or $\mu \gg M$, can produce a large value for the side jump conductivity.

Based on Eq. (5.18) and Eq. (5.19) we come to the conclusion that $\sigma_{xy}^{tot.m.sj} = \sigma_{xy}^{m.sj} + \sigma_{xy}^{m.ad} = \sigma_{yx}^{tot.m.sj}$, with

$$\sigma_{xy}^{tot.m.sj} = \sigma_{yx}^{tot.m.sj} = \frac{(2-\cos 2\theta)\sigma_{yy}^{m.s} - \sigma_{xx}^{m.s}}{4m\sigma_0}. \tag{5.21}$$

Therefore, while in the presence of magnetic scatterers $\sigma_{xy}^{tot.m.sj} = \sigma_{yx}^{tot.m.sj}$

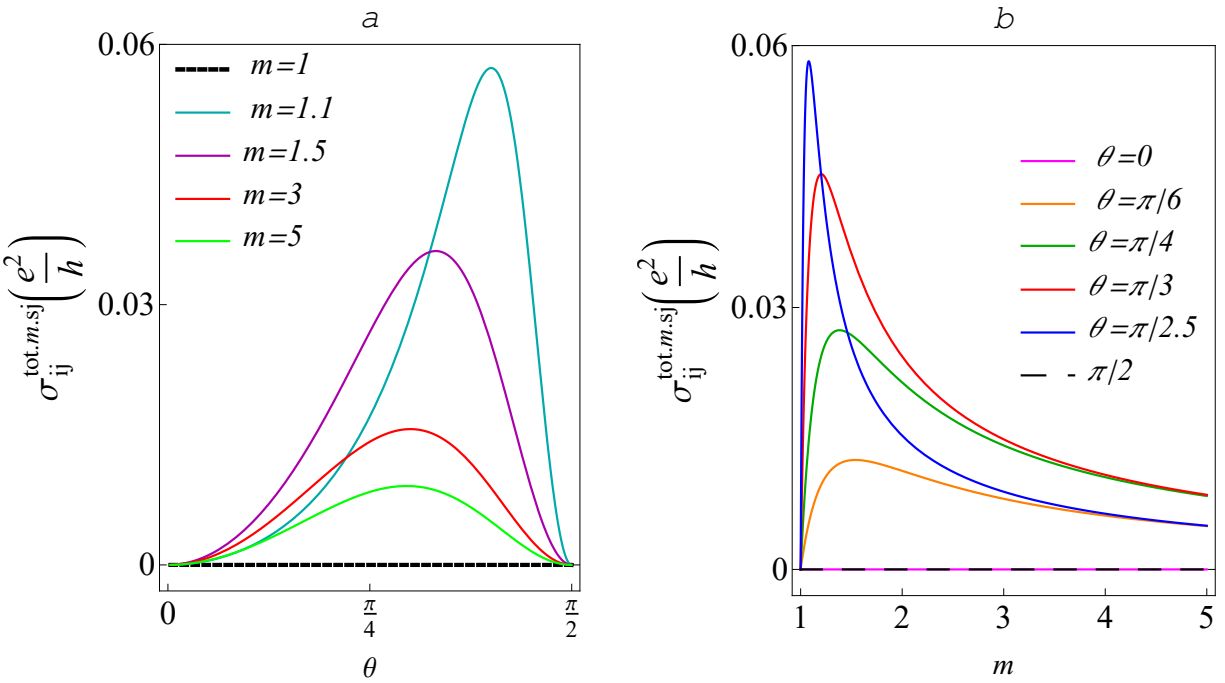

Figure 5.7: $\sigma_{ij}^{tot.m.sj}$ is plotted in terms of θ for some values of m in panel a, and in terms of m for some different values of θ in panel b.

and hence the side jump itself has an isotropic feature relative to the direction of the external electric field, this transverse conductivity somehow measures the anisotropy of the system when $\theta = 0$, being the difference between the two components of the longitudinal conductivities $\sigma_{xx}^{m.s}$ and $\sigma_{yy}^{m.s}$.

In addition, using Eq. (5.18) and Eq. (5.19) we find $\sigma_{xy}^{tot.m.sj} = \sigma_{xy}^{m.sj} + \sigma_{yx}^{m.sj}$. Furthermore, as Fig. 5.5 shows $\sigma_{yx}^{m.sj} < 0$, then we can rewrite $\sigma_{xy}^{tot.m.sj} = |\sigma_{xy}^{m.sj}| - |\sigma_{yx}^{m.sj}|$. Finally since always $\sigma_{xy}^{tot.m.sj} \geq 0$, we can conclude that $|\sigma_{xy}^{m.sj}| \geq |\sigma_{yx}^{m.sj}|$. This inequality surprisingly proves our already made prediction just based on looking at the profile of $\mathbf{v}_k^{m.sj}$.

Figs. 5.7(a) and 5.7(b) show $\sigma_{ij}^{tot.m.sj}$ in terms of θ and m respectively. In this figure for two cases θ=0 and $\theta = \frac{\pi}{2}$, $\mathbf{J}^{m.ad}$ and $\mathbf{J}^{m.sj}$ cancel out each other and there is no net conductivity due to the side jump effect. Within $0 < \theta < \frac{\pi}{2}$, $\sigma_{xy}^{tot.m.sj}$ has a minimum value at $m = 1$, thereafter increases sharply within interval of $1 \leq m \lesssim 1.5$, until it reaches its maximum value. By further increasing m, the net side jump conductivity decreases until it reaches zero in the limit of $m \to \infty$ or a gapless system. In short, in order to have a maximal total side jump conductivity arising from just magnetic impurities, we need to put the chemical potential just above the lowest state in the surface band

structure and also tune the orientation of the surface magnetization within the interval $\frac{\pi}{3} < \theta < \frac{\pi}{2}$.

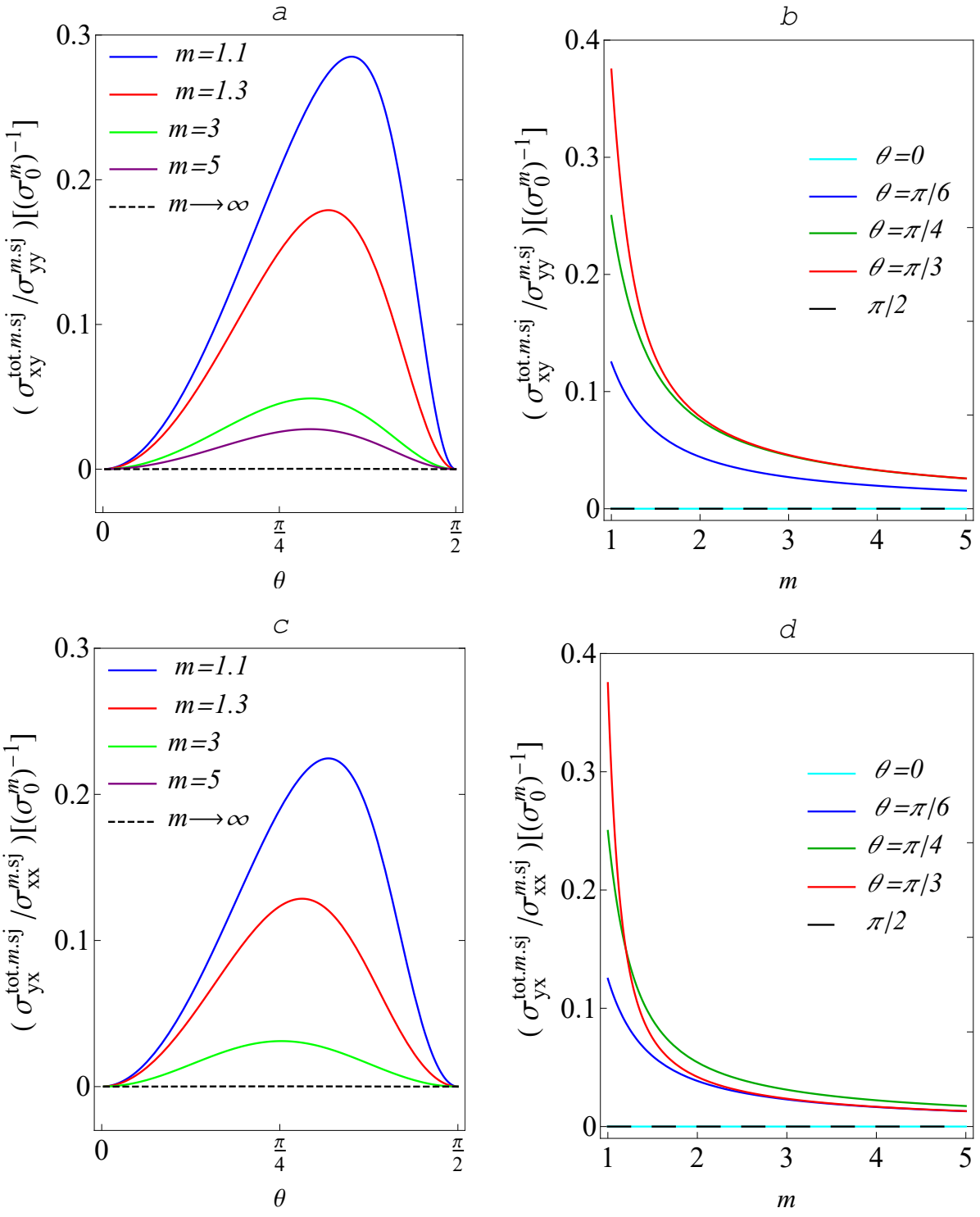

Figure 5.8: $\sigma_{xy}^{tot.m.sj}$ / $\sigma_{yy}^{m.s}[(\sigma_0^{m.s})^{-1}]$ is plotted in terms of θ for some different values of m in panel a, and against m for some different values of θ in panel b. $\sigma_{yx}^{m.sj}$ / $\sigma_{xx}^{to.m.s}[(\sigma_0^{m.s})^{-1}]$ is plotted in terms of θ and m in panel c and d, respectively.

The longitudinal and transverse conductivities both depend on the spatial orientation of the magnetic impurities and the value of the Fermi energy.

Then, to have maximal longitudinal conductivity and minimal transverse conductivity, or vice versa, m and θ have to be well adjusted. Hence, to study the relative importance of the transverse conductivity arising from the magnetic side jump effect, Fig. 5.8 is provided. According to this figure the ratio $\sigma_{xy}^{tot.m.sj}/\sigma_{yy}^{m.sj}$ or $\sigma_{yx}^{tot.m.sj}/\sigma_{xx}^{m.sj}$ is maximal when the surface magnetization is aligned at $\theta \sim \frac{\pi}{3}$ (see Figs. 5.8(a) and 5.8(c)), and the chemical potential lies on the bottom of the conduction band (see Figs. 5.8(b) and 5.8(d)).

Finally, we consider the non-magnetic scattering events, and using Eq. (5.17) we arrive at

$$\sigma_{xy}^{tot.nm.sj} = -\sigma_{yx}^{tot.nm.sj} = \frac{2(1-m^2)}{m(m^2+3)}, \tag{5.22}$$

where $\sigma_{ij}^{tot.nm.sj} = \sigma_{ij}^{tot.nm.sj} + \sigma_{ij}^{tot.nm.ad}$. These results also coincide with the ones reported in Ref. [24]. Thus also this contribution to the side jump conductivity is isotropic (ignoring the sign difference). Fig. 5.9 shows $\sigma_{xy}^{tot.sj}$ in terms of θ and m, where $\sigma_{xy}^{tot.sj} = \sigma_{xy}^{tot.m.sj} + \sigma_{xy}^{tot.nm.sj}$. As Fig. 5.9 shows $\sigma_{xy}^{tot.sj}$ has a negligible sensitivity against θ. It can easily be verified that this is true also for $\sigma_{yx}^{tot.sj}$. Therefore, among the two different types of impurities, the non-magnetic impurities contribution to the side jump conductivity $\sigma_{ij}^{tot.sj}$ dominates.

We also want to stress that both $\sigma_{yx}^{tot.m.sj}$ and $\sigma_{yx}^{tot.nm.sj}$ have positive signs for all values of m and θ, hence $\sigma_{yx}^{tot.sj}$ is always positive. However, $\sigma_{xy}^{tot.m.sj}$ and $\sigma_{xy}^{tot.nm.sj}$ have opposite signs. Consequently, $\sigma_{xy}^{tot.sj}$ could change sign if one changes m or θ. Fig. 5.9 shows this sign change at the boundaries of the black region in this figure.

Finally, notice that even though the concentration of impurities does not appear in the final expression for $\sigma_{ij}^{tot.sj}$, this contribution does originate from the presence of impurities. There are two parameters which play an important role in the transport of electrons during their side jump, the so called side jump relaxation time and the side jump velocity. The first one is inversely proportional to the concentration of impurities, though the second one is directly proportional to the concentration of impurities. Therefore, interestingly, their product is independent of the concentration of impurities.

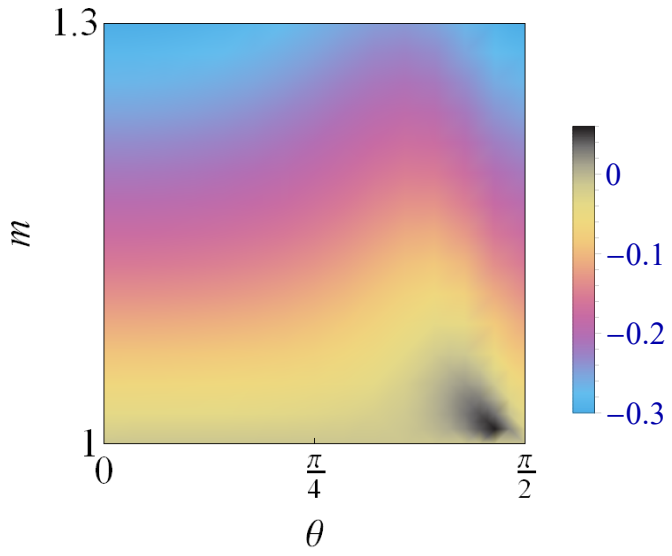

Figure 5.9: $\sigma_{xy}^{tot.sj}$ is plotted in terms of θ and m.

5.2.1.3 Intrinsic Skew Scattering

As we already indicated, skew scattering contributes to the AHE by two distinct terms. Here, we call the first term conventional skew scattering and the second term intrinsic skew scattering. The first term depends on the concentration of impurities and introduces g_k^{a1} in the distribution function f_k, and the other term which is independent of the concentration of impurities adds g_k^{a2} to f_k. Since we deal now with the intrinsic regime in which the first term is very negligible, we just keep the second term. The associated contribution to the second term is $J^{sk2} = -e\sum_k g_k^{a2} v_k$. In order to find J^{sk2}, we first need to calculate $w_{kk'}^{(4)}$ through Eq. (2.57) and then by solving Eq. (2.72) we find g_k^{a2}. Our result for both kinds of impurities are

$$\begin{aligned} w_{kk'}^{(4.m)} =& [w_0^{(4)}\gamma(\gamma^2-1)\cos 2\theta(\sin\phi_k\cos\phi_{k'} - \sin[\phi_{k'}-\phi_k]) \\ & - w_0^{(4)}\gamma(\gamma^2-1)(\sin[\phi_{k'}-\phi_k] + \sin\phi_{k'}\cos\phi_k) + \\ & w_0^{(4)}\gamma^2\sqrt{1-\gamma^2}\sin 2\theta(2\sin\phi_k - \sin\phi_{k'})]\delta(\varepsilon_k - \varepsilon_{k'}), \end{aligned} \tag{5.23}$$

$$w_{kk'}^{(4.nm)} = \frac{3\pi(n_{inm}V_0^2)^2}{4\hbar}\frac{M\,k^2}{\varepsilon_k^3}\delta(\varepsilon_k - \varepsilon_{k'})\sin(\phi_k - \phi_{k'}), \tag{5.24}$$

with $w_0^{(4)} = \dfrac{\pi(n_{im}J^2S_m^2)^2}{4\hbar^3 v_F^2}$. Inserting these scattering rates in Eq. (2.72) and using the already found $w_{kk'}^{(2.m)}$ and g_k^s expressions, we obtain the following

transversal conductivities associated to scattering off magnetic and non-magnetic impurities

$$\sigma_{xy}^{m.sk2} = \frac{16(g-2)[m^2-1]\left(-\cos 4\theta + (m^2+2)\cos 2\theta + 2m^2 + 2\right)}{m\left([g+2]\cos 2\theta + [g+4]m^2 - 2\right)\left(g\cos 4\theta + 2[g-2]m^2\cos 2\theta + g - 4\right)}, \tag{5.25}$$

$$\sigma_{yx}^{m.sk2} = \frac{4(g-2)\left(b\cos 2\theta - g[2(g+1)m^4 + g - 2] - [g-2][g+2m^2]\cos 4\theta + 8m^4 - 4m^2 + 8\right)}{g\ m\left([g+2m^2]\cos 2\theta + [g+2]m^2\right)\left([g-2][\cos 2\theta + m^2] + \cos 4\theta - 1\right)}, \tag{5.26}$$

$$\sigma_{xy}^{nm.sk2} = -\sigma_{yx}^{nm.a2} = -\frac{3}{2}\frac{(m^2-1)^2}{m(m^2+3)^2}, \tag{5.27}$$

with $b = 2[(-2g^2 + g + 8)m^2 - 2gm^4 + g]$. Note that $\sigma_{ij}^{m.sk2} = 0$ for $m = 1$ (the insulating regime) or in the limit of large m (the perfect metallic regime). If we align all the surface magnetic impurities perpendicular to the surface of the TI ($\theta = 0$), the corresponding conductivity is isotropic (ignoring the difference in sign) $\sigma_{xy}^{m.sk2}[\theta = 0] = -\sigma_{yx}^{m.sk2}[\theta = 0] = \dfrac{12\left(m^2-1\right)^2}{m\left(3m^2+1\right)^2}$. Also in case of $\theta = \dfrac{\pi}{2}$ this intrinsic contribution of the skew scattering is isotropic $\sigma_{xy}^{m.sk2}[\theta = \dfrac{\pi}{2}] = \sigma_{yx}^{m.sk2}[\theta = \dfrac{\pi}{2}] = \dfrac{4}{3\ m}$.

To study $\sigma_{ij}^{m.sk2}$, Eq. (5.25) and Eq. (5.26) are illustrated in Fig. 5.10. As it is clear from Fig. 5.10(a), $\sigma_{xy}^{m.sk2}$ increases with increasing θ for all values of m, and reaches a maximum in the interval $\frac{\pi}{4} < \theta < \frac{\pi}{2}$. Fig. 5.10(b) shows $\sigma_{xy}^{m.sk2}$ as function of m for some values of θ. Each curve in this figure shows a maximum value in the interval $1 \leq m \leq 2$, followed by a sharp decrease. Interesting all curves in Fig. 5.10(b) approach zero in the limit $m \to \infty$.

Figs. 5.10(c) and 5.10(d) present $\sigma_{yx}^{m.sk2}$ in terms of θ and m, respectively. Surprisingly $\sigma_{yx}^{m.sk2}$ is negative for $0 \leq \theta < \frac{\pi}{3}$ and has a positive value for $\frac{\pi}{3} < \theta \leq \frac{\pi}{2}$. This contribution changes sign if one changes the spatial orientation of the surface magnetization from 0 to $\frac{\pi}{2}$. According to Fig. 5.10(d), for all given values of θ, $|\sigma_{yx}^{m.sk2}|$ starts from zero at $m = 1$, then increases till it reaches a maximum value within the interval $1 \leq m \leq 2$, after which it decreases. Also in agreement with Fig. 5.10(d) which shows that the $\sigma_{yx}^{m.sk2}$ at $\theta = \frac{\pi}{2}$ is positive for all values of m, the blue curve in this panel is positive for all values of m.

We will see in section 5.2.2 that the conventional skew scattering contribution to the conductivity $\sigma_{ij}^{m.sk1}$ can be turned off by rotating the surface

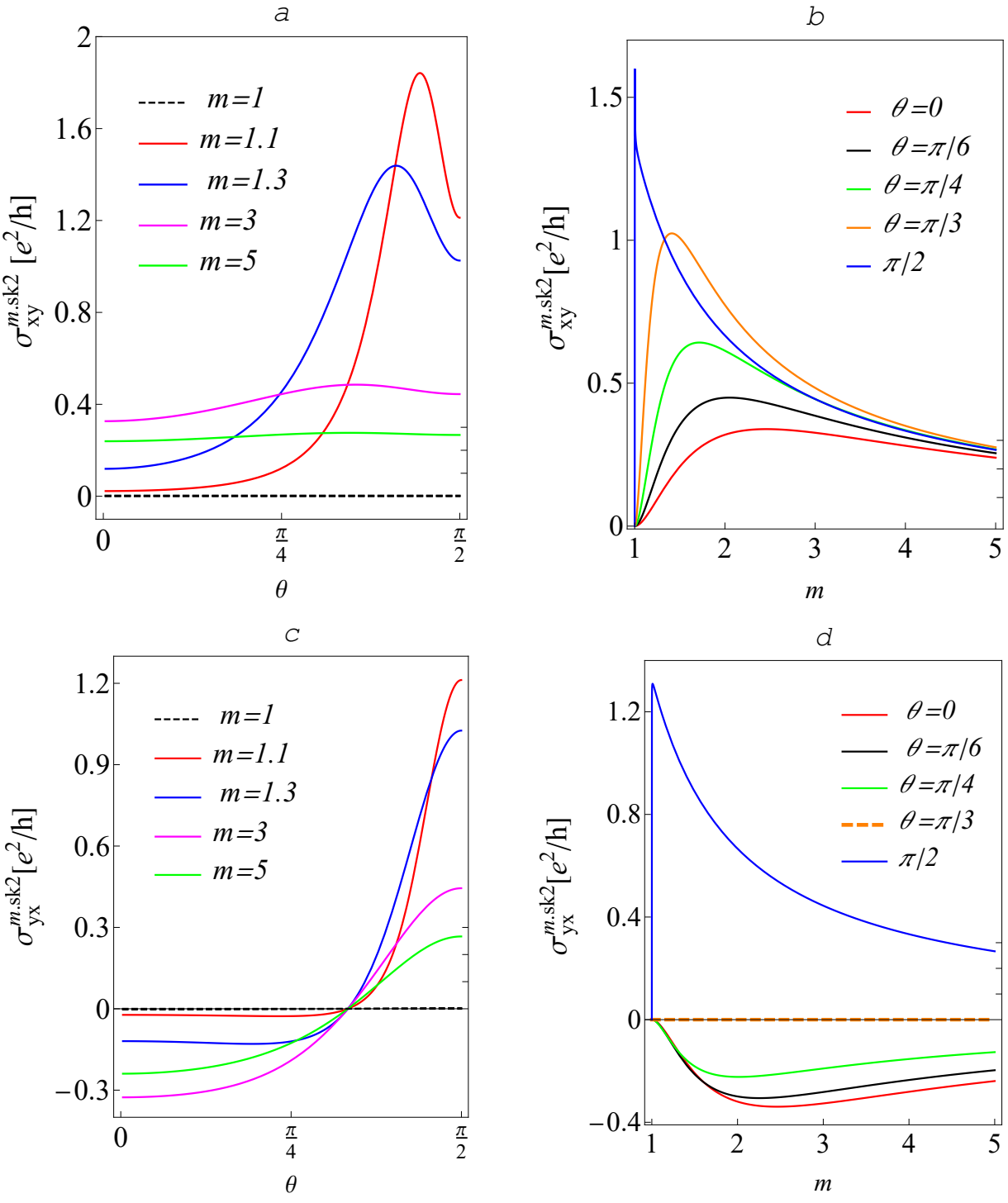

Figure 5.10: $\sigma_{xy}^{m.sk2}$ is plotted in terms of θ and against m in panels a and b, respectively. $\sigma_{yx}^{m.sk2}$ is plotted is plotted against θ and m in panels c and d, respectively.

magnetization to lie on the surface of the TI. However, this orientation of the magnetization cannot turn off $\sigma_{ij}^{m.sk2}$, but it can be turned off by increasing the Fermi level. Furthermore, in case the external electric field is directed in the $\hat{x}$ direction, $\sigma_{yx}^{m.sk2}$ vanishes if $\theta = \frac{\pi}{3}$.

As we evaluated the relative importance of the magnetic side jump contribution in Fig. 5.8, we will do the same with the intrinsic skew scattering contribution. Accordingly, the two ratios $\sigma_{xy}^{m.sk2}/\sigma_{yy}^{m.s}$ and $\sigma_{yx}^{m.sk2}/\sigma_{xx}^{m.s}$ are illustrated in Fig. 5.11. Following this figure, the fraction of electrons that undergo intrinsic skew scattering reaches the maximum value when $0.4\pi < \theta < \frac{\pi}{2}$ and the chemical potential is placed very close to the bottom of the conduction band, regardless of the direction of the external electric field. Besides, by driving the system into the fully metallic regime, the relative importance of the intrinsic skew scattering becomes negligible.

Finally, we consider the contribution due to the spin independent intrinsic skew scattering to the AHE, given in Eq. (5.27). This expression indicates that this conductivity is isotropic and also like $\sigma_{ij}^{m.sk2}$ it disappears for large values of m. By obtaining the two components of the intrinsic skew scattering related condunctivitis $\sigma_{ij}^{m.sk2}$ and $\sigma_{ij}^{nm.sk2}$, we have found $\sigma_{ij}^{tot.sk2} = \sigma_{ij}^{m.sk2} + \sigma_{ij}^{nm.sk2}$.

In case that the external electric field is exerted along the $\hat{y}$-direction and the surface magnetization is aligned perpendicular to the surface of the TI, we find $\sigma_{xy}^{tot.sk2}(\theta = 0) = -\frac{3(m^2-1)^2(m^4-42m^2-71)}{2m(3m^4+10m^2+3)^2}$. In the other interesting situation that the external electric field is along the same direction but the surface magnetization lies on the surface of the TI, one can show that $\sigma_{xy}^{tot.sk2}(\theta = \frac{\pi}{2}) = \frac{-m^4+66m^2+63}{6m(m^2+3)^2}$. In addition, one can show that $\sigma_{xy}^{tot.sk2}(m = 1) = 0$ and $\sigma_{xy}^{tot.sk2}(m \to \infty) = 0$.

Now, if one changes the direction of the external electric field from $\hat{y}$ to $\hat{x}$ and aligns the surface magnetization again perpendicular to the surface of the TI, one can show that $\sigma_{yx}^{tot.sk2}(\theta = 0) = \frac{3(m^2-1)^2(m^4-42m^2-71)}{2m(m^2+3)^2(3m^2+1)^2}$. In the other interesting situation that the external electric field is still in the $\hat{x}$-direction, but the surface magnetization lies on the surface of the TI, $\sigma_{yx}^{tot.sk2}(\theta = \frac{\pi}{2}) = \frac{17m^4+30m^2+81}{6m(m^2+3)^2}$. Also, like $\sigma_{xy}^{tot.sk2}$, the conductivity $\sigma_{yx}^{tot.sk2}$ vanishes at the insulator and perfect metallic condition. While $\sigma_{ij}^{m.sk2}$ behaves isotropically with respect to the external electric field direction, not only at

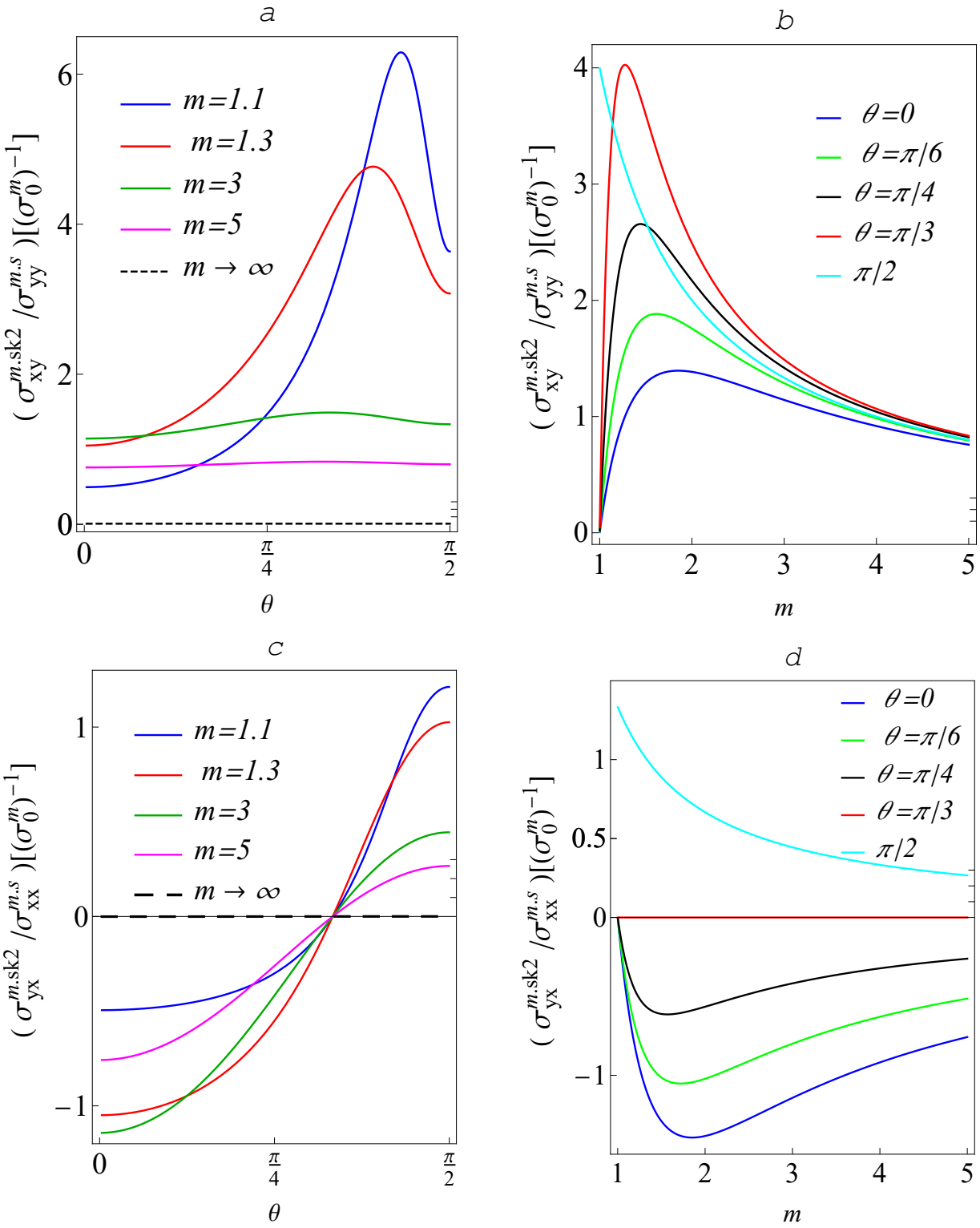

Figure 5.11: $\sigma_{xy}^{m.sk2}$ / $\sigma_{yy}^{m.s}[(\sigma_0^{m.s})^{-1}]$ is shown in terms of θ for some different values of m in panel a, and against m for some different values of θ in panel b. $\sigma_{yx}^{m.sk2}$ / $\sigma_{xx}^{to.m.s}[(\sigma_0^{m.s})^{-1}]$ is plotted against θ and m in panels c, d.

$\theta = 0$ but also at $\theta = \frac{\pi}{2}$, $\sigma_{ij}^{tot.sk2}$ is isotropic just at $\theta = 0$.

$\sigma_{xy}^{tot.sk2}$ and $\sigma_{yx}^{tot.sk2}$ are illustrated respectively in panel a and b of Fig. 5.12, in terms of θ and m. The white lines in these two panels specify the (θ, m) combinations for which the corresponding conductivity is zero. Panel a shows that, for $1 < m \lesssim 2$, $\sigma_{xy}^{tot.sk2}$ undergoes a considerable change with respect to θ. Putting the chemical potential just above the gap and also aligning the surface magnetization close to the surface of the TI ($\frac{\pi}{3} \lesssim \theta \lesssim \frac{\pi}{2}$) causes the system to reach its maximum value for $\sigma_{xy}^{tot.sk2}$. It is also clear from panel a that there is just a small (θ, m) region with a significant $\sigma_{xy}^{tot.sk2}$, while in panel b a broad region shows a significant conductivity $\sigma_{yx}^{tot.sk2}$.

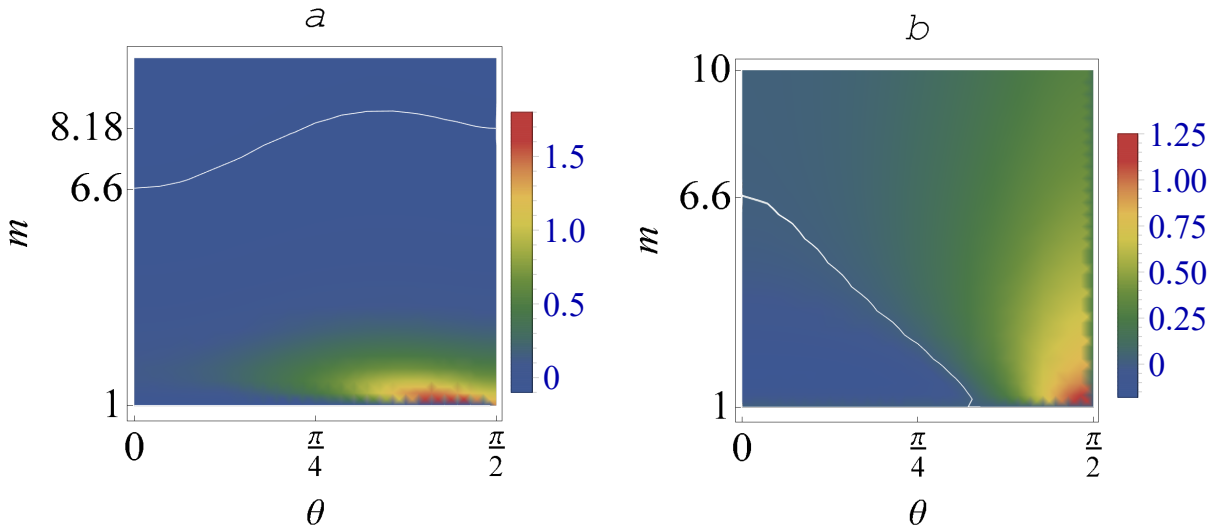

Figure 5.12: $\sigma_{xy}^{tot.sk2}$ and $\sigma_{yx}^{tot.sk2}$ as functions of θ and m, are plotted in panel a and b, respectively.

5.2.1.4 Total AHE in the intrinsic regime

After devoting sections 5.2.1, to the different contributions to the AHE in the intrinsic regime, we are ready to discuss $\sigma_{ij}^{int.AHE} = \sigma_{ij}^{an} + \sigma_{ij}^{tot.sj} + \sigma_{ij}^{tot.sk2}$. The result is illustrated in Fig. 5.13. Based on this figure, we observe that $\sigma_{ij}^{int.AHE}$ is anisotropic. The black dashed line in panel a of this figure indicates the (m, θ) combinations for which $\sigma_{xy}^{int.AHE}[m, \theta] = 0$. Accordingly, tuning (m, θ) around this dashed line leads to a sign change in $\sigma_{xy}^{int.AHE}$. As it its clear from panel b of this figure $\sigma_{yx}^{int.AHE}$ has always a persistent positive sign against any change in θ or m. Also, note that like the contribution of the

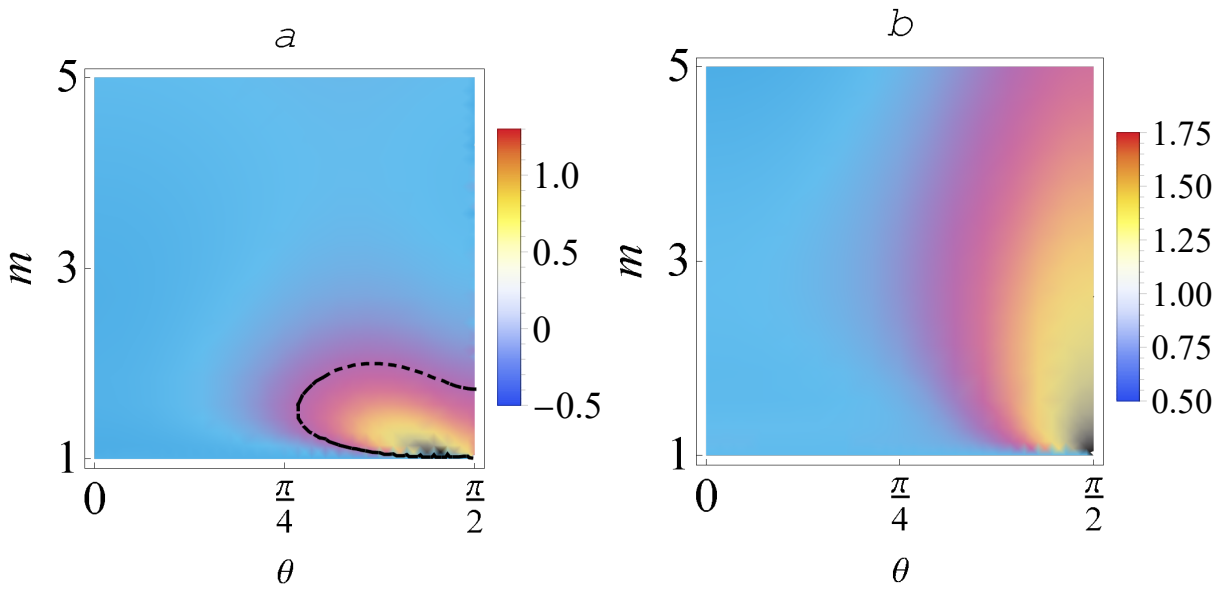

Figure 5.13: $\sigma_{xy}^{int.AHE}[\theta,m]$ and $\sigma_{yx}^{int.AHE}[\theta,m]$ are plotted in panel a and b, respectively.

intrinsic skew scattering, tuning the Fermi level just above the gap and also aligning the magnetization close to the surface, the maximum value for both components $\sigma_{yx}^{int.AHE}$ and $\sigma_{xy}^{int.AHE}$ is attained.

At the end of this section, we consider two special magnetization orientations $\theta = 0$ and $\frac{\pi}{2}$. The total intrinsic anomalous Hall conductivities corresponding to these two important cases are

$$\sigma_{xy}^{int.AHE}[\theta=0] = \frac{m^6+95m^4+79m^2-207}{2\left(m^2+3\right)^2\left(3m^3+m\right)}, \tag{5.28}$$

$$\sigma_{yx}^{int.AHE}[\theta=0] = \frac{m^6-81m^4-49m^2+225}{2\left(m^2+3\right)^2\left(3m^3+m\right)}, \tag{5.29}$$

$$\sigma_{xy}^{int.AHE}[\theta=\frac{\pi}{2}] = -\frac{29m^4+54m^2+45}{6m\left(m^2+3\right)^2}, \tag{5.30}$$

$$\sigma_{yx}^{int.AHE}[\theta=\frac{\pi}{2}] = \frac{17m^4+62m^2+81}{2m\left(m^2+3\right)^2}. \tag{5.31}$$

Above expressions are shown in Fig. 5.14. According to this figure, the anomalous Hall conductivity of the system with in-plane magnetization in the intrinsic regime is much larger than the conductivity of the same system in the same regime with fully out-of-plane magnetization. For a system with

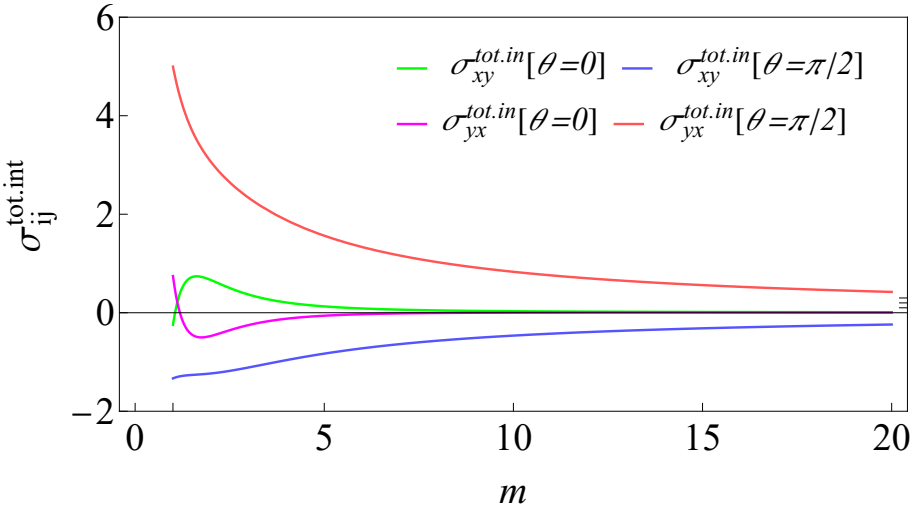

Figure 5.14: $\sigma_{ij}^{int.AHE}$ is plotted as function of m for two values of $\theta = 0$ and $\theta = \frac{\pi}{2}$.

fully out of plane easy axis magnetization ($\theta = 0$) and Fermi level close to the bottom of conduction band, the skew scattering contribution is negligible and the other two contributions control the AHE with comparable size. For the same system but with in-plane easy axis magnetization ($\theta = \frac{\pi}{2}$), surprisingly the contribution arising from skew scattering dominates the AHE. Remarkably, all contributions to the AHE in this regime vanish for a system in the fully metallic state (i.e. a large value of m), whatever the value of θ.

5.2.2 The extrinsic regime

According to our classification in Eq. (5.6), two terms control the AHE. As we already explained, $\sigma_{ij}^{in.AHE}$ is negligible against $\sigma_{ij}^{ext.AHE}$ in the extrinsic regime. Then neither the Berry-phase curvature nor the side jump play a role in $\sigma_{ij}^{ext.AHE}$, and the skew scattering is the only involved effect to the AHE in this regime, by its conventional component $\mathbf{J}^{sk1} = \sum_k \mathbf{v}_k g_k^{a1}$. Since g_k^{a1} is inversely proportional to the concentration of the impurities, $\sigma_{ij}^{tot.sk1} = \sigma_{ij}^{ext.AHE}$ dominates the AHE in a very dilute regime. From Eq. (2.56) we obtain $w_{kk'}^{(3a.m)}$ for a magnetic scattering event and $w_{kk'}^{(3a.nm)}$ for a nonmagnetic scattering event

$$w_{kk'}^{(3a.m)} = w_0^{(3a.m)} \cos\theta \sin\alpha_k, \tag{5.32}$$

$$w_{kk'}^{(3a.nm)} = w_0^{(3a.nm)} \sin\alpha_k, \tag{5.33}$$

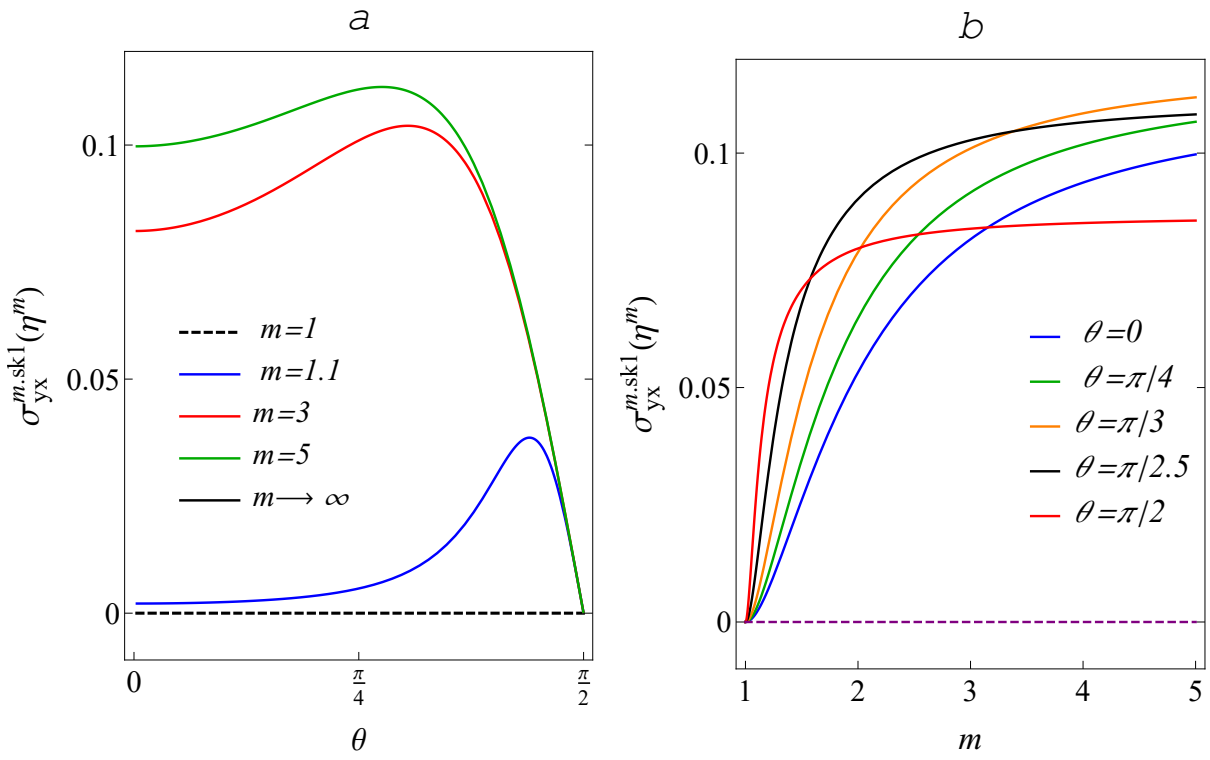

Figure 5.15: $\sigma_{yx}^{m.sk1}$ is plotted in terms of θ and m in panel a and b, respectively.

with $w_0^{(3a.m)} = -\dfrac{\pi\, n_{im} J^3 S_m^3 k^2}{2\,\hbar\,\varepsilon_k}\delta(\varepsilon_k - \varepsilon_{k'})$ and $w_0^{(3a.nm)} = -\dfrac{\pi\, n_{inm} V_0^3 M k^2}{2\,\hbar\,\varepsilon_k^2}\delta(\varepsilon_k - \varepsilon_{k'})$. The factor $\cos\theta$ in the above expression implies that the z component of magnetization is responsible for the conventional skew scattering in our system. In addition the factor $\sin\alpha_k$ shows that the corresponding event is asymmetric under the exchange of indexes $\boldsymbol{k} \longleftrightarrow \boldsymbol{k}'$. The result for non-magnetic scatterers, Eq. (5.33), is again in agreement with the literature (see Eq. (70) in Ref. [24]). Substituting $w_{kk'}^{(3a.m)}$ in Eq. (2.71) gives us the corresponding mean free paths $\lambda_i^{m.a1}(k)(i = 1,2)$, from which we obtain the distribution function $g_k^{m.a1}$ using Eq. (2.68), and subsequently the following corresponding conductivity for scattering off magnetic impurities (for more details see the Appendix 5.C):

$$\sigma_{xy}^{m.sk1} = \eta^m \frac{4(2-g)(\cos 2\theta + m^2)(m^2-1)\cos\theta}{[g\cos 4\theta + 2(g-2)m^2\cos 2\theta + g - 4][(g+2)\cos 2\theta + (g+4)m^2 - 2]}, \tag{5.34}$$

with $\eta^m = \dfrac{\mu}{n_{im} S_m J}$. Also, we show that $\sigma_{yx}^{m.sk1} = -\sigma_{xy}^{m.sk1}$.

Fig. 5.15(a), shows that $\sigma_{yx}^{m.sk1}[\eta^m]$ smoothly increases by increasing θ,

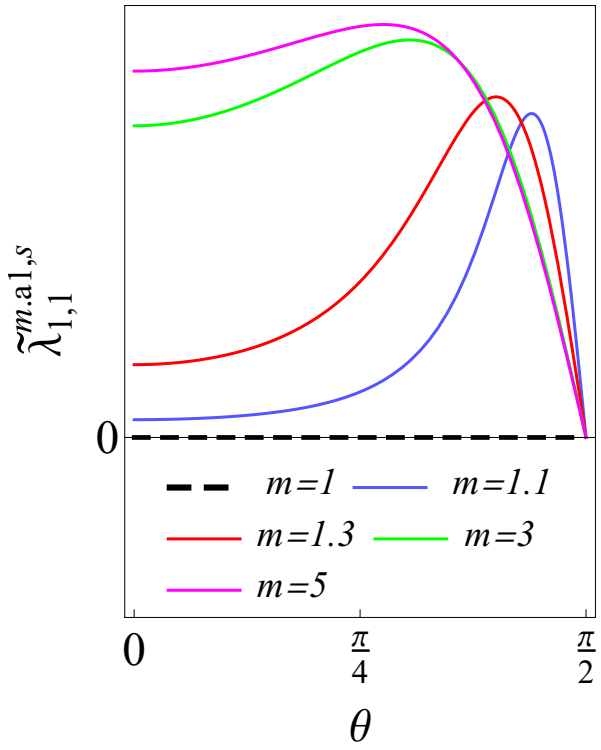

Figure 5.16: Effective mean free path of electrons during extrinsic skew scatterings are plotted against θ, when $\mathbf{E} = E\ \hat{x}$.

until it reaches a maximum in the interval $\frac{\pi}{4} < \theta < \frac{\pi}{2}$. Thereafter it sharply decreases until it vanishes at $\theta = \frac{\pi}{2}$. Panel *b* shows that putting the surface of the system into the insulator regime, i.e. $m = 1$, turns off the transverse conductivity $\sigma^{m.sk1}_{yx}$, regardless of the orientation of the magnetization. For larger values of m, $\sigma^{m.sk1}_{yx}$ increases with increasing m. In addition, as shown by the green curve in panel *a*, the conductivity saturates at $\sigma^{m.sk1}_{yx}(m \to \infty) = \eta^m \frac{\cos\theta}{6 + 3\cos 2\theta}$ for very large values of m. Thus by closing the gap or driving the system into a perfect metallic regime, conventional skew scattering still has a non-zero contribution in the conductivity of the system. This feature reveals one of the main differences between the magnetic skew scattering contribution and the other contributions which vanish in a gapless system or in the perfect metallic regime.

Since the conductivity of electrons during conventional magnetic skew scattering depends on $\mathbf{v}_k$ and $g^{m.a1}_k$ (see Appendix 5.C), its behavior with respect to θ can be easily traced by looking at the behaviour of $\mathbf{v}_k$ and $g^{m.a1}_k$ against θ. As $\mathbf{v}_k$ is independent of θ, studying $g^{m.a1}_k$ against θ is sufficient for this purpose. Considering that $\sigma^{m.sk1}_{yx} = -\sigma^{m.sk1}_{xy}$, we just discuss the dis-

tribution function associated to $\sigma_{yx}^{m.sk1}$, $g_k^{m.a1} = eE\lambda_{1k}^{m.a1}\frac{\partial f^0}{\partial \varepsilon_k}$. Among all terms in the Fourier expansion of $\lambda_{1k}^{m.a1}$, just $\tilde{\lambda}_{1,1}^{m.a1,s} = \frac{Jn_{im}S_m}{\hbar v_F}\lambda_{1,1}^{m.a1,s}$ is relevant. Fig. 5.16 clearly demonstrates that when θ increases, $\tilde{\lambda}_{1,1}^{m.a1,s}$ and consequently the number of electrons participating in the conventional magnetic skew scattering increase very smoothly, and decrease again after a certain value of θ, and further turn off at the $\theta = \frac{\pi}{2}$. Considering the shown trend in Fig. 5.16, the behavior of the contribution of the extrinsic skew scattering in the AHE can be understood.

Repeating the same calculations for the conventional skew scattering contribution due to scattering of non-magnetic impurities, we obtain the following expression for the conductivity

$$\sigma_{yx}^{nm.sk1} = -\sigma_{xy}^{nm.sk1} = \eta^{nm}\frac{(m^2-1)^2}{m(m^2+3)(5+3m^2)}, \tag{5.35}$$

with $\eta^{nm} = \frac{\mu}{n_{inm}V_0}$. The minimum value of $|\sigma_{ij}^{nm.sk1}[m]|$ is obtained in those systems with the Fermi level just above the bottom of the conduction band, and the maximum value is reached in a system with $m = 3.5$. Eq. (5.35) does not coincide completely with Eq. (72) in Ref. [24], which might be due to an extra approximation that is made in Ref. [24]. Like all the previously discussed contributions, this contribution is zero for an insulating surface $m = 1$. In contrast to $\sigma_{ij}^{m.sk1}$, this contribution is absent in the perfect metallic regime $m \to \infty$. Since $\sigma_{ij}^{tot.sk1} = \sigma_{ij}^{m.sk1} + \sigma_{ij}^{nm.sk1} = -\sigma_{ji}^{tot.sk1}$, we just discuss $\sigma_{yx}^{tot.sk1}$ in the remaining part.

Fig. 5.17 shows $\sigma_{yx}^{tot.sk1}[\eta^{nm}]$ in terms of θ and m for two different values of $\nu = \frac{\eta^m}{\eta^{nm}}$, $\nu = 0.1$ and $\nu = 100$ in panels a and b, respectively, for the particular case of $n_{im} = n_{inm}$. It shows that increasing m increases $\sigma_{yx}^{tot.sk1}$, while increasing ν decreases this conductivity. In addition, this contribution becomes insignificant for small values of m, independent of the value of ν and θ. Also note that, in contrary to the total contribution of the side jump and intrinsic skew scattering, the total contribution of the conventional skew scattering never changes its sign, whatever the value of θ, m or E.

There are some experimental and theoretical evidences that the surface magnetization of a TI is preferentially orientated in the plane of the surface or perpendicular to it [6, 40]. For these orientations, $\theta = 0$ and $\frac{\pi}{2}$, $\sigma_{yx}^{tot.sk1}[\eta^{nm}]$

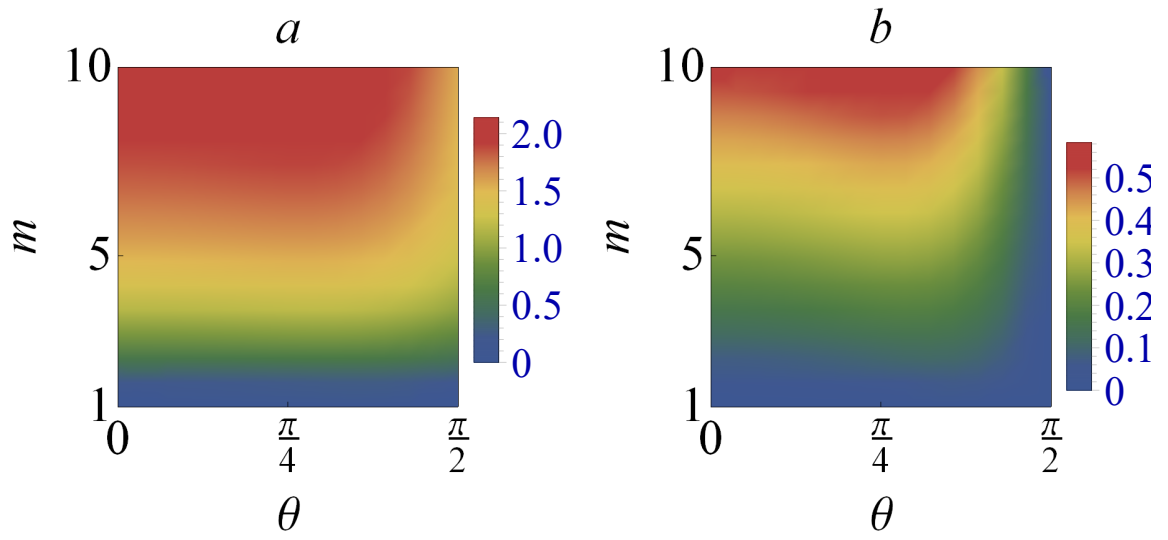

Figure 5.17: $\sigma_{yx}^{tot.sk1}[\eta^{nm}]$ is plotted in terms of θ and m for $\nu = 0.1$ and $\nu = 100$ in panel a and b, respectively.

is given by

$$\sigma_{yx}^{tot.sk1}[\theta = 0] = -\frac{\nu - \nu m^2}{3m^2 + 1} + \frac{m^4 - 2m^2 + 1}{3m^5 + 14m^3 + 15m}, \tag{5.36}$$

$$\sigma_{yx}^{tot.sk1}[\theta = \frac{\pi}{2}] = \frac{\left(m^2 - 1\right)^2}{2\left(3m^4 + 14m^2 + 15\right)}. \tag{5.37}$$

Investigations of the above expressions show that $\sigma_{yx}^{tot.sk1}[\theta = 0]$ does not vary much against m for small values of ν. However, for large ν values, it undergoes a large change with respect to m. Moreover, since the magnetic skew scattering of the Fermi electrons has no contribution to the AHE in a system with in-plane magnetization, the $\sigma_{yx}^{tot.sk1}[\theta = \frac{\pi}{2}]$ does not change with ν.

5.2.3 The intermediate regime

In this regime, extrinsic and intrinsic terms both contribute to the AHE with comparable sizes. Fig. 5.18 is shown to discuss the behavior of the conductivity σ_{ij}^{AHE} in terms of θ and m for some values of $n_{im}(= n_{inm})$ at an arbitrary $\nu = \frac{\eta^m}{\eta^{nm}} = 0.83$. The First and second row present σ_{xy}^{AHE} and σ_{yx}^{AHE}, respectively. In the first, second and third column $n_{im} = 0.4$, 0.7 and 1, respectively. As it is shown in panels a, b and c there is a crossover from the positive values

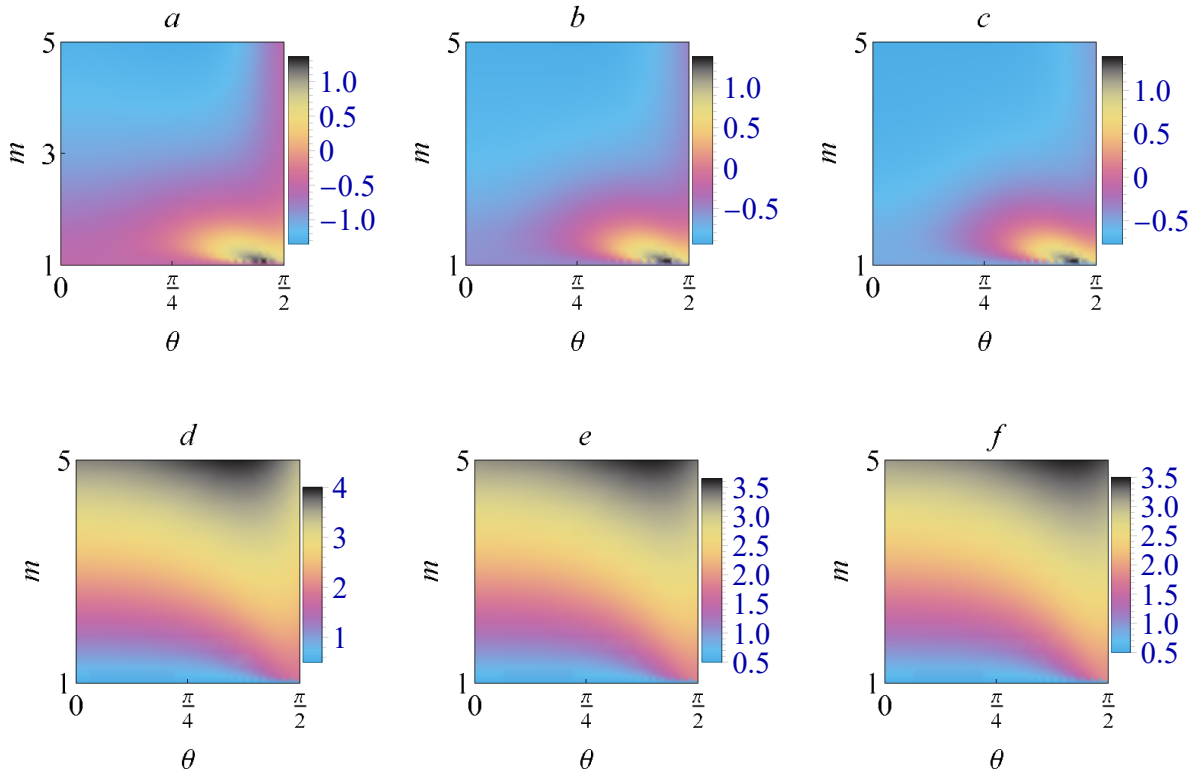

Figure 5.18: σ_{xy}^{AHE} and σ_{yx}^{AHE} are plotted respectively in the first and second row, in terms of θ and m, for some values of n_{im}. First, second and third column correspond to $n_{im} = 0.4$, 0.7 and 1, respectively.

to the negative values for the corresponding conductivity. In addition, the maximum value of σ_{xy}^{AHE} occurs if we place the Fermi level close to the bottom of the conduction band and also adjust the surface magnetization close to $\frac{\pi}{2}$. Surprisingly, in contrast to σ_{xy}^{AHE}, the second row illustrates that σ_{yx}^{AHE} is always positive. This term in panel d, e and f gets its maximum value for large values of m (close to 5) and a magnetization within $\frac{\pi}{4} \leq \theta \leq \frac{\pi}{2}$. Then, although these two components of σ_{ij}^{AHE} behave differently respect to given parameters, they share this feature that they get their maximum value around $\theta \simeq \frac{\pi}{2}$.

Moreover, as all panels in Fig. 5.19 except panels a and d show, σ_{xy}^{AHE} undergoes a sign change with respect to n_{im}. This sign change in the anomalous Hall conductivity has recently been observed experimentally [6]. Remarkably, for specific impurity concentrations, the AHE can two times undergo a sign change by increasing the Fermi level m, as panel b and e of Fig. 5.19 show. This interesting sign change of the AHE is inherited from the non-

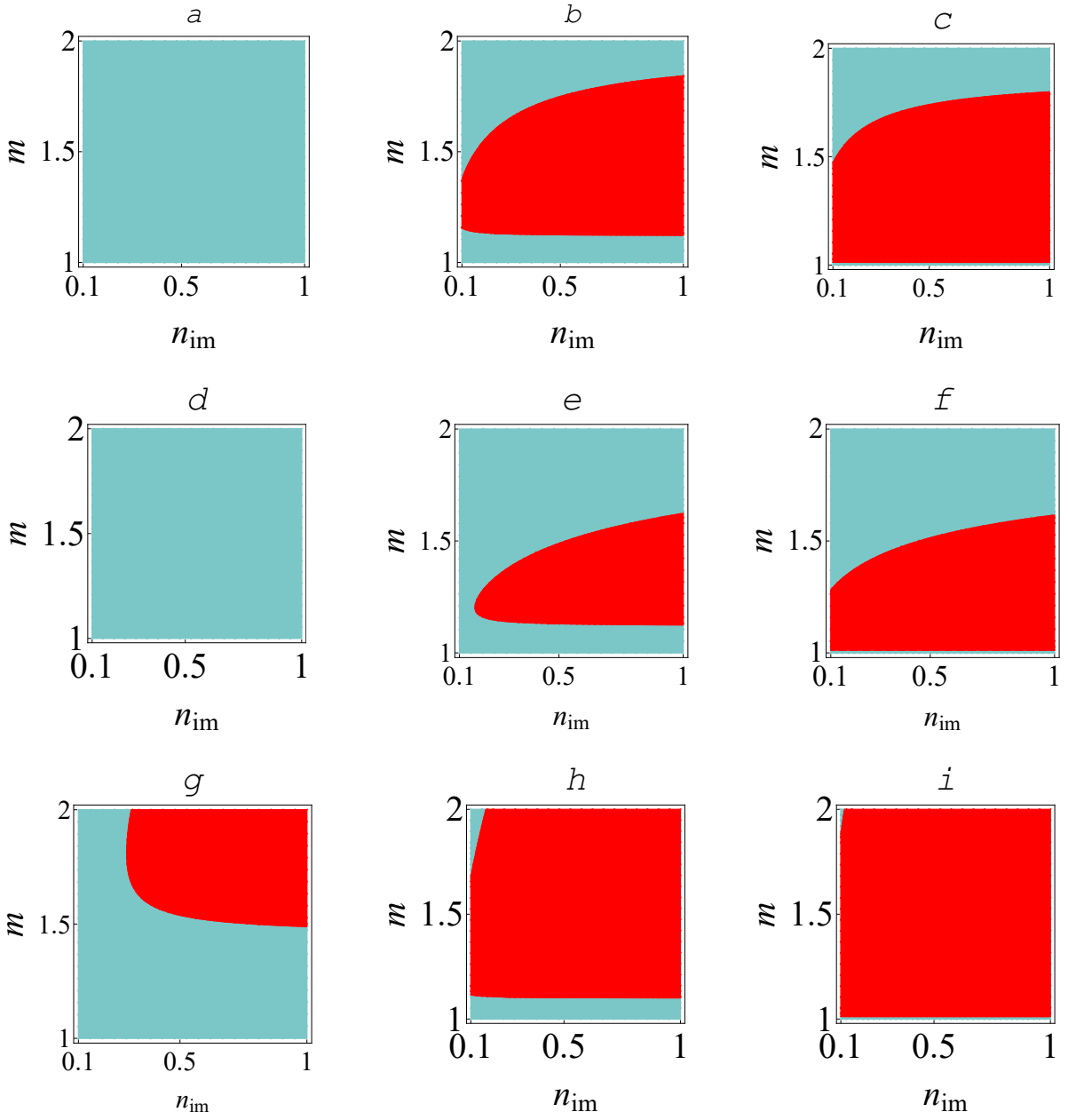

Figure 5.19: σ_{xy}^{AHE} is plotted in terms of n_{im} and m for some values of θ and ν. The cyan part corresponds to negative values of σ_{xy}^{AHE} and the red part corresponds to positive values. The first, second and third row correspond to $\nu = 10$, 0.1 and 0, respectively. Also, first, second and third column correspond to $\theta = \frac{\pi}{6}$, $\frac{\pi}{3}$ and 0.44π, respectively.

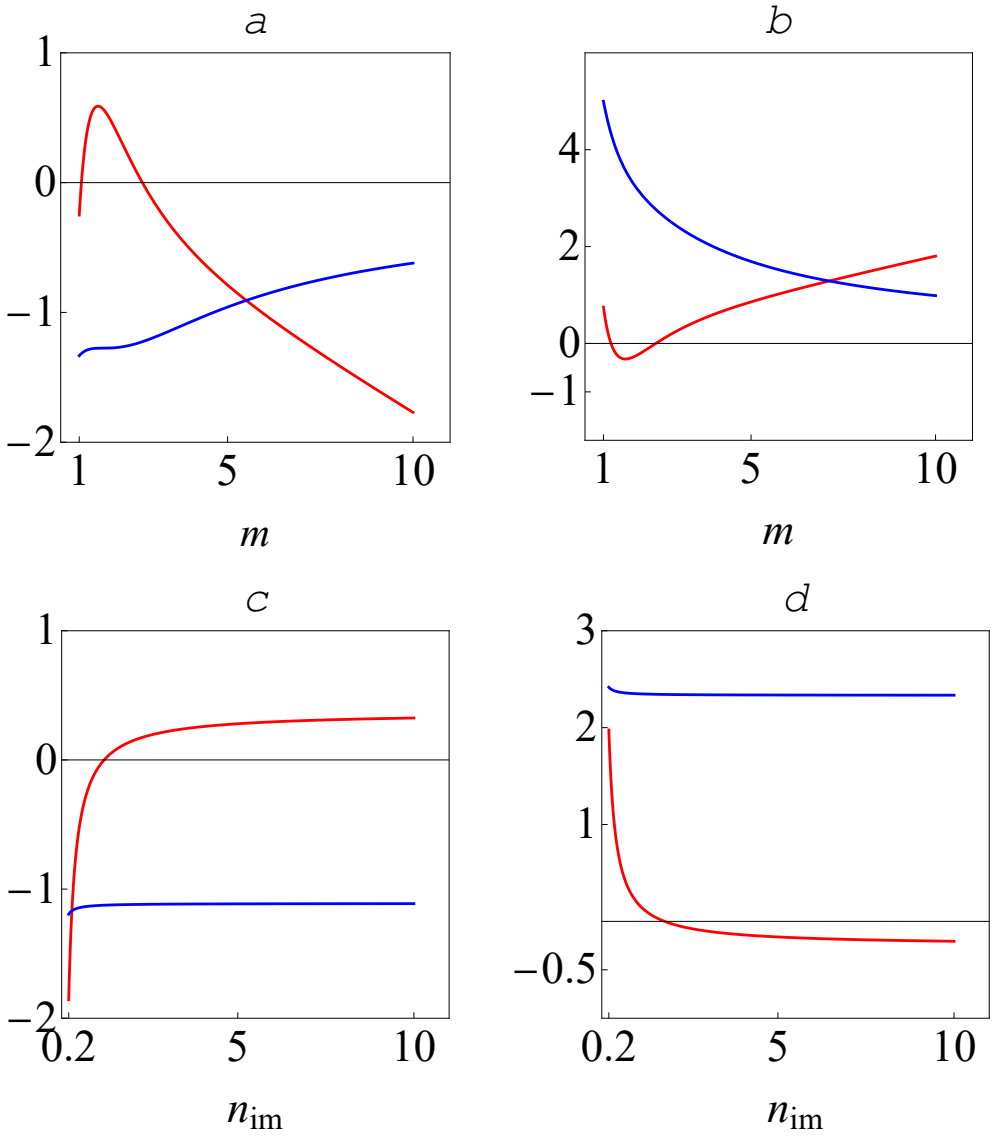

Figure 5.20: σ_{xy}^{AHE} and σ_{yx}^{AHE} are plotted in the first and the second column, respectively. In the first row, these conductivities are plotted against m for $n_{im} = n_{inm} = 1$ and $\nu = 1$. In the second row against n_{im} for $m = 3$ and $\nu = 1$. The red and blue curves correspond to the cases θ=0 and $\frac{\pi}{2}$, respectively. It is clear that, in contrast to the case $\theta = \frac{\pi}{2}$, sign changes occur with respect to m or n_{im} for $\theta = 0$.

monotonic behavior of all the contributions to the AHE. In addition, this non-monotonic behaviour of the AHE distinguishes it from the corresponding reported longitudinal conductivity [33].

Finally, like in previous sections, we briefly discuss the two cases $\sigma_{ij}^{AHE}[\theta = 0]$ and $\sigma_{ij}^{AHE}[\theta = \frac{\pi}{2}]$. All red curves in Fig. 5.20, corresponding to $\sigma_{ij}^{AHE}[\theta = 0]$ undergo a sign change via changing m or n_{im}, in contrary to $\sigma_{ij}^{AHE}[\frac{\pi}{2}]$(blue curve) which does not show such a sign change. Therefore, since the AHE in

this regime is very anisotropic, observing its sign change with respect to m or n_{im}, requires properly adjusting all the involved parameters, the direction of external electric field, the orientation of the surface magnetization, the position of the Fermi level, the concentration of the impurities and also the ratio of the non-magnetic scattering potential to the magnetic scattering potential. In addition, note that in the absence of magnetic impurities, we can write the total AHE as

$$\sigma_{ij}^{AHE} = \sigma_{ij}^{an} + \sigma_{ij}^{tot.nm.sj} + \sigma_{ij}^{nm.sk1} + \sigma_{ij}^{nm.sk2}. \tag{5.38}$$

For $ij = xy$, one can show, based on Eqs. (5.8), (5.22), (5.35) and (5.27), that $\sigma_{xy}^{an} < 0$, $\sigma_{xy}^{tot.nm.sj} < 0$, $\sigma_{xy}^{nm.sk1} < 0$ and $\sigma_{ij}^{nm.sk2} < 0$. Obviously, in the absence of magnetic impurities $\sigma_{xy}^{AHE} < 0$ for all $m \geq 1$. For $ij = yx$, considering that $\sigma_{yx}^{an} = -\sigma_{xy}^{an}$, $\sigma_{yx}^{tot.nm.sj} = -\sigma_{xy}^{tot.nm.sj}$, $\sigma_{yx}^{nm.sk1} = -\sigma_{xy}^{nm.sk1}$ and $\sigma_{yx}^{nm.sk2} = -\sigma_{xy}^{nm.sk2}$, it is clear that in the absence of magnetic impurities $\sigma_{yx}^{AHE} > 0$ for all $m \geq 1$. Therefore, we can conclude that, in the presence of just non-magnetic impurities, the AHE never undergoes a sign change, whatever the direction of E. The absence of this sign change in the AHE in a system with only non-magnetic impurities has been already reported in both the non-crossing [24] as the crossing regime [15].

Table 5.1 and Fig. 5.21 help us to figure out the story behind the observed sign changes in this and previous sections. In case the external electric field is exerted perpendicular to the plane of the surface magnetization, all contributions to the AHE have a positive sign, except the one produced by the magnetic intrinsic skew scattering $\sigma_{ij}^{m.sk2}$ which, depending on (m,θ) can have a positive or negative sign. When the external electric field is exerted parallel to the plane of the surface magnetization, all contributions to the AHE have negative sign, except those arising from the magnetic side jump and the magnetic intrinsic skew scattering. In the first case (i.e. the electric field is along $\hat{x}$), $\sigma_{yx}^{m.sk2}$ has a negative sign only within $0 \leq \theta \leq \frac{\pi}{3}$, as also shown in Fig. 5.10. However, since this negative value is insignificant compared to the sum of the positive terms, the anomalous Hall conductivity always has a persistent positive sign against (m, θ), if $E = E\hat{x}$. Regarding the second case (i.e. the electric field is along $\hat{y}$), all involved mechanisms contribute to the

	Sign of the different contributions to the *AHE*							
Electric field	σ_{ij}^{in}	$\sigma_{ij}^{tot.m.sj}$	$\sigma_{ij}^{tot.nm.sj}$	$\sigma_{ij}^{m.sk1}$	$\sigma_{ij}^{nm.sk1}$	$\sigma_{ij}^{m.sk2}$	$\sigma_{ij}^{nm.sk2}$	AHE
E = E $\hat{x}$	+	+	+	+	+	+ , -	+	+
E = E $\hat{y}$	-	+	-	-	-	+	-	+ , -

Table 5.1: The signs of the different contributions to the AHE are summarized. $E = E\hat{x}$ is perpendicular to the plane of the surface magnetization (yz-plane) and $E = E\hat{y}$ is parallel to the plane of the surface magnetization.

AHE with negative sign except the magnetic side jump and the magnetic intrinsic skew scattering.

Accordingly, depending on the value of m, θ, η^m and η^{nm}, the anomalous Hall conductivity can have a negative or positive sign. In order to produce an anomalous Hall current with persistent sign against any change in θ, m, η^{nm} and η^n, either the sum of the terms with negative sign or the sum of the terms with positive sign should dominate the AHE.

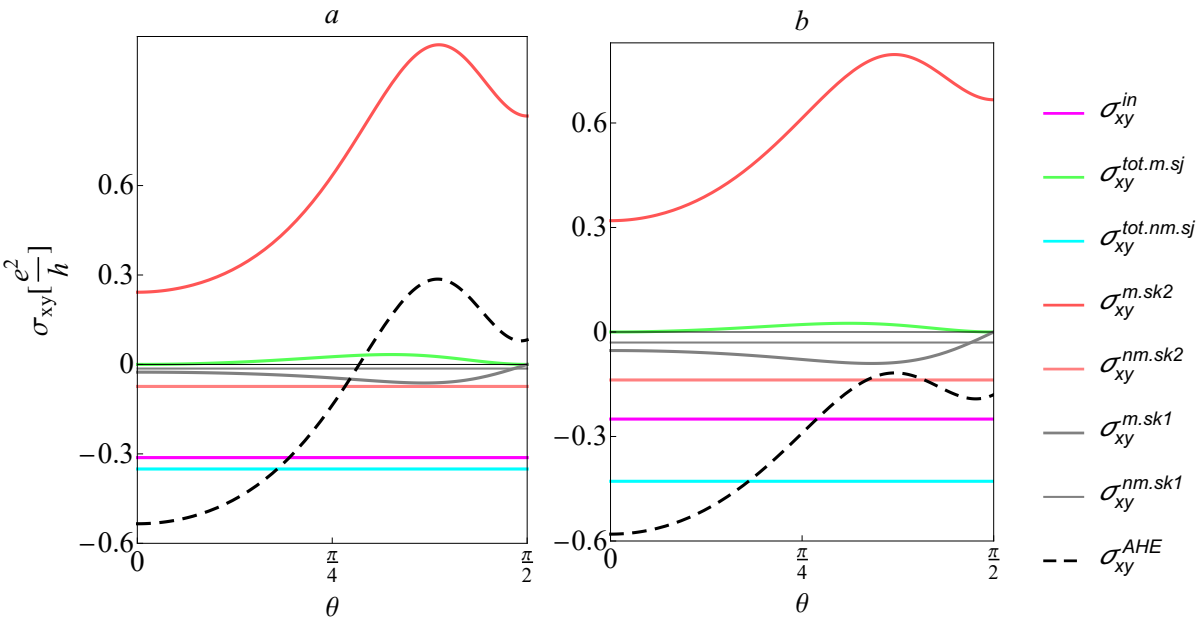

Figure 5.21: All contributions to the AHE (solid lines and the total conductivity (dashed line), plotted against θ. In panel a, $m = 1.6$, $n_{im} = n_{inm} = 1$, $\eta^m = \eta^{nm} = 0.8$ and in panel b, $m = 2$, $n_{im} = n_{inm} = 1$, $\eta^m = \eta^{nm} = 1$.

An example is shown in Fig. 5.21. In panel a, the significant positive

component $\sigma_{xy}^{m.sk2}$ is large enough to overwhelm the sum of the negative contributions and finally imposes a sign change in σ_{xy}^{AHE} via tuning θ around $\frac{\pi}{4}$. Though, if we just increase m from $m = 1.6$ (in panel a) to $m = 2$ (in panel b) and keep the other variables unchanged, the relative importance of $\sigma_{xy}^{m.sk2}$ weakens and eventually leads to the appearance of the AHE with a persistent negative sign, as shown in panel b of this figure.

5.3 Summary

In this chapter, the anomalous Hall conductivity of a 3D TI is investigated systematically using the semi-classical Boltzmann approach along with a modified relaxation time scheme, in terms of the Fermi level (ε_F) and the band gap ($2M$), the spatial orientation of the surface magnetization θ and also the concentration of magnetic and non-magnetic impurities. There are three contributions to the AHE: the intrinsic effect (arising from a nonzero Berry curvature), the side jump effect, and the skew scattering effect. They are competing to dominate the anomalous Hall conductivity of the system. By applying a fully analytical method, we investigate how the spatial orientation of the surface magnetization and also the value of $m = \varepsilon_F/M$ influence the transport of the massive Dirac Fermions on the surface of a 3D TI, doped with a static point like randomly placed, magnetic and non-magnetic impurities.

Since the contribution of non-magnetic impurities to the AHE has been investigated by others before [24], here we mainly focus on the effect of magnetic impurities on the AHE. Concerning the side jump contribution, by tuning the surface magnetization near the TI surface and putting the Fermi level just above the bottom of the conduction band, one can turn off and on the total side jump contribution in the presence of both kinds of impurities.

Next, the contributions coming from conventional and intrinsic skew scattering are investigated. Contrary to the total magnetic side jump contribution, which vanishes in a fully metallic regime, the conductivity corresponding to magnetic conventional skew scattering surprisingly gets its maximal value in this regime. However, similar to the side jump magnetic contribution, it disappears in a system with in-plane magnetization. In the presence of

non-magnetic impurities, the total contribution of the conventional skew scattering is still isotropic, and in the metallic regime, it reaches a significant value if the magnetization is out of the plane.

The skew scattering effect contributes to the AHE through an additional correction, called the intrinsic term. Our results show that, despite the previous conventional contribution, this contribution does not vanish at $\theta = \frac{\pi}{2}$. Besides, this intrinsic contribution disappears at the fully metallic regime, just like the side jump contribution. Remarkably, by applying an external electric field perpendicular to the in-plane component of the magnetization and tuning θ around $\theta = \frac{\pi}{3}$, one can turn off this term.

By considering all these observations, we conclude that in the metallic regime (or the gapless regime), the conventional skew scattering dominates the AHE in a system with a low concentration of magnetic impurities. Out of this very dilute regime, by tuning θ around $\frac{\pi}{2}$ and m around 1 and also exerting an external electric field perpendicular to the in-plane component of the magnetization, the AHE gets its maximal reachable value. Suppose the extrinsic and intrinsic terms contribute to the AHE with comparable sizes (the intermediate regime). In that case, one can observe a sign change in the anomalous Hall conductivity not only via tuning the Fermi level or the spatial orientation of the surface magnetization but surprisingly also via tuning the concentration of the impurities for a specific range of the other parameters. Let us highlight that the found AHE's non-monotonic behavior, which perfectly distinguishes it from the longitudinal conductivity, manifests itself in the found sign change. Besides, this sign change of the AHE does not occur in the absence of magnetic impurities.

To calculate the current density of the system $\mathbf{J} = -e\sum_k \mathbf{v}_k f_k$, we need to find the following three terms in the velocity of the electrons $\mathbf{v}_k = \mathbf{v}_k + \mathbf{v}_k^{an} + \mathbf{v}_k^{sj}$ and also the following five terms in the distribution function of the Dirac fermions $f_k = f^0 + g_k^s + g_k^{a1} + g_k^{a2} + g_k^{ad}$. These terms in the velocity of the electrons are calculated in the main text of this work. The next step is to calculate the equilibrium distribution function of the Dirac fermions. As the dynamics of these fermions during scattering off non-magnetic impurities is isotropic, it can be treated by the widely used relaxation time scheme. Here we go through the details of the calculation of all introduced corrections to the conductivity of the system that arise from scattering by magnetic impurities. Based on Eq. (2.68), in order to find g_k^p, first the associated mean free paths λ_i^p have to be calculated. In section 5.A we first clarify the procedure to obtain $\lambda_i^{m.s}$. In section. 5.B, Sec. 5.C and finally in section. 5.D, we go through the calculation of $\lambda_i^{m.ad}$, $\lambda_i^{m.sk1}$, $\lambda_i^{m.sk2}$, respectively.

5.A Longitudinal magnetic mean free paths

To find the system's longitudinal conductivity, we need to find the distribution function of the electrons during their conventional scattering off magnetic impurities. According to Eq. (2.68) and Eq. (2.69), we arrive at

arrive at

$$v_k \cdot \hat{x_i} = \sum_{k'} w_{kk'}^{(2.m)} \left[\lambda_i^{m.s}(k) - \lambda_i^{m.s}(k')\right], \tag{5.A.1}$$

where $w_{kk'}^{(2.m)}$ is transition rate of magnetic scatterings. Replacing the mean free path with its Fourier expansion $\lambda_i^{m.s}(k,\theta) = \sum_{n=1}^{\infty}[\lambda_i^0(k) + \lambda^{m.s,c}{}_{i,n}(k)\cos n\phi_k +$

$\lambda_{i,n}^{m.s,s}(k)\sin n\phi_k]$ leads to

$$v_{0k}\cdot\hat{x}_i=\sum_{k'}\sum_{n=1}^{\infty}w_{kk'}^{(2.m)}(\ \lambda_i^0+\lambda_{i,n}^{m.s,c}[\cos n\phi_k-\cos n\phi_{k'}]+\lambda_{i,n}^{m.s,s}[\sin n\phi_k-\sin n\phi_{k'}]). \tag{5.A.2}$$

where $\hat{x}_1=\hat{x}$ and $\hat{x}_2=\hat{y}$. Before continuing our discussion, note that conservation of the number of particles imposes

$$N=\sum_k f_k^0=\sum_k(f_k^0+g_k^s+g_k^{ad}+g_k^{a1}+g_k^{a2}). \tag{5.A.3}$$

Therefore, $\sum_k\ (g_k^s+g_k^{ad.}+g_k^{a1}+g_k^{a2})=0$, and hence all the constant terms in the Fourier expansions for λ_i^0 are zero. After some calculations we obtain

$$\lambda_i^{m.s}(k,\theta)=\frac{\alpha_i^{m.s,0}+(\alpha_i^{m.s,c}+\delta_{i,1})\cos\phi_k+(\alpha_i^{m.s,s}+\delta_{i,2})\sin\phi_k}{2(\beta_k\cos\phi_k+1)\left(\gamma_k^2\cos 2\theta+1\right)}\lambda_0^{m.s}, \tag{5.A.4}$$

where $\lambda_0^{m.s}=\frac{4\hbar^3v_F^3\sqrt{1-\gamma_k^2}}{n_{im}J^2S_m^2\varepsilon_k}$, $\beta_k=\dfrac{\gamma_k\sqrt{1-\gamma_k^2}\sin 2\theta}{\gamma_k^2\cos 2\theta+1}$, $\alpha_i^{m.s,s}=(\gamma_k^2-1)\dfrac{\lambda_{i,1}^{m.s,s}}{\lambda_0^{m.s}}$, and $\alpha_i^{m.s,0}=\gamma_k\sqrt{1-\gamma_k^2}\sin 2\theta\ \dfrac{\lambda_{i,1}^{m.s,c}}{\lambda_0^{m.s}}$, $\alpha_i^{m.s,c}=\left(1-\gamma_k^2\right)\left(2\sin^2\theta-1\right)\dfrac{\lambda_{i,1}^{m.s,c}}{\lambda_0^{m.s}}$. As it is clear from the equations above, $\lambda_{i,1}^{m.s,c}$ and $\lambda_{i,1}^{m.s,s}$ are the only two required Fourier coefficients of $\lambda_i^{m.s}$, as the other higher order Fourier coefficients ($n>1$) are a function of these two primary coefficients. These crucial Fourier coefficients can be obtained straightforwardly as follows:

$$\begin{cases}\pi\lambda_{i,1}^{m.s,c}-\int_0^{2\pi}\dfrac{\alpha_i^{m.s,0}+(\alpha_i^{m.s,c}+\delta_{i,1})\cos\phi_k+(\alpha_i^{m.s,s}+\delta_{i,2})\sin\phi_k}{2(\beta_k\cos\phi_k+1)\left(\gamma_k^2\cos 2\theta+1\right)}\lambda_0^{m.s}\cos\phi_k d\phi_k=0\\ \pi\lambda_{i,1}^{m.s,s}-\int_0^{2\pi}\dfrac{\alpha_i^{m.s,0}+(\alpha_i^{m.s,c}+\delta_{i,1})\cos\phi_k+(\alpha_i^{m.s,s}+\delta_{i,2})\sin\phi_k}{2(\beta_k\cos\phi_k+1)\left(\gamma_k^2\cos 2\theta+1\right)}\lambda_0^{m.s}\sin\phi_k d\phi_k=0\end{cases}. \tag{5.A.5}$$

After solving the above set of integral equations, we arrive at:

$$\lambda_{1,1}^{m.s,c}=\frac{4\ \hbar^3v_F^3}{n_{im}J^2S_m^2\varepsilon_k}\frac{\sqrt{1-\gamma_k^2}}{1+\Gamma_k+\left(1+\Gamma_k\gamma_k^2\right)\cos 2\theta}\ ,\lambda_{1,1}^{m.s,s}=0, \tag{5.A.6}$$

$$\lambda_{2,1}^{m.s,c}=0,\qquad\lambda_{2,1}^{m.s,s}=\frac{4\ \hbar^3v_F^3}{n_{im}J^2S_m^2\varepsilon_k}\frac{\sqrt{1-\gamma_k^2}}{1-\gamma_k^2+(1+\Gamma_k)(1+\gamma_k^2\cos 2\theta)}\ , \tag{5.A.7}$$

where $\Gamma = \left(1 - \frac{\gamma_k^2(1-\gamma_k^2)\sin^2 2\theta}{(1+\gamma_k^2\cos 2\theta)^2}\right)^{1/2}$. Putting the found nonzero Fourier coefficient $\lambda_{1,1}^{m.s,c}$ and $\lambda_{2,1}^{m.s,s}$ in Eq. (5.A.4) gives

$$\lambda_1^{m.s} = \frac{A_k\cos\phi_k + \gamma_k\sin 2\theta\sqrt{1-\gamma_k^2}}{[1+\beta_k\cos\phi_k][1+\gamma_k^2\cos 2\theta][A+[1-\gamma_k^2]\cos 2\theta]}\frac{\lambda_0^{m.s}}{2}, \tag{5.A.8}$$

$$\lambda_2^{m.s} = \frac{(1+\Gamma_k)\sin\phi_k}{[1+\beta_k\cos\phi_k][1+A_k-\gamma_k^2]}\frac{\lambda_0^{m.s}}{2}, \tag{5.A.9}$$

where $A_k = (1+\Gamma_k)(1+\gamma_k^2\cos 2\theta)$. Therefore, the resultant correction to the distribution function of the electrons due to the conventional scattering of electrons from magnetic impurities is

$$g_k^{m.s} = eE\left[\frac{A_k\cos\phi_k + \gamma_k\sin 2\theta\sqrt{1-\gamma_k^2}}{[1+\beta_k\cos\phi_k][1+\gamma_k^2\cos 2\theta][A_k+[1-\gamma_k^2]\cos 2\theta]}\frac{\lambda_0^{m.s}}{2}\cos\chi + \frac{(1+\Gamma_k)\sin\phi_k}{[1+\beta_k\cos\phi_k][1+A_k-\gamma_k^2]}\frac{\lambda_0^{m.s}}{2}\sin\chi\right]\partial_{\varepsilon_k}f^0\,. \tag{5.A.10}$$

5.B Side jump associated mean free paths

As it was indicated in the main text, electrons during scattering off magnetic impurities undergo a side jump which changes the velocity of the electrons and also their distribution function. This leads to the following two corrections to the conductivity $\sigma_{ij}^{m.sj}$, $\sigma_{ij}^{m.ad}$. Since we have already found the associated distribution function $g_k^{m.s}$, we needn't to calculate $\sigma_{ij}^{m.sj}$, thus in this section we just present the details of calculating $\sigma_{ij}^{m.ad}$. As before, we ignore the side jump of the electrons during their skew scattering. As we did to calculate $g_k^{m.ad}$, we replace $\lambda_i^{m.ad}$ in Eq. 2.70 with their Fourier expansions $\lambda_i^{m.ad}(k,\theta) = \sum_{n=1}^{\infty}[\lambda_{i,n}^{m.ad,c}\cos n\phi_k + \lambda_{i,n}^{m.ad,s}\sin n\phi_k]$. By assuming that the external electric field is exerted along $\hat{x}_i$, Eq. (2.70) is converted into

$$v_k^{m.sj}\cdot\hat{x}_i = \sum_{k'}\sum_{n=1}^{\infty} w_{kk'}^{(2.m)}(\ \lambda_{i,n}^{m.ad,c}[\cos n\phi_k - \cos n\phi_{k'}] + \lambda_{i,n}^{m.ad,s}[\sin n\phi_k - \sin n\phi_{k'}]). \tag{5.B.1}$$

Using the already found functions $\mathbf{v}_k^{m.sj}$ in Eq. (5.13) and using Eq. (5.11), we arrive at

$$\lambda_i^{m.ad}(k,\theta)=\frac{\alpha_i^{m.ad,0}+[\alpha_i^{m.ad,c}-\delta_{i,2}]\cos\phi_k+(\alpha_i^{m.ad,s}+[2-\cos 2\theta]\,\delta_{i,1})\sin\phi_k}{2[\beta_k\cos\phi_k+1][\gamma_k^2\cos 2\theta+1]}\lambda_0^{m.ad}, \tag{5.B.2}$$

where $\alpha_i^{m.ad,0}=\gamma_k\sqrt{1-\gamma_k^2}\sin 2\theta\ \dfrac{\lambda_{i,1}^{m.ad,c}}{\lambda_0^{m.ad}}$, $\alpha_i^{m.ad,c}=\left(1-\gamma_k^2\right)\left(2\sin^2\theta-1\right)\dfrac{\lambda_{i,1}^{m.ad,c}}{\lambda_0^{m.ad}}$, $\alpha_i^{m.ad,s}=(\gamma_k^2-1)\dfrac{\lambda_{i,1}^{m.ad,s}}{\lambda_0^{m.ad}}$ and $\lambda_0^{m.ad}=\frac{\hbar v_F}{2\varepsilon_k}\gamma_k\sqrt{1-\gamma_k^2}$. Finally we have to solve the set of equations

$$\begin{cases}\pi\lambda_{i,1}^{m.ad,c}-\int_0^{2\pi}\dfrac{\alpha_i^{m.ad,0}+[\alpha_i^{m.ad,c}-\delta_{i,2}]\cos\phi_k+(\alpha_i^{m.ad,s}+[2-\cos 2\theta]\,\delta_{i,1})\sin\phi_k}{2[\beta_k\cos\phi_k+1][\gamma_k^2\cos 2\theta+1]}\lambda_0^{m.ad}\cos\phi_k\,d\phi_k=0\\ \pi\lambda_{i,1}^{m.ad,s}-\int_0^{2\pi}\dfrac{\alpha_i^{m.ad,0}+[\alpha_i^{m.ad,c}-\delta_{i,2}]\cos\phi_k+(\alpha_i^{m.ad,s}+[2-\cos 2\theta]\,\delta_{i,1})\sin\phi_k}{2[\beta_k\cos\phi_k+1][\gamma_k^2\cos 2\theta+1]}\lambda_0^{m.ad}\sin\phi_k\,d\phi_k=0\end{cases}. \tag{5.B.3}$$

Their solution is

$$\lambda_{1,1}^{m.ad,s}=\frac{[\sqrt{1-\beta_k^2}-1][\cos 2\theta-2]}{\beta_k^2[1+\gamma_k^2\cos 2\theta]+[\sqrt{1-\beta_k^2}-1][\gamma_k^2-1]}\lambda_0^{m.ad},\quad \lambda_{1,1}^{m.ad,c}=0, \tag{5.B.4}$$

$$\begin{aligned}&\lambda_{2,1}^{m.ad,c}=-\frac{1}{[\,[\sqrt{1-\beta_k^2}-\beta_k^2]\gamma_k^2+1]\cos 2\theta-\beta_k^2+\sqrt{1-\beta_k^2}+\beta_k\gamma_k\sqrt{1-\gamma_k^2}\sin 2\theta+1}\lambda_0^{m.ad},\\ &\lambda_{2,1}^{m.ad,s}=0.\end{aligned} \tag{5.B.5}$$

Inserting $\lambda_{1,1}^{m.ad,s}$ and $\lambda_{2,1}^{m.ad,c}$ in Eq. (5.B.2) leads to

$$\lambda_1^{m.ad}(k,\theta)=\frac{(2-\cos 2\theta)\sin\phi_k}{\left(1+\gamma_k^2\cos 2\theta+\beta_k^{-1}[\sqrt{1-\beta_k^2}-1][\gamma_k^2-1]\right)\,[1+\beta_k\cos\phi_k]}\lambda_0^{m.ad}, \tag{5.B.6}$$

$$\lambda_2^{m.ad}(k,\theta)=-\frac{\gamma_k\sqrt{1-\gamma_k^2}\sin 2\theta+c_k\,\cos\phi_k}{2[1+\beta_k\cos\phi_k][1+\gamma_k^2\cos 2\theta][c_k+(1-\gamma_k^2)\cos 2\theta]}\lambda_0^{m.ad}, \tag{5.B.7}$$

where $c_k=(1-\beta_k^2+\sqrt{1-\beta_k^2})(1+\gamma_k^2\cos 2\theta)+\beta_k\gamma_k\sqrt{1-\gamma_k^2}\sin 2\theta$.

Finally, the associated correction to the distribution function of the electrons arising from the side jump can be written as, based on Eq. (2.68),

$$g_k^{m.ad} = \frac{eE\lambda_0^{m.ad}\partial_{\varepsilon_k} f^0}{[1+\beta_k\cos\phi_k]} \frac{(2-\cos 2\theta)\sin\phi_k\cos\chi}{(1+\gamma_k^2\cos 2\theta+\beta_k^{-1}[\sqrt{1-\beta_k^2}-1][\gamma_k^2-1])} - \frac{eE\lambda_0^{m.ad}\partial_{\varepsilon_k} f^0}{[1+\beta_k\cos\phi_k]} \frac{\gamma_k\sqrt{1-\gamma_k^2}\sin 2\theta + c_k\ \cos\phi_k}{2[1+\gamma_k^2\cos 2\theta][c_k+(1-\gamma_k^2)\cos 2\theta]}\sin\chi] \tag{5.B.8}$$

5.C Conventional skew scattering associated mean free path

The conventional and intrinsic skew scattering contribute to the conductivity of the system via changing the distribution function of the electrons, as the velocity of the electrons does not change, in contrary to the side jump effect. Based on Eq. (2.64)

$$g_k^{m.a1} = \frac{\sum_{k'} w_{kk'}^{(2.m)} g_{k'}^{m.a1} + \sum_{k'} w_{kk'}^{(3a.m)} \left(g_{k'}^{m.s} - g_k^{m.s}\right)}{\sum_{k'} w_{kk'}^{(2.m)}}. \tag{5.C.1}$$

Since $g_k^{m.s}$ has been already found, we just need to find $g_k^{m.a1}$. By using Eq. (5.32), it can be straightforwardly proven that $\sum_{k'} w_{kk'}^{(3a.m)} = 0$. Therefore Eq. (5.C.1) can be rewritten in terms of the mean free paths as

$$\lambda_i^{m.a1}(k,\theta) = \frac{\sum_{k'} w_{kk'}^{(3a.m)} \lambda_i^{m.s}(k',\theta) + \sum_{k'} w_{kk'}^{(2.m)} \lambda_i^{m.a1}(k',\theta)}{\sum_{k'} w_{kk'}^{(2.m)}}. \tag{5.C.2}$$

Using expansions $\lambda_i^{m.a1}(k,\theta) = \sum_{n=1}^{\infty}[\lambda^{m.a1,c}{}_{i,n}(k)\cos n\phi_k + \lambda_{i,n}^{m.a1,s}(k)\sin n\phi_k]$, we get

$$\lambda_i^{m.a1}(k,\theta) = \frac{\alpha_i^{m.a1,0} + [\alpha_i^{m.a1,c} - \delta_{i,2}\frac{Js_m\cos\theta\ k^2}{2\varepsilon_k}\lambda_{i,1}^{m.s,s}]\cos\phi_k + [\alpha_i^{m.a1,s} + \delta_{i,1}\frac{Js_m\cos\theta\ k^2}{2\varepsilon_k}\lambda_{i,1}^{m.s,c}]\sin\phi_k}{2(1+\gamma_k^2\cos 2\theta)(1+\beta_k\cos\phi_k]}, \tag{5.C.3}$$

where $\alpha_i^{m.a1,0} = \gamma_k\sqrt{1-\gamma_k^2}\sin 2\theta\ \lambda_{i,1}^{m.a1,c}$, $\alpha_i^{m.a1,c} = \left(1-\gamma_k^2\right)\left(2\sin^2\theta - 1\right)\lambda_{i,1}^{m.a1,c}$, $\alpha_i^{m.a1,s} = (\gamma_k^2-1)\lambda_{i,1}^{m.a1,s}$. Four unknown crucial Fourier coefficients $\lambda_{i,1}^{m.a,c}$ and

$\lambda_{i,1}^{m.a1,s}$ can be found through solving a set of equations such Eq. (5.A.5) and Eq. (5.B.3). After solving this set of equations, we arrive at

$$\lambda_{1,1}^{m.a1,s} = \frac{\hbar v_F}{J n_{im} S_m} \frac{2(1-\gamma_k^2)\sqrt{1-\gamma_k^2}\ \cos\theta}{[1+\Gamma_k+\cos 2\theta+\gamma_k^2\ \Gamma_k \cos 2\theta][2+\Gamma_k+\gamma_k^2\ \Gamma_k \cos 2\theta-2\gamma^2\sin^2\theta]}, \tag{5.C.4}$$

$$\lambda_{2,1}^{m.a1,c} = \frac{\hbar v_F}{J n_{im} S_m} \frac{4(1-\Gamma_k)\sqrt{1-\gamma_k^2}(1+\gamma_k^2\cos 2\theta)\ \cos\theta}{[\gamma_k^2(\Gamma_k+1)\cos 2\theta-\gamma_k^2+\Gamma_k+2][\gamma_k^2(\Gamma_k\cos 4\theta+\Gamma_k-2)+2(\Gamma_k-1)\cos 2\theta]}, \tag{5.C.5}$$

and $\lambda_{1,1}^{m.a1,c} = \lambda_{2,1}^{m.a1,s} = 0$. Inserting the resultant non-zero Fourier coefficients in Eq. (5.C.3), one obtains the mean free paths of the electrons during magnetic conventional skew scattering:

$$\lambda_1^{m.a1}(k,\theta) = -\frac{\hbar v_F}{J S_m n_{im}} \frac{(1+\Gamma_k)\ \cos\theta\ \sin\phi_k}{[(\Gamma_k\gamma_k^2+1)\cos 2\theta+\Gamma_k+1][p_k+p_k\beta_k\cos\phi_k]}, \tag{5.C.6}$$

$$\lambda_2^{m.a1}(k,\theta) = \frac{\hbar v_F}{J S_m n_{im}} \frac{\cos\theta\{[(4-4\Gamma_k)\cos 2\theta+(2\Gamma_k-3)\gamma_k^2+(2\Gamma_k-1)\gamma_k^2\cos 4\theta]\cos\phi_k+B_k\}}{[1+\gamma_k^2\cos 2\theta]\ [\Gamma_k\gamma_k^2\cos 4\theta+(2\Gamma_k-2)\cos 2\theta+(\Gamma_k-2)\gamma_k^2][p_k+p_k\beta\cos\phi_k]}, \tag{5.C.7}$$

$p_k = \{\gamma^2[(\Gamma_k+1)\cos 2\theta-1]+\Gamma_k+2\}(1-\gamma_k^2)^{-3/2}$, $B_k = 2(1-\gamma_k^2)^{-1/2}\gamma_k(\Gamma_k-1)(1+\gamma_k^2\cos 2\theta)\sin 2\theta$.

Finally, the associated correction to the distribution function of the electrons arising from the side jump can be written, based on Eq. (2.68), as

$$g_k^{m.a1} = \alpha^{m.a1}\left(\frac{[(4-4\Gamma_k)\cos 2\theta-2\gamma_k^2+(2\Gamma_k-1)\gamma_k^2(\cos 4\theta+1)]\cos\phi_k+B_k}{(1+\gamma_k^2\cos 2\theta)\ (\Gamma_k\gamma_k^2\cos 4\theta+(2\Gamma_k-2)\cos 2\theta+(\Gamma_k-2)\gamma_k^2)}\sin\chi - \frac{(1+\Gamma_k)\ \ \sin\phi_k\cos\chi}{(\Gamma_k\gamma_k^2+1)\cos 2\theta+\Gamma_k+1}\right), \tag{5.C.8}$$

with $\alpha^{m.a1} = \dfrac{eE\partial_{\varepsilon_k}f^0}{p_k+p_k\beta_k\cos\phi_k}\dfrac{\hbar v_F}{J S_m n_{im}}$.

5.D Intrinsic skew scattering associated mean free path

Like the conventional skew scattering, this contribution to the skew scattering just alters the distribution function of the electrons and leaves the velocity of

the electrons unchanged. Using Eq. (2.66), which connects the conventional magnetic scattering of electrons to their intrinsic magnetic skew scattering, we arrive at

$$\sum_{k'} w_{kk'}^{(4m)} \left[\lambda_i^{m.s}(k) - \lambda_i^{m.s}(k')\right] + \sum_{k'} w_{kk'}^{(2.m)} \left[\lambda_i^{m.a2}(k) - \lambda_i^{m.a2}(k')\right] = 0, \tag{5.D.1}$$

which after rewriting gives

$$\lambda_i^{m.a2} = \frac{\sum_{k'} w_{kk'}^{(2.m)} \lambda_i^{m.a2}(k') + w_{kk'}^{(4.m)} \left[\lambda_i^{m.s}(k') - \lambda_i^{m.s}(k)\right]}{\sum_{k'} w_{kk'}^{(2.m)}}. \tag{5.D.2}$$

Applying the Fourier expansions of the mean free paths $\lambda_i^{m.a2}$ as $\lambda_i^{m.a2}(k) = \sum_{n=1}^{\infty}[\lambda_{i,n}^{m.a2,c} \cos n\phi_k + \lambda_{i,n}^{m.a2,s} \sin n\phi_k]$ leads to

$$\lambda_i^{m.a2} = \frac{\sum_{k',n} w_{kk'}^{(2.m)} [\lambda_{i,n}^{m.a2,c} \cos n\phi_{k'} + \lambda_{i,n}^{m.a2,s} \sin n\phi_{k'}] + \sum_{k'} w_{kk'}^{(4.m)} \left[\lambda_i^{m.s}(k') - \lambda_i^{m.s}(k)\right]}{\sum_{k'} w_{kk'}^{(2.m)}}. \tag{5.D.3}$$

Using the already found $w_{kk'}^{(2.m)}$, $w_{kk'}^{(4.m)}$ and $\lambda_i^{m.s}(k')$, we arrive at

$$\begin{aligned}
\lambda_i^{m.a2} = & \left([\gamma_k^3 - \gamma_k]\left([2\cos 2\theta + 1]\lambda_{i,1}^{m.s.c} \sin\phi_k - \lambda_{i,1}^{m.s.s} [\cos 2\theta + 2]\cos\phi_k\right) - \gamma_k^2\sqrt{1-\gamma_k^2}\ \lambda_{i,1}^{m.s.s} \sin 2\theta\right) \alpha_1^{m.a2} \\
& + \left(\frac{1}{2}[\gamma_k^2 - 1]\ \lambda_{i,1}^{m.a2.s} \sin\phi_k + \frac{1}{2}[\gamma_k^2 - 1]\ \lambda_{i,1}^{m.a2.c} \cos 2\theta \cos\phi_k + \frac{1}{2}\gamma_k\sqrt{1-\gamma_k^2}\ \lambda_{i,1}^{m.a2.c} \sin 2\theta\right) \alpha_0^{m.a2} \\
& - 4\ \lambda_i^{m.s}\gamma_k\sqrt{1-\gamma_k^2} \sin\phi_k \sin 2\theta\ \alpha_1^{m.a2},
\end{aligned} \tag{5.D.4}$$

where

$$\alpha_0^{m.a2} = \frac{1}{\gamma_k^2 \cos 2\theta + \gamma_k\sqrt{1-\gamma_k^2} \sin 2\theta \cos\phi_k + 1}, \tag{5.D.5}$$

and

$$\alpha_1^{m.a2} = \frac{n_{im} J^2 S_m^2}{8\hbar^2 v_F^2} \frac{1}{\gamma_k^2 \cos 2\theta + \gamma_k\sqrt{1-\gamma_k^2} \sin 2\theta \cos\phi_k + 1}. \tag{5.D.6}$$

These two crucial non-zero Fourier coefficients $\lambda_{1,1}^{m.s,c}$ and $\lambda_{2,1}^{m.s,s}$ are given in Eq. (5.A.6) and Eq. (5.A.7). Four unknown crucial Fourier coefficients $\lambda_{i,1}^{m.a2,c}$

and $\lambda_{i,1}^{m.a2,s}$ can be obtained by solving a set of equations as we did in Eq. (5.A.5) or Eq. (5.B.3). After solving this set of equations, we arrive at

$$\lambda_{1,1}^{m.a2.s}[\frac{\hbar v_F}{\varepsilon_k}]=\frac{8(\gamma_k-\Gamma_k\gamma_k)\left(\gamma_k^4(\Gamma_k-2)(\Gamma_k+1)+\gamma_k^2(\Gamma_k-1)\left(\gamma_k^2\Gamma_k+1\right)\cos 4\theta-\xi_k\cos 2\theta+\gamma_k^2+2\Gamma_k^2+\Gamma_k-2\right)}{\Gamma_k\sqrt{1-\gamma_k^2}\left([\gamma_k^2\Gamma_k+1]\cos 2\theta+\Gamma_k+1\right)\left((\cos 2\theta[\Gamma_k-1]-\sin^2 2\theta\,)\gamma_k^2+\Gamma_k-1\right)}, \tag{5.D.7}$$

$$\lambda_{2,1}^{m.a2.c}[\frac{\hbar v_F}{\varepsilon_k}]=\frac{16\gamma_k\sqrt{1-\gamma_k^2}[\Gamma_k-1]\left(-\gamma_k^2\cos 4\theta+[2\gamma_k^2+1]\cos 2\theta+2\gamma_k^2+2\right)}{\left(\gamma_k^2(\Gamma_k+1)\cos 2\theta-\gamma_k^2+\Gamma_k+2\right)\left(\gamma_k^2(\Gamma_k\cos 4\theta+\Gamma_k-2)+2(\Gamma_k-1)\cos 2\theta\right)}, \tag{5.D.8}$$

where $\xi_k=\gamma_k^2\left(\Gamma_k[\gamma_k^2-4\Gamma_k+1]+4\right)-2\Gamma_k$, $\lambda_{1,1}^{m.a2.c}=\lambda_{2,1}^{m.a2.s}=0$. We can express the correction to the distribution function of the electrons due to the magnetic intrinsic skew scattering as

$$\begin{aligned}
g_k^{m.a2} =&\left([\gamma_k^3-\gamma_k]([2\cos 2\theta+1]\lambda_{1,1}^{m.s.c}\sin\phi_k-\lambda_{1,1}^{m.s.s}\,[\cos 2\theta+2]\cos\phi_k)-\gamma_k^2\sqrt{1-\gamma_k^2}\;\lambda_{1,1}^{m.s.s}\;\sin 2\theta\right)\alpha_2^{m.a2}\\
&+\left(\frac{1}{2}[\gamma_k^2-1]\;\lambda_{1,1}^{m.a2.s}\sin\phi_k+\frac{1}{2}[\gamma_k^2-1]\;\lambda_{1,1}^{m.a2.c}\;\cos 2\theta\cos\phi_k+\frac{1}{2}\gamma_k\sqrt{1-\gamma_k^2}\;\lambda_{1,1}^{m.a2.c}\;\sin 2\theta\right)\alpha_3^{m.a2}\\
&-4\;\lambda_1^{m.s}\gamma_k\sqrt{1-\gamma_k^2}\sin\phi_k\sin 2\theta\;\alpha_2^{m.a2}\\
&+\left([\gamma_k^3-\gamma_k]([2\cos 2\theta+1]\lambda_{2,1}^{m.s.c}\sin\phi_k-\lambda_{2,1}^{m.s.s}\,[\cos 2\theta+2]\cos\phi_k)-\gamma_k^2\sqrt{1-\gamma_k^2}\;\lambda_{2,1}^{m.s.s}\;\sin 2\theta\right)\alpha_4^{m.a2}\\
&+\left(\frac{1}{2}[\gamma_k^2-1]\;\lambda_{2,1}^{m.a2.s}\sin\phi_k+\frac{1}{2}[\gamma_k^2-1]\;\lambda_{2,1}^{m.a2.c}\;\cos 2\theta\cos\phi_k+\frac{1}{2}\gamma_k\sqrt{1-\gamma_k^2}\;\lambda_{2,1}^{m.a2.c}\;\sin 2\theta\right)\alpha_5^{m.a2}\\
&-4\;\lambda_2^{m.s}\gamma_k\sqrt{1-\gamma_k^2}\sin\phi_k\sin 2\theta\;\alpha_4^{m.a2},
\end{aligned} \tag{5.D.9}$$

$\alpha_2^{m.a2}=eE\partial_{\varepsilon_k}f^0\alpha_1^{m.a2}\cos\chi$, $\alpha_3^{m.a2}=eE\partial_{\varepsilon_k}f^0\alpha_0^{m.a2}\cos\chi$, $\alpha_4^{m.a2}=eE\partial_{\varepsilon_k}f^0\alpha_1^{m.a2}\sin\chi$, $\alpha_5^{m.a2}=eE\partial_{\varepsilon_k}f^0\alpha_0^{m.a2}\sin\chi$.

As we already proved $\lambda_{1,1}^{m.s,s}=0$ and $\lambda_{2,1}^{m.s,c}=0$, finally we can write the final expression for the correction to the distribution function of the electrons as

$$\begin{aligned}
g_k^{m.a2} =&\sin\phi_k\left([\gamma_k^3-\gamma_k][2\cos 2\theta+1]\lambda_{1,1}^{m.s.c}\alpha_2^{m.a2}+\frac{1}{2}[\gamma_k^2-1]\;\lambda_{1,1}^{m.a2.s}\alpha_3^{m.a2}-4\;\lambda_1^{m.s}\gamma_k\sqrt{1-\gamma_k^2}\sin 2\theta\;\alpha_2^{m.a2}\right)\\
&+\frac{1}{2}[\gamma_k^2-1]\;\lambda_{1,1}^{m.a2.c}\;\cos 2\theta\;\alpha_3^{m.a2}\cos\phi_k+\frac{1}{2}\gamma_k\sqrt{1-\gamma_k^2}\;\lambda_{1,1}^{m.a2.c}\;\sin 2\theta\alpha_3^{m.a2}\\
&+\sin\phi_k\left([\gamma_k^3-\gamma_k][2\cos 2\theta+1]\lambda_{2,1}^{m.s.c}\alpha_4^{m.a2}+\frac{1}{2}[\gamma_k^2-1]\;\lambda_{2,1}^{m.a2.s}\alpha_5^{m.a2}-4\;\lambda_2^{m.s}\gamma_k\sqrt{1-\gamma_k^2}\sin 2\theta\;\alpha_4^{m.a2}\right)\\
&+\left(\lambda_{2,1}^{m.s.s}\,[\cos 2\theta+2][\gamma_k-\gamma_k^3]\alpha_4^{m.a2}+\frac{1}{2}\alpha_5^{m.a2}[\gamma_k^2-1]\;\lambda_{2,1}^{m.a2.c}\;\cos 2\theta\right)\cos\phi_k\\
&-\frac{1}{2}\gamma_k\sqrt{1-\gamma_k^2}\;\sin 2\theta(\;2\alpha_4^{m.a2}\gamma_k\lambda_{2,1}^{m.s.s}-\lambda_{2,1}^{m.a2.c}\;\alpha_5^{m.a2}).
\end{aligned} \tag{5.D.10}$$

BIBLIOGRAPHY

[1] S. Das *et al.*, J. Appl. Phys. **93**, 8098 (2003).

[2] S. K. Wong *et al.*, IEEE Trans. Magn. **46**, 2409 (2010).

[3] R. Yu *et. al.*, Science **329**, 61(2010).

[4] X. Kou *et. al.*, Phys. Rev. Lett. Science **113**, 137201(2014).

[5] Y. Xing *et. al.*, New J. Phys. **20**, 043011(2018).

[6] N. Liu,*et al.* Nat. Commun. **9**, 1282(2018).

[7] Y. Ni *et. al.*, IEEE Transactions on Magnetics **52**, 4002304(2016).

[8] D. Culcer, Physica E **44**, 860 (2012).

[9] D. Culcer et al., Phys. Rev. Rev. B **82**, 155457 (2010).

[10] W. Allen, *et al.*, Phy. Rev. B **70**, 125320 (2004).

[11] T. Jungwirth, Phys. Rev. Lett. **88**, 207208 (2002).

[12] Y. Taguchi, Science **291**, 2573 (2001).

[13] H. Ishizuka and N. Nagaosa, Sci. Adv. **4**, 9962 (2018).

[14] Z. Fang *et al.*, Science **302**, 92 (2003).

[15] I. A. Ado *et al.*, EPL **111**, 37004 (2015).

[16] I. A. Ado *et al.*, Phys. Rev. B **96**, 235148 (2017).

[17] D. Culcer and S. D. Sarma, Phys. Rev. B **83**, 245441 (2011).

[18] W. Kohn and J. M. Luttinger, Phys. Rev. **108**, 590 (1957).

[19] R. karplus and J. M. Luttinger, Phys. Rev. **95**, 1154 (1954).

[20] J. M. Luttinger, Phys. Rev. **112**, 739 (1958).

[21] J. Smit, Physica **21**, 877 (1955).

[22] J. Smit, Physica **24**, 39 (1958).

[23] L. Berger, Phys. Rev. B **2**, 4559 (1970).

[24] N. A. Sinitsyn *et al.*, Phys. Rev. B **75** 045315 (2007).

[25] V. Keskin *et al.*, Appl. Phys. Lett. **102**, 022416 (2013).

[26] T. Liang *et al.*, Nature Physics **14**, 451(2018).

[27] W. J. Xu *et al.*, EPL **90**, 27004 (2010).

[28] W. J. Fan *et al.*, J. Phys. D: Appl. Phys. **48**, 195004 (2015).

[29] K. Takahashi *et al.*, Sci. Adv. **4**, 7880 (2018).

[30] A. Popescu *et al.*, Phys. Rev. B **97**, 140407 (2018).

[31] A. Diaz-Fernandez *et al.*, Sci. Rep. **8**, 8058 (2017).

[32] Y. L. Chen *et al.*, Science **329**, 659 (2010).

[33] A. Sabalipour *et al.* J. Phys.: Condens. Matter **27** 115301(2015).

[34] N. A. Sinitsyn, J. Phys.: Condens. Matter **20**, 023201 (2008) .

[35] N. A. Sinitsyn *et al.*, Phys. Rev. B **73**, 075318 (2006).

[36] N. A. Sinitsyn *et al.*, Phys. Rev. B **72**, 045346 (2005).

[37] K. V'yborny *et al.*, Phys. Rev. B **79**, 045427 (2009).

[38] C. Xiao *et a* Phys. Rev.B **95**, 035426 (2017).

[39] G. D. Mahan, *Condensed Matter in a Nutshell* (Princeton University Press, 2011).

[40] G. Rosenberg and M. Franz, Phys. Rev. B **85**, 195119 (2012).

CHAPTER 6

SUMMARY AND OUTLOOK

In the last chapter of my PhD thesis, I summarize my findings that were thoroughly discussed in the preceding chapters, as well as describe ongoing projects and present some proposals for future study.

6.1 Summary

In this doctoral thesis, I have studied in chapter 3 and 4 the longitudinal charge transport in magnetic topological ultra-thin films (MTF), and in chapter 5 the anomalous Hall effect (AHE) on the surface of a magnetic topological insulator (3DMT) is studied. Continuum effective model Hamiltonians were used to characterize the low-energy properties of electrons in these systems. The Boltzmann transport formalism is used to calculate the distribution function of electrons in non-equilibrium conditions. The transport properties of electrons are explored employing this formalism for a system containing short-range, point-like, and randomly arranged magnetic and non-magnetic impurities.

The first chapter describes the topological phases of matter in two and three dimensions and their main characteristics. The Boltzmann continuum model is explained in chapter 2. Because of the strong intrinsic spin-orbit coupling in topological insulators, the interaction between conducting electrons and magnetic impurities is anisotropic. This chapter describes how to use a

modified relaxation time approach to incorporate this anisotropy within the Boltzmann equation and how to solve this equation.

Chapter 3 investigates charge transport in MTF in the absence of the substrate (a free-standing MTF). Because these systems are very thin, the wave functions of electrons in the top and bottom surface states overlap, creating a finite size effect gap between two degenerate bands. However, the magnetic proximity effect of a topological ultra-thin film in contact with a ferromagnet removes this degeneracy and generates two non-degenerate bands. Short-range and randomly distributed dilute magnetic impurities induce a transition selection rule, which controls electrons intraband and interband scatterings. This transition selection rule is quite sensitive to the spin orientation of the magnetic impurities and the Fermi level position. According to our findings, this system has two distinct transport regimes. A dissipationless charge current is achievable if all of the magnetic impurities are arranged in-plane and just one subband participates in charge transport. However, when both conduction subbands contribute to the electronic current, charge transport in a free-standing MTF is always dissipative.

Regardless of the regime in which the system is operating, the found conductivity is extremely sensitive to the direction of the external electric field. In addition, our data propose a criterion for defining a crossover from a 3DMT to a free-standing MTF. When all of the magnetic impurities in a 3DMT are in-plane, the measured charge conductivity is unaffected by the gap. In contrast to this system, the charge conductivity in a MTF with in-plane magnetic impurities is extremely sensitive to the gap. As a result, by varying the system's thickness and then rechecking the sensitivity of the charge conductivity to the gap, the critical thickness of the system for which a crossover from a 3DMT to an MTF happens can be determined.

In chapter 4, we apply the same approach as in chapter 3 to demonstrate how charge transport in a MTF reacts to a substrate or gate voltage. Our calculation reveals two different regimes for charge transport in this system, as seen for a free-standing MTF. Surprisingly, our results demonstrate that even in the presence of a substrate, a dissipationless charge current can be generated. In other words, even if the system contains a large number of

magnetic impurities, electrons do not sense them and carry charge without dissipation. Most significantly, we found that outside of this regime, the response of charge transport to changes in the orientation of the magnetic impurities can be well controlled by the substrate or a gate voltage.

In chapter 5, using the modified Boltzmann continuum approach and a generalized relaxation time approximation, the anomalous Hall conductivity on the surface of a 3DMT is studied in terms of the Fermi level, the mass of the Dirac Fermions, the orientation of the surface magnetization, and the concentration of magnetic and non-magnetic impurities. Three mechanisms are responsible for the anomalous Hall conductivity: the intrinsic effect (owing to a nonzero Berry curvature), the side jump effect, and the skew scattering effect. They compete in different regimes to dominate the anomalous Hall effect.

We calculate the contributions of all three mechanisms to the scattering of massive Dirac fermions by magnetic and nonmagnetic impurities analytically. Our findings for the AHE in this system identify three transport regimes based on the relative importance of the various involved mechanisms. We observed a sign change in the anomalous Hall conductivity not only by changing the Fermi level or the impurity concentration, but also, and surprisingly, by adjusting the spatial orientation of the surface magnetization. Our results explain the physics behind this experimentally observed sign shift.

Since the experimentally observed AHE only gives the total anomalous Hall conductivity and not each of the engaged contributions separately, it is difficult to study each contribution separately. However, our theoretical results can help experimentalists to push the whole system into a regime in which only one mechanism contributes to the AHE, enabling them to investigate just one of the three involved mechanisms.

6.2 Ongoing projects and plans for the future

The charge transport in a MTF is investigated in chapters 3 and 4 in a linear regime where the finite size induced gap is constant. However, experimental findings indicate that when the number of quintuple layers (QL) that are

engaged in the transport varies, the finite size generated gap changes (see reference 5 in chapter 3). Our current ongoing research explores the transport properties of a multilayer of Bi_2Se_3 with thicknesses ranging from one to 50 quintuple layers (QL). When the system thickness varies, the band structure, spin structure, energy gap, and induced gate voltage all change, influencing charge transport. Our results demonstrate that charge transport in this system is significantly different in two regimes: when the system is less than six quintuple layers thick (ultra thin-film regime) and when the system is more than six quintuple layers thick (3D regime).

Furthermore, in another ongoing project, we are examining the effect of asymmetric magnetization on the charge transport in a thick magnetic topological film when it is subjected to a gate voltage. Magnetically doped TIs with different magnetization (for example inward and outward) on opposite sides can serve as an ideal host medium for axion state manifestation. The nontrivial Z_2 index is preserved in axion insulators by inversion symmetry rather than time-reversal symmetry. Axion insulators' naturally gapped surfaces result in a half-quantized surface anomalous Hall conductivity. Note, in each of the studies described in this thesis, the magnetization is oriented in the same direction all across the system.

Aside from these ongoing projects, we are very interested in studying the charge transport of electrons at higher energies. In this thesis, we concentrate on low energy electrical transport. However, terms such as quadratic-in-momentum and anisotropic hexagonal-warping should be included in the effective Hamiltonian beyond this low energy regime. We anticipate that incorporating the hexagonal warping correction of the Fermi surface into our calculation can significantly alter the system's transport characteristics.

CHAPTER 7

SAMENVATTING EN TOEKOMSTIG ONDERZOEK

In het laatste hoofdstuk van mijn doctoraatsthesis vat ik mijn bevindingen samen die grondig werden besproken in de voorgaande hoofdstukken en bespreek ook een aantal lopende projecten en enkele voorstellen voor toekomstig onderzoek.

7.1 Samenvatting

In hoofdstuk 3 en 4 van deze doctoraatsthesis bestudeer ik het longitudinale ladingstransport in magnetische topologische ultra-dinne films (MTF), en in hoofdstuk 5 werd het 'anomalous' Hall-effect (AHE) op het oppervlak van een magnetische topologische isolator (3DMT) bestudeerd. De eigenschappen van elektronen bij lage energie werden beschreven door continue effectieve model Hamiltonianen. Het Boltzmann transportformalisme werd gebruikt om de distributiefunctie van elektronen uit evenwichtstoestand te bepalen. De elektrontransporteigenschappen werden op basis van dit formalisme bestudeerd voor systemen met korte dracht, puntachtige en willekeurig geplaatste magnetische en niet-magnetische onzuiverheden.

Het eerste hoofdstuk beschrijft de topologische fases van materie in twee en drie dimensies en hun belangrijkste eigenschappen. Het Boltzmann formalisme wordt behandeld in hoofdstuk 2. Omdat topologische isolatoren een sterke spin-baan koppeling bezitten, is de interactie tussen geleidende elektro-

nen en magnetische onzuiverheden anisotropisch. Dit hoofdstuk beschrijft hoe een aangepaste relaxatietijd aanpak gebruikt kan worden om deze anisotropie binnen het Boltzmann formalisme te beschrijven en hoe deze vergelijkingen op te lossen.

Hoofdstuk 3 onderzoekt het ladingstransport in een vrijstaande MTF. Omdat deze systemen zeer dun zijn, overlappen de golffuncties van elektronen gelokaliseerd in het bovenste en onderste oppdervlak, en onstaat er een eindige bandkloof in de twee ontaarde banden. Echter, in een topologische ultra dunne film in contact met een ferromagneet zal deze ontaarding verdwijnen door het magnetische nabijheidseffect. Korte dracht en willekeurig verdeelde magnetische onzuiverheden zorgen voor selectieregels, die bepalend zijn voor de intraband en interband elektronenverstrooiingen. Deze selectieregel is zeer gevoelig aan de spinoriëntatie van de magnetische onzuiverheden en de positie van het Ferminiveau. Volgens onze bevindingen heeft dit systeem twee kenmerkende transportregimes. Een dissipatieloze stroom is mogelijk als alle magnetische onzuiverheden in het vlak zijn geöriënteerd en als slechts een subband meedoet aan het ladingstransport. Echter, wanneer beide conductiesubbanden bijdragen aan de elektronenstroom is het ladingstransport in een vrijstaande MTF steeds dissipatief.

Onafhankelijk van het regime waarin het systeem zich bevindt, blijkt de conductiviteit extreem gevoelig te zijn aan de richting van het extern aangelegd elektrisch veld. Daarnaast kon een criterium opgesteld worden om de overgang van een 3DMT naar een vrijstaande MTF te definiëren. Voor een 3DMT geldt dat als alle magnetische onzuiverheden in het vlak liggen, de gemeten ladingsgeleiding niet beïnvloed wordt door de bandkloof. Echter in een MTF met magnetische onzuiverheden georiënteerd in het vlak blijkt het ladingstransport net heel gevoelig te zijn aan de bandkloof. Als gevolg kan door het variëren van de dikte van het systeem en het testen van de afhankelijkheid van het ladingstransport aan de bandkloof de kritische dikte bepaald worden die de overgang van een 3DMT naar een MTF aangeeft.

In hoofdstuk 4 wordt dezelfde aanpak als in hoofdstuk 3 gebruikt om te bestuderen hoe ladingstransport in een MTF verandert door de aanwezigheid van een substraat of door een aangelegde gate spanning. Onze resultaten

tonen aan dat nog steeds een dissipatieloze ladingsstroom kan gegenereerd worden. Daarnaast vonden we dat buiten dit regime de respons van het ladingstransport op veranderigen in de oriëntatie van de magnetische onzuiverheden goed gecontroleerd kan worden door zo'n gate spanning.

In hoofdstuk 5 werd op basis van de aangepaste Boltmann continuum aanpak en de veralgemeende relaxatietijd benadering de 'anomalous' Hall conductiviteit op het oppervlak van een 3DMT bestudeerd als functie van het Ferminiveau, de massa van de Dirac fermionen, de oriëntatie van de oppervlaktemagnetisatie en de concentratie aan magnetische en niet-magnetische onzuiverheden. Drie mechanismen zijn verantwoordelijk voor het 'anomalous' Hall effect (AHE): het intrinsieke effect (t.g.v. een Berry kromming die niet verdwijnt), het 'side jump' effect en het 'skew scattering' effect. Zij domineren het AHE in verschillende regimes.

De verschillende bijdragen van elk mechanisme tot de verstrooiing van massieve Dirac fermionen door magnetische en niet-magnetische onzuiverheden werden analytisch uitgerekend. Onze resultaten tonen dat er ook drie verschillende transportregimes geïdentificeerd kunnen worden op basis van het relatieve belang van de verschillende mechanismen. Daarnaast werd een tekenverandering geobserveerd in de 'anomalous' Hall geleiding die niet enkel geïnduceerd kan worden door het Ferminiveau of de concentratie aan onzuiverheden, maar ook door de oriëntatie van de oppervlaktemagenisatie. Deze inzichten verklaren ook de experimenteel geobserveerde tekenverandering.

Aangezien experimenteel steeds de totale 'anomalous' Hall geleiding gemeten wordt en niet elke bijdrage apart, is het ook moeilijk om de verschillende mechanismen apart te bestuderen. Echter, onze theoretische resultaten kunnen experimentatoren helpen om het volledige systeem in een welbepaald regime te brengen waarin slechts één mechanisme bijdraagt tot het AHE, om zo wel te kunnen focussen op slechts één bijdrage.

7.2 Lopende projecten en toekomstig onderzoek

Het ladingstransport in een MTF werd in hoofdstuk 3 en 4 onderzocht in een lineair regime en waarbij de geïnduceerde bandkloof constant is. Echter, experimenteel vindt men dat wanneer het aantal 'quintuple' lagen (QLs) betrokken in het transport verandert, ook de geïnduceerde bandkloof verandert. Momenteel onderzoeken we daarom de transporteigenschappen van een multilaag Bi_2Se_3 waarbij de dikte varieert van 1 tot 50 QLs. Als de dikte verandert, verandert de bandenstructuur, de spinstructuur, de energiekloof en de geïnduceerde gate spanning, hetgeen het ladingstransport zal wijzigen. Onze resultaten tonen aan dat in dit systeem twee duidelijke regimes kunnen onderscheiden worden: het ultra-dunne regime waarbij het systeem minder dan 6 QLs dik is, en het 3D regime als het systeem dikker is.

Daarenboven onderzoeken we de invloed van asymmetrische magnetisatie op het ladingstransport in een dikke magnetische topologische film met een aangelegde gate spanning. Magnetisch gedopeerde TIs met tegengestelde magnetisatie op tegenoverliggende oppervlakken vormen een excellent host medium voor de axion-toestand. Axion-toestanden trekken heel wat aandacht omdat hun niet-triviale Z_2 index behouden wordt via inversiesymmetrie in plaats van tijdsomkeersymmetrie. Het is intrigerend dat de gegapte oppervlaktetoestanden van axion-isolatoren leiden tot een half-gekwantiseerde oppervlakte 'anomalous' Hall geleiding.

Daarnaast wensen we ook het ladingstransport te exploreren van elektronen bij hogere energieën, waar we in deze thesis nog focussen op lage-energie fysica. Termen kwadratisch in de impuls en anisotrope hexagonale warping moeten dan mee in rekening gebracht worden. We anticiperen dat het in rekening brengen van de hexagonale warping een grote invloed zal hebben op de transportkarakteristieken.

LIST OF PUBLICATIONS

- *Amir Sabzalipour, Moslem Mir, Mohammad Zarenia and Bart Partoens*,"Charge transport in magnetic topological ultra-thin films: the effect of structural inversion asymmetry", ***Journal of Physics: Condensed Matter 33, 325702 (2021)***.
- *Amir Sabzalipour, Moslem Mir, Mohammad Zarenia and Bart Partoens*,"Two distinctive regimes in the charge transport of a magnetic topological ultra thin film", ***New Journal of Physics 22, 123004 (2020)***.
- *Amir Sabzalipour and Bart Partoens*, "Anomalous Hall effect in magnetic topological insulators: Semiclassical framework", **Physical Review B *100*, 035419 (2019)**.
- *Amir Sabzalipour, Jahanfar Abouie, Saeed Abedinpour*, "Anisotropic conductivity in magnetic topological insulators", **Journal of Physics: Condensed Matter *27*, 115301 (2015)**.
- *Amir Sabzalipour, et al.* , "Thickness-dependent evolution of the charge transport of 3D topological insulator Bi_2Se_3 film with a thickness from one quintuple layer (QL) to 6 QL.", In preparation.
- *Amir Sabzalipour, et al.* , "Charge transport in thick topological films with asymmetric magnetization on opposite surfaces", In preparation.